# Modeling and flow dynamics of dilute wormlike micelle solutions

by

Richard J. Hommel

A dissertation submitted in partial fulfillment of

the requirements for the degree of

Doctor of Philosophy

(Chemical and Biological Engineering)

at the

UNIVERSITY OF WISCONSIN - MADISON

2024

Date of final oral examination: February 26, 2024

This dissertation is approved by the following members of the Final Oral Committee:

Michael D. Graham, Professor, Chemical and Biological Engineering

Reid C. Van Lehn, Associate Professor, Chemical and Biological Engineering

Whitney Loo, Assistant Professor, Chemical and Biological Engineering

Jennifer Franck, Assistant Professor, Mechanical Engineering

*In loving memory of Dexter.*

# Acknowledgments

There are so many people who, through their love and support, have played a role in the successful completion of this thesis and life chapter. I am fortunate to have occupied this place at this time with so many people who have made this journey not only possible, but worth it.

I am forever grateful to my family, who have supported, celebrated, and encouraged me throughout this journey. Even at a distance, I have never felt absent of your love. Thank you for trusting me to see this chapter through, and giving me the support to do so.

To Mike Graham, it has been a privilege and joy to work with you. You have been and continue to be my role model, both in science and life. I am so thankful for the guidance you have given, the knowledge you have shared, and the patience you have offered. I have confidence as a researcher and scientist because of you.

To my Committee, although not the same as it started, thank you for seeing me to the end. You have challenged my ideas and offered new perspectives, and I am grateful for the opportunity to learn from, and share my research with, you.

To Joelle Frechette, thank you for the encouragement and support to pursue a PhD. I will always be grateful to you for allowing a young, clueless student with no research experience to join your group. You are an inspiration and a role model, and I am thankful for your advocacy and guidance.

I am eternally grateful to Kevin Zeng for sharing your empathy, humility, and brilliance; you are the embodiment of an exceptional scientist and a life-long friend. You have kept me

grounded and driven, and I am so thankful to call you my friend.

To Carlos Pérez De Jesús, I am so fortunate that of all the people in this world I was able to share this journey with you. You are passionate and balanced, and the most supportive friend anyone could ask for. I am excited to see all the ways you brighten this world.

To Bryce Connors, thank you for keeping me sane, socialized, and fed during a global pandemic. To Ricardo Constante-Amores, I am grateful for your friendship and the compassion and support you have given me. To Eric Yu, you are driven and definition of a caring friend. To Alec Linot, you are brilliant and embody perseverance; you have shown me to balance hard work with life and hobbies, and I am so thankful to have learned from you.

I am grateful to everyone who I have been fortunate enough to spend time with in the Graham Group. Ashwin Shekar, you were an amazing and supportive mentor. To Daniel Floryan, Xiao Zhang, Xiaopo Cheng, Alex Guo, Charlie Young, Andrew Fox, Manish Kumar, and Jake Buzhardt I am grateful to have shared knowledge and friendships with all of you.

To Erin Toohey, I am constantly in awe of your ability to uplift those around you. The support, love, and attentiveness you share can make anyone feel like the most important person in the world. I am so thankful for your friendship, and I look forward to the endless years of laughs, brunches, and joy we will share.

To Zach Oliver, I am thankful for you. You are my loudest cheerleader, even when it feels like there is nothing to cheer for. Thank you for listening to every story that runs long and every small detail of an unimportant day. Thank you for sharing Freddie and Blue. Thank you for your laughs and dances, and your love and patience. Every time I have doubted myself, every time I have faltered, every time I have wondered if this journey is worth it, there you are. How fortunate I am to have ended up here with you.

Finally, I am forever grateful to my plants; you have taught me patience, you have taught me the simple joys of a new leaf and a budding flower, you have taught be balance and steadiness, you have taught me to be resilient but flexible, and you have taught me that growth does not always come from where you expect.

# Abstract

Surfactant solutions are found in numerous commercial and industrial applications, from detergents and cosmetics to fracking and heat-transfer fluids. Surfactant solutions that form wormlike micelles are found to display complex rheological behavior and exhibit many instabilities ranging from finger-like structures to vorticity banding. These solutions have also been found to display drag reduction at levels comparable to, and in some cases exceeding, those of polymer solutions. Despite their practical importance and a plethora of experiments demonstrating their interesting rheology, the dynamics and flow behaviors of wormlike micelle solutions remain poorly understood, particularly from theoretical and computational perspectives. There are currently few models able to predict and capture dilute wormlike micelle rheology, and even fewer that can be implemented in computational fluid dynamics simulations. Motivated by this lack and the numerous applications for these solutions, the main objectives in this thesis are to develop an accurate and tractable model for dilute wormlike micelle solutions and to use this model in simulations to study complex flow phenomena.

In Chapter 1, we introduce many of the concepts associated with viscoelastic fluids and motivate this study by exploring applications of dilute wormlike micelle solutions. We then dive into the chemistry of wormlike micelle solutions, before giving an overview of their complex rheology and the numerous instabilities that can develop in these flows. Since much of this thesis is focused on the development of models for wormlike micelle solutions, we summarize the derivations and predictions of some of the most widely studied models for

these systems and focus on their successes and drawbacks.

In Chapter 2, we derive a model for dilute wormlike micelle solutions, the reformulated reactive rod model (RRM-R); the RRM-R, which treats micelles as reactive Brownian rods undergoing reversible scission and fusion, is an improvement to a previous model (the RRM) meant to establish the model on a more physical grounding. We show that the model can predict many of the key rheological features of dilute wormlike micelle solutions: shear-thickening and -thinning, non-zero normal stress differences, and a reentrant flow curve. We demonstrate the ability of the RRM-R to predict both steady and transient dynamics, affirming its potential for studying instability formation, and show that it can be successfully fit to experimental data.

After having derived and established the RRM-R, we then employ it in Chapter 3 to study the development of instabilities in circular Couette flow. We apply a stability analysis of the steady states and find that the spatial-dependence of the stress gives rise to flow profiles with mixed local stabilities. Using simulations we find that the RRM-R captures finger-like instabilities, which consist of branching structures of highly elongated, anisotropically-oriented micelles. These 'fingers' have previously been identified in experiments of dilute wormlike micelle solutions. The instability is identified to be 2D in nature, with 3D variations arising as secondary effects. We also show that the RRM-R can capture vorticity banding, and that this banded state is linearly stable to perturbations.

In Chapter 4 we extend the works of the previous chapter to focus on plane Poiseuille flow of dilute wormlike micelle solutions. The spatial-dependence of the stress causes the flow to 'jump' between upper and lower branches of the constitutive curve, giving rise to a state that resembles viscosity-stratified flows. As has been observed for viscosity-stratified flows, we find that the 'interface' between regions is unstable due to a combination of viscosity mismatch and a normal stress jump across the interface. The destabilized flow fluctuates around the unstable region of the constitutive curve. The resulting instability resembles the finger-like structures observed in circular Couette flow, but now both longwave and

shortwave structures appear; the longwave structures are observed to resemble mushroom patterns seen in core-annular channel flow. We perform 3D simulations and find that the initial instability is 2D.

We switch gears in Chapter 5 to focus on deriving a thermodynamically consistent version of the RRM-R. There has been a recent push in the rheology community to re-derive many well-studied models for viscoelastic fluids, as well as derive new models, using the generalized bracket framework of non-equilibrium thermodynamics; this framework allows researchers to enforce conservation of energy and non-negative entropy generation in these models. Motivated by this push, we use the single generator bracket framework of non-equilibrium thermodynamics to derive three models, two based on the general evolution and relaxation of a structural variable and a third that considers the dynamics of micelles as a reversible reaction. We employ Poisson and dissipation brackets along with a description of the system Hamiltonian to ascertain and ensure the thermodynamic admissibility of these models. This section also provides a substantial background into applying non-equilibrium dynamics to fluid systems.

Finally, we conclude this thesis with a summary of our findings and proposals for future directions in Chapter 6. These future directions are focused on (1) improvements to the RRM-R to account for micelle flexibility and population distributions, (2) investigating the RRM-R in new flow types and domains, and (3) using the RRM-R to study more complex instabilities, turbulence, and drag reduction in dilute wormlike micelle solutions.

# Contents

**1 General introduction** **1**

1.1 Introduction to viscoelastic fluids . . . . . 3

1.1.1 Drag reduction . . . . . 7

1.2 Introduction to wormlike micelles . . . . . 8

1.2.1 Composition and chemistry . . . . . 9

1.2.2 Rheology and instabilities . . . . . 12

1.3 Modeling wormlike micelle solutions . . . . . 16

1.3.1 Cates and Turner . . . . . 17

1.3.2 Vasquez-Cook-McKinley . . . . . 20

1.3.3 Bautista-Manero-Puig . . . . . 23

1.3.4 Brownian rods . . . . . 25

1.3.5 Reactive rod model . . . . . 29

1.4 Outline of this work . . . . . 34

**2 Constitutive modeling of dilute wormlike micelle solutions** **36**

2.1 Introduction . . . . . 37

2.2 Model description . . . . . 42

2.2.1 Rigid Brownian rods . . . . . 43

2.2.2 Reactive Brownian rods . . . . . 44

2.2.3 Reactive rod model (RRM) . . . . . 46

2.2.4 Reformulated reactive rod model (RRM-R) . . . . . 46
2.2.5 Shear flow . . . . . 53
2.2.6 Uniaxial extensional flow . . . . . 54
2.3 Results and Discussion . . . . . 55
2.3.1 Steady shear: parameter dependence . . . . . 56
2.3.2 Steady shear: experimental comparison . . . . . 61
2.3.3 Startup of steady shear . . . . . 65
2.3.4 Uniaxial extension: experimental comparison . . . . . 72
2.4 Conclusions . . . . . 73

**3 Instabilities in circular Couette flow with a reentrant flow curve 75**
3.1 Introduction . . . . . 75
3.2 Governing equations . . . . . 82
3.2.1 Brownian rods . . . . . 83
3.2.2 RRM-R . . . . . 84
3.2.3 Circular Couette flow . . . . . 88
3.2.4 Circular Couette flow: steady state . . . . . 90
3.3 Computational methods . . . . . 92
3.4 Results and Discussion . . . . . 93
3.4.1 Steady states in reentrant WLM solutions . . . . . 94
3.4.2 Finger-like instabilities in 2D . . . . . 101
3.4.3 Finger-like instabilities in 3D . . . . . 112
3.4.4 Vorticity banding . . . . . 119
3.5 Conclusions . . . . . 122
3.6 Appendix A: Additional figures for CCF . . . . . 125

**4 Interfacial instabilities in plane Poiseuille flow 129**
4.1 Introduction . . . . . 130

4.2 Governing equations . . . 139
4.2.1 Brownian rods . . . 140
4.2.2 RRM-R . . . 141
4.2.3 Plane Poiseuille flow . . . 143
4.3 Computational methods . . . 145
4.4 Results and Discussion . . . 146
4.4.1 Reentrant plane Poiseuille flow . . . 147
4.4.2 Convection-free interfacial instabilities in 2D . . . 149
4.4.3 Interfacial instabilities with convection in 2D . . . 164
4.4.4 Convection-free interfacial instabilities in 3D . . . 170
4.5 Conclusions . . . 174
4.6 Appendix A: Additional figures for PPF . . . 176

**5 Modeling using non-equilibrium thermodynamics 179**

5.1 Introduction . . . 181
5.2 SGBF-NET Formalism . . . 185
5.2.1 Identification of state variables . . . 187
5.2.2 Defining the Hamiltonian . . . 187
5.2.3 Formulation of the Poisson bracket . . . 188
5.2.4 Formulation of the dissipation bracket . . . 189
5.2.5 Derivation of the governing equations . . . 191
5.2.6 Verification of thermodynamic admissibility . . . 193
5.3 Reformulated reactive rod model (RRM-R) . . . 194
5.3.1 Brownian rods . . . 194
5.3.2 RRM-R . . . 196
5.4 Structural model - A (SM-A) . . . 198
5.5 Structural model - B (SM-B) . . . 210
5.6 Structural model - C (SM-C) . . . 212

5.7 Conclusions . . . . . 221

**6 Conclusions and Future Work** **222**

6.1 General summary . . . . . 222

6.2 Future work . . . . . 224

6.2.1 Effects of the RRM-R flow curve on instabilities . . . . . 224

6.2.2 Instabilities in other geometries . . . . . 228

6.2.3 Linear stability analysis . . . . . 239

6.2.4 Effects of inertia on finger-like instabilities . . . . . 240

6.2.5 Improvements to the RRM-R . . . . . 242

6.2.6 Drag reduction and elastoinertial turbulence . . . . . 243

**References** **245**

# List of Figures

1.1 Representative flow curves for different non-Newtonian fluids on (a) shear stress ($\tau_{xy}$) vs. shear rate ($\dot{\gamma}$) and (b) viscosity ($\eta$) vs. shear rate curves. . . 6

1.2 Friction factor vs. Reynolds number for a variety of polymer and surfactant systems [1, 2]. . . . . 8

1.3 Representative flow curves for fluids that can support (a) shear banding and (b) vorticity banding. The curve in (a) shows a shear rate that is a multivalued function of shear stress, while (b) shows a shear stress that is a multivalued function of shear rate. The blue areas indicate regions of the flow curve that are multivalued and can support banding. . . . . 13

1.4 Schematic of a rigid rod with length $L$ and director $\mathbf{u}$ subject to an imposed velocity gradient $\mathbf{K} = \boldsymbol{\nabla}\mathbf{v}$. . . . . 18

1.5 Steady shear flow curves for the RRM with $\alpha = 5$, $\beta = 500$, and varying $k$; (a) normalized viscosity, (b) micelle shear stress, (c) micelle length, and (d) orientation parameter. Figure based on [3]. . . . . 33

2.1 Normalized micellar viscosity vs. shear rate in simple shear flow: (a) effect of $a$, (b) effect of $k_{ga}$, (c) effect of $k_{b0}$, and (d) effect of $k_{bt}$ with $m = 3$ and $D_{r,0} = 1$. . . . . 56

2.2 Mean micelle length normalized by equilibrium length vs. shear rate in simple shear flow: (a) effect of $a$, (b) effect of $k_{ga}$, (c) effect of $k_{b0}$, and (d) effect of $k_{bt}$ with $m = 3$ and $D_{r,0} = 1$. . . . . 58

2.3 Normalized first normal stress difference vs. shear rate in simple shear flow: (a) effect of $a$, (b) effect of $k_{ga}$, (c) effect of $k_{b0}$, and (d) effect of $k_{bt}$ with $m = 3$ and $D_{r,0} = 1$. . . . . 59

2.4 Fits (lines) to experimental data of (a) shear viscosity vs. shear rate and (b) mean micelle length vs. shear rate. Experimental data corresponds to solutions of 250 ppm, 500 ppm, and 1000 ppm CTAB/NaSal in water obtained by Liu and Pine [4]. Corresponding parameter values are shown in Table 2.1. 63

2.5 Fits (lines) to experimental data of (a) shear viscosity vs. shear rate and (b) mean micelle length vs. shear rate. Experimental data corresponds to solutions of (red) 1000 ppm CTASal in water obtained by Ohlendorf et al. [5], and (purple) 1500 ppm and (blue) 1000 ppm ODMAO in water obtained by Tamano et al. [6]. Corresponding parameter values are shown in Table 2.2. . 65

2.6 Micellar contribution to the shear viscosity (normalized by zero-shear viscosity), ensemble average orientation components, and normalized length vs. dimensionless time in transient startup of steady shear flow for a range of applied Pe numbers. Both sets of parameters in (a)-(e) and (b)-(f) yield equivalent steady states but varying transient behavior. . . . . 67

2.7 Micellar contribution to the shear viscosity (normalized by zero-shear viscosity), ensemble average orientation components, and normalized length vs. dimensionless time in transient startup of steady shear flow for a range of applied Pe numbers clearly demonstrating stress-overshoot phenomenon. . . 69

2.8 Fits (lines) to experimental data (symbols) of (a) shear viscosity vs. shear rate and (b) micelle length vs. shear rate. Experimental data corresponds to solutions of (green) $0.05wt\%$ and $0.1wt\%$ CTAVB in water obtained by Landàzuri et al. [7]. Corresponding parameter values are shown in Table 2.3. 71

2.9 (a) Fits (lines) to experimental data of transient shear induction time vs. shear rate for solutions of $0.05wt\%$ and $0.1wt\%$ CTAVB in water and (b) corresponding transient viscosity growth vs. time response for the $0.05wt\%$ solution (blue). Experimental data was obtained by Landàzuri et al. [7]. Corresponding parameter values are shown in Table 2.3. . . . . 72

2.10 Fits (lines) to experimental data of extensional viscosity vs. strain rate for dilute (red) and semi-dilute (blue) CPyCl/NaSal solutions undergoing steady uniaxial extensional flow [8]. Corresponding parameter values are shown in Table 2.4. . . . . 73

3.1 Example of a reentrant flow curve in which there is a region where the shear stress, $\tau_{xy}$, is a multivalued function of the shear rate, $\dot{\gamma}$. The light blue area shows the reentrant region of the flow curve. . . . . 78

3.2 Schematic of circular Couette geometry. Left: top-down ($r\theta$) view of domain. Right: side view of domain. . . . . 90

3.3 Constitutive curves for the RRM-R with parameters: $m = 3$, $k_{b0} = 10^{-2}$, $k_{ga} = 1500$, $k_{bt} = 10$, and $a = 2.5$. (a) Micelle (red), Newtonian (blue), and total shear stress (purple), (b) length of micelles, (c) components of the orientation tensor, and (d) normalized viscosity vs. applied Péclet number. . 95

3.4 Upper and lower branch steady states for Pe = 0.01 at varying curvatures. (a) Local micelle shear stress and (b) local micelle length projected onto the governing constitutive curves, where the local Péclet number, $\mathrm{Pe}_l$, is calculated from the velocity profile throughout the gap. (c) Local micelle shear stress and (d) local micelle length over the gap radius. Line colors are red: $\epsilon = 1.00$, orange: $\epsilon = 0.50$, green: $\epsilon = 0.20$, and blue: $\epsilon = 0.10$. The yellow rectangle indicates the unstable region of the flow curve ($\partial\tau^m_{r\theta}/\partial\dot{\gamma} < 0$). . . . . 98

3.5 Shear rate-curvature state-space stability diagram. Dashed lines show the existence limits for the lower (cyan) and upper (orange) branches respectively. The cyan markers are the maximum Pe on the lower branch that will support a steady state; all Pe on the lower branch below this line are stable, shown by the cyan-shaded region. The orange markers are the minimum Pe on the upper branch that will support a steady state; all Pe on the upper branch above this line are stable, shown by the orange-shaded region. In the green-shaded region both the lower and upper branches exist and are stable. In the yellow-shaded region both the lower and upper branches are unstable or do not exist. The stars show the local shear stress profiles across the gap at the indicated Pe and $\epsilon$. . . . . 100

3.6 Steady state local constitutive curve for $\epsilon = 1$. The red markers are the micelle shear stress at the inner cylinder, and the blue markers are the micelle shear stress at the outer cylinder. The dashed red and blue lines represent steady states that were not explicitly calculated. The purple vertical lines connecting the markers show the local micelle shear stress throughout the gap at that Pe. The yellow rectangle shows the region where, at a given Pe, the flow will fall into the locally unstable region. . . . . 102

3.7 Upper and lower branch steady states for Pe = 0.0225 at $\epsilon = 1$. (a) Local micelle shear stress and (b) local micelle length projected onto the governing constitutive curves, where the local Péclet number, $\mathrm{Pe}_l$, is calculated from the velocity profile throughout the gap. (c) Local micelle shear stress and (d) local micelle length over the gap radius. The orange line corresponds to the upper branch and the cyan line corresponds to the lower branch. The yellow rectangle indicates the unstable region where $\partial\tau_{r\theta}^m/\partial\dot{\gamma} < 0$. . . . . 103

3.8 Snapshots of (top) micelle length, (middle) micelle orientation, and (bottom) radial velocity in start-up of steady shear flow with applied shear rate Pe = 0.0225. . . . . 106

3.9 Snapshots of micelle length in start-up of steady shear flow with applied shear rate Pe = 0.024. . . . . 107

3.10 Snapshot of micelle length with contours at blue: $L = 8$, yellow: $L = 9$, and red: $L = 10$ for start-up of steady shear flow with Pe = 0.024. . . . . 108

3.11 Upper and lower branch steady states for Pe = 0.015 at $\epsilon = 1$. (a) Local micelle shear stress and (b) local micelle length projected onto the governing constitutive curves, where the local Péclet number, $\mathrm{Pe}_l$, is calculated from the velocity profile throughout the gap. (c) Local micelle shear stress and (d) local micelle length over the gap radius. The orange line corresponds to the upper branch and the cyan line corresponds to the lower branch. The yellow rectangle indicates the unstable region where $\partial\tau_{r\theta}^m/\partial\dot{\gamma} < 0$. . . . . 109

3.12 Snapshots of (top) micelle length, (middle) micelle orientation, and (bottom) radial velocity for decreasing shear flow from an applied shear rate of Pe = 0.04 to Pe = 0.015. . . . . 110

3.13 Top row: Snapshots of micelle length for decreasing shear flow from an applied shear rate of Pe = 0.015 to Pe = 0.01. Bottom row: Snapshots of micelle length for decreasing shear flow from an applied shear rate of Pe = 0.025 to Pe = 0.01. . . . . 112

3.14 Snapshots of micelle length for increasing shear flow from rest to an applied shear rate of Pe = 0.0225 in a 3D domain with $R_I = 1$ and $h = 0.2$. Top: $r\theta$-slice at $z = 0$ and bottom: $r\theta$-slice at $z = 0.1$. . . . . 115

3.15 Snapshots of the radial velocity for increasing shear flow from rest to an applied shear rate of Pe = 0.0225 in a 3D domain with $R_I = 1$ and $h = 0.2$. Top: $r\theta$-slice at $z = 0$ and bottom: $r\theta$-slice at $z = 0.1$. . . . . 115

3.16 Snapshots of micelle length in the $rz$-plane at $\theta = \pi$ for increasing shear flow from rest to an applied shear rate of Pe = 0.0225 in a 3D domain with $R_I = 1$ and $h = 0.2$. The stationary inner cylinder is on the left and the rotating outer cylinder is on the right. . . . . 116

3.17 Structures of micelle length for increasing shear flow from rest to an applied shear rate of Pe = 0.0225 in a 3D domain with $R_I = 1$ and $h = 0.2$. Top: $t = 40$, middle: $t = 50$, and bottom: $t = 60$. Structures show regions of $L \geq 5$, indicating substantial micelle elongation. . . . . 116

3.18 Snapshots of micelle length when decreasing the shear rate from Pe = 0.04 to Pe = 0.015 in a 3D domain with $R_I = 1$ and $h = 0.2$. . . . . 118

3.19 Snapshots of micelle length in the $rz$-plane at $\theta = \pi$ for decreasing the shear rate from Pe = 0.04 to Pe = 0.015 in a 3D domain with $R_I = 1$ and $h = 0.2$. The stationary inner cylinder is on the left and the rotating outer cylinder is on the right. . . . . 118

3.20 Steady state local micelle shear stress vs. applied Péclet number for $\epsilon = 0.1$. The red markers are the micelle shear stress at the inner cylinder, and the blue markers are the micelle shear stress at the outer cylinder. The dashed red and blue lines represent steady states that were not explicitly calculated. The purple vertical lines connecting the markers show the local micelle shear stress throughout the gap at that Pe. The yellow rectangle shows the region where, at a given Pe, the flow will fall into the locally unstable region. . . . . 120

3.21 Snapshots of the final (a) length, (b) $S_{r\theta}$, and (c) azimuthal velocity for a vorticity banded initial condition. The curvature is $\epsilon = 0.1$, the height is $h = 1$, and the applied shear rate is $\mathrm{Pe} = 0.01$. The rotating outer cylinder is on the right. . . . . 122

3.22 Plots of final (a) length, (b) $S_{r\theta}$, and (c) azimuthal velocity over the cylinder height at different radial locations for a vorticity banded initial condition. Orange: $r = R_I + 0.1d$ and cyan: $r = R_I + 0.5d$. The curvature is $\epsilon = 0.1$, the height is $h = 1$, and the applied shear rate is $\mathrm{Pe} = 0.01$. . . . . 123

3.23 Plots of deviation from steady state values for (a) length and (b) $S_{r\theta}$ over time after some small random perturbation to a steady vorticity banded state with $\epsilon = 0.1$, $h = 1$, and $\mathrm{Pe} = 0.01$. . . . . 123

3.24 Upper and lower branch steady states for $\mathrm{Pe} = 0.0225$ at varying curvatures. (a) Local micelle shear stress and (b) local micelle length projected onto the governing constitutive curves, where the local Péclet number, $\mathrm{Pe}_l$, is calculated from the velocity profile throughout the gap. (c) Local micelle shear stress and (d) local micelle length over the gap radius. Line colors are red: $\epsilon = 1.00$, orange: $\epsilon = 0.50$, green: $\epsilon = 0.20$, and blue: $\epsilon = 0.10$. The yellow rectangle indicates the unstable region of the flow curve ($\partial \tau^m_{r\theta} / \partial \dot{\gamma} < 0$). . . . . 127

3.25 Plot of micelle length over $\theta$ at $t = 40$ and $r = R_I + 0.1d$ for start-up of steady shear flow with an applied shear rate of Pe = 0.0225. The orange line corresponds to the M2 mesh and the cyan to the M3 mesh. . . . . 127

3.26 Micelle length over $\theta$ at $t = 40$ and $r = R_I + 0.1d$ for start-up of steady shear flow with an applied shear rate of Pe = 0.0225 in 2D (orange) and 3D (cyan). The 3D slice is taken at $z = 0$, but the flow here shows no $z$-dependence. . . 128

4.1 (Reproduced from Section 3.1) Example of a reentrant flow curve in which there is a region where the shear stress, $\tau_{xy}$, is a multivalued function of the shear rate, $\dot{\gamma}$. The light blue area shows the reentrant region of the flow curve. 132

4.2 Schematic of plane Poiseuille geometry. . . . . 145

4.3 (Reproduced from Section 3.4.1) Constitutive curves for the RRM-R with parameters: $m = 3$, $k_{b0} = 10^{-2}$, $k_{ga} = 1500$, $k_{bt} = 10$, and $a = 2.5$. (a) Micelle (red), Newtonian (blue), and total shear stress (purple), (b) length of micelles, (c) components of the orientation tensor, and (d) normalized viscosity vs. applied Péclet number. . . . . 148

4.4 Steady state (a) micelle length and (b) streamwise velocity for PPF at Pe = 0.01. 150

4.5 Steady state (a) local micelle length and (b) local micelle shear profiles vs. local Pe superimposed onto the governing constitutive curves for (cyan) Pe = 0.01 and (orange) Pe = 0.015. . . . . 151

4.6 Snapshots of micelle length for start-up PPF with an applied shear rate of Pe = 0.04. . . . . 153

4.7 Snapshots of streamwise velocity for start-up PPF with an applied shear rate of Pe = 0.04. . . . . 153

4.8 (a) Local streamwise velocity and (b) local shear rate profiles across the channel over several time points and at $x = 1.5$ for start-up PPF with an applied shear rate of Pe = 0.04. . . . . 154

4.9 Snapshots of wall-normal velocity for start-up PPF with an applied shear rate of Pe = 0.04. . . . . 155
4.10 Snapshots of micelle length for start-up PPF with an applied shear rate of Pe = 0.04. . . . . 157
4.11 Snapshots of micelle length with overlays of streamwise velocity contours for start-up PPF with an applied shear rate of Pe = 0.04. . . . . 158
4.12 Snapshots of first column: micelle shear stress, second column: micelle length, third column: first normal stress difference, and fourth column: vorticity for start-up PPF with an applied shear rate of Pe = 0.04. . . . . 159
4.13 Several time points of (a) local micelle length and (b) local micelle shear vs. local Pe profiles projected onto the governing constitutive curves for Pe = 0.04. 160
4.14 Snapshots of micelle length for start-up PPF with an applied shear rate of Pe = 0.06. . . . . 162
4.15 Snapshots of streamwise velocity at later times for start-up PPF with an applied shear rate of Pe = 0.06. . . . . 163
4.16 Snapshots of micelle length in different box lengths, $l$, for start-up PPF with an applied shear rate of Pe = 0.04. . . . . 163
4.17 Streamwise-averaged (a) micelle length and (b) micelle shear stress sampled at $y = 0.5$ for varying Re with Pe = 0.04. . . . . 166
4.18 (a) Local streamwise velocity and (b) local shear rate profiles across the channel over several time points and at $x = 1.5$ for start-up PPF with an applied shear rate of Pe = 0.04 and Re = 100. . . . . 166
4.19 Snapshots of micelle length for start-up PPF with an applied shear rate of Pe = 0.04 and Re = 0.01. . . . . 167
4.20 Snapshots of micelle length for start-up PPF with an applied shear rate of Pe = 0.04 and Re = 100. . . . . 169

4.21 Snapshots of micelle length in 3D for start-up PPF with an applied shear rate of Pe = 0.04. Time points are indicated above each snapshot; each snapshot shows the a slice in the $xy$-plane on the left, taken at $z = 0.05$, and a slice in the $yz$-plane on the right, taken at $x = 0$. The length is $l = 3$ with width $w = 0.1$. . . . . 171

4.22 Structures of micelle length in 3D for start-up PPF with an applied shear rate of Pe = 0.04. Time points are indicated above each snapshot. The length is $l = 3$ with width $w = 0.1$. Only the lower half of the domain ($y \leq 0$) is shown for clarity. Structures show regions of $L \geq 5$, indicating substantial micelle elongation. . . . . 172

4.23 Snapshots of micelle length for start-up PPF with an applied shear rate of Pe = 0.04. The first column shows simulations run with the M1 mesh, the second column the M2 mesh, and the third column shows simulations run with the M3 mesh. . . . . 177

4.24 Intermediate time snapshots of first column: micelle shear stress, second column: micelle length, third column: first normal stress difference, and fourth column: vorticity for start-up PPF with an applied shear rate of Pe = 0.04. . 178

4.25 Snapshots of micelle length for start-up PPF with an applied shear rate of Pe = 0.03. . . . . 178

6.1 Constitutive curves for the RRM-R with parameters: $m = 3$, $k_{b0} = 10$, $k_{ga} = 1200$, $k_{bt} = 7$, and $a = 3.5$. (a) Micelle (red), Newtonian (blue), and total shear stress (purple), (b) length of micelles, (c) components of the orientation tensor, and (d) normalized viscosity vs. applied Péclet number. . . . . 225

6.2 Steady state (a) total shear stress, (b) micelle length, (c) $S_{r\theta}$, and (d) $S_{\theta\theta}$ in circular Couette flow for varying curvatures (different line styles) at Pe = 2. The dashed black line corresponds to the simple shear (i.e., zero curvature) limit. . . . . 227

6.3 $\theta$-averaged (a) total shear stress, (b) micelle shear stress, (c) $S_{r\theta}$, and (d) micelle length for start-up of CCF flow with Pe = 2; line styles correspond to sampling at different radial locations: $R_1$ is close to the inner cylinder, $R_2$ is in the middle of the gap, and $R_3$ is close to the outer cylinder. . . . . 227

6.4 Micelle length vs. Pe for the RRM-R with parameters: $m = 3$, $k_{b0} = 10^{-2}$, $k_{bt} = 10$, $a = 2.5$, and varying $k_{ga}$. . . . . 229

6.5 Snapshots of initial reentrant instability formation for the RRM-R with parameters: $m = 3$, $k_{b0} = 10^{-2}$, $k_{bt} = 10$, $a = 2.5$, and varying $k_{ga}$. . . . . 229

6.6 Schematic of cross-slot flow. Flow enters through the horizontal arms with uniform velocity $U$ and isotropic, equilibrium length micelles. Flow exits through the vertical arms with a zero-gradient pressure boundary condition. The half-channel width is $d = 1$. . . . . 231

6.7 Constitutive curves for the RRM-R in uniaxial extensional flow with parameters: $m = 3$, $k_{b0} = 10^{-2}$, $k_{ga} = 1500$, $k_{bt} = 10$, and $a = 2.5$. (a) Micelle (red), Newtonian (blue), and total shear stress (purple), (b) length of micelles, (c) components of the orientation tensor, and (d) normalized viscosity vs. applied Péclet number. . . . . 232

6.8 Snapshots of micelle length at $t = 80$ for cross-slot flow with Pe = 0.005. The top figure shows the inlet channels and the bottom figure shows the outlet channels. . . . . 233

6.9 Snapshots of micelle length at $t = 10$ for cross-slot flow with Pe = 0.015. The top figure shows the inlet channels and the bottom figure shows the outlet channels. . . . . 234

6.10 Schematic of plane Couette flow. . . . . 237

6.11 (a) Micelle length and (b) orientation parameter over time and averaged over $xy$ at two different vorticity locations. The flow was seeded with an initial condition directly on the unstable region of the flow curve (i.e., middle branch); at $z = z^+$ the micelle length was perturbed up slightly, and at $z = z^-$ it was perturbed down slightly. . . . . 238

6.12 Snapshot of micelle length for vorticity banded flow at long times. The initial condition was vorticity banded. . . . . 238

6.13 Snapshots of micelle length for CCF with Pe = 0.0225 and velocity convection. The first column contains snapshots at $t = 40$, the second at $t = 65$, and the times of snapshots in the third column are specified on the figure. From top to bottom the rows are: Re = $10^{-6}$, Re = $10^{-4}$, Re = $10^{-2}$, Re = $10^{1}$. . . . . 241

6.14 (Reproduced from Section 1.1.1) Friction factor vs. Reynolds number for a variety of polymer and surfactant systems [1, 2]. . . . . 244

# 1

# General introduction

The works presented in this thesis are targeted at leveraging modeling and simulation tools to better understand the rheology and flow dynamics of dilute wormlike micelle solutions. Wormlike micelles (also called rodlike or cylindrical micelles) are formed from the self-assembly of amphiphilic surfactant molecules and can show a wide array of rheological behaviors that make them essential to many commercial products and industrial processes. Broadly, the aims of this work are to (1) develop and accurate and tractable model for dilute wormlike micelle solutions and (2) use this model in computational fluid dynamics (CFD) simulations for understanding instabilities, turbulence, drag reduction, and other phenomena in these flows. Industrially, these goals are motivated both by the ubiquity of wormlike micelles in processes and products as well as developing a better understanding of the breadth of rheological properties displayed by these solutions so that they can be effectively deployed in new settings. Academically, wormlike micelle solutions exhibit a number of unique instabilities that have yet to be fully explored.

A full description of the rheology of dilute wormlike micelle (WLM) solutions is given in Section 1.2, but to summarize these solutions have been shown to exhibit remarkable flow dynamics ranging from pronounced shear-thickening and -thinning regimes to flow-induced structure (FIS) formation, as well as numerous instabilities in shear and extensional flows [9, 10, 11, 12, 13]. These properties, among others, have lead to the widespread use of

WLM solutions in numerous fields. Specifically, in commercial products WLMs are found in: detergents, emulsions, coatings, and paints, and in industrial processes they are used: in closed-loop district heating and cooling, in oil and gas applications as heat-transfer fluids, and in oil-recovery operations as fracking fluids [14, 15].

Wormlike micelle solutions have also demonstrated turbulent drag reduction at levels comparable to, and in some cases exceeding, that of polymer solutions. It has been known for several decades that the addition of a small amount of polymer molecules can significantly reduce turbulent drag by up to 80% [1, 16]. Unfortunately, polymer additives suffer from mechanical degradation in regions of high shear or extension, such as those seen in the pumps needed to drive fluid transport, requiring the need for constant replacement in order to maintain the desired levels of drag reduction. More recent research has shown that dilute surfactant solutions forming wormlike micelles also provide significant levels of drag reduction, comparable to the levels seen in polymer solutions [2]. Additionally, micelles are self-assembled structures, meaning that they are not susceptible to the mechanical degradation that polymers are. This self-assembly, combined with their incredible drag reduction, makes WLM solutions ideal candidates for reducing drag in the transport of fluids.

Despite the benefits of dilute WLM solutions, their adoption as drag-reducing agents has been limited, remaining mostly confined to small districts in Japan [17, 18]. Much of this limitation stems from the fact that the behavior and dynamics of these fluids in complex flows, and specifically the development of instabilities in these flows, is not well understood especially compared to the flow of polymer solutions. In this work, we aim to expand understanding of flow instabilities in dilute WLM solutions and elucidate the mechanisms underlying these instabilities.

The following introduction is set-up as a primer for key concepts in rheology and modeling of complex fluids. The introduction is laid out as follows: In Section 1.1 we provide a brief introduction into the basics of viscoelastic fluids and the broad categorizations for rheological behaviors. In Section 1.1.1 we give an overview of drag reduction and turbulence

in viscoelastic fluids; harnessing and exploiting drag reduction using viscoelastic fluids is the application with the greatest possible energy and cost savings. In Section 1.2 we then dive into the main focus of this thesis, wormlike micelle solutions; this section first focuses on the chemistry and composition of these solutions before discussing their rheological properties. We also discuss many instabilities that can arise in these systems. Section 1.3 provides an overview of the most widely studied models for WLM solutions, including a description of their derivations and predictions. Finally, in Section 1.4 we provide an outline of the remaining chapters.

## 1.1 Introduction to viscoelastic fluids

Viscoelastic fluids are encountered in a vast array of fields including: biology/anatomy [19], oil-recovery [20], material processing, transportation/robotics [21], and even astronomy [22]. Viscoelastic fluids, as their name suggests, are both viscous and elastic. To understand viscoelasticity, it is first helpful to understand the two limiting cases of purely viscous and purely elastic materials.

Typical small-molecule liquids (e.g., water, liquid argon) are purely viscous; they have no 'memory' of past deformations, and their behavior is only dependent on the applied deformation. Purely viscous fluids are called Newtonian. The stress in these fluids is a linear function of the applied shear rate, which is related to the velocity gradient. The relationship between the stress and shear rate in a fluid is commonly understood through Newton's law:

$$\tau = \eta\dot{\gamma}, \tag{1.1}$$

where $\tau$ is the stress, $\dot{\gamma}$ is the shear rate, and $\eta$ is the proportionality constant, defined as the fluid viscosity. For a Newtonian fluid the viscosity is constant.

While fluids tend to be viscous, solids tend to be elastic. Similar to the linear relationship between stress and shear rate in Newtonian fluids, Hookean solids display a linear relationship

between the stress and strain. This relationship can be understood through Hooke's law:

$$\tau = E\epsilon, \tag{1.2}$$

where $\epsilon$ is the strain and $E$ is the elasticity modulus. These materials have a 'memory' of past deformations, as these can affect the present stress in the material. In simple terms, the stress in Newtonian materials is related to how fast the material is deformed, whereas the stress in Hookean materials is related to the distance the material is deformed.

Viscoelastic fluids show behavior that falls between the two limiting cases of Newtonian or Hookean; the stress in these fluids depends on both the shear rate and the strain [23]. The quintessential viscoelastic fluid, at least in the chemical engineering field, is a dilute polymer solution. These solutions comprise long-chain polymer molecules (e.g., PMMA) dissolved at dilute concentrations in viscous fluids. Polymers are much larger than the small molecules of Newtonian fluids and consequently the stress relaxation time scales are much longer; this increased time scale means that local microstructure in the fluid can be altered, leading to deviations from the Newtonian viscosity model [19].

In polymers, the slowest time scale is often related to the time for a polymer molecule to return to its equilibrium configuration after being stretched [24]. As polymers are stretched by the flow, the fluid microstructure becomes anisotropic and altered, thereby changing the bulk fluid properties and showing non-Newtonian behavior. For polymers, the flow rate at which non-Newtonian behavior sets in can be quantified by the Weissenberg number, $\mathrm{Wi} = \lambda\dot{\gamma}$, where $\lambda$ is the relaxation time of the fluid and $\dot{\gamma}$ is the shear rate [25]. The Weissenberg number acts as a dimensionless shear rate that measures the ratio of elastic to viscous forces and characterizes the deviations of a polymer from equilibrium [26]. For $\mathrm{Wi} \ll 1$ the fluid behavior is Newtonian-like as polymers can relax before becoming stretched by the flow field; for $\mathrm{Wi} \geq 1$, however, polymers are stretched and non-Newtonian behavior arises [24]. For rigid polymers, relaxation to equilibrium occurs through rotational diffusion, which is

quantified by the rotational diffusion constant, $D_r^{-1} \sim \lambda$; in these cases the Weissenberg number is replaced by the rotational Péclet number, $\mathrm{Pe} = \dot{\gamma}/D_r$ [26].

Non-Newtonian behavior forms an extremely broad umbrella since it contains every fluid that deviates from the simple Newtonian (i.e., linear) constitutive relation. Under this umbrella are many more specific categories that tend to sort fluids based on their viscosity under shear. As discussed above, a Newtonian viscosity is constant under all shear rates. Many fluids - such as polymers, blood, paints, and ketchup - are shear-thinning, meaning that their viscosity decreases with increasing shear rate. Conversely, other fluids - such as cornstarch mixtures, dilute wormlike micelle solutions, and pastes - are shear-thickening, meaning that their viscosity increases with increasing shear rates. Finally, some fluids - such as toothpaste, slurries, and concentrated suspensions - can exhibit a yield-stress, meaning that a certain stress must be applied in order for these materials to flow; below this critical stress the material behaves as a solid, while above it behaves as a fluid. Fluids that show a yield-stress are often called Bingham plastics [27]. Many real materials can exhibit some or all of these properties where the presence of more than one of these indicates competing mechanisms and multiple time scales [25]. Example flow curves for all of these types of fluids are displayed in Fig. 1.1, where (a) shows the shear stress ($\tau_{xy}$) vs. shear rate ($\dot{\gamma}$) and (b) shows the corresponding viscosity ($\eta$) vs. shear rate curves.

The often complex microstructure and relationship between stress and shear in non-Newtonian fluids can give rise to numerous flow phenomena that are not observed in Newtonian fluids. One well-known phenomenon is the rod-climbing effect (also called the Weissenberg effect [24]). Consider a stationary beaker containing a viscous fluid with a rotating rod placed vertically into the center of the fluid from above; in a Newtonian fluid, the rotating rod will cause the fluid to decrease in height near the center of the beaker as fluid is pushed outward toward the edges by the centrifugal force. In polymer solutions, however, the opposite effect is observed as the fluid at the center of the beaker actually appears to climb up the rod. Additionally, the change in fluid height is much more dramatic in polymer

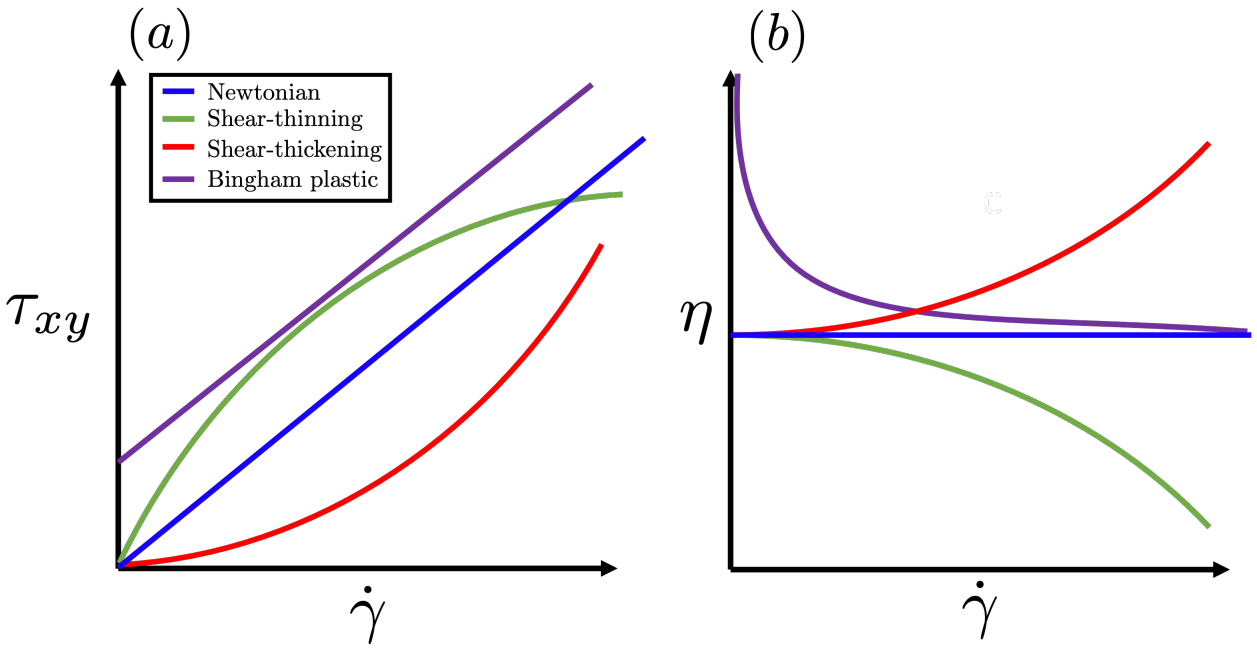


**Figure 1.1:** Representative flow curves for different non-Newtonian fluids on (a) shear stress ($\tau_{xy}$) vs. shear rate ($\dot{\gamma}$) and (b) viscosity ($\eta$) vs. shear rate curves.

solutions than Newtonian fluids [24]. Rod climbing is a result of 'hoop' stresses that arise through the stretching of polymer molecules along streamlines in the $\theta$- direction. As polymers stretch along streamlines they generate a radially inward stress that squeezes material inward and, if strong enough, forces the material to appear to climb the rod [26].

Viscoelasticity can also give rise to numerous other phenomena, such as: die swell [28], elastic recoil [29], long filament lifetimes [30], instabilities, and others [24]. A large portion of the rheology field is dedicated to understanding and predicting these phenomena, both out of industrial relevance and academic interest. From an industrial perspective, instabilities and non-Newtonian behaviors can force drastic alterations to processes involving complex fluids. For example, these phenomena can have a significant effect on extrusion, bottle filling, pumping, foaming, mixing, and others [31]. Moreover, new phenomena are constantly being observed and uncovered as new complex fluids are developed and employed.

### 1.1.1 Drag reduction

One of the primary applications of complex fluids, and specifically dilute polymer solutions, is the reduction of turbulent drag. It has been known for several decades that the addition of a small amount of polymer molecules can significantly reduce turbulent drag by up to 80% [1, 16]. Interestingly, while drag reduction is found to increase with increasing polymer concentration, the drag reduction eventually asymptotes and no further drag reduction is observed for increasing concentration; this maximum extent of drag reduction, called the maximum drag reduction asymptote (MDRA), appears to be independent of polymer chemistry [32]. The drag reducing capabilities of polymer additives have made them essential tools in many applications involving the transport of fluid, from oil pipelines to heating and cooling districts [33]. Unfortunately, polymer additives suffer from mechanical degradation in regions of high shear or extension, such as those seen in the pumps needed to drive fluid transport, requiring the need for constant replacement in order to maintain the desired levels of drag reduction.

More recent research has shown that dilute surfactant solutions forming wormlike micelles also provide significant levels of drag reduction, comparable to the levels seen in polymer solutions [2]. As in the polymer case, the extent of drag reduction in surfactant solutions is also seen to asymptote. Figure 1.2 shows a plot of friction factor vs. Reynolds number measured in various experiments of polymer and surfactant solutions. It is desirable to have the lowest friction factor, $f = \Delta p d/\rho L U^2$, possible. The dashed black line shows the friction factor for Newtonian turbulence, which is much larger than the other data shown. The solid black line corresponds to laminar flow, which gives the lowest drag possible. The blue markers show experimental data of various surfactant-additive systems, and the other colored markers show the experimental data for various polymer-additive systems. The red and blue lines are empirical fits for the polymer and surfactant MDRA, respectively. The drag-reducing capabilities of micelle solutions clearly rivals that of polymers; additionally, micelles are self-assembled structures, meaning that they are not susceptible to the mechanical degradation

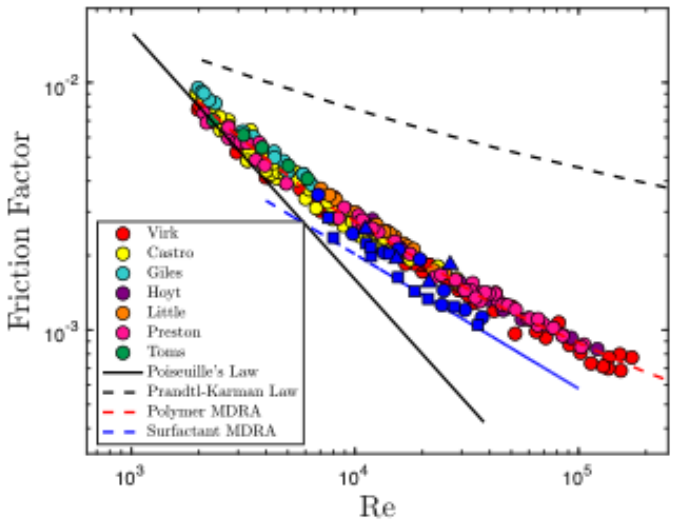


**Figure 1.2:** Friction factor vs. Reynolds number for a variety of polymer and surfactant systems [1, 2].

that polymers are. This self-assembly, combined with their incredible drag reduction, makes WLM solutions ideal candidates for reducing drag in the transport of fluids.

There has been a great deal of research into the mechanisms of drag reduction in polymer solutions [34, 32, 33, 35, 36, 37]. Research has demonstrated that polymer solutions show a transition from inertial turbulence, which we will refer to as Newtonian turbulence, to elastoinertial turbulence (EIT). While Newtonian turbulence is dominated by quasi-streamwise vortices, EIT tends to be dominated by spanwise-oriented vortices [36]. There has been little, if any, research into the mechanisms of drag reduction in surfactant-additive solutions, nor has there been research into the structure of turbulence in these solutions. We aim to address the lack of studies in these areas through the development of a computationally tractable model for wormlike micelle solutions.

## 1.2 Introduction to wormlike micelles

The works in this thesis are concerned with modeling and simulations of dilute wormlike micelle solutions. Wormlike, also called rodlike or cylindrical, micelle solutions are a subclass of viscoelastic fluids that are formed when amphiphilic surfactant molecules are dissolved in a

viscous fluid. Wormlike micelles are cylindrical structures that have often been called 'living polymers' due to a combination of their lengths and ability to reform and re-structure due to a series of self-assembly processes [38]. In this section, we first discuss the composition and chemistry of micelles, including energetic and packing arguments into the size and shape of these self-assembled structures. We then focus on the rheology of wormlike micelle solutions, as well as instabilities that can form in these solutions. Finally, since much of this work is focused on modeling WLM solutions, we give an overview into the derivation and predictions of some of the most widely studied models.

### 1.2.1 Composition and chemistry

Wormlike micelles are aggregate structures that are formed from the self-assembly of amphiphilic surfactant molecules. Surfactants, so-named as a portmanteau of 'surface-active agents,' typically consist of bulky hydrophilic head groups and long hydrophobic tails. The amphiphilic nature of these molecules enables them to adsorb to the interface between two immiscible fluids, leading to a significant reduction in the surface or interfacial tension [15]. The surface-activity, and the accompanying reduction in surface tension, of these molecules makes them invaluable for applications such as: emulsification, wetting, and both foaming and anti-foaming [39].

When dissolved in a fluid above a certain concentration, the critical micelle concentration (CMC), surfactants can no longer populate the crowded interface and will begin to assemble in the bulk solution [40]. This concentration signals the transition from behavior as individual molecules to collective behavior as aggregate structures. Specifically, surfactants will begin to self-assemble into larger structures where the geometry of the structures depends on the size, shape, and chemistry of the surfactant molecules, as well as the pH, salinity, and polarity of the fluid. Importantly, these aggregate structures are not chemically bonded and can thus break and reform easily, as well as undergo transitions to other geometries, which is important for understanding the dynamics of micelles in flow.

The geometry of the self-assembled structures is well characterized by the packing parameter, $P$, which models surfactants as cones with volume, $v$, radius, $a_h$, and length $l_c$ [40]. The radius of the cone is directly related to the size of the hydrophilic head group, while the length is related to the length of the hydrophobic tail. The packing parameter is given by

$$P = \frac{v}{a_h l_c}. \tag{1.3}$$

This treatment predicts that for $P < 1/3$ spherical micelles will form, for $1/3 < P < 1/2$ cylindrical micelles will form, and for $1/2 < P < 1$ vesicles and extended bilayers will form; for $P > 1$ inverted structures are predicted [40]. This theory is not meant to be precise since it ignores chemical and thermodynamic considerations and, moreover, the geometric parameters can not be calculated from first principles. However, this treatment is useful for understanding self-assembly broadly as well as the effects of changing simple geometric parameters such as tail length.

In this thesis we will exclusively focus on wormlike micelles so it is helpful to go more in depth into the chemical properties of these structures. To help us understand the chemical and thermodynamical properties of wormlike micelles we turn to work by Larson [15]. From a geometrical perspective, wormlike micelles differ from spherical micelles in that the curvature is not constant across their surface; this variable curvature means that surfactants must balance optimal and non-optimal configurations. For a long wormlike micelle with length $L$ and core radius $R_c$, the aggregation number (i.e., the number of surfactants in a micelle) is given by $n = 2\pi R_C L/a_h$. It is assumed that the core radius adjust itself so that the head group area, $a_h$, is at its optimal value everywhere except for the hemispherical ends of the cylinder; on the cylinder ends, the area per head group (calculated assuming a hemispherical geometry) is $a_s = 3a_0/2$. As a consequence of this optimization along the cylinder body, the chemical potential $\mu_n^0$ for a surfactant in a wormlike micelle varies with aggregation only because of the end caps (i.e., the chemical potentials of two wormlike micelles with different

lengths are equal) [40].

The free energy of micellization, $F_{\text{mic}}(n)$, which gives the change in free energy required for the assembly of surfactants into a micelle, is

$$F_{\text{mic}}(n) = n\mu_r^0 + n_s(\mu_s^0 - \mu_r^0), \tag{1.4}$$

where $\mu_s^0$ is the chemical potential of a surfactant in the hemispherical end cap, $\mu_r^0$ is the chemical potential of a surfactant in the cylindrical body, and $n_s$ is the number of surfactants in an end cap. The overall chemical potential for a surfactant molecules is $F_{\text{mic}}/n$ so that the difference in chemical potential between a micelle with $n$ surfactants and a micelle with one surfactant is

$$\mu_n^0 - \mu_1^0 = \mu_r^0 - \mu_1^0 + \frac{n_s}{n}(\mu_s^0 - \mu_r^0) \equiv E_\infty + \frac{E_{\text{sciss}}}{n}. \tag{1.5}$$

In this expression, $E_{\text{sciss}} \equiv \mu_r^0 - \mu_1^0$ is the free energy per surfactant molecule for the formation of an infinite cylinder and $E_\infty \equiv n_s(\mu_s^0 - \mu_r^0)$ is the free energy for micelle scission, which is equivalent to the free energy for the formation of two end caps [15, 40]. Finally, this chemical potential gives rise to an exponential distribution of micelle lengths

$$X_n \approx n \exp\left(-n/\sqrt{X e^{(E_{\text{sciss}}/k_B T)}}\right) \exp\left(-E_{\text{sciss}}/k_B T\right), \tag{1.6}$$

where $X$ is the total mole fraction of surfactant and $X_n$ is the mole fraction of surfactants in an $n$-sized aggregate [40]. This is a very broad distribution, which can be understood from the fact that micelles of any length are indistinguishable from one another since the chemical potential is only non-optimal at end caps, of which each micelle has two. Of course there is a driving force to minimize the number of end caps by forming longer micelles, however this is entropically unfavorable.

### 1.2.2 Rheology and instabilities

Much of the interest and research into wormlike micelles centers around their unique rheological properties. Broadly, wormlike micelles can display shear-thickening and -thinning [41, 42], extensional-hardening [43], non-zero normal stress differences [44], flow-induced structure [45, 46], shear banding [47, 12, 48, 49], vorticity banding [47, 50], reentrant (e.g., multivalued) flow curves [51, 52, 50], and numerous instabilities [4]. While wormlike micelle solutions can display many of these properties, the exact behavior of a given WLM solution is highly dependent on its concentration [14].

In the upper semi-dilute and concentrated regimes, WLM solutions typically show shear-thinning behavior reminiscent of long-chain polymer solutions. Micelles in this regime do not exist as independent structures, but rather form complex, entangled networks. These entanglements occur as micelles grow far beyond their persistence lengths and begin to wind and curve [49]. These networks can move and relax through a variety of mechanisms: scission, reptation, and shuffling, and importantly because these structures are not chemically cross-linked they can also undergo 'ghost'-point crossings, where two strands will seemingly pass through one another [53, 38, 54]. Shear-thinning in this regime is attributed to restructuring of the network and the breaking of entanglements. These higher concentrations also tend to exhibit, under appropriate conditions, the well-known shear banding (or gradient banding) instability. This instability is characterized by a macroscopically 'banded' flow in which the fluid separates into two distinct regions where the fluids in either region support equivalent shear stresses but unique shear rates [47, 55]. The separation of these two regions is often observable through differences in turbidity and/or birefringence, indicating that micelles in each region are distinguishable by differences in length and orientation.

The development of shear-banding requires a flow curve in which the shear rate, $\dot{\gamma}$, is a multivalued function of shear stress, $\tau_{xy}$. An example of this non-monotonic flow curve is shown in Fig. 1.3a. This flow curve is characterized by a region where $\partial\tau_{xy}/\partial\dot{\gamma} \leq 0$ at intermediate shear rates, separated by two regions where $\partial\tau_{xy}/\partial\dot{\gamma} > 0$ at low and high shear

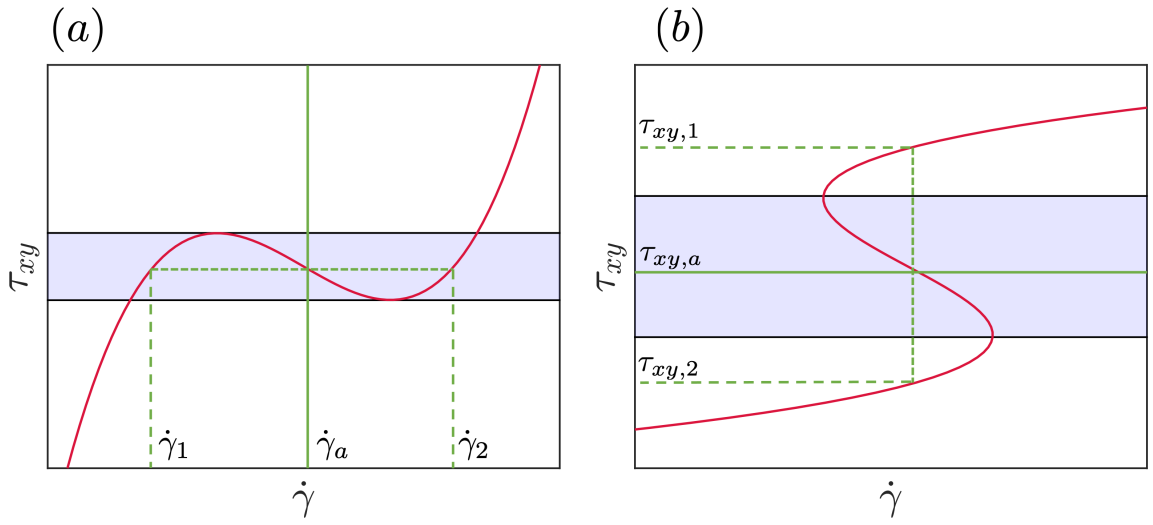


**Figure 1.3:** Representative flow curves for fluids that can support (a) shear banding and (b) vorticity banding. The curve in (a) shows a shear rate that is a multivalued function of shear stress, while (b) shows a shear stress that is a multivalued function of shear rate. The blue areas indicate regions of the flow curve that are multivalued and can support banding.

rates, respectively. In the region where the shear stress is a decreasing function of shear rate, the flow is unstable to non-homogeneous flow [56]; in controlled shear rate flow, the application of a shear rate, $\dot{\gamma}_a$, that falls in this region will often cause the flow to separate into two distinct regions of equal shear stress but unique shear rates, $\dot{\gamma}_1$ and $\dot{\gamma}_2$, resulting in a piecewise velocity profile. This separation is known as shear banding since it occurs along the shear (i.e., gradient) direction, but for clarity should be referred to as gradient banding to distinguish from vorticity banding (which also occurs in shear flows). There has been extensive research into shear-banding [57].

In the dilute and semi-dilute regimes, micelles exist as nearly rigid rods with persistence lengths in the range of $\sim \mathcal{O}(10-100\text{nm})$ and contour lengths on similar scale [58, 59, 60, 61, 5]. In this regime, WLM solutions typically exhibit pronounced shear-thickening behavior associated with the formation of flow-induced structure (FIS); at high deformation rates this thickening gives way to stark shear-thinning induced by the breakdown of FIS and strong orientation of the micelles [62]. Flow-induced structure in the dilute regime takes the form of elongated wormlike micelles that can be several times longer than the equilibrium micelle length, in some cases yielding micelles with lengths on the order of microns [46].

While a direct measurement of micelle length in flow is challenging, it is possible to make estimates of the micelle length by analyzing the effect of flow on the solution viscosity. Prud'homme and Warr related the critical strain rate, the strain at which the extensional viscosity is maximized, in an opposed jet device to the length of micelles by assuming that the micelle relaxation time was solely due to scission kinetics [63]. By approximating the tension along the micelle body and assuming an upper bound on the micelle scission energy, they directly related the critical strain rate to the micelle length. Through this analysis and by comparing to the mean micelle length at zero shear rate, the authors determined that micelles were significantly elongated by the extensional flow field. Similarly, Omidvar and coworkers used an asymptotic analysis of the FENE-P model to relate the extensional viscosity of the micelle solution to the micelle length [64]. By assuming that the micelle length could be related to the FENE-P extensibility parameter, they were able to relate increases in the extensional viscosity to elongation of the micelle lengths, finding significant elongation of the micelles by the flow field.

In addition to shear-thickening and -thinning, dilute WLM solutions can display a reentrant, or multivalued, flow curve in which the shear stress is a multivalued function of shear rate, shown in Fig. 1.3b. In a stress controlled rheometer, the application of a shear stress, $\tau_{xy,a}$, that falls in the region where $\partial\tau_{xy}/\partial\dot{\gamma} \leq 0$ will cause the flow to separate into two distinct regions that support equivalent shear rates but unique shear stresses, $\tau_{xy,1}$ and $\tau_{xy,2}$; this separation is known as vorticity banding since it occurs along the vorticity axis [50]; this instability is a relatively uncommon phenomenon, but has been observed in charged colloidal suspensions, rodlike colloids, onion surfactants, biphasic polymer blends, and of course dilute WLM solutions [65, 66, 52, 67, 50, 68]. Similar to gradient banding, these bands can often be visualized by differences in turbidity and birefringence [47, 50]. While there has been extensive theoretical and experimental treatment of shear banding (see [47, 57] for comprehensive reviews), vorticity banding remains a poorly understood phenomenon. This lack of understanding arises due to both fewer fluids that exhibit reentrant flow curves and

fewer constitutive models that can predict reentrant flow curves, thus restricting the study of vorticity banding from both experimental and computational approaches.

In addition to vorticity banding, dilute WLM solutions have been shown to exhibit 'finger'-like instabilities; these finger-like instabilities develop in circular Couette flow and appear as unstructured streaks and threads that span the flow gap [69, 70]. Using a circular Couette device, Liu and Pine [4] observed these finger-like structures in controlled-shear rate flows of $\sim \mathcal{O}(10^2 - 10^3)$ ppm equilmolar CTAB/NaSal solutions; using small angle light scattering (SALS), they revealed reversible finger-like structures that, upon increasing shear rate, grew outwards from the inner cylinder into the flow gap. The emergence of these structures required a finite induction time, typically on the order of minutes, and resulted in an elevated shear stress corresponding to significant shear-thickening. The authors observed that the fingers repeatedly grew until they reached the outer cylinder before retracting towards the center of the cell and beginning to grow again. Hu and coworkers [71] observed similar structures in a solution of equimolar 7.5 mM TTAA/NaSal that exhibited a reentrant flow curve. Similar to Liu and Pine, the authors observed that increasing either the shear rate or shear stress beyond some critical value induced shear-thickened structures that originated at the inner cylinder and grew outwards to fill the gap. In stress-controlled experiments, they observed that increasing the applied stress into the multivalued region of the flow curve resulted in a FIS front that steadily grew to some radial position along the gap before stopping and holding at a steady gap location; the point along the gap where the FIS front stopped depended on the applied stress. When increasing the shear stress beyond the multivalued region, the authors observed that the FIS encompassed the entire gap. In shear rate-controlled experiments, the authors observed transient behavior that was similar to the stress-controlled experiments, but found that the steady behavior was different; notably the system was either void of FIS or exhibited FIS that filled the entire gap depending on whether the applied shear rate was below or above the critical value, respectively.

Finger-like instabilities have not been observed in channel flows of dilute wormlike mi-

celle solutions, though instabilities have been found in cross-slot flow. Dubash and coworkers [72] investigated different concentrations of CTAB/NaSal solutions that spanned the dilute (shear-thickening and -thinning) to concentrated (purely shear-thinning) regimes in a microfluidic cross-slot device. The WLM solutions they investigated did not display reentrant flow curves and they did not observe any finger-like instabilities, however, they did observe the development of of unsteady flow. The extension rates where the flow became unsteady corresponded to regions of the flow curve that show shear-thickening and -thinning. The authors concluded that the instability was elastically driven because it developed at Reynolds numbers below the critical value for instabilities in Newtonian fluids.

## 1.3 Modeling wormlike micelle solutions

In the following section, we outline a few of the prominent models for wormlike micelle solutions. As we will discuss, a consequence of the dramatic dependence of wormlike micelle rheology on concentration is that models for WLM solutions are typically only valid for a specific range of concentrations, and it is unlikely that a single model will be able to capture the full behavior of WLMs from the dilute to concentrated regimes. This inability is not unexpected since many polymer models should also only be employed in specific concentration ranges (although many researchers will ignore this!). The range of behaviors between concentration regimes also means that there have been numerous and varied approaches to modeling and understanding WLM solutions, each with their own successes and pitfalls. Perhaps the greatest challenge in developing these models is the balance of accuracy with computational efficiency; we desire a model that accurately captures the physics and dynamics of WLM solutions, but for this model to be useful it also must retain sufficient tractability such that it can be implemented and studied both analytically and in computational fluid dynamics simulations. Although there is no easy solution to this challenge, there has been a significant and relatively successful effort over the last three decades to develop robust

models for WLM solutions.

The existing models for WLM solutions can be loosely lumped into three categories: population balance models, coupled fluidity models, and microstructural models. Population balance models treat each unique micelle length as an individual species, leading to a distribution of lengths that can be either continuous or discrete depending on the model. The dynamics and behavior of each species are tracked individually and used the predict the bulk or collective behavior of the system. Coupled fluidity models involve the coupling of viscoelastic fluid models (e.g., Upper-convected Maxwell, FENE-P) to an evolution equation for the 'fluidity' of micelles; in theory the fluidity is meant to capture the build-up and breakdown of micelle structure, and in practice is simply the inverse of the solution viscosity. Finally, microstructural models aim to capture the underlying physics of the micelle system by treating WLMs as a reaction system. These models make phenomenological and mechanistic arguments about the micelle kinetics and are thus able to capture a diverse range of reaction and relaxation phenomena.

### 1.3.1 Cates and Turner

One of the earliest treatments of WLM solutions was by Cates and Turner (CT) [73, 74], who aimed to generate a population balance model that accounted for different stress relaxation mechanisms associated with wormlike micelles, specifically micelle scission and rotational diffusion. In their work, CT treat WLMs as completely stiff and make the assumption that all micellar reaction kinetics only involve collinear rods. Following this assumption, micelles subjected to flow exhibit a positive feedback mechanism whereby the flow field tends to align the rods, aligned rods experience enhanced fusion and elongation, and elongated rods have decreased angular mobility and are thus able to grow even longer. At high enough shear rates in this model, rods experiencing this positive feedback can be elongated to the point that the system undergoes a gelation transition and forms ordered phases [74].

CT developed their model by considering a probability distribution function, $\psi(L, \mathbf{u})$, for

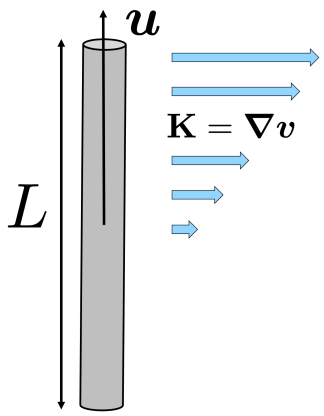


**Figure 1.4:** Schematic of a rigid rod with length $L$ and director $\mathbf{u}$ subject to an imposed velocity gradient $\mathbf{K} = \boldsymbol{\nabla}\mathbf{v}$.

rods with length $L$ and director $\mathbf{u}$. A schematic is shown in Fig. 1.4. The director $\mathbf{u}$ points along the axis of the rods and can be thought of as the trajectory of a point on the surface of a unit sphere (i.e., $|\mathbf{u}| = 1$). The density of material with orientation $\mathbf{u}$ is

$$\rho(\mathbf{u}) = \int_{\Omega} \psi(L, \mathbf{u}) L \mathrm{d}L. \tag{1.7}$$

CT considered steady states of the system that are given by solutions to

$$\dot{\psi} = F_1[\psi] + F_2[\psi] = 0, \tag{1.8}$$

where $F_1[\psi]$ accounts for rotational diffusion and convection and $F_2[\psi]$ accounts for scission and fusion reactions. Under a constant imposed velocity, $\mathbf{v}$, and gradient, $\mathbf{K} = \boldsymbol{\nabla}\mathbf{v}$, the form of $F_1[\psi]$ is well-known [75]:

$$F_1[\psi] = \mathcal{R} \cdot \left[ D(L) \mathcal{R} \psi(L, \mathbf{u}) - \mathbf{u} \times \mathbf{K} \cdot \mathbf{u} \psi(L, \mathbf{u}) \right], \tag{1.9}$$

where $\mathcal{R} \equiv \mathbf{u} \times \partial / \partial \mathbf{u}$ is the angular gradient or rotational operator. In index notation $\mathcal{R}_j = e_i \epsilon_{ijk} \partial / \partial u_k$. The first term in this expression is from angular diffusion and the second is from torque on a rod subject to a flow.

The form of $F_2[\psi]$ is obtained by assuming that micelles undergo random unimolecular

scission with a fixed probability per unit length, $k$. Further, the fusion of two collinear rods with orientation $\mathbf{u}$ and lengths $L$ and $L'$ occurs at the rate $k'\psi(L,\mathbf{u})\psi(L',\mathbf{u})$ with rate constant $k'$. CT enforce $k'/k = 2\exp(E)$, where $E$ is the local free energy for scission of a micelle. The reaction kinetics of the micelle solution are then given by

$$F_2[\psi] = -kL\psi(L,\mathbf{u}) + 2k\int_\Omega \psi(L,\mathbf{u})\mathrm{d}L + \frac{k'}{2}\int_\Omega \psi\left(L',\mathbf{u}\right)\psi\left(L-L',\mathbf{u}\right)\mathrm{d}L' - k'\psi(L,\mathbf{u})\int_\Omega \psi\left(L',\mathbf{u}\right)\mathrm{d}L'. \tag{1.10}$$

In the above expression, the first term corresponds to a rod of length $L$ breaking to form two shorter rods, the second term corresponds to a longer rod breaking to form a rod of length $L$, the third term represents two shorter rods fusing to form a rod of length $L$, and the last term represents a rod of length $L$ fusing with another rod to form a longer rod. Reactions alone are unable to redistribute rods between angles so that the angle-dependent rod length, $\lambda(\mathbf{u})$, is arbitrary. The steady state distribution for a micelle system only under the influence of reactions, $F_2[\psi] = 0$, is

$$\psi(L,\mathbf{u}) = \exp(-E)\exp(-L/\lambda(\mathbf{u})). \tag{1.11}$$

One drawback of this model is that a full solution to Eq. (1.8) for arbitrary flows is not possible without introducing new assumptions and limits [73]. For example, let $\tau = 1/k\lambda_0$ be the characteristic relaxation time of the system with characteristic rod length $\lambda_0$; the 'fast-breaking limit' is defined as $\tau \to 0$. In this limit, Eq. (1.8) can be solved in the case of potential flows. Additionally, although an exact solution is not possible, the model does predict a gelation transition in extensional flow when the extension rate exceeds some critical value. It is important to note that description of this transition as a 'gel' does not imply cross-linking, rather it indicates the appearance of extremely long and anisotropic rods. Equation (1.8) can not be exactly solved in shear flows and in the slow-breaking limit without further simplifications, though scaling arguments are possible.

The model proposed and developed by Cates and Turner has been extremely influential for the study of wormlike micelle solutions. In particular, the balance of orientation relaxation with micellar kinetics has become a staple of most, if not all, WLM solution models. As will be discussed, the reactive rod model and its descendants draw heavily from the picture described by Cates and Turner. Moreover, this model clearly describes the physics of structure formation that dominate these systems.

There are significant limitations with this model, however, notably the inability to find exact solutions except in the cases of strong limitations and restrictions. CT also do not write down an evolution equation for the stress tensor, which is a necessity for use in practical applications. Additionally, the inclusion of a continuous length distribution is prohibitive for the implementation of this model in CFD simulations due to sheer computational expense. More recent models for WLM solutions have learned from these drawbacks, often enforcing a discrete length distribution and including the necessary constitutive relation. Although the work by Cates and Turner has its limitations, it has been foundational in the development of improved micelle models.

### 1.3.2 Vasquez-Cook-McKinley

The Vasquez-Cook-McKinley (VCM) model is based on a discrete version of a 'living polymer' theory developed by Cates [76, 77, 78, 79]. This is the same Cates as the Cates and Turner model, who extended the work to both account for micelle entanglements and provide a constitutive relation for the micelle stress. The VCM model is meant to describe concentrated WLM solutions that form entangled networks and notably display a shear banding instability. This thesis is primarily focused on wormlike micelle solutions in the dilute regime, which display drastically different dynamics compared to solutions in the concentrated regime; it is instructive, however, to include the VCM model in this work because it the most widely studied model for WLM solutions.

The VCM model starts by considering the coexistence of two species of wormlike micelles

modeled as Hookean dumbbells; species $A$ have length $L$ and are able to break at their center to form species $B$ with length $L/2$. Species $B$ are able to react end-to-end to reform species $A$. This reaction scheme is a discretization of the one proposed by Cates and Turner [74, 73, 79], which allowed for micelles to break with equal probability at any point along their length, as well as micelles of any length to fuse together. The simplification to a discrete length distribution is crucial for allowing this model to be deployed in complex flows as well as for studying spatial variations that arise in shear banding.

The full derivation of the VCM model is given [76], but in summary the model starts from a probability density distribution, $\psi_i$, for each species, $i$, whose dynamics are governed by the Smoluchowski equation (also called the Fokker-Planck equation [80]). We do not show the Smoluchowski equation here since it will be included in Section 1.3.4. The Smoluchowski equation is integrated over the conformation space to obtain evolution equations for the number density and conformation of each species. After appropriate non-dimensionalization the governing equations are

$$\mu \frac{Dn_A}{Dt} = 2\delta_A \nabla^2 n_A - \delta_A \nabla\nabla : \mathbf{A} + \frac{1}{2} c_B n_B^2 - c_A n_A, \tag{1.12a}$$

$$\mu \frac{Dn_B}{Dt} = 2\delta_B \nabla^2 n_B - 2\delta_B \nabla\nabla : \mathbf{B} - c_B n_B^2 + 2c_A n_A, \tag{1.12b}$$

$$\mu \overset{\nabla}{\mathbf{A}} + \mathbf{A} - n_A \mathbf{I} - \delta_A \nabla^2 \mathbf{A} = c_B n_B \mathbf{B} - c_A \mathbf{A}, \tag{1.13a}$$

$$\epsilon\mu \overset{\nabla}{\mathbf{B}} + \mathbf{B} - \frac{n_B}{2}\mathbf{I} - \epsilon\delta_B \nabla^2 \mathbf{B} = -2\epsilon c_B n_B \mathbf{B} + 2\epsilon c_A \mathbf{A}. \tag{1.13b}$$

In these equations, $n_A$ and $n_B$ are the number density of species $A$ and $B$, respectively, $\mathbf{A}$ and $\mathbf{B}$ are the configuration tensors, $\mathbf{I}$ is the unit tensor, $\mu$ is the ratio of the relaxation time of the long chains to the effective relaxation time of the network, $\epsilon$ is the ratio of the relaxation time of the short chains to the relaxation of the long chains, $\delta_A$ and $\delta_B$ are diffusion constants for each species, $c_A$ is the dimensionless breakage rate, and $c_B$ is the dimensionless

reformation rate. The $\nabla$ over a variable indicates the upper convected derivative, defined by

$$\overset{\nabla}{\mathbf{A}} = \frac{\mathrm{D}\mathbf{A}}{\mathrm{D}t} - (\nabla\mathbf{v})^{\top} \cdot \mathbf{A} - \mathbf{A} \cdot \nabla\mathbf{v}. \tag{1.14}$$

For completeness, the configuration tensors are defined by

$$\mathbf{C} = \int \mathbf{Q}\mathbf{Q}\psi_C \mathrm{d}\mathbf{Q} = \{\mathbf{Q}\mathbf{Q}\}_C, \quad C = A, B, \tag{1.15}$$

where $\mathbf{Q}$ is the end-to-end vector of a chain. The extra stress from the micelle network is

$$\boldsymbol{\tau} = (n_A + n_B)\mathbf{I} - (\mathbf{A} + 2\mathbf{B}). \tag{1.16}$$

Finally, the breakage and reformation rate are defined as

$$c_A = c_{A_{eq}} + \frac{1}{3}\xi\mu\left(\dot{\boldsymbol{\gamma}} : \frac{\mathbf{A}}{n_A}\right), \tag{1.17a}$$

$$c_B = c_{B_{eq}}, \tag{1.17b}$$

where $\dot{\boldsymbol{\gamma}} = \nabla\mathbf{v} + \nabla\mathbf{v}^T$ is the rate-of-strain tensor. The parameter $\xi$ is meant to capture capture stress-induced micelle breakage. For small values of $\xi$ micelles are able to stretch more leading to a large build-up of extensional stress; for $\xi = 0$ micelles actually become infinitely extensible leading to unphysical behavior. For larger values of $\xi$ micelles are more easily broken.

One of the key successes of the VCM model is that it is able to predict a non-monotonic flow curve (Fig. 1.3a) , which is a necessary condition for capturing shear banding. Indeed, the VCM model is the predominant model used for studying the development, dynamics, and stability of shear banding fluids [81, 82, 83]. Moreover, the VCM model is used to make direct comparisons to experiments involving concentrated WLM solutions [84]. It has also been shown that the VCM model can be efficiently implemented in CFD simulations, where

it can predict shear banding and other flow phenomena in a variety of domains [85, 86, 87]. There has also been work to re-derive the VCM model in a thermodynamically consistent framework [88], which we will elaborate on in Chapter 5.

The VCM model is perhaps the most successful and widely used models for wormlike micelle solutions, however, it is exclusively meant for studying concentrated wormlike micelle solutions. In this thesis, we are focused on the behavior of dilute WLM solution, which as discussed in Section 1.2.2, vastly differs from that of concentrated solutions. Many of the phenomena we wish to study (e.g., drag reduction and vorticity banding) are found in dilute solutions, and thus can not be adequately studied with the VCM model.

### 1.3.3 Bautista-Manero-Puig

The Bautista-Manero-Puig (BMP) model was develop for looking at wormlike micelle solutions that span a range of concentrations [89, 90, 7]; as the behavior of WLM solutions changes drastically with concentration, this goal is ambitious. There are numerous iterations of the BMP model that are meant to improve and iterate on the additional formulation, but in this background we fill focus on the generalized-BMP model.

The BMP model is derived from the extended irreversible thermodynamics (EIT) formalism, which aims to derive models in a thermodynamically consistent manner (more on this in Chapter 5). This framework results in a model that amounts to coupling the Oldroyd-B model [91], a common viscoelastic model for studying Boger fluids [92], to Fredrickson's fluidity equation [93], which has been used to study thixotropic systems. The fluidity equation, where the fluidity of a fluid is defined as the inverse of the viscosity, accounts for the buildup and breakdown of microstructure, which in the BMP model corresponds to the buildup and breakdown of micelles and gives rise to the desired shear-thickening and -thinning behavior.

The generalized BMP model is defined by the equations:

$$\frac{\mathrm{d}\phi}{\mathrm{d}t} = \frac{1}{\tau_0}(\phi_0 - \phi) + k_0(\phi_\infty - \phi)\boldsymbol{\sigma} : \mathbf{D}, \tag{1.18}$$

$$\boldsymbol{\sigma} + \tau_2 \frac{\phi_0}{\phi} \overset{\nabla}{\boldsymbol{\sigma}} = \frac{1}{\phi}\mathbf{D}, \tag{1.19}$$

where $\boldsymbol{\sigma}$ is the stress tensor, $\mathbf{D}$ is the rate-of-strain tensor, $\phi$ is the solution fluidity, $\phi_0$ is the zero shear-rate fluidity, $\phi_\infty$ is the infinite shear-rate fluidity, $k_0$ is a kinetic parameter, $\tau_1$ and $\tau_2$ are both relaxation times, and the $\nabla$ over a variable indicates the upper-convected derivative of that quantity. In order to remain consistent with the thermodynamic derivation, the parameter $k_0$ is a function of the second invariants of $\mathbf{D}$ and $\boldsymbol{\sigma}$. For reference, the three invariants ($I_i$) of a tensor ($A$) are:

$$I_1(\mathbf{A}) = \mathrm{tr}(\mathbf{A}) \tag{1.20a}$$

$$I_2(\mathbf{A}) = \frac{1}{2}\left(\mathrm{tr}(\mathbf{A})^2 - \mathrm{tr}(\mathbf{A}^2)\right) \tag{1.20b}$$

$$I_3(\mathbf{A}) = \det(\mathbf{A}). \tag{1.20c}$$

The BMP model can capture both shear-thickening and -thinning, a reentrant flow curve Fig. 1.3b, a non-monotonic flow curve Fig. 1.3a, and has shown success in capturing experimental data of dilute and concentrated wormlike. The fact that this model can predict curves that could support both vorticity and shear banding makes this model very useful for studying these complex phenomena. Indeed, the BMP model has been used in CFD studies to look at pressure-driven channel flow instabilities [94], flow past a sphere [95], and instabilities in expansion-contraction geometries [96]. Despite the prediction of a reentrant flow curve it does not appear that the BMP model has been used to look at vorticity banding, possibly because this model is better suited for describing concentrated WLM solutions. Indeed, while the BMP model can technically describe dilute wormlike micelle solutions, it

is most often used to study shear-banding [97].

The BMP model does have its drawbacks; notably the model parameters do not have a clear physical connection to the underlying microstructural dynamics of WLM solutions, and the inclusion of dependence on the invariants of the stress and strain-rate tensors limits the computational efficiency of this model. Moreover, the dependence on the Oldroyd-B model presents difficulties in extensional flow, where the infinite elasticity of the dumbbells (which are used to derive the model) results in a divergent extensional viscosity [98]. Finally, the ability of the BMP to capture phenomena associated with both dilute and concentrated WLM solutions is not necessarily a positive attribute since the physics and dynamics of these solutions vary drastically with concentration; consequently, although this model may predict similar behavior to experiments, it may not be capturing the microstructural basis and kinetics properly.

There has been recent work expanding the BMP framework to develop new models for WLM solutions. Tamano and coworkers [99] took inspiration from the BMP model and coupled the fluidity equation to both the FENE-P and Giesekus equations, both of which are widely used for studying viscoelastic fluids, to develop the f-FENE-P and f-Giesekus models, respectively. These two models, like the BMP, can capture both shear-thickening and -thinning as well as stress-overshoot in start-up flows, and has been successful in fitting experimental data of dilute WLM solutions. Additionally, the f-FENE-P model is particularly well-suited for CFD simulations since many direct numerical simulation (DNS) codes are already developed for the FENE-P equation [34]. Unfortunately, the f-FENE-P and f-Giesekus models are both unable to predict a reentrant or non-monotonic flow curve, thus restricting their use in studying banding.

### 1.3.4 Brownian rods

Before moving to the next model for wormlike micelle solutions, it is critical to outline the governing equations used for modeling Brownian rod suspensions. This background is impor-

tant because the framework developed for the dynamics of Brownian rod suspensions serves as the basis for the model used throughout this work - the reformulated reactive rod model (RRM-R) - as well as its predecessor, the reactive rod model (RRM, see Section 1.3.5). Both the RRM and RRM-R treat wormlike micelle solutions as suspensions of rigid, Brownian rods that are able to undergo reversible scission and fusion; thus, to fully understand these models, it is crucial to outline the underlying non-reactive Brownian rod framework. This section will draw heavily from work by Doi and Edwards [75].

Beginning with similar starting blocks to Section 1.3.1, consider a long, rigid rod in a viscous fluid with viscosity $\eta_s$ undergoing rotational and translational diffusion. The rod is characterized by length $L$, radius $b$, and unit director vector $\mathbf{u}$, which points along the rod axis. For the non-polar rods we will consider $\mathbf{u}$ is indistinguishable from $-\mathbf{u}$. The rotational diffusion of the rod can be thought of as a particle undergoing a random walk on the surface of the unit sphere. The rotational friction constant of the rod is [80]

$$\zeta_r = \frac{\pi \eta_s L^3}{3 \ln(L/2b)}. \tag{1.21}$$

Let $\psi(\mathbf{u}; t)$ be the probability distribution function of $\mathbf{u}$ and $\mathbf{K}$ be a velocity gradient acting on a rod, the Smoluchowski equation for rotational diffusion is [75]

$$\frac{\partial \psi}{\partial t} = \frac{1}{\zeta_r} \mathcal{R} \cdot [k_B T \mathcal{R} \psi + \psi \mathcal{R} U] - \mathcal{R} \cdot (\mathbf{u} \times \mathbf{K} \cdot \mathbf{u} \psi), \tag{1.22}$$

where again $\mathcal{R} \equiv \mathbf{u} \times \partial / \partial \mathbf{u}$ is the rotational gradient operator and $U$ is an arbitrary external potential that can depend on the rod orientation (e.g., a magnetic force). For this work we will only consider the effects of a velocity field so we set $U = 0$. The form of Eq. (1.22) may be intimidating, but note that it is simply the convection-diffusion equation for probability and comes from

$$\frac{\partial \psi}{\partial t} = -\frac{\partial}{\partial \mathbf{u}} \cdot (\boldsymbol{\omega} \times \mathbf{u} \psi) = -\mathcal{R} \cdot (\boldsymbol{\omega} \psi), \tag{1.23}$$

where $\boldsymbol{\omega}$ is the angular velocity of the rod, which comes from hydrodynamic arguments [75]. Equation (1.22) can be rewritten in terms of the rotational diffusion constant

$$D_r = \frac{k_B T}{\zeta_r} = \frac{3 k_B T \ln(L/b)}{\pi \eta_s L^3}. \tag{1.24}$$

The Smoluchowski equation for translational diffusion can be similarly derived, though now we must consider differences between parallel and perpendicular motion. The friction coefficients for parallel and perpendicular motion are [26]

$$\zeta_\parallel = \frac{2\pi\eta_s L}{\ln(L/b)}, \tag{1.25a}$$

$$\zeta_\perp = 2\zeta_\parallel, \tag{1.25b}$$

respectively. The Smoluchowski equation is then obtained by substituting the velocity of the rod under an imposed flow, $\mathbf{v}$, into the continuity equation for probability

$$\frac{\partial \psi}{\partial t} = -\frac{\partial}{\partial \mathbf{R}} \cdot (\mathbf{v}\psi) - \mathcal{R} \cdot (\boldsymbol{\omega}\psi), \tag{1.26}$$

where $\mathbf{R}$ is the center-of-mass of the rod. Note that we have included the additional conservation term for angular diffusion so that by substituting $\mathbf{v}$ and $\boldsymbol{\omega}$ into this expression we obtain the Smoluchowski equation for both rotational and translational motion:

$$\begin{aligned} \frac{\partial \psi}{\partial t} = \frac{\partial}{\partial \mathbf{R}} \cdot \left[ D_\parallel \mathbf{uu} + D_\perp (\mathbf{I} - \mathbf{uu}) \right] \cdot \frac{\partial \psi}{\partial \mathbf{R}} - \frac{\partial}{\partial \mathbf{R}} \cdot (\mathbf{K} \cdot \mathbf{R}\psi) \\ + D_r \mathcal{R} \cdot [k_B T \mathcal{R}\psi + \psi \mathcal{R} U] - \mathcal{R} \cdot (\mathbf{u} \times \mathbf{K} \cdot \mathbf{u}\psi). \end{aligned} \tag{1.27}$$

Here, $D_\parallel = k_B T/\zeta_\parallel$ and $D_\perp = k_B T/\zeta_\perp$ are the diffusion constants for parallel and orthogonal motion, respectively.

The goal is now to determine how the rod orientation changes under a weak velocity gradient and in the absence of an external force ($U = 0$). The rod orientation is tracked

using the orientation tensor,

$$\mathbf{S} = \langle \mathbf{uu} \rangle = \int \mathbf{uu}\psi \mathrm{d}\mathbf{u}, \tag{1.28}$$

which can also be written in traceless form

$$\widehat{\mathbf{S}} = \mathbf{S} - \frac{1}{3}\mathbf{I}. \tag{1.29}$$

To calculate an evolution equation for $\mathbf{S}$, Eq. (1.22) is multiplied by $\mathbf{uu} - \mathbf{I}/3$ and integrated by parts, yielding [75]:

$$\frac{\partial \mathbf{S}}{\partial t} = -6D_r \left( \mathbf{S} - \frac{1}{3}\mathbf{I} \right) + \mathbf{K} \cdot \mathbf{S}^\top + \mathbf{S} \cdot \mathbf{K}^\top - 2\mathbf{K} : \langle \mathbf{uuuu} \rangle. \tag{1.30}$$

This equation fully describes the evolution of the orientation tensor for a dilute collection of rods subject to flow. The first term on the right-hand side accounts for Brownian motion; this term acts to drive the suspension to isotropy (e.g., $\mathbf{S} = \mathbf{I}/3$), and in the absence of flow is the only term that remains. The remaining terms on the right-hand side account for the orientation of rods by the velocity gradient. Notice that the last term in this expression includes the fourth-order tensor $\langle \mathbf{uuuu} \rangle$ (i.e., the fourth moment of $\mathbf{u}$); the presence of this term indicates that Eq. (1.30) is not closed. In order to close this expression we require an evolution equation for $\langle \mathbf{uuuu} \rangle$, however, this evolution equation would then include a dependence on $\langle \mathbf{uuuuuu} \rangle$, which itself would depend on higher moments. Thus, in order to obtain a closed-form evolution equation for $\mathbf{S}$ we must supply a 'closure approximation'. At the moment we will leave this expression open and return to it later, but note that multiple closure approximations are possible [100, 101, 102].

Finally, to complete the evolution equations for a dilute solution of Brownian rods we need to calculate the rod contributions to the solutions stress. Doi and Edwards [75] consider two components, a viscous stress and an elastic stress. The viscous stress contribution is obtained by relating it to the work done by the frictional force for a rod undergoing an

infinitesimal motion relative to the bulk fluid, and is found to be

$$\boldsymbol{\tau}^V = \frac{nk_BT}{2D_r}\mathbf{K} : \langle \mathbf{uuuu} \rangle, \tag{1.31}$$

where $n$ is the number density of rods. Similarly, the elastic stress is calculated by relating it to the change in free energy for an infinitesimal deformation, and is given by

$$\boldsymbol{\tau}^E = 3nk_BT\left(\mathbf{S} - \frac{1}{3}\mathbf{I}\right). \tag{1.32}$$

Notice how, similar to Eq. (1.30), in the absence of flow the viscous stress vanishes and all that remains is the elastic stress that acts to return the solution to isotropy. Also, the viscous stress contains the fourth moment of $\mathbf{u}$, which again will require a decoupling approximation.

The rheological properties of Brownian rods are not particularly interesting; they are weakly shear-thinning, which occurs as a result of rods orienting along the flow direction. Because rods do not stretch they induce very little extensional stress, which is in stark contrast to dilute polymer solutions that can support massive extensional stresses that give rise to very interesting elastic and viscoelastic instabilities.

### 1.3.5 Reactive rod model

The reactive rod model (RRM) was developed by Dutta and Graham [3] as a tensor constitutive model for predicting the flow dynamics of dilute wormlike micelle solutions. The RRM serves as the predecessor for the model developed and used in much of this work, the reformulated reactive rod model (RRM-R), and it is thus necessary to fully describe the development and predictions of this model. The RRM was developed with the intent of capturing the shear-thickening and -thinning, flow-induced structure (FIS) formation, and reentrant flow curves associated with dilute WLM solutions. This model adopts a framework that treats dilute WLM solutions as suspensions of Brownian rods undergoing reversible scission and fusion. The mechanisms in the RRM are largely based on those presented by

Turner and Cates [74, 73], which was discussed in Section 1.3.1; the flow-induced alignment of micelles allows for increased micelle fusion through collinear, end-to-end collisions. As micelles become elongated, hydrodynamic stresses develop along the backbone and act to break micelles into shorter segments.

The basis of the RRM is the same as that of Brownian rods, described in Section 1.3.4. A micelle is taken to have length $L$, radius $b$, and orientation tensor $\mathbf{S}$. The evolution of the orientation is described by Eq. (1.30) and the micelle contribution to the stress is given by the summation of the elastic, Eq. (1.32), and viscous, Eq. (1.31), stresses. In order to allow for fusion and scission of micelles, the length of the micelles is taken to be a dynamic property that can change with time and flow. Conservation of mass is enforced through conservation of surfactants, defined by

$$n_0 L_0 = nL, \tag{1.33}$$

where $n_0$ and $L_0$ are the equilibrium micelle number density and length, respectively. These equilibrium values are constant, whereas $n$ and $L$ vary. The rotational diffusion constant of the rods depends on length and must also be modified to account for the difference in diffusivities for rods of length $L_0$ and $L$,

$$D_r = \frac{D_{r,0}}{L^{*3}} \left( \frac{\ln L^* + m}{m} \right), \tag{1.34}$$

where $D_r$ is the diffusion constant for a rod of length $L$, $D_{r0}$ is the rotational diffusivity of the rods at equilibrium (i.e., $L = L_0$), $L^* = L/L_0$ is the dimensionless rod length, and $m = \ln(L_0/2b)$ is a constant that depends on the initial aspect ratio of the rods.

Dutta and Graham next develop an equation for the micelle length by making mechanistic arguments about the reaction scheme. Notably, this model is not meant to perfectly capture the chemical and thermodynamic properties of micelle fusion and scission, but rather act as a phenomenological model for the reaction kinetics. The micelle evolution equation is

written in general form

$$\frac{\mathrm{d}L^*}{\mathrm{d}t^*} = R_a + R_s, \tag{1.35}$$

where $R_a$ represents alignment-induced growth and $R_s$ represents the spontaneous growth and breakdown of micelles. The alignment-induced growth term is assumed to increase linearly with rod alignment, where rod alignment is tracked through the scalar orientation parameter,

$$\widehat{S} = \sqrt{\frac{3}{2}\left(\widehat{\mathbf{S}} : \widehat{\mathbf{S}}\right)}. \tag{1.36}$$

Thus,

$$R_a = k\widehat{S}, \tag{1.37}$$

where $k$ is a constant. The spontaneous term is taken to be proportional to the deviation of the length from its equilibrium value. Additionally, in order to capture the idea that long rods are broken down by hydrodynamic stresses, it is assumed that there is some maximum rod length, $L^*_{\max}$, that acts as the longest a rod can become without breaking. As $L$ approaches $L^*_{\max}$ the breakage rate should increase rapidly, motivating a FENE-like dependence (i.e., finitely extensible nonlinear elastic) [24]. It is also assumed that the maximum rod length has the form $L^*_{\max} = \alpha + \beta/\mathrm{Pe}$, where $\alpha$ and $\beta$ are model parameters and Pe is the dimensionless shear rate. This form captures the idea that hydrodynamic stresses increase with increasing deformation rate, yielding an inverse relationship with the shear rate. Combining these features,

$$R_s = \frac{\lambda}{1 - \left(\frac{L^*}{\alpha + \frac{\beta}{\mathrm{Pe}}}\right)^2}\left(1 - L^*\right), \tag{1.38}$$

and the overall evolution equation for micelle length is

$$\frac{\mathrm{d}L^*}{\mathrm{d}t} = \frac{\lambda}{1 - \left(\frac{L^*}{\alpha + \frac{\beta}{\mathrm{Pe}}}\right)^2}\left(1 - L^*\right) + k\widehat{S}. \tag{1.39}$$

For completion, the micelle stress is given by

$$\boldsymbol{\tau}^m = 3nk_BT\left(\mathbf{S} - \frac{1}{3}\mathbf{I}\right) + \frac{nk_BT}{2D_r}\mathbf{K} : \langle \mathbf{uuuu} \rangle. \tag{1.40}$$

The last thing needed to complete this model is a closure approximation for the fourth moment of $\mathbf{u}$. The RRM uses a closure by Dhont and Briels [103], which interpolates between exact expressions at equilibrium and at perfect alignment:

$$\mathbf{K} : \langle \mathbf{uuuu} \rangle \approx \frac{1}{5}[\mathbf{S}\cdot\mathbf{D} + \mathbf{D}\cdot\mathbf{S} - \mathbf{S}\cdot\mathbf{S}\cdot\mathbf{D} - \mathbf{D}\cdot\mathbf{S}\cdot\mathbf{S} + 2\mathbf{S}\cdot\mathbf{D}\cdot\mathbf{S} + 3(\mathbf{S}:\mathbf{D})\mathbf{S}], \tag{1.41}$$

where $\mathbf{D} = (\mathbf{K} + \mathbf{K}^\top)/2$ is the rate of strain tensor and the double dot product is defined by $\mathbf{A} : \mathbf{B} = \mathrm{tr}(\mathbf{A}\cdot\mathbf{B}^\top)$. Equations (1.30), (1.39), (1.40) and (5.31) form a closed set of governing equations describing the dynamics of a reactive Brownian rod solution meant to represent the rheology and behavior of dilute wormlike micelle solutions.

Using this framework, the RRM has shown success in capturing experimental observations of dilute WLM solutions, specifically in steady flows [3]. Additionally, one of the key successes of the RRM is that it is able to capture a reentrant flow curve, suggesting that it could be useful for studying vorticity banding. The simplicity and tractability of the RRM also indicates that this model could be efficiently implemented in CFD studies for looking at more complex phenomena.

Figure 1.5 shows example for curves for the RRM in steady shear flow, with (a) normalized viscosity, (b) micelle shear stress, (c) micelle length, and (d) orientation parameter; the parameters are $\alpha = 5$, $\beta = 500$, and varying $k$. We can see that by varying $k$ over a small range the RRM can predict a wide array of behaviors, and specifically is able to capture the distinct shear-thickening and -thinning of dilute WLM solutions. These curves emphasize the fact that the RRM serves as an excellent proof-of-concept model - the framework of reactive Brownian rods is rich and suitable for describing dilute WLM solutions.

The RRM does have its pitfalls, however, that necessitate the development of improve-

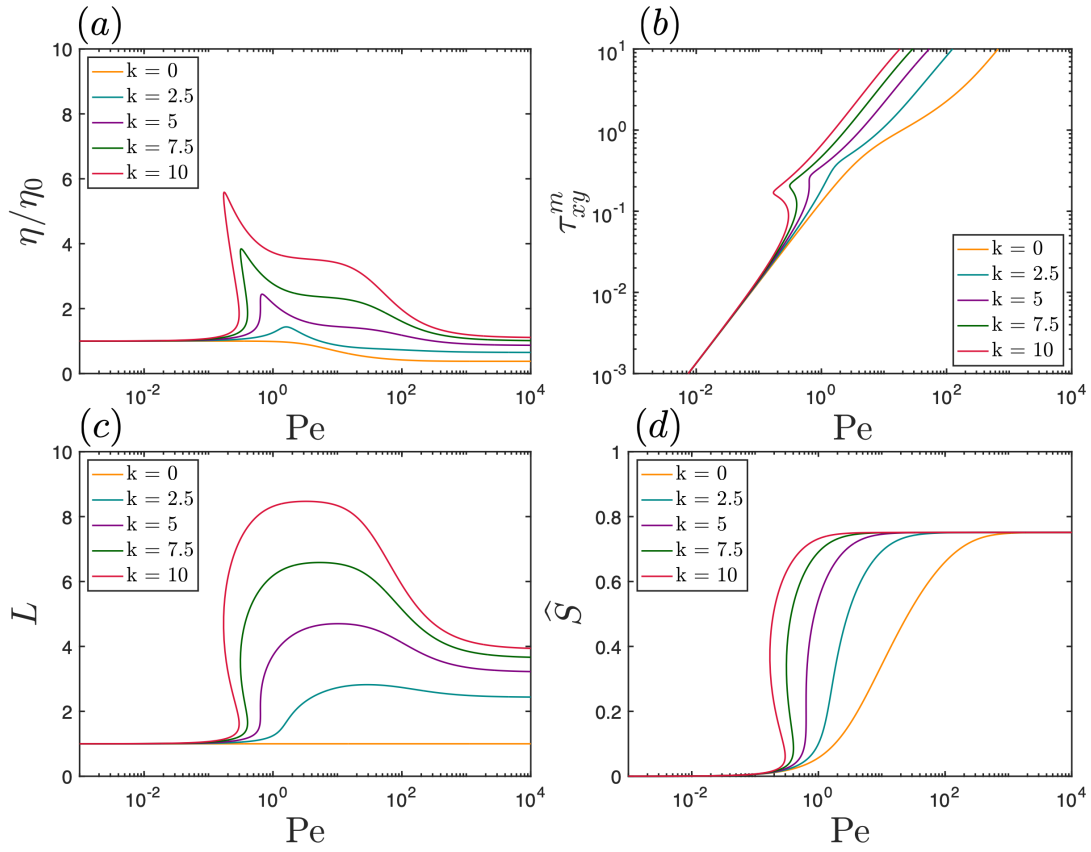


**Figure 1.5:** Steady shear flow curves for the RRM with $\alpha = 5$, $\beta = 500$, and varying $k$; (a) normalized viscosity, (b) micelle shear stress, (c) micelle length, and (d) orientation parameter. Figure based on [3].

ments through further model iterations. Notably, the plateau in the viscosity at intermediate shear rates (see Fig. 1.5a for $k = 10$) is not seen in experiments; further, the plateau in the micelle length, Fig. 1.5c, at high shear rates is unphysical since we expect micelles to be shredded into short segments at high flow rates. This feature is due to the nature of the proposed length equation, which was constructed phenomenologically and lacks clear physical insights. Finally, although not presented here, the RRM significantly struggles in predicting transient dynamics, which is a critical shortcoming if the RRM is to be used for looking at instabilities or drag reduction. In Chapter 2, we will address the struggles of the RRM through the development of a new model for WLM solutions that relies on more physical, though still mechanistic, arguments to develop a reaction equation for the micelle length.

## 1.4 Outline of this work

The main objects of this thesis are to develop an accurate and tractable model for dilute wormlike micelle solutions and to use this model in analysis and simulations to understand the rheology and formation of instabilities in these solutions. We also aim to establish and ensure the thermodynamic consistency of our model, as well as derive new models in a non-equilibrium thermodynamics framework.

The remainder of this thesis is divided into five chapters, each addressing aspects of these objectives and aims. In Chapter 2, we derive a model for dilute wormlike micelle solutions. This model, the reformulated reactive rod model (RRM-R), treats WLM solutions as suspensions of reactive Brownian rods undergoing reversible scission and fusion reactions. We show that this model can predict shear-thickening and -thinning, transient dynamics, and a reentrant flow curve; the RRM-R can also be successfully fit to a variety of experimental data.

In Chapter 3, we use the RRM-R in computational fluid dynamics simulations of circular Couette flow, specifically studying flows that show reentrant constitutive curves. Using these

simulations, we show that the RRM-R can predict finger-like instabilities that have previously only been observed in experiments. We then expand these simulations in Chapter 4 to look at instabilities in plane Poiseuille flow; we show that the RRM-R predicts an 'interfacial' instability that strongly resembles instabilities in viscosity-stratified flows.

In Chapter 5, we attempt to establish the thermodynamic consistency of the RRM-R, as well as derive new models for dilute WLM solutions using the single generator bracket framework of non-equilibrium thermodynamics. This framework has shown recent success in deriving thermodynamically consistent models for concentrated WLM solutions, cement pastes, and aggregating blood suspensions [88, 104, 105]. Finally, in Chapter 6 we summarize our key findings and pose promising directions for future work.

# 2

# Constitutive modeling of dilute wormlike micelle solutions [1]

In this section we present a reformulation of the 'reactive rod model' (RRM) of Dutta and Graham [Dutta, Sarit and Graham, Michael D., *JNNFM* 251 (2018)], a constitutive model for describing the behavior of dilute wormlike micelle solutions. The RRM treats wormlike micelle solutions as dilute suspensions of rigid Brownian rods undergoing reversible scission and growth in flow. Evolution equations for micelle orientation and stress contribution are coupled to a kinetic reaction equation for a collective micelle length, producing dynamic variations in the length and rotational diffusivity of the rods. This model has previously shown success in capturing many critical steady-state rheological features of dilute wormlike micelle solutions, particularly shear-thickening and -thinning, non-zero normal stress differences, and a reentrant shear stress-shear rate curve, and could fit a variety of steady state experimental data. The present work improves on this framework, which showed difficulty in capturing transient dynamics and high-shear behavior, by reformulating the kinetic equation for micelle growth on a more microstructural (though still highly idealized) basis. In particular, we allow for micelle growth associated with strong alignment of rods and breakage

[1] The text of this chapter is adapted from the publication by R.J. Hommel and M. D. Graham *JNNFM*, **295**, 104606, 2021.

due to tensile stresses along the micelles. This new formulation captures both steady and transient shear rheology in good agreement with experiments. We also find good agreement with available steady state extensional rheology.

## 2.1 Introduction

Surfactants are amphiphilic molecules consisting of bulky hydrophilic head groups bonded to long-chain hydrophobic tails; beyond some concentration, the critical micelle concentration (CMC), surfactants self-assemble into aggregate structures whose geometry is dictated by the size, shape, and chemistry of the surfactant molecules as well as temperature and the salinity of the solution [40, 106, 45, 54]. Among these aggregate structures are spherical and wormlike or rodlike micelles, as well as vesicles and bilayers. At sufficiently high concentrations, wormlike micelles can entangle and form large-scale networks and branched structures, transitioning into a highly viscoelastic gel-like phase. The application of an external field (e.g. flow), or increased temperature, can disrupt these networks and force micelles into distinct structures [107, 46, 108].

Herein we focus on dilute surfactant solutions that form wormlike micelles (WLMs); these solutions have been shown to exhibit remarkable flow dynamics ranging from pronounced shear-thickening and -thinning regimes to shear-induced structure (SIS) formation, as well as numerous instabilities in shear and extensional flows [9, 10, 11, 12, 13]. The addition of small amounts of wormlike micelle-forming surfactants to turbulent flows can produce up to an $80 - 90\%$ reduction in turbulent drag, which in some cases can exceed the drag-reducing capabilities of the most widely used polymer solutions [109, 1, 2]. Moreover, the self-assembling capabilities of these micellar solutions, through which surfactants are able to reassemble into aggregate structures following mechanical deformations, can also be exploited to overcome the well-known shear-induced breakdown of polymer chains in the pumping of turbulent flows. There has even been recent interest in leveraging the shear-thickening and

-thinning properties of dilute surfactant solutions to form less environmentally destructive carrier fluids in oil recovery operations [14]. The ubiquity of surfactant solutions, including widespread use in household and commercial products, has motivated numerous studies over recent decades into understanding the rheology, dynamics, and flow behavior of these solutions.

Experiments have demonstrated that the behavior of wormlike micelle solutions drastically changes with concentration [14]. In the upper semi-dilute and concentrated regimes, WLM solutions typically show shear-thinning behavior reminiscent of long-chain polymer solutions. These higher concentration solutions also tend to exhibit, under appropriate conditions, the well-known shear-banding (or gradient banding) instability. This instability is characterized by the development of a macroscopically "banded" flow in which fluid separates into two distinct regions of equal shear stress but each supporting a unique shear rate [47, 55]. The separation of these two regions is often observable through differences in turbidity and/or birefringence. There has been extensive theoretical and experimental treatment of this instability (see [47, 57] for a comprehensive review).

In the dilute and lower semi-dilute regimes, WLM solutions exhibit pronounced shear-thickening behavior associated with the formation of SISs; at high deformation rates this thickening gives way to stark shear-thinning induced by the breakdown of SISs and strong orientation of the micelles [62, 61]. In the dilute regime, SISs take the form of elongated wormlike micelles that can be several times longer than the equilibrium micelle length, in some cases yielding micelles with lengths on the order of microns [45, 46]. In addition to this shear-thickening and -thinning behavior, dilute WLM solutions can display reentrant, or multivalued, flow curves (shear stress vs. shear rate); the existence of a reentrant flow curve is a necessary condition for a relatively unique vorticity banding instability [50]. In contrast to the shear-banding instability of higher concentrations, vorticity banding requires that a single shear rate be able to support multiple shear stresses. In circular Couette flow, this instability manifests as stacked "bands" along the vorticity axis, where adjacent bands

support distinct shear stresses. Again, similar to gradient banding, these bands can often be visualized by differences in turbidity and birefringence [47, 50].

There have been a number of theoretical treatments and models put forth to explain and predict the behavior and dynamics of WLM solutions. The proposed models can be loosely lumped into three categories: population balance models, coupled fluidity models, and microstructural models. One of the earliest treatments of WLM solutions was by Cates and Turner [110, 73] with the aim of generating a population balance model that accounted for the different stress relaxation mechanisms associated with wormlike micelles, namely micelle scission and rotational diffusion. This work led to the development of an evolution equation for the probability distribution function for a micelle of given length and orientation by considering a reversible kinetic reaction scheme: a given micelle can rupture at any point along its length to form two shorter micelles, while two collinear micelles can also fuse into a single, larger micelle. The model assumes that rods must be strongly aligned for fusion to occur in order to avoid the large energetic penalty associated with bent micelles; this collinearity assumption results in a positive feedback mechanism owing to the decreased angular mobility of longer rods, and this feedback can incur a gelation transition in which micelle length diverges sharply. Further, the competition between relaxation mechanisms yields two distinct limits: a fast-breaking (scission-dominated) limit and a slow-breaking (rotation-dominated) limit.

The Cates and Turner model has shown good agreement with experiments, however, the presence of a continuous spectrum of lengths in this model greatly restricts both its use in studying more complex flows and its incorporation into fluid-dynamical studies. Nevertheless, this model provides a strong mechanistic basis for understanding the dynamics of WLM solutions, and has been used as a foundation for other WLM models both in the dilute and concentrated regimes [76, 3]. We omit a thorough review of the remaining population balance type models as these have been developed primarily for understanding the behavior of concentrated WLM solutions, and thus fall outside the scope of the present work. Read-

ers interested in the modeling and dynamics of concentrated WLM solutions are directed to the Vazquez-Cook-McKinley (VCM) model [76, 78], the simplified tube approximation for rapid-breaking micelles (STARM) model by Peterson and Cates [111], and Brownian dynamics simulations of the VCM and reformulated VCM models by Adams and coworkers [112].

We now turn our attention back to models for dilute WLM solutions, and in particular to coupled fluidity models; as the name suggests these models couple well-known and well-studied models for general viscoelastic fluids (e.g. Oldroyd-B, FENE-P, Giesekus) to a fluidity (inverse viscosity) evolution equation originally proposed by Fredrickson for studying thixotropic systems [93]. The fluidity equation accounts for spontaneous 'buildup' and shear-induced 'breakdown' of microstructure in the fluid. By coupling the fluidity equation to the Oldroyd-B equation, Bautista et al. [113] have formed the BMP model, which is able to predict both shear-thickening and shear-thinning behavior. More recently, Manero et al. [90] developed the generalized BMP model, where the model's kinetic parameters are taken as functions of the second invariants of both deformation rate and stress tensors, expanding the model to allow for reentrant behavior. This model has also been used successfully by Lanzàzuri et al. [7] to predict the steady and transient behavior of CTAB and CTAVB solutions and has shown good agreement with experimental results. However, the BMP model lacks a clear connection between model parameters and the underlying microstructural dynamics of WLM solutions and the use of the Oldroyd-B equation presents difficulties in extensional flows due to a divergent extensional viscosity [98].

More recently, Tamano et al. [99] have taken inspiration from the BMP model and have coupled a fluidity equation to the Giesekus and FENE-P models to form the f-Giesekus and f-FENE-P models, respectively. This formulation results in four dimensionless parameters accounting for micelle breakdown and build-up (e.g. elongation) timescales, infinite and zero-shear viscosity ratios, and maximum extensibility of micelles. Using this formulation the authors simultaneously capture shear-thickening and -thinning, which is not possible

using either of the pure Giesekus and FENE-P models. Further, the transient behavior of this model, in particular in startup of steady shear flow, demonstrates a stress overshoot that is similar to experimental observations of WLM solutions. The f-FENE-P model does suffer from an inability to predict nonzero second normal stress differences, an artifact of the original FENE-P model's inability to do so, and there is some difficulty in predicting the steepness of viscosity vs. shear rate data as well as the magnitude of shear-thickening seen in experiments. Notably, however, this formulation is particularly well-suited for implementation in direct numerical simulations (DNS) given that the majority of simulations for viscoelastic polymer solutions are already formulated on the FENE-P and Giesekus constitutive equations.

The present work concerns the last class of wormlike micelle models – microstructural models – and in particular focuses on a reformulation of the reactive rod model (RRM), a tensor constitutive model proposed by Dutta and Graham [3]. The RRM takes a phenomenological, but highly microstructurally-motivated, approach to modeling WLMs and treats dilute wormlike micelle solutions as suspensions of rigid Brownian rods able to undergo reversible growth and scission in flow. The model couples evolution equations governing the ensemble average orientation of rods and micelle stress contribution to an evolution equation for the collective length of micelles, where micelle number density and length are constrained by conservation of surfactant molecules. We provide more details on the modeling framework of the RRM in Section 4.2, but note that it follows mechanisms proposed by Turner and Cates [73], namely growth due to flow-induced alignment of micelles and spontaneous scission along the lengths of micelles. The RRM has shown success in capturing experimental observations of dilute WLM solutions, and is able to capture flow curve multiplicity, a necessary condition for vorticity banding, as well as nonzero normal stress differences. While this model provides a proof of principle that the modeling structure of rigid Brownian rods is rich enough to capture many key features associated with dilute WLM solutions, it does have difficulty in predicting transient flow and high-shear results. Further, the nature of

the proposed length equation lacks clear physical insights that, if present, would allow for more precise understanding of rheological behavior. The motivation of the present work is to further develop the RRM by developing a length evolution equation based more closely on WLM dynamics in flow, with the aim of forming a model that is both accurate in predicting WLM rheology and tractable enough for implementation in DNS and in the study of more complex flows.

## 2.2 Model description

The complete derivation of the *reactive rod model* (RRM) is described in [3] and summarized in Section 1.3.5. As discussed above, this modeling framework takes inspiration from theoretical treatments by Cates and Turner [110]. In summary, dilute wormlike micelle solutions are treated as suspensions of rigid Brownian rods undergoing reversible scission and growth. Rods fuse end-to-end (reducing the energetic penalty associated with the micellar end caps), but only when they are highly aligned – otherwise the energy penalty arising from forming a long but bent micelle is too large for fusion to take place [15, 110]. The application of flow tends to align the rods. This alignment is balanced by rotational diffusivity of the rods acting to return the suspension to isotropy. The fundamental assertion of the RRM is that rods are able to react (fuse) in flow to form longer rods, and that the reaction rate increases with increasing rod alignment. Consequently, a positive feedback mechanism exists between rod growth and alignment owing to the smaller rotational diffusivity of longer rods. It is assumed that rod growth is countered by hydrodynamic stresses acting along the lengths of the rods and these stresses, which increase with increasing length, can induce breakage events into shorter rods.

### 2.2.1 Rigid Brownian rods

The underlying theory of a non-reactive suspension of rigid Brownian rods is given in both [3, 75], which we briefly review before delving into the complete RRM. We begin with a uniform collection of rods with length $L_0$, radius $b$, and number density $n_0$ suspended in a Newtonian solvent with viscosity $\eta_s$. The orientation of a single rod is described by the unit director vector $\boldsymbol{u}$. The suspension is subjected to an arbitrary, homogeneous flow with velocity $\boldsymbol{v}$ and transpose velocity gradient $\boldsymbol{K} = \boldsymbol{\nabla v}^\top$. The orientation tensor $\boldsymbol{S}$ describes the average collective orientation of the suspension and is given by the second moment of $\boldsymbol{u}$

$$\boldsymbol{S} = \langle \boldsymbol{uu} \rangle = \int \boldsymbol{uu} \psi \mathrm{d}\boldsymbol{u}, \tag{2.1}$$

where $\psi$ is the probability distribution function of $\boldsymbol{u}$. The time evolution of $\boldsymbol{S}$ in a homogeneous flow can be found by multiplying the rotational Smoluchowski equation

$$\frac{\partial \psi}{\partial t} = D_{r,0} \mathcal{R}^2 \psi - \mathcal{R} \cdot (\boldsymbol{u} \times \boldsymbol{K} \cdot \boldsymbol{u} \psi), \tag{2.2}$$

where $\mathcal{R} \equiv \boldsymbol{u} \times \frac{\partial}{\partial \boldsymbol{u}}$ and $D_{r,0}$ is the rotational diffusion coefficient of a rod, by $\boldsymbol{S}$ and integrating over $\boldsymbol{u}$ [75]. We then have for the time evolution of $\boldsymbol{S}$

$$\frac{\mathrm{d}\boldsymbol{S}}{\mathrm{d}t} = -6 D_{r,0} \left( \boldsymbol{S} - \frac{1}{3} \boldsymbol{I} \right) + \boldsymbol{K} \cdot \boldsymbol{S}^\top + \boldsymbol{S} \cdot \boldsymbol{K}^\top - 2 \boldsymbol{K} : \langle \boldsymbol{uuuu} \rangle, \tag{2.3}$$

where $\boldsymbol{I}$ is the unit tensor and the double dot product is defined as $\boldsymbol{A} : \boldsymbol{B} = \mathrm{Tr}(\boldsymbol{A} \cdot \boldsymbol{B}^\top)$.

The total stress of the suspension is given by the sum of the solvent $\boldsymbol{\tau}_s$ and micellar $\boldsymbol{\tau}_m$ contributions

$$\boldsymbol{\tau} = \boldsymbol{\tau}_s + \boldsymbol{\tau}_m, \tag{2.4}$$

where

$$\boldsymbol{\tau}_s = 2 \eta_s \boldsymbol{D} \tag{2.5}$$

is the Newtonian solvent contribution with rate of deformation tensor $\boldsymbol{D} = \frac{1}{2}(\boldsymbol{K} + \boldsymbol{K}^\top)$ and

$$\boldsymbol{\tau}_m = 3n_0 k_B T \left( \boldsymbol{S} - \frac{1}{3}\boldsymbol{I} \right) + \frac{n_0 k_B T}{2D_{r,0}} \boldsymbol{K} : \langle \boldsymbol{uuuu} \rangle \tag{2.6}$$

is the additional stress due to the presence of rods. Here, $k_B$ is the Boltzmann constant and $T$ is the temperature. Equations (2.3) and (2.6) notably contain the fourth moment $\langle \boldsymbol{uuuu} \rangle$, an evolution equation for which depends on the sixth moment of $\boldsymbol{u}$, which in turn depends on higher moments. To proceed analytically, it is then necessary to supply a closure approximation for the product $\boldsymbol{K} : \langle \boldsymbol{uuuu} \rangle$. While numerous approximations are possible (see, for example: [75, 114, 101]), we use an approximation from Dhont and Briels [103] that interpolates between exact expressions in the limits of isotropy (equilibrium) and complete alignment:

$$\boldsymbol{K} : \langle \boldsymbol{uuuu} \rangle \approx \frac{1}{5}[\boldsymbol{S}\cdot\boldsymbol{D} + \boldsymbol{D}\cdot\boldsymbol{S} - \boldsymbol{S}\cdot\boldsymbol{S}\cdot\boldsymbol{D} - \boldsymbol{D}\cdot\boldsymbol{S}\cdot\boldsymbol{S} + ... \\ 2\boldsymbol{S}\cdot\boldsymbol{D}\cdot\boldsymbol{S} + 3(\boldsymbol{S}:\boldsymbol{D})\boldsymbol{S}]. \tag{2.7}$$

### 2.2.2 Reactive Brownian rods

As discussed above, a key feature of the RRM is that it allows micelles, modeled as rigid rods, to undergo reversible scission and growth by allowing the collective length and number density of the suspension to be dynamic properties that evolve with time and flow. Consider a suspension of rods at equilibrium initially with number density $n_0$ and representative length $L_0$; in practice the length of a wormlike micelle suspension follows an exponential distribution [15], but to make analytical progress it is assumed that a single, representative length is able to suitably characterize the system. The radius $b$ of the rods is taken to be constant. The evolution of length $L$ and number density $n$ are constrained at all times by the surfactant mass balance

$$nL = n_0 L_0. \tag{2.8}$$

Everywhere below, $n$ will be determined by this equation.

The rotational diffusion constant for a rod of length $L_0$ and radius $b$ is given by [75]

$$D_{r,0} = \frac{3k_BT}{\pi\eta_s L_0^3} \ln\left(\frac{L_0}{2b}\right). \tag{2.9}$$

In the RRM, the constant rotational diffusion coefficient of the simple rigid rod model is replaced by the length-dependent coefficient

$$D_r = \frac{D_{r,0}}{L^{*3}} \left(\frac{\ln L^* + m}{m}\right), \tag{2.10}$$

where $L^* = L/L_0$ is the dimensionless micelle length and $m = \ln[L_0/(2b)]$ is a constant related to the initial aspect ratio of the rods. Substituting Eq. (2.10) into Eqs. (2.3) and (2.6), we find

$$\frac{\mathrm{d}\boldsymbol{S}}{\mathrm{d}t} = -6D_r\left(\boldsymbol{S} - \frac{1}{3}\boldsymbol{I}\right) + \boldsymbol{K}\cdot\boldsymbol{S}^\top + \boldsymbol{S}\cdot\boldsymbol{K}^\top - 2\boldsymbol{K} : \langle \boldsymbol{uuuu}\rangle \tag{2.11}$$

and

$$\boldsymbol{\tau}_m = 3nk_BT\left(\boldsymbol{S} - \frac{1}{3}\boldsymbol{I}\right) + \frac{nk_BT}{2D_r}\boldsymbol{K} : \langle \boldsymbol{uuuu}\rangle. \tag{2.12}$$

The rod orientation of the suspension is tracked by introducing a scalar orientational order parameter

$$\widehat{S} = \sqrt{\frac{3}{2}\widehat{\boldsymbol{S}} : \widehat{\boldsymbol{S}}}, \tag{2.13}$$

where $\widehat{\boldsymbol{S}} = \boldsymbol{S} - \frac{1}{3}\boldsymbol{I}$ is the traceless part of $\boldsymbol{S}$. This order parameter varies between $\widehat{S} = 0$ for isotropic rods and $\widehat{S} = 1$ for perfectly aligned rods. The orientation and stress equations are rendered dimensionless by introducing a nondimensional time $t^* = D_{r,0}t$ and Péclet number $\mathrm{Pe} = \dot{\gamma}/D_{r,0}$ in shear flow and $\mathrm{Pe} = \dot{\epsilon}/D_{r,0}$ in extensional flow. Note that the description and equations above are valid for both the original RRM and the reformulation (RRM-R), the only variation between the two models is in the length evolution equation, discussed below.

### 2.2.3 Reactive rod model (RRM)

To allow for variability of rod length the original RRM introduces a length evolution equation of the form

$$\frac{\mathrm{d}L^*}{\mathrm{d}t^*} = R_a + R_s, \tag{2.14}$$

where $R_a$ represents alignment-induced growth of micelles and $R_s$ collectively represents spontaneous fusion and breakdown of micelles. The model assumes that alignment-induced growth increases linearly with rod alignment, while spontaneous growth and breakage are assumed to be proportional to the instantaneous deviation from equilibrium micelle length, $L_0$. The RRM introduces the idea of a maximum length $L^*_{\max}$ beyond which micelles are broken down by hydrodynamic stresses, and since these stresses increase with increasing deformation rates, $L^*_{\max}$ must decrease with increasing Pe. Moreover, the breakdown rate is assumed to increase without bound as $L$ approaches $L^*_{\max}$, suggesting a FENE-like form for $R_s$. Using these assumptions, the RRM proposes a complete length evolution equation of the form

$$\frac{\mathrm{d}L^*}{\mathrm{d}t^*} = \frac{\lambda}{1 - \left(\frac{L^*}{\alpha + \frac{\beta}{\mathrm{Pe}}}\right)^2}(1 - L^*) + k\widehat{S}, \tag{2.15}$$

where $\lambda$, $k$, $\alpha$, and $\beta$ are model parameters. Equations (2.7), (2.11), (2.12) and (2.15) now form a closed set of equations describing the orientation, stress, and length of a suspension of reactive Brownian rods.

### 2.2.4 Reformulated reactive rod model (RRM-R)

The original formulation of the RRM does an excellent job in capturing some of the most commonly seen phenomena in dilute wormlike micelle rheology, namely shear- and extensional-thickening and -thinning, reentrant (i.e. multivalued) shear stress, and non-zero normal stress differences. It also makes progress in putting forth a tractable constitutive model that has potential for implementation in CFD simulations. In this way, the original RRM acts as

a proof-of-principle, indicating that the coupling of orientation, stress, and length evolution equations has great potential in the modeling of dilute wormlike micelle rheology.

However, the original formulation of the RRM has difficulty in accurately capturing phenomena associated with transient flows (e.g. inception of steady shear), which is a significant obstacle for future implementation in CFD studies. This difficulty arises from the nature of length evolution equation (Eq. (2.15)), which notably depends only on Pe number (which is fixed for a given flow) and not on stress (which depends on flow type and time). Importantly, this lack of stress dependence prevents the original RRM from fully distinguishing between shear and extensional flows, or between steady and transient flows. Further, while the length equation in the original RRM does incorporate experimental insights about micellar rheology, such as alignment-induced growth and spontaneous growth and breakdown, there is not a clear physical grounding underlying the structure of the proposed equation. To address this, we present a new length evolution equation that considers in greater depth the microscopic mechanisms underlying micellar reversible scission dynamics. This new formulation incorporates mechanistic parameters that represent distinct microstructural phenomena, thus facilitating more direct comparisons with surfactant rheology and chemistry. It must be acknowledged that this new model still does not attempt to capture the distribution of micelle lengths, nor does it encompass other effect such as formation of branched or laterally-associating micelles.

We begin our reformulation with a similar approach to the original RRM, assuming a length evolution equation that balances growth and breakdown of micelles

$$\frac{\mathrm{d}L}{\mathrm{d}t} = R_g + R_b, \tag{2.16}$$

where $R_g \geq 0$ is the rate of micelle growth and $R_b \leq 0$ is the rate of micelle breakdown.

**Micelle growth rate**

Beginning with $R_g$, we assume that the rate of growth consists of two distinct types: spontaneous growth, $R_{g,s}$, and alignment-induced growth, $R_{g,a}$

$$R_g = R_{g,s} + R_{g,a}. \tag{2.17}$$

Spontaneous growth must occur both in the presence and absence of flow and, as we will address later, must balance with spontaneous breakage in a quiescent suspension to maintain equilibrium. Spontaneous growth, $R_{g,s}$, which occurs when the ends of two micelles randomly collide, must increase with number density and thus we propose a form

$$R_{g,s} = n^2 k_{g0}, \tag{2.18}$$

where $n$ is number density and $k_{g0}$ [$\mathrm{m^7 s^{-1}}$] is a spontaneous growth rate coefficient. The choice of a quadratic dependence on number density is due to the bimolecular nature of a collision event. We note that because we limit our framework to dilute solutions, interactions between micelles, and therefore spontaneous growth events, should occur infrequently.

Now turning our attention to alignment-induced growth, a feature of both Cates and Turner's work as well as the original RRM, we assume that this type of growth must depend on both the alignment and collision frequency of rods. We capture this idea with a functional form

$$R_{g,a} = f(\widehat{S})g(\nu), \tag{2.19}$$

where $\nu$ is collision frequency. We assume a separable form here to make analytical progress, though this may not be the case. Rod alignment is captured by the orientational order parameter $\widehat{S}$, and the bimolecular nature of a combination event suggests a quadratic dependence on order

$$f(\widehat{S}) = k_{ga,1}\widehat{S}^2, \tag{2.20}$$

where $k_{ga,1}$ is a kinetic growth parameter.

There are two possible mechanisms for collisions – diffusion and flow. A simple approximation for collision frequency due to flow is $\nu = n^2||\boldsymbol{D}||$. Here, $\nu$ depends on $\boldsymbol{D}$ rather than $\boldsymbol{K}$ because strain and the relative motion of micelles, as opposed to rigid rotation, produces collisions. Again, the bimolecular nature of growth suggests a quadratic dependence on number density. Ignoring variation in number density with flow rate we thus approximate that the collision frequency due to flow scales linearly with Pe number.

Now turning our attention towards collisions due to diffusion, we can show that translational diffusivity alone, and not strain induced by the flow, is sufficient to induce end-to-end collisions. The mean squared displacement $\Delta r^2$ behaves as

$$\left\langle \Delta r^2 \right\rangle = 6 D_{\text{eff}} t, \tag{2.21}$$

where $D_{\text{eff}} = (D_{\parallel} + 2D_{\perp})/3$ is the effective translational diffusion coefficient for the rod, and $D_{\parallel}$ and $D_{\perp} \approx D_{\parallel}/2$ are the diffusivities parallel and perpendicular to the rod axis, respectively [115]. The parallel diffusivity is given by

$$D_{\parallel} = \frac{k_B T \ln(L/b)}{2\pi\eta_s L} \tag{2.22}$$

[75]. For a typical wormlike micelle of length $L \sim \mathcal{O}(10\text{ nm})$ and radius $b \sim \mathcal{O}(1\text{ nm})$ in an aqueous solution at room temperature, we find from Eq. (2.22) that $D_{\parallel} \sim \mathcal{O}(10^{-11}\text{ m}^2\text{s}^{-1})$.

We estimate the average distance between between rods as $x_{\text{avg}} \sim n^{-1/3}$. We consider a dilute surfactant solution with concentration $\sim \mathcal{O}(1\text{ mM})$ and an estimated $\sim \mathcal{O}(10^2)$ surfactant molecules per rod, giving a rod number density of $\sim \mathcal{O}(10^{23}\text{ rods/m}^3)$, and thus an average distance between rods of $x_{\text{avg}} \sim 10^{-8}$ m. Using Eq. (2.21), we calculate that end-to-end collision events occur on the order of $\sim \mathcal{O}(10^{-5}\text{ s})$. This fact that diffusion-driven collision events occur on such a short timescale indicates that diffusion alone is enough to account for collision-induced growth. Of course, at sufficiently high shear rates (e.g. $\gtrsim 10^4$

$s^{-1}$), such as in turbulent flows, convective and diffusive timescales will become comparable and this approximation will no longer hold; however, the majority of rheological experiments occur below this high shear regime. We therefore can discard the convective shear dependence in the alignment-induce growth term, leaving us with $g(\nu) = k_{ga,2}n^2$, and our overall growth rate is

$$R_g = n^2 k_{g0} + k_{ga} n^2 \widehat{S}^2, \tag{2.23}$$

where $k_{ga}$ $[m^7 s^{-1}]$ is an overall alignment-induced growth coefficient.

**Micelle breakage rate**

We now turn our attention to the micellar breakage rate $R_b$. Similar to the growth rate, we consider two distinct types of breakage: spontaneous breakage, $R_{b,s}$, and tension-induced breakage, $R_{b,t}$

$$R_b = R_{b,s} + R_{b,t}. \tag{2.24}$$

Spontaneous breakage, like growth, occurs in both the presence and absence of flow and must increase with rod length. These considerations suggest a spontaneous breakage rate of the form

$$R_{b,s} = -k_{b0} L, \tag{2.25}$$

where $k_{b0}$ $[s^{-1}]$ is a rate constant. At equilibrium spontaneous growth and breakage must balance such that

$$0 = n_0^2 k_{g0} - k_{b0} L_0. \tag{2.26}$$

This relation, along with the surfactant mass balance (Eq. (3.7)), allows us to rewrite $k_{g0}$ in terms of $k_{b0}$.

Now considering breakage under flow, we assume that as rods become sufficiently long they will be broken down by hydrodynamic stresses. Although this mechanism was incor-

porated in the original RRM, we propose here a more physical grounding for the functional form of the breakage term, by specifically taking this rate to be affected by the tensile force $\boldsymbol{T}$ at the midpoint of a rod. This force acts along the direction of the rod, so can be written $\boldsymbol{T} = T\boldsymbol{u}$. Now we note that the stress $\boldsymbol{\tau}_m$ exerted on the fluid by the rods is approximated by

$$\boldsymbol{\tau}_m \sim n(\boldsymbol{T}L\boldsymbol{u}) = n(TL\boldsymbol{u}\boldsymbol{u}). \tag{2.27}$$

Here the term in parentheses estimates the force dipole exerted by a micelle on the fluid [115]. Taking the dot product with $\boldsymbol{u}$ on both the left and right, noting that $\boldsymbol{u}\cdot\boldsymbol{\tau}_m\cdot\boldsymbol{u} = \boldsymbol{u}\boldsymbol{u} : \boldsymbol{\tau}_m$, and solving for $T$ yields

$$T \sim \frac{\boldsymbol{u}\boldsymbol{u} : \boldsymbol{\tau}_m}{nL}. \tag{2.28}$$

We can further simplify this expression by estimating $\boldsymbol{u}\boldsymbol{u}$ as its ensemble average $\boldsymbol{S}$ and applying the surfactant balance $nL = n_0L_0$ to find that

$$T \sim \frac{\boldsymbol{S} : \boldsymbol{\tau}_m}{n_0L_0}. \tag{2.29}$$

Viewing the micelle tension as increasing the likelihood that a micelle will overcome the free energy barrier to scission [15] motivates the use of an Arrhenius-type breakage rate expression:

$$R_{b,t} = -k_{bt}\left[\exp\left(\frac{a}{k_BT}\frac{\boldsymbol{S} : \boldsymbol{\tau}_m}{n_0L_0}\right) - 1\right], \tag{2.30}$$

where $k_{bt}$ $[ms^{-1}]$ is a tension-induced breakage coefficient and $a$ $[m]$ acts as constant for micelle scission. Note that $Ta$ has units of work, and thus one could view $a$ as the distance the two halves of the micelle need to be pulled apart to break it in half. In our fitting of experimental data, we find $a$ to be on the order of nanometers, which is physically reasonable. This term has been structured so that at rest, (i.e. when $\boldsymbol{S} : \boldsymbol{\tau}_m = 0$), the tension-induced breakage rate vanishes entirely. Substituting Eqs. (2.25) and (2.30) into Eq. (2.24) gives our

overall breakage rate

$$R_b = -k_{b0}L - k_{bt}\left[\exp\left(\frac{a}{k_BT}\frac{\boldsymbol{S}:\boldsymbol{\tau}_m}{n_0L_0}\right) - 1\right] \tag{2.31}$$

**Overall length evolution**

Substituting Eqs. (2.23) and (2.31) into Eq. (2.16) gives our dimensional length evolution equation

$$\frac{\mathrm{d}L}{\mathrm{d}t} = k_{g0}n^2 + k_{ga}n^2\widehat{S}^2 - k_{b0}L - k_{bt}\left[\exp\left(\frac{a}{k_BT}\frac{\boldsymbol{S}:\boldsymbol{\tau}_m}{n_0L_0}\right) - 1\right]. \tag{2.32}$$

We can further simplify this expression using Eq. (2.26) and the surfactant mass balance to obtain

$$\frac{\mathrm{d}L}{\mathrm{d}t} = k_{b0}\left(\frac{L_0^3}{L^2} - L\right) + k_{ga}(n_0L_0)^2\frac{\widehat{S}^2}{L^2} - k_{bt}\left[\exp\left(\frac{a}{k_BT}\frac{\boldsymbol{S}:\boldsymbol{\tau}_m}{n_0L_0}\right) - 1\right]. \tag{2.33}$$

We render Eq. (2.33) dimensionless by introducing a nondimensional time $t^* = tD_{r,0}$ and length $L^* = L/L_0$

$$\frac{\mathrm{d}L^*}{\mathrm{d}t^*} = k_{b0}^*\left(\frac{1}{L^{*2}} - L^*\right) + k_{ga}^*\frac{\widehat{S}^2}{L^{*2}} - k_{bt}^*\left[\exp\left(a^*\boldsymbol{S}:\boldsymbol{\tau}_m^*\right) - 1\right], \tag{2.34}$$

where

$$\boldsymbol{\tau}_m^* = \frac{\boldsymbol{\tau}_m}{n_0k_BT}, \tag{2.35}$$

and

$$k_{b0}^* = \frac{k_{b0}}{D_{r,0}}, \quad k_{ga}^* = \frac{k_{ga}n_0^2}{D_{r,0}L_0}, \quad k_{bt}^* = \frac{k_{bt}}{D_{r,0}L_0}, \quad a^* = \frac{a}{L_0}. \tag{2.36}$$

We have now introduced four dimensionless groups: $k_{b0}^*$, $k_{ga}^*$, $k_{bt}^*$, and $a^*$. In order, $k_{b0}^*$ represents the ratio of relaxation due to spontaneous breakage and relaxation due to diffusion (i.e. realignment), $k_{ga}^*$ acts as a measure of the ratio of growth due to alignment to diffusion, $k_{bt}^*$ represents the ratio of relaxation due to tension-induced breakage and relaxation due to

diffusion, and finally, $a^*$, as noted above, functions as a dimensionless length that must be overcome for tension-induced scission to occur. Equations (2.7), (2.10) to (2.12) and (2.34) form a closed set of ODEs governing the time-evolution of a dilute wormlike micelle solution modeled as reactive Brownian rods.

### 2.2.5 Shear flow

For a simple shear velocity profile $\boldsymbol{v} = [\dot{\gamma}y, 0, 0]^\top$ with Pe number $\mathrm{Pe} = \dot{\gamma}/D_{r,0}$, substituting our closure relation Eq. (2.7) into the orientation equation Eq. (2.11) and supplying Eq. (2.10) to account for variation in the rotational diffusivity gives

$$\frac{\partial S_{xx}}{\partial t^*} = -\frac{6}{L^{*3}}\left(\frac{\ln L^* + m}{m}\right)\left(S_{xx} - \frac{1}{3}\right) - \frac{2}{5}\,\mathrm{Pe}\,S_{xy}\left(-4 + 4S_{xx} - S_{yy}\right), \tag{2.37a}$$

$$\frac{\partial S_{yy}}{\partial t^*} = -\frac{6}{L^{*3}}\left(\frac{\ln L^* + m}{m}\right)\left(S_{yy} - \frac{1}{3}\right) - \frac{2}{5}\mathrm{Pe}S_{xy}\left(1 + 4S_{yy} - S_{xx}\right), \tag{2.37b}$$

$$\frac{\partial S_{zz}}{\partial t^*} = -\frac{6}{L^{*3}}\left(\frac{\ln L^* + m}{m}\right)\left(S_{zz} - \frac{1}{3}\right) - \frac{6}{5}\mathrm{Pe}S_{xy}S_{zz}, \tag{2.37c}$$

$$\frac{\partial S_{xy}}{\partial t^*} = -\frac{6}{L^{*3}}\left(\frac{\ln L^* + m}{m}\right)S_{xy} - \frac{\mathrm{Pe}}{5}\left[6S_{xy}^2 + S_{xx} - 4S_{yy} - \left(S_{xx} - S_{yy}\right)^2\right]. \tag{2.37d}$$

Likewise we have the components of the stress tensor

$$\tau^*_{m,xx} = \frac{3}{L^*}\left(S_{xx} - \frac{1}{3}\right) + \frac{m\mathrm{Pe}L^{*2}}{10\left(\ln L^* + m\right)}S_{xy}\left(1 + 4S_{xx} - S_{yy}\right), \tag{2.38a}$$

$$\tau^*_{m,yy} = \frac{3}{L^*}\left(S_{yy} - \frac{1}{3}\right) + \frac{m\mathrm{Pe}L^{*2}}{10\left(\ln L^* + m\right)}S_{xy}\left(1 + 4S_{yy} - S_{xx}\right), \tag{2.38b}$$

$$\tau^*_{m,zz} = \frac{3}{L^*}\left(S_{zz} - \frac{1}{3}\right) + \frac{3m\mathrm{Pe}L^{*2}}{10\left(\ln L^* + m\right)}S_{xy}S_{zz}, \tag{2.38c}$$

$$\tau^*_{m,xy} = 3\frac{S_{xy}}{L^*} + \frac{m\mathrm{Pe}L^{*2}}{20\left(\ln L^* + m\right)}\left[6S_{xy}^2 + S_{xx} + S_{yy} - \left(S_{xx} - S_{yy}\right)^2\right]. \tag{2.38d}$$

In simple shear flow our length evolution Eq. (2.34) becomes

$$\frac{\mathrm{d}L^*}{dt^*} = k_{b0}^* \left( \frac{1}{L^{*2}} - L^* \right) + k_{ga}^* \frac{\widehat{S}^2}{L^{*2}} - k_{bt}^* \left[ 1 - \exp\left( a^* \boldsymbol{S} : \boldsymbol{\tau}_m^* \right) \right], \tag{2.39}$$

with

$$\boldsymbol{S} : \boldsymbol{\tau}_m^* = S_{xx}\tau_{m,xx}^* + S_{yy}\tau_{m,yy}^* + S_{zz}\tau_{m,zz}^* + 2S_{xy}\tau_{m,xy}^*, \tag{2.40}$$

and with scalar orientation parameter

$$\widehat{S} = \left[ \frac{3}{2} \left\{ \left( S_{xx} - \frac{1}{3} \right)^2 + \left( S_{yy} - \frac{1}{3} \right)^2 + \left( S_{zz} - \frac{1}{3} \right)^2 + 2S_{xy}^2 \right\} \right]^{\frac{1}{2}}, \tag{2.41}$$

where $S_{xx} + S_{yy} + S_{zz} = 1$.

### 2.2.6 Uniaxial extensional flow

Following similar steps for uniaxial extensional flow with velocity profile $\boldsymbol{v} = [-\dot{\epsilon}x/2, -\dot{\epsilon}y/2, \dot{\epsilon}z]^\top$ and Pe number $\mathrm{Pe} = \dot{\epsilon}/D_{r,0}$, our orientation equations are

$$\frac{\partial S_{xx}}{\partial t^*} = -\frac{6}{L^{*3}} \left( \frac{\ln L^* + m}{m} \right) \left( S_{xx} - \frac{1}{3} \right) - \frac{9}{5}\mathrm{Pe} S_{xx} S_{zz}, \tag{2.42a}$$

$$\frac{\partial S_{zz}}{\partial t^*} = -\frac{6}{L^{*3}} \left( \frac{\ln L^* + m}{m} \right) \left( S_{zz} - \frac{1}{3} \right) - \frac{9}{5}\mathrm{Pe} \left( S_{zz}^2 - S_{zz} \right). \tag{2.42b}$$

Likewise we have the components of the stress tensor

$$\tau_{m,xx}^* = \frac{3}{L^*} \left( S_{xx} - \frac{1}{3} \right) + \frac{m\mathrm{Pe}L^{*2}}{20\left( \ln L^* + m \right)} S_{xx} \left( 9S_{zz} - 5 \right), \tag{2.43a}$$

$$\tau_{m,zz}^* = \frac{3}{L^*} \left( S_{zz} - \frac{1}{3} \right) + \frac{m\mathrm{Pe}L^{*2}}{20\left( \ln L^* + m \right)} \left( 9S_{zz}^2 + S_{zz} \right). \tag{2.43b}$$

Our length evolution Eq. (2.34) in uniaxial extension becomes

$$\frac{\mathrm{d}L^*}{dt^*} = k^*_{b0}\left(\frac{1}{L^{*2}} - L^*\right) + k^*_{ga}\frac{\widehat{S}^2}{L^{*2}} - k^*_{bt}\left[1 - \exp\left(a^*\boldsymbol{S} : \boldsymbol{\tau}^*_m\right)\right], \tag{2.44}$$

with

$$\boldsymbol{S} : \boldsymbol{\tau}^*_m = S_{xx}\tau^*_{m,xx} + S_{yy}\tau^*_{m,yy} + S_{zz}\tau^*_{m,zz}, \tag{2.45}$$

and with scalar orientation parameter

$$\hat{S} = \left[\frac{3}{2}\left\{\left(S_{xx} - \frac{1}{3}\right)^2 + \left(S_{yy} - \frac{1}{3}\right)^2 + \left(S_{zz} - \frac{1}{3}\right)^2\right\}\right]^{\frac{1}{2}}, \tag{2.46}$$

where symmetry requires $S_{xx} = S_{yy} = (1 - S_{zz})/2$.

## 2.3 Results and Discussion

The organization of this section is as follows: in Section 2.3.1 we characterize the effects of the four dimensionless parameters in the RRM-R on steady shear flow and show that by varying the parameters we can capture many key features associated with WLM solution rheology. In Section 2.3.2 we fit our model to experimental data reported in literature for steady shear flows and demonstrate that the model is able to predict the behavior of both dilute and semi-dilute WLM solutions, as well as the behavior of both cationic and non-ionic surfactant solutions. We then turn our attention to transient flows in Section 2.3.3 by characterizing the predictions of the RRM-R in startup of steady shear flow; we further show excellent agreement in simultaneously fitting our model to both steady and transient shear experimental data. Finally, in Section 2.3.4, we briefly show that the RRM-R is able to suitably predict the behavior of steady extensional flows of wormlike micelle solutions.

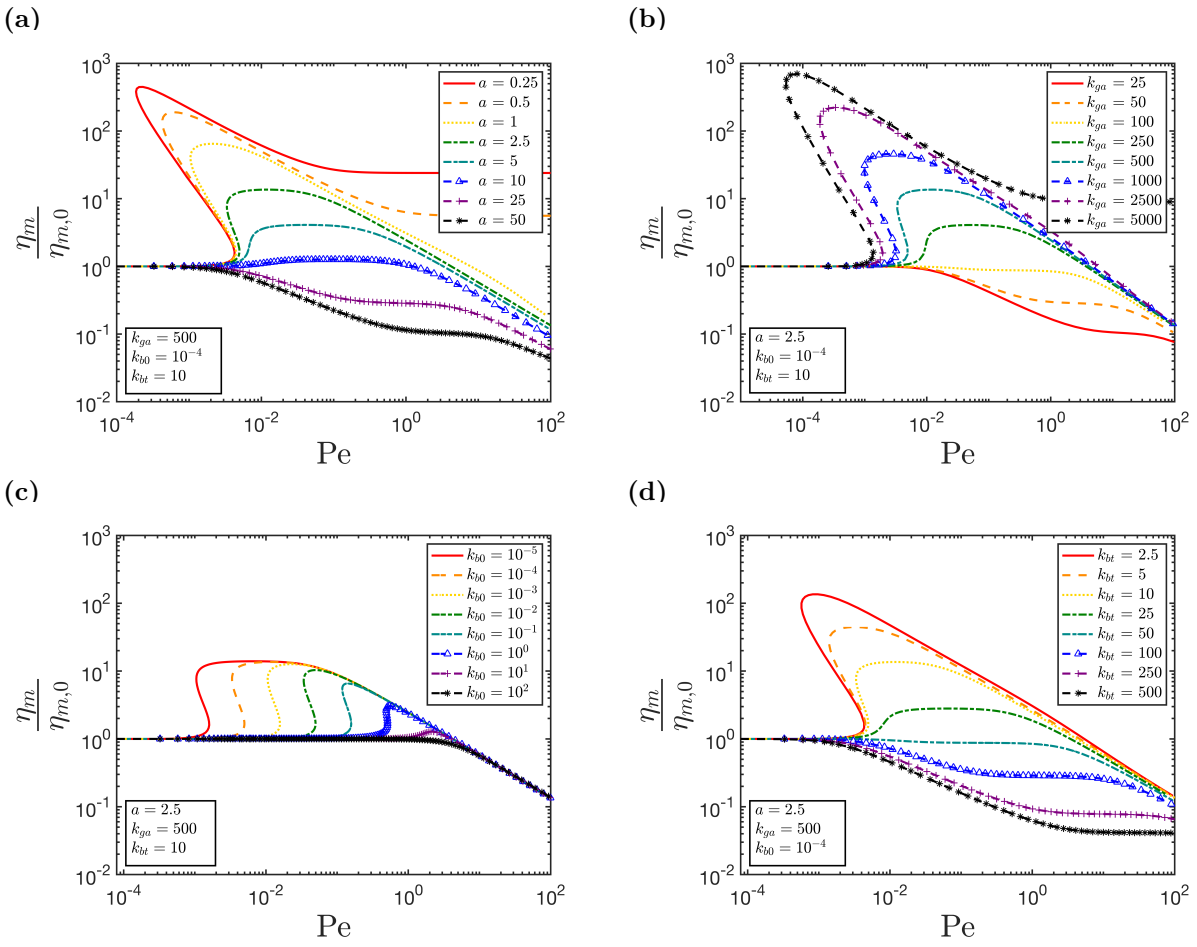


**Figure 2.1:** Normalized micellar viscosity vs. shear rate in simple shear flow: (a) effect of $a$, (b) effect of $k_{ga}$, (c) effect of $k_{b0}$, and (d) effect of $k_{bt}$ with $m = 3$ and $D_{r,0} = 1$.

### 2.3.1 Steady shear: parameter dependence

In this section we survey the behavior of the model over a wide range of parameters. Our aim here is not to capture specific experimental observations – that will be done in the subsequent sections. We have combined the discussions of the normalized micelle contribution to the viscosity ($\eta_m/\eta_{m,0}$), Fig. 2.1, and normalized micelle length ($L/L_0$), Fig. 2.2, as functions of Pe number ($\mathrm{Pe} = \dot{\gamma}/D_{r,0}$) as they tend to show nearly identical parameter dependence. Note that for convenience we have dropped the asterisks from all dimensionless parameters for the remainder of this manuscript. Figures 2.1(a) and 2.2(a) show the effect of the exponential breakage parameter $a$ with $k_{b0} = 10^{-4}$, $k_{ga} = 500$, and $k_{bt} = 10$; we see that increasing the value of $a$ decreases the magnitude of shear-thickening and micelle elongation and as $a$

is increased beyond some limit prescribed by a combination of the other three parameters (here $a \gtrsim 10$), the suspension transitions to a purely shear-thinning fluid. In this shear-thinning regime ($a = 25, 50$) we see that the suspension undergoes distinctly two thinning regimes separated by a plateau that extends over almost a decade of shear rates. This result reflects the fact that two mechanisms for shear-thinning exist in the model: alignment of the rods with flow and tension-induced rod breakage. To the best of our knowledge this plateau behavior that extends into the high-shear rate regime is not typically observed in experiments; however, a similar plateau in the intermediate-shear rate regime has been observed [116], though at high enough shear rates this eventually gives way to shear-thinning.

In regimes where the suspension shear-thickens ($a \lesssim 10$), the viscosity can be seen to thicken to over 100 times its zero-shear value and the micelle length increases by almost 50 times its equilibrium value, consistent with experimental observations of flow-induced structures in dilute wormlike micelle solutions [45, 69]. This regime contains a significant transition where values of $a$ below some threshold (here $\approx 4$) exhibit reentrant behavior (i.e. multivalued stress-shear rate curve). In this reentrant region the fluid can take on three steady state stresses for a given shear rate; all three of the stress values are accessible via a strain-controlled experiment, whereas a shear rate-controlled experiment will exhibit hysteresis and jump between the minimum and maximum stresses, leaving the intermediate stress inaccessible. Finally, we see that for small enough values of $a$ ($\lesssim 1$) the viscosity and length plateau at high Pe numbers. Intuitively we expect high shear rates and stresses to break apart micelles, leading to lengths (and consequently viscosities) that asymptotically approach zero. While this may be nonphysical behavior, it is easily avoided by ensuring $a$ exceeds a necessary threshold.

Figures 2.1(b) and 2.2(b) show the effect of the alignment-induced growth parameter $k_{ga}$ with $a = 2.5$, $k_{b0} = 10^{-4}$, and $k_{bt} = 10$. The effect of increasing $k_{ga}$ is nearly equivalent to decreasing $a$, where larger values of $k_{ga}$ (and smaller values of $a$) induce stronger shear-thickening and micelle elongation. At $k_{ga} = 5000$ we see that the viscosity increases to nearly

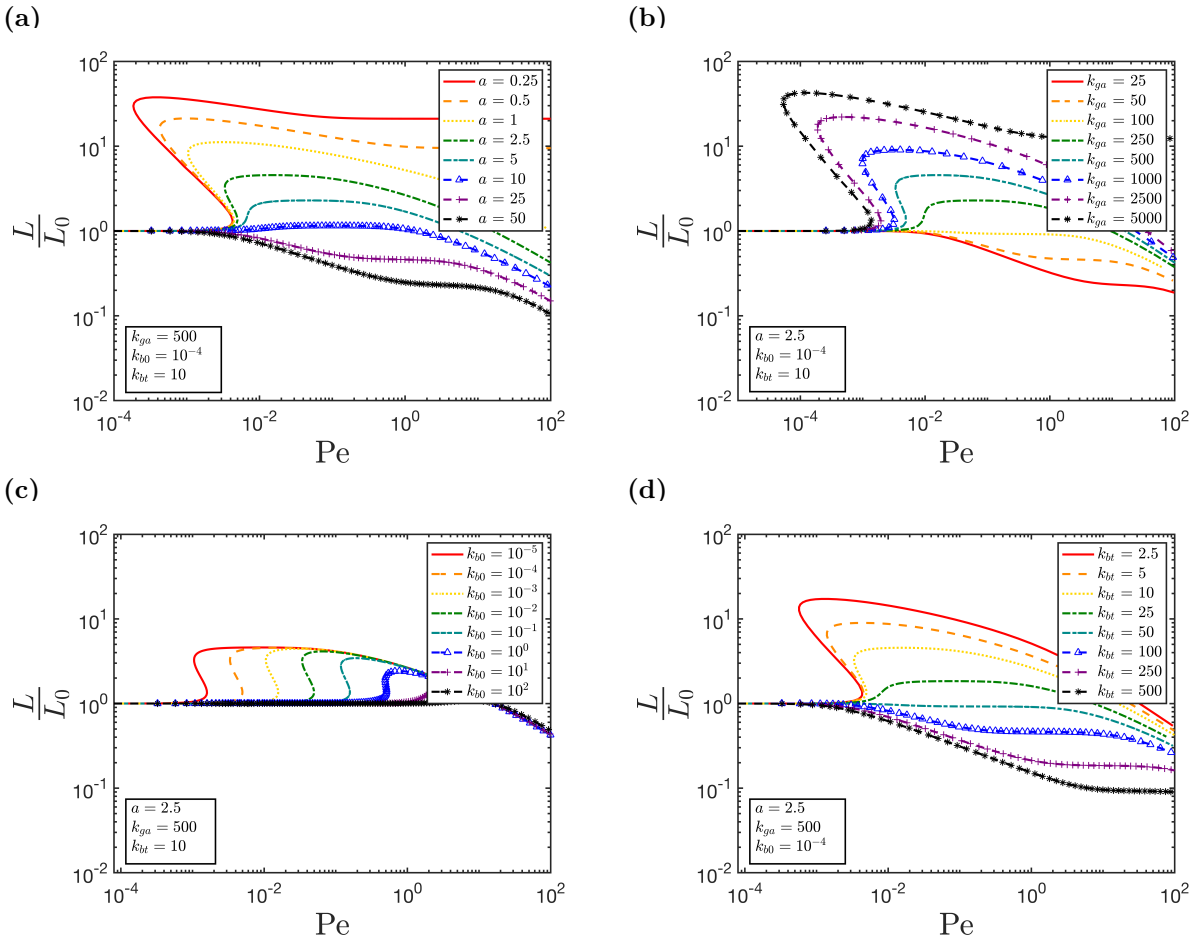


**Figure 2.2:** Mean micelle length normalized by equilibrium length vs. shear rate in simple shear flow: (a) effect of $a$, (b) effect of $k_{ga}$, (c) effect of $k_{b0}$, and (d) effect of $k_{bt}$ with $m = 3$ and $D_{r,0} = 1$.

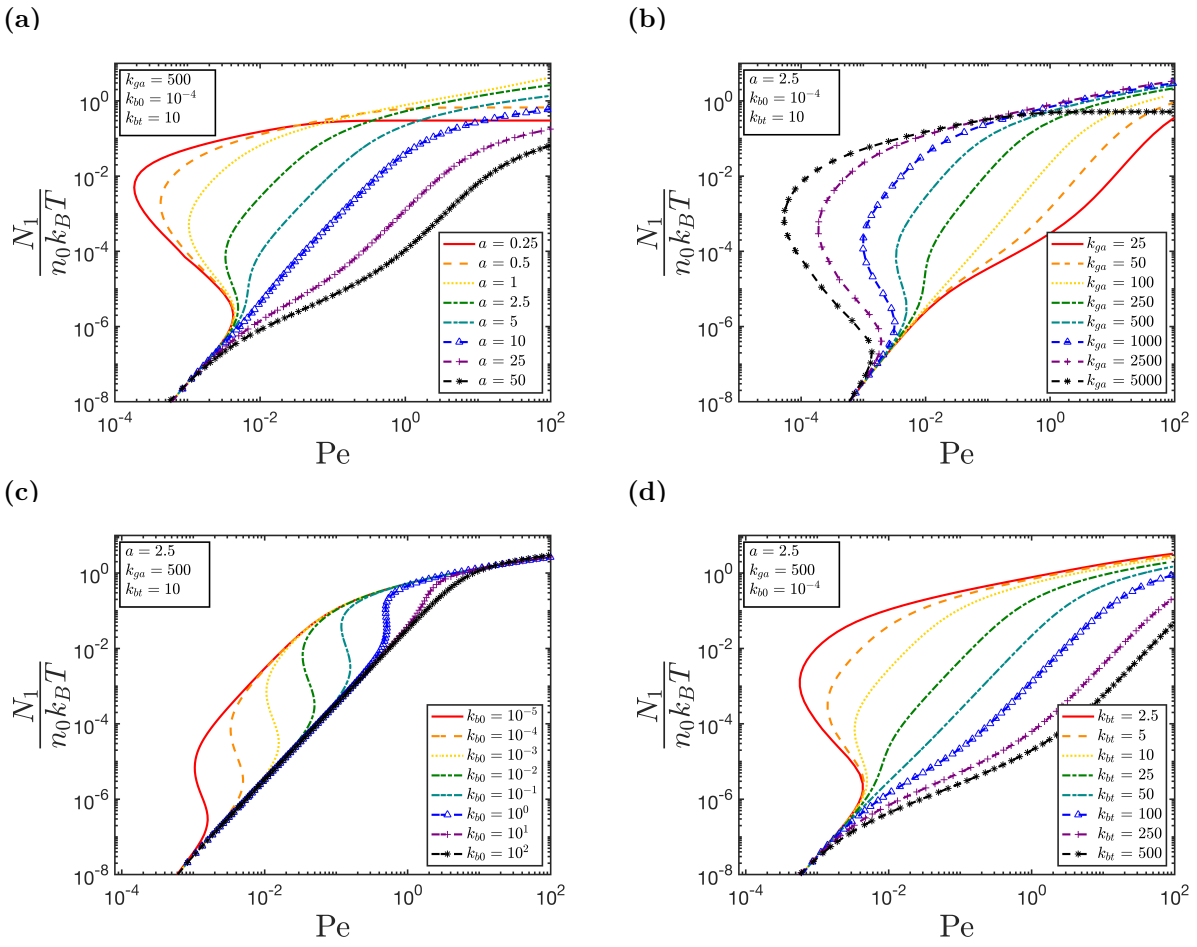


**Figure 2.3:** Normalized first normal stress difference vs. shear rate in simple shear flow: (a) effect of $a$, (b) effect of $k_{ga}$, (c) effect of $k_{b0}$, and (d) effect of $k_{bt}$ with $m = 3$ and $D_{r,0} = 1$.

1000-times its zero-shear value; we also see for this parameter value that the viscosity and length plateau at high Pe numbers, which although nonphysical can be avoided by tuning the relationship between $a$ and $k_{ga}$. The effects of the breakage coefficient $k_{bt}$ are shown in Figs. 2.1(d) and 2.2(d) and very nearly mirror the effects of $a$ so we will not discuss them in greater detail.

The most unique parameter effect can be seen by varying the spontaneous breakage parameter $k_{b0}$ in Figs. 2.1(c) and 2.2(c). We see that increasing $k_{b0}$ increases the critical shear rate for shear-thickening and elongation to occur, but not necessarily the magnitude of thickening or extent of elongation. Recalling that $k_{b0}$ describes the ratio of relaxation due to breakage to relaxation due to rotational diffusion, this increase in the critical shear rate

can be understood by the fact that larger values of $k_{b0}$ correspond to a greater propensity for undergoing a breakage event rather than rotation, and thus a system will prefer to relax by breaking rather than aligning with the flow. An equivalent effect is achieved by decreasing the rotational diffusion constant $D_{r,0}$, which acts to restrict the rods from aligning and in turn restricts micellar growth. The effect of $k_{b0}$ on the magnitude of thickening and elongation is somewhat complicated: at large values of $k_{b0}$, increasing $k_{b0}$ further acts to decrease the magnitude of thickening, while at smaller values ($k_{b0} \lesssim 10^{-3}$) there is no effect on the magnitude of thickening, only the critical shear rate. Notably, different behavior due to variations in $k_{b0}$ can only be seen at low shear rates, while at high shear rates all curves collapse onto identical shear-thinning profiles. This collapse is the result of increased stress that drives the breakdown of elongated micellar structures.

A recent study by Tamano et al. [99] that coupled a fluidity equation to well-known constitutive equations (e.g. Giesekus and FENE-P) to produce both thinning and thickening behaviors (see Section 2.1) identified a nearly identical effect when varying their parameter $R_{bd}$. Similar to $k_{b0}$ in the RRM-R, $R_{bd}$ represents the ratio of the micelle breakdown timescale ($\lambda_{bd}$) to the relaxation time of the fluid ($\lambda$). The fact that these two parameters, which are intended to represent equivalent ratios but exist in two distinct models, yielded extremely similar behavior is quite interesting and worthy of further exploration.

All parameter regimes in Fig. 2.1, excluding curves that show high shear-plateaus, undergo the same power-law thinning $\eta \propto \dot{\gamma}^n$ with $n = -2/3$ at high shear rates. This is in contrast to the high-shear behavior of simple Brownian rods of infinite aspect ratio, which exhibit power-law thinning with $n = -1/3$ [117, 118]. At finite aspect ratio the viscosity plateaus as $\mathrm{Pe} \to \infty$. These behaviors are not well-captured using closures, because while the rods spend most of their time aligned with the flow, the high-shear viscosity is dominated by the stress arising during the infrequent flipping of the rods, an effect not accounted for in closures. (The $n = -2/3$ scaling would be correct for the simple rigid rod case if the stress were dominated by the aligned rods.) We are unaware of experimental or modeling

results that indicate what the correct scaling behavior should be at very high Pe. We note that we are able to achieve good agreement with the degree of shear thinning found in the experiments shown below.

Figure 2.3 shows the role of the four parameters on the normalized first normal stress difference $N_1/n_0k_BT$, where $N_1 = \tau_{xx} - \tau_{yy}$, of the suspension as a function of Pe number. Figures 2.3(a) and 2.3(d) show that increasing $a$ and $k_{bt}$ act to reduce $N_1$ and transition the curve away from reentrant behavior. In Fig. 2.3(b) we have that opposite effect, increasing $k_{ga}$ increases $N_1$ and develops a reentrant profile. Figure 2.3(c) shows that increasing $k_{b0}$ forces the increase of the normal stress difference to higher Pe numbers, consistent with Fig. 2.1. This plot clearly shows two power-law relationships between the first normal stress and Pe number, where at low-to-intermediate shear rates $N_1 \propto \mathrm{Pe}^2$ which transitions at high shear rates to $N_1 \propto \mathrm{Pe}^{1/3}$. This is again in contrast to high-shear behavior of non-reactive rods which demonstrate a $N_1 \propto \mathrm{Pe}^{2/3}$ relationship [118]. As discussed above, the origins of this disagreement are as of yet not fully understood but likely stem from either (1) higher-order stress-length coupling or (2) closure approximations. While this power-law relationship is more difficult to observe in Figs. 2.3(a), 2.3(b) and 2.3(d), we can see traces of it for $2.5 \leq a \leq 25$, $100 \leq k_{ga} \leq 1000$, and $10 \leq k_{bt} \leq 100$. This new formulation of the RRM, like the original, is able to capture non-zero second normal stress differences $N_2$; although we do not show plots here, $N_2$ follows the same trends as $N_1$ but is negative and roughly two orders of magnitude smaller, which is consistent with other literature reports for viscoelastic fluids [24].

### 2.3.2 Steady shear: experimental comparison

In this section we turn to comparisons between our model and literature results for steady shear flow. Model parameters were obtained by generating roughly $7^4$ steady state flow curves (seven different values of each of the four parameters) and plotting the experimental data of interest on each of these curves; we inspected each curve to obtain an approximate

'best fit' and then fine-tuned this set by repeating this process with a range of parameters within a few percent of the 'best fit' values. We then took the new 'best fits' and performed small tweaks to obtain our final fit parameters. We should also note that determination of ideal fitting parameters for the RRM-R is a nonlinear optimization problem and we therefore cannot guarantee the existence of a unique global minimum (i.e. a unique parameter set). Although we do emphasize that the highly idealized nature of our model means that we should not attach too much physical significance to the values of model parameters, we do see consistency that at least suggests parameters are relatively constant for a given solution composition (e.g. CTAB/NaSal), with the greatest deviations occurring in the most concentrated (semi-dilute) solutions. Note that in Figs. 2.4(a), 2.5(a) and 2.8(a) we are showing the *total* solution viscosity ($\eta = \eta_s + \eta_m$) where the solvent viscosity is taken to be that of water.

The first data set we consider is for a CTAB/NaSal solution in water, from Liu and Pine [4]. Figure 2.4(a) shows fits of our model to steady shear viscosity as a function of shear rate for increasing concentrations. Model parameters are shown in Table 2.1. The measurements were made using a double-wall Couette rheometer with an inner cylinder diameter of 25 mm and gap width of 1 mm. We find strong agreement between fits and experimental data, particularly in capturing the onset of shear-thickening and transition to shear-thinning. We are notably unable to capture the weak initial shear-thinning at low shear rates that occurs in semi-dilute surfactant solutions ($\geq$ 500 ppm); shear-thinning in this regime is attributed to disruption of micellar networks that can form at equilibrium, a phenomenon that is not considered in our treatment.

Figure 2.4(b) shows model predictions for the normalized mean micelle length as a function of shear rate. We find that our model predicts that the mean micelle length increases by about two times in the most concentrated solution and almost four times in the most dilute. While length was not measured in the study by Liu and Pine, these length changes are consistent with other experimental results [108].

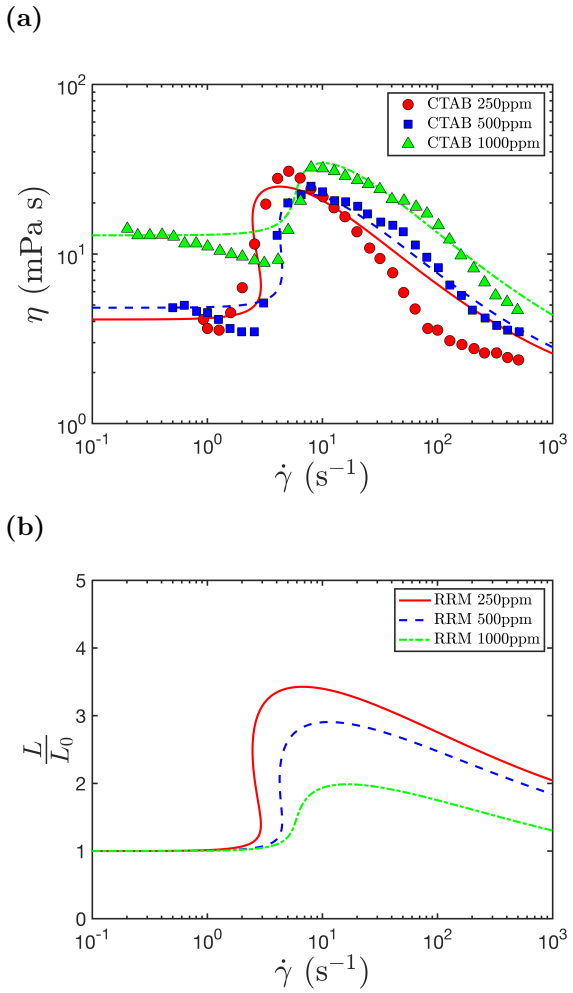


**Figure 2.4:** Fits (lines) to experimental data of (a) shear viscosity vs. shear rate and (b) mean micelle length vs. shear rate. Experimental data corresponds to solutions of 250 ppm, 500 ppm, and 1000 ppm CTAB/NaSal in water obtained by Liu and Pine [4]. Corresponding parameter values are shown in Table 2.1.

**Table 2.1:** Dimensional RRM-R parameters for experimental data (Fig. 2.4) of CTAB/NaSal solutions [4].

| Composition | CTASal | CTASal | CTASal |
|---|---|---|---|
| $c$ [ppm] | 250 | 500 | 1000 |
| $k_{b0}$ [s$^{-1}$] | $1.4 \times 10^{-2}$ | $2.8 \times 10^{-2}$ | $6.3 \times 10^{-2}$ |
| $k_{ga}$ [$\mu$m$^7$] | $6.1 \times 10^{-6}$ | $3.9 \times 10^{-6}$ | $2.0 \times 10^{-6}$ |
| $k_{bt}$ [m s$^{-1}$] | $1.1 \times 10^{-4}$ | $1.2 \times 10^{-4}$ | $8.1 \times 10^{-5}$ |
| $a$ [nm] | 1.3 | 1.6 | 2.2 |
| $D_{r,0}$ [s$^{-1}$] | 55 | 55 | 25 |

We also make comparisons to data from [5] for both cationic and non-ionic wormlike micelle solutions. Figure 2.5 shows fits to experimental steady shear viscosity as a function of shear rate data, as well as micelle length predictions. Red data corresponds to a solution of 1000 ppm cationic CTASal in water, measured in a low-shear, circular Couette viscometer at 20 °C with a gap width of 0.320 mm [5]. Blue and purple data correspond to solutions of 1000 ppm and 1500 ppm non-ionic ODMAO in water, respectively, measured with a capillary viscometer with inner diameter 5.045 mm [6]. Our model is able to capture the strong shear-thickening and -thinning regimes, particularly that of the cationic solution. Although we see some difficulty in capturing the zero-shear viscosity of the cationic solution (red), this difference less than 1 mPa s and is thus relatively insignificant. We note that the work by Ohlendorf and coworkers [5] shows markedly different behaviors for a given wormlike micelle solution by simply changing the gap width of the circular Couette device, indicating the possible presence of instabilities such as vorticity banding.

It is worth drawing attention to model predictions for the rotational diffusion coefficient. Looking at Tables 2.1 and 2.2, we see that predictions for $D_{r,0}$ range from $\sim 10\,\mathrm{s}^{-1}$ to $\sim 1000\,\mathrm{s}^{-1}$, whereas for a typical micelle length of a few hundred angstroms Eq. (2.10) predicts values of $D_{r,0}$ on the order of $10^5\,\mathrm{s}^{-1}$. Further, for rigid rods we can relate the relaxation time of the bulk fluid to the rotational diffusivity by $\lambda = 1/6D_{r,0}$, where for wormlike micelle solutions $\lambda$ is typically on the order of $1 - 10^1$ s; we can then see that our predictions of $D_{r,0}$ yield relaxation times that fall significantly below experimental reports. This discrepancy between experimental measurements of WLM solution relaxation times and theoretical predictions using Eq. (2.10) and based on the framework proposed by Cates and Turner – shear-thickening occurs when the shear is strong enough to overcome rotational diffusion – is well-established in literature [119, 120]. Many studies have attempted to address this inconsistency; notably, Barentin and Liu [41] proposed a mechanism in which micelles form networks of bundles with some success. In our model, there is strong reason to believe that the disparity between predictions and experimental measurements arises from

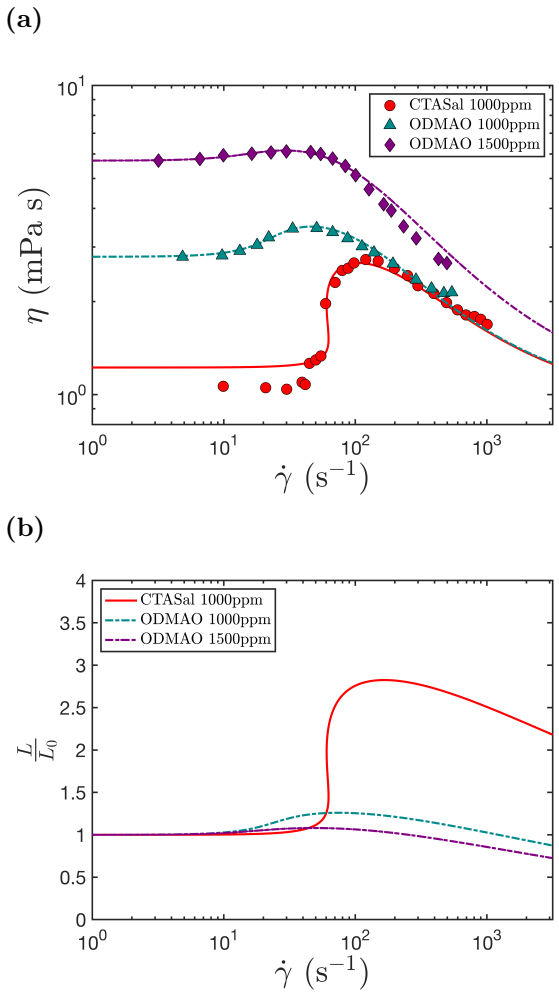


**Figure 2.5:** Fits (lines) to experimental data of (a) shear viscosity vs. shear rate and (b) mean micelle length vs. shear rate. Experimental data corresponds to solutions of (red) 1000 ppm CTASal in water obtained by Ohlendorf et al. [5], and (purple) 1500 ppm and (blue) 1000 ppm ODMAO in water obtained by Tamano et al. [6]. Corresponding parameter values are shown in Table 2.2.

the neglect of charge and hydrodynamic interactions, as well as certain collision mechanisms. In particular, the assumption that collisions are primarily end-to-end in nature ignores the possibility of 'phantom crossings' that have been observed in dissipative particle dynamics studies [121].

### 2.3.3 Startup of steady shear

One of the primary pitfalls of the previous RRM formulation is its difficulty in capturing the *transient* dynamics of dilute surfactant solutions. Accurately describing transient dynamics

**Table 2.2:** Dimensional RRM-R parameters for experimental data (Fig. 2.5) of CTASal and ODMAO solutions obtained by [5] and [6], respectively.

| Composition | CTASal | ODMAO | ODMAO |
|---|---|---|---|
| $c$ [ppm] | 1000 | 1000 | 1500 |
| $k_{b0}$ [$s^{-1}$] | 1.2 | $2.5 \times 10^{-1}$ | $1.5 \times 10^{-1}$ |
| $k_{ga}$ [$\mu m^7$] | $8.6 \times 10^{-6}$ | $2.2 \times 10^{-5}$ | $7.8 \times 10^{-6}$ |
| $k_{bt}$ [m $s^{-1}$] | $2.0 \times 10^{-3}$ | $1.1 \times 10^{-4}$ | $6.8 \times 10^{-5}$ |
| $a$ [nm] | 3.1 | 2.5 | 3.0 |
| $D_{r,0}$ [$s^{-1}$] | 800 | 50 | 30 |

is crucial for studying complex and turbulent flows. Additionally, it is important to note that properly fitting experimental data requires both steady *and* transient data. The reason for this requirement is that at steady state, Eq. (2.34) can be multiplied by any positive scalar value and still produce the same steady shear viscosity vs. shear rate curve. However, multiplying by a scalar does alter transient data, particularly the induction times ($t_{\text{ind}}$) and overshoots seen in startup of steady shear flows. Thus, if we wish to completely describe dilute WLM solutions, we must be able to accurate predict both steady and transient data in tandem.

We assess the capabilities of the model at capturing transient dynamics by evaluating its behavior in startup of steady shear flow. An initially isotropic fluid at rest is subjected starting at $t = 0$ to a constant shear rate $\dot{\gamma}$. We use an explicit, fourth-order Runge-Kutta scheme implemented in Matlab (`ode45`) to time-step Eqs. (2.37) to (2.39) and (2.41). In evaluating the success of the RRM-R at predicting transient dynamics, we are looking particularly at induction times, the time required for stress growth to occur, as well as stress overshoot, where the stress (and viscosity) is seen to overshoot its steady state value.

Figures 2.6(a) and 2.6(b) show the time- and applied shear rate-dependent micellar contribution to viscosity as a function of dimensionless time for three decades of Pe numbers. Viscosity is normalized by the steady zero-shear viscosity, which importantly is not equal to the viscosity at $t = 0$ (discussed in detail below). Darker lines corresponds to larger Pe numbers and the black dotted line corresponds to $\eta_m(t, \dot{\gamma})/\eta_{m,0} = 1$. We see that there are distinctly two thickening regimes present; the first, which is identical for all applied shear

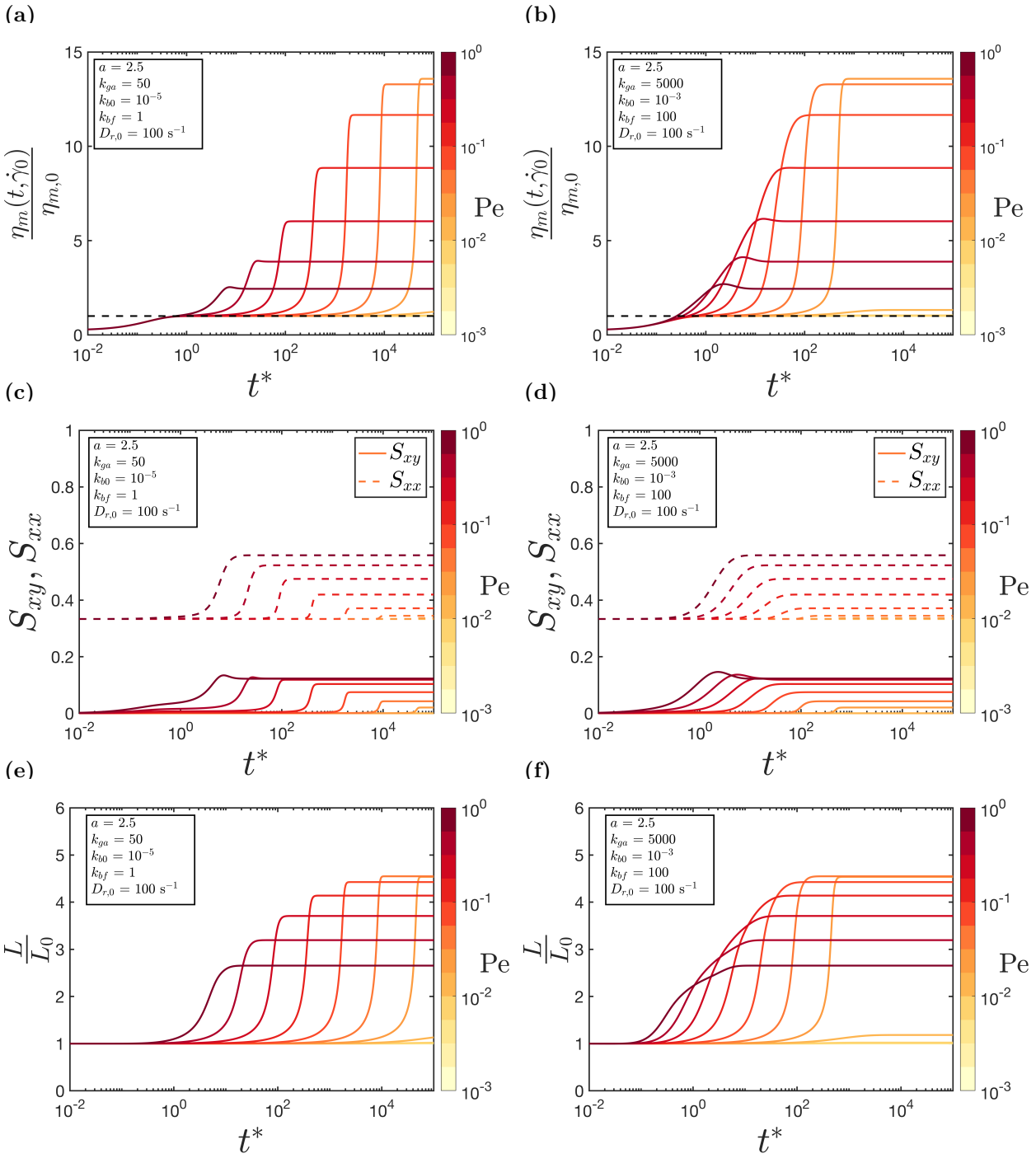


**Figure 2.6:** Micellar contribution to the shear viscosity (normalized by zero-shear viscosity), ensemble average orientation components, and normalized length vs. dimensionless time in transient startup of steady shear flow for a range of applied Pe numbers. Both sets of parameters in (a)-(e) and (b)-(f) yield equivalent steady states but varying transient behavior.

rates, occurs at very short times and is due to near-equilibrium alignment of rods. This slight thickening of the viscosity is caused by weak alignment of rods in the $S_{xy}$ direction, as seen in Figs. 2.6(c) and 2.6(d); this alignment is also seen in purely (i.e. non-reactive) Brownian rod suspensions and can be found analytically for startup of steady shear flow by solving for the near-equilibrium behavior of the rods. I.e. to leading order at small Pe, the transient viscosity is given by

$$\eta_m(t^*) = \frac{n_0 k_B T}{30 D_{r,0}} \left(4 - 3\mathrm{e}^{-6t^*}\right). \tag{2.47}$$

We can clearly see for short times $\eta_m(t^* \ll 1) = \frac{n_0 k_B T}{30 D_{r,0}}$ which increases to $\eta_m(t^* \to \infty) = \frac{2 n_0 k_B T}{15 D_{r,0}}$. We can also verify this by comparing Fig. 2.6(c) and Fig. 2.6(e), in which growth in $S_{xy}$ can be seen occurring prior to elongation of micelles.

The second thickening regime ($t^* \gtrsim 1$) can be attributed to elongation of the representative micellar length in tandem with rod alignment. We clearly see that the induction time $t_{\mathrm{ind}}$, qualitatively defined here as the time for viscosity (and therefore stress) growth to occur, decreases with increasing shear rate, a trend that has been observed in experiments of WLM solutions [7, 70]. In fact, as we will demonstrate later on, a distinctive power-law relationship between $t_{\mathrm{ind}}$ and the applied shear rate $\dot{\gamma}_0$ can be observed, $t_{\mathrm{ind}} \propto {\dot{\gamma}_0}^{-n}$, where $1 \lesssim n \lesssim 3$, which again agrees well with experimental observations in literature [7].

One feature of transient dynamics of dilute wormlike micelle solutions, particularly in startup of steady shear flow, is a viscosity (or stress) overshoot, in which the viscosity of the solution is observed to exceed its steady state viscosity before settling to the steady state value, oftentimes after a number of decaying oscillations [122]. We can see slight instances of this overshoot in Fig. 2.6(b), particularly for $\mathrm{Pe} > 10^{-1}$, but it is more clearly seen in Fig. 2.7(a) where we have increased the relative growth parameter $k_{ga}$ by a factor of four compared to Fig. 2.6. By 'relative' we mean in relation to $k_{b0}$ and $k_{bt}$. Comparing Fig. 2.7(a) with Fig. 2.7(b) and Fig. 2.7(c), we see that this overshoot is solely a product

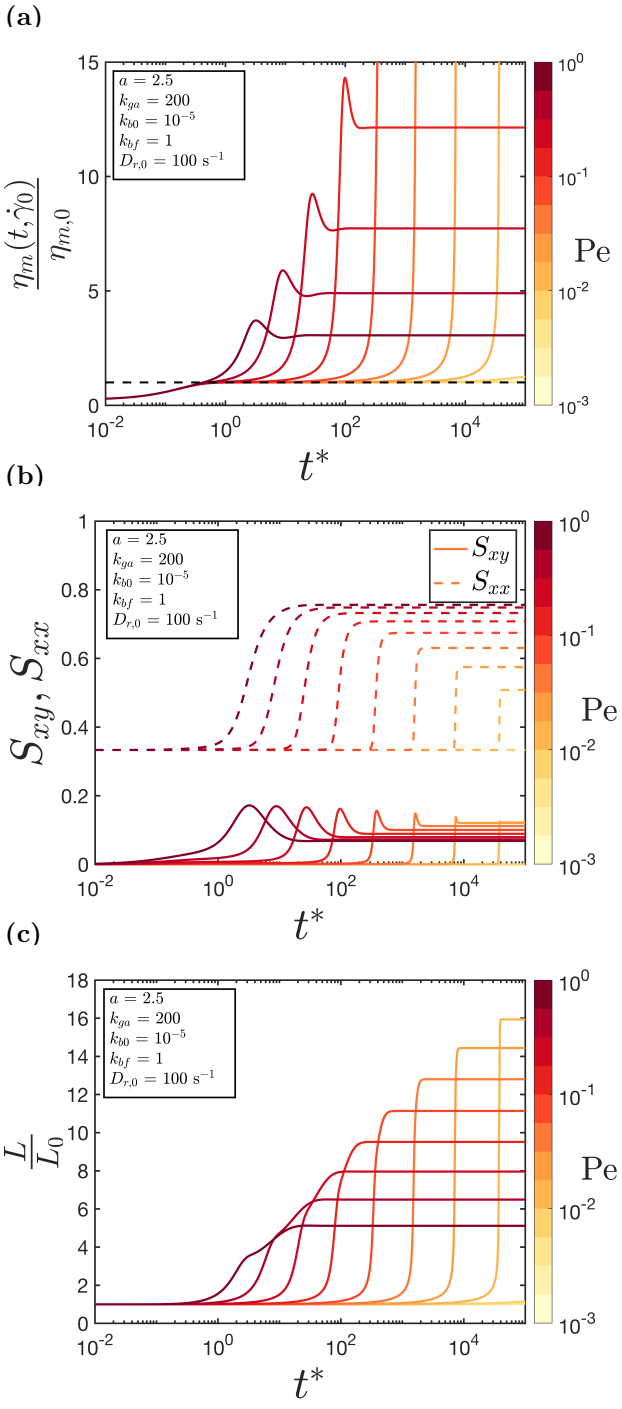


**Figure 2.7:** Micellar contribution to the shear viscosity (normalized by zero-shear viscosity), ensemble average orientation components, and normalized length vs. dimensionless time in transient startup of steady shear flow for a range of applied Pe numbers clearly demonstrating stress-overshoot phenomenon.

of 'over'-alignment in the $S_{xy}$ direction as there is no apparent overshoot in the micelle length, though notably in regions where $\eta_m$ and $S_{xy}$ are observed to overshoot there is a distinct change in the slope of $L^*$ vs. $t^*$. It is also interesting that the micelle length remains a monotonic function of time even following the viscosity overshoot, whereas $\eta_m$ and $S_{xy}$ do not. Stress overshoot also occurs in simple (i.e. constant length) Brownian rod suspensions and thus variations in micelle length are not necessary for an overshoot to occur. The monotonicity of the micelle length curve highlights the fact that micelle alignment and micelle elongation, although interrelated, are distinct phenomena.

We now turn from general features of the model to specific comparisons with experimental data that provide both steady and transient results. Figure 2.8 shows the (a) steady state shear viscosity and (b) micelle length as a function of shear rate for $0.05wt\%$ and $0.1wt\%$ CTAVB in water solutions obtained by Landàzuri et al. [7]. Fits (lines) using the reformulated RRM are shown for steady shear viscosity. Table 2.3 shows the dimensional model parameters. We see that the model is well-suited for capturing steady shear viscosity and that predictions for length elongation are about 3.5 times the equilibrium length. Figure 2.9(a) shows the corresponding predictions for the induction time ($t_{\text{ind}}$) as a function of applied shear rate for the same data sets [7]. Fits are shown as lines. Note that we have taken the induction time to be defined as the time for stress growth to occur *after* the viscosity increases to the steady state zero-shear viscosity, otherwise all curves would yield the same $t_{\text{ind}}$. As discussed previously, we can see a strong power-law relationship in Fig. 2.9(a) in which $t_{\text{ind}} \propto {\dot{\gamma}_0}^{-n}$. We find for the $0.05wt\%$ CTAVB solution that $n = 2.05$ and for the $0.1wt\%$ we find $n = 2.20$. The agreement between model predictions and experimental data for both steady and transient flows is quite good, and underscores the ability of our reformulated model to capture the dynamics of dilute wormlike micelle solutions. Figure 2.9(b) shows the RRM-R predictions for transient micellar viscosity growth as a function of time which were used to generate the $t_{\text{ind}}$ vs. applied shear rate plot (Fig. 2.9(a)); explicit experimental data of viscosity (and stress) growth as a function of time were not available for this data set.

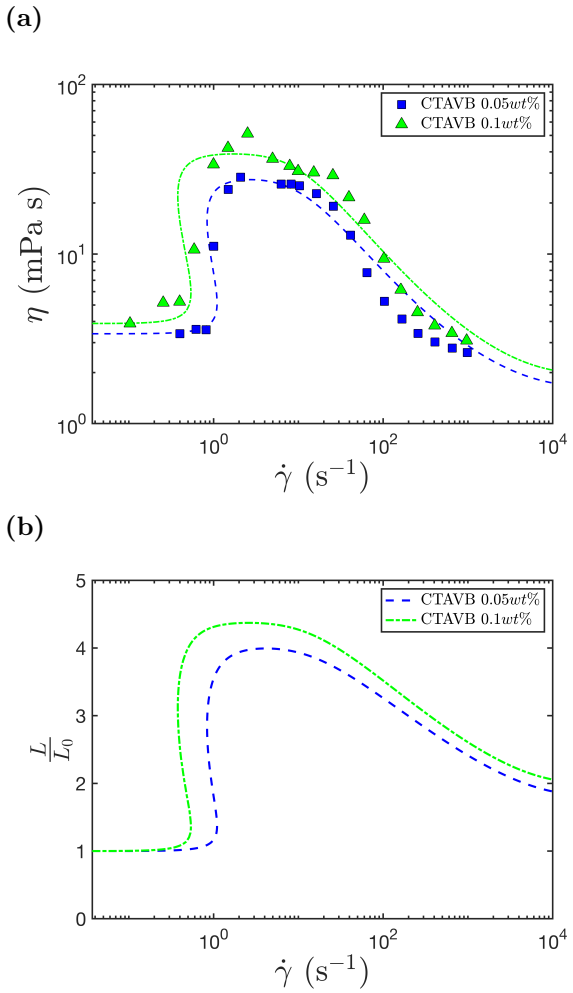


**Figure 2.8:** Fits (lines) to experimental data (symbols) of (a) shear viscosity vs. shear rate and (b) micelle length vs. shear rate. Experimental data corresponds to solutions of (green) $0.05wt\%$ and $0.1wt\%$ CTAVB in water obtained by Landàzuri et al. [7]. Corresponding parameter values are shown in Table 2.3.

**Table 2.3:** RRM-R parameters for experimental data (Figs. 2.8 and 2.9) of CTAVB solutions [7].

| Composition | CTAVB | CTAVB |
|---|---|---|
| $c$ [ppm] | 500 | 1000 |
| $k_{b0}$ [$s^{-1}$] | $1.9 \times 10^{-3}$ | $3.6 \times 10^{-3}$ |
| $k_{ga}$ [$\mu m^7$] | $4.3 \times 10^{-6}$ | $1.9 \times 10^{-5}$ |
| $k_{bt}$ [m $s^{-1}$] | $2.2 \times 10^{-4}$ | $2.3 \times 10^{-3}$ |
| $a$ [nm] | 2.0 | 2.5 |
| $D_{r,0}$ [$s^{-1}$] | 120 | 140 |

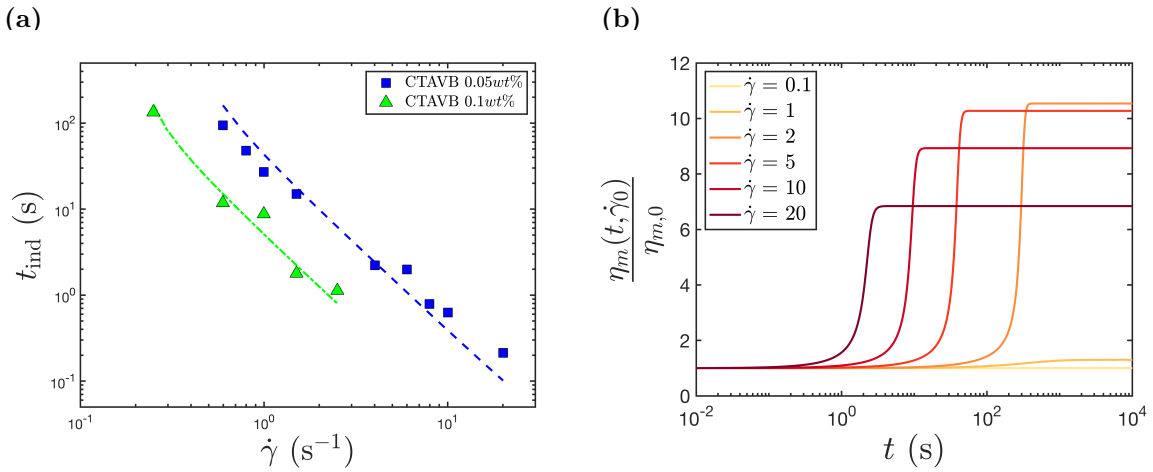


**Figure 2.9:** (a) Fits (lines) to experimental data of transient shear induction time vs. shear rate for solutions of $0.05wt\%$ and $0.1wt\%$ CTAVB in water and (b) corresponding transient viscosity growth vs. time response for the $0.05wt\%$ solution (blue). Experimental data was obtained by Landàzuri et al. [7]. Corresponding parameter values are shown in Table 2.3.

### 2.3.4 Uniaxial extension: experimental comparison

Having verified that our model is well-equipped to capture experimental results of dilute WLM solutions in both steady and transient shear flow, we turn our attention to extensional flows. Turbulent flows are dominated by extension and thus accurate prediction of extensional flow behavior is crucial if we aim to capture the mechanisms associated with surfactant-additive drag reduction in these flows [123]. There are limited results of steady extensional flows of wormlike micelle solutions, primarily owing to the difficulty in performing these experiments. Walker and coworkers used an RFX opposed jet device to measure the extensional viscosity of semi-dilute concentrations of CPyCl/NaSal solutions in brine [8]. These solutions are clearly not dilute, a fact that can easily be gleaned by noting that the zero-strain viscosities far exceed the viscosity of water. Fits to the experimental data are shown in Fig. 2.10, while model parameters are shown in Table 2.4. As we can from Fig. 2.10, the RRM-R is able to accurately predict the strain-hardening and -softening behavior observed in extensional flows of WLM solutions. Notably we have some difficulty in fitting the high-strain rate experimental data, which can likely be attributed to the non-dilute nature of the solutions; some fitting difficulty may also arise from the presence of pre-shear and/or

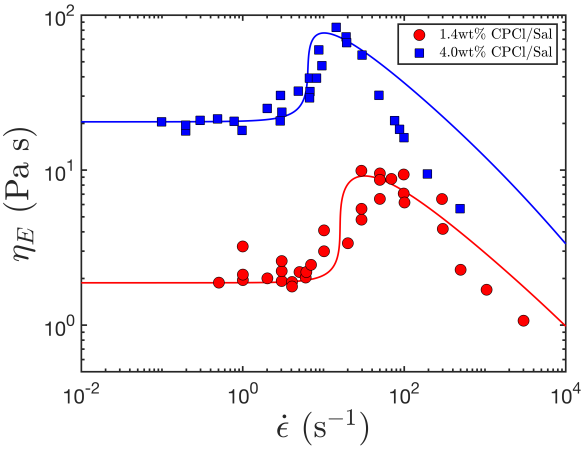


**Figure 2.10:** Fits (lines) to experimental data of extensional viscosity vs. strain rate for dilute (red) and semi-dilute (blue) CPyCl/NaSal solutions undergoing steady uniaxial extensional flow [8]. Corresponding parameter values are shown in Table 2.4.

**Table 2.4:** RRM-R parameters for experimental data (Fig. 2.10) of CPyCl/NaSal solutions [8].

| Composition | CPyCl | CPyCl |
|---|---|---|
| $c$ [wt%] | 1.4 | 4.0 |
| $k_{b0}$ [s$^{-1}$] | 0.50 | 0.68 |
| $k_{ga}$ [$\mu$m$^7$] | $7.0 \times 10^{-11}$ | $2.2 \times 10^{-11}$ |
| $k_{bt}$ [m s$^{-1}$] | $2.0 \times 10^{-4}$ | $2.3 \times 10^{-5}$ |
| $a$ [nm] | 1.5 | 2.5 |
| $D_{r,0}$ [s$^{-1}$] | 100 | 15 |

micellar slippage effects that can often occur in these devices [124].There has recently been significant interest in transient extensional experiments of dilute WLM solutions, notably capillary breakup extensional rheology (CaBER). We have performed preliminary work that suggests the RRM-R is well-suited for modeling CaBER and similar experiments, and we expect to communicate these findings in future work.

## 2.4 Conclusions

We have presented a reformulation (RRM-R) of the reactive rod constitutive model (RRM) that treats dilute surfactant solutions forming wormlike micelles as a suspension of rigid Brownian rods undergoing reversible scission and growth in flow. The model couples equations governing the ensemble average orientation, stress, and length of micelles to produce

a dynamic set of equations allowing for the collective micelle length to elongate and breakdown. This framework produces steady shear viscosity vs. shear rate curves that exhibit drastic shear-thickening and shear-thinning regimes. Fits with the RRM-R to experimental data yields excellent agreement. The model depends on four dimensionless parameters describing: the spontaneous combination and breakdown of micelles ($k^*_{b0}$), growth due to alignment and collision of micelles ($k^*_{ga}$), and breakdown of micelles by tensile stresses ($k^*_{bt}$ and $a^*$). Certain combinations of parameters, particularly those where $k^*_{ga}$ is large and/or $k^*_{bt}$ and $a^*$ are small, produce reentrant (i.e. multivalued) steady state stress vs. shear rate curves, which is a necessary condition for a vorticity banding instability; this reentrant behavior indicates that the RRM-R is well-suited for studying this well-documented but poorly understood instability. Other parameter spaces, in which $k^*_{ga}$ is small and/or $k^*_{bt}$ and $a^*$ are large, do not undergo shear-thickening but rather show purely shear-thinning behavior. Although our model is intended to capture the behavior of dilute wormlike micelle solutions, we have shown that it is able to predict, at least partly, the behavior of semi-dilute solutions.

The proposed model is also able to predict transient flow dynamics, in particular startup of steady shear flow, that well-aligns with observations seen in literature. The model predicts a power-law relationship between induction time and applied shear rate, which has been reported by numerous literature sources. The ability of the model to predict steady and transient flow behavior in tandem indicates that this constitutive formulation can be used in fluid-dynamics studies of complex flow behavior and instabilities. There is currently a limited understanding of dilute wormlike micelle solutions in turbulent flows and the manner in which they are able to achieve strong drag reduction; further, there has been limited research into the numerous instabilities, particularly the vorticity banding instability, present in dilute surfactant solutions. This model takes a large step towards uncovering these as-yet poorly understood phenomena.

# 3

# Instabilities in circular Couette flow with a reentrant flow curve [1]

## 3.1 Introduction

Surfactants are amphiphilic molecules consisting of hydrophilic head groups bonded to long hydrophobic tails; when dissolved in water at some concentration above the critical micelle concentration (CMC), surfactants self-assemble into larger aggregate structures. The geometry of these structures is dictated by the size, shape, and chemistry of the surfactant molecules as well as the temperature and salinity of the solution [40, 106, 45, 54]. One class of these aggregate structures are wormlike (or rodlike) micelles, which can display a large range of varied structure and behavior depending on the concentration regime. In the dilute regime, wormlike micelles (WLMs) exist as nearly rigid rods with persistence lengths in the range of $\sim \mathcal{O}(10 - 100\text{nm})$ and contour lengths on a similar scale [61, 125, 59, 60, 5]. In the concentrated regime, WLMs can grow far beyond their persistence lengths to form entangled networks and branched structures, transitioning the solution into a highly viscoelastic gel-like phase [126]. In intermediate semi-dilute regimes, the behavior of WLMs depends on

[1] The text of this chapter is adapted from the publication by R.J. Hommel and M. D. Graham *JNNFM*, **324**, 105183, 2024.

the applied flow or forcing; at rest and low forcing (e.g., low shear rates) these WLMs often form entangled structures, while under the application of stronger flows these structures are dismantled and the WLMs show behavior that more closely resembles the dilute regime.

Wormlike micelles can be found in a wide variety of commercial products, such as detergents, coatings, and emulsifiers, as well as industrial processes, such as in environmentally friendly carrier fluids for oil recovery operations [14]. WLM solutions are also of great practical interest because they can provide significant levels of drag reduction in the transport of turbulent fluids. Notably, the addition of small amounts of wormlike micelle-forming surfactants to turbulent flows can produce up to an 80% reduction in turbulent drag, which is comparable to the drag-reducing capabilities of widely used polymer solutions [109, 1, 2]. Additionally, polymer molecules are shredded into short chain constituent segments by high-shear regions and must be continually replaced to achieve consistent drag reduction; wormlike micelles, however, are self-assembling and thus can overcome this shredding by reassembling following any mechanical degradation. Despite these benefits, the adoption of WLMs as drag-reducing agents has been limited, remaining mostly confined to areas of Japan for use in closed-loop heating and cooling districts [17, 18]. Some of this limitation stems from chemical considerations regarding the amphiphilic nature of surfactants, specifically that changing the solvent can affect the aggregation and structuring of these molecules [127, 128]; other limitation stems from the fact that the behavior and dynamics of these fluids in complex flows, and specifically the development of instabilities in these flows, is not well understood especially compared to the flow of polymer solutions. In this work, we aim to expand understanding of flow instabilities in dilute WLM solutions and elucidate the mechanisms underlying these instabilities.

Throughout this work we will focus exclusively on wormlike micelles in the dilute to semi-dilute regime. Wormlike micelle solutions in this regime are known to undergo both shear-thickening and shear-thinning, where thickening occurs at moderate shear rates followed by thinning at higher shear rates [9, 10, 11, 12, 13, 62, 61]. This thickening and thinning behavior

is related to the formation and subsequent breakdown of flow-induced structure (FIS) that takes the form of elongated and aligned micelles. Specifically, at moderate shear rates WLMs have been observed to align with the flow and undergo significant elongation, whereby the average length of micelles in solution can increase to several times the equilibrium length [46]. While a direct measurement of micelle length in flow is challenging, it is possible to make estimates of the micelle length by analyzing the effect of flow on the solution viscosity. Prud'homme and Warr related the critical strain rate, the strain at which the extensional viscosity is maximized, in an opposed jet device to the length of micelles by assuming that the micelle relaxation time was solely due to scission kinetics [63]. By approximating the tension along the micelle body and assuming an upper bound on the micelle scission energy, they directly related the critical strain rate to the micelle length. Through this analysis and by comparing to the mean micelle length at zero shear rate, the authors determined that micelles were significantly elongated by the extensional flow field. Similarly, Omidvar and coworkers used an asymptotic analysis of the FENE-P model to relate the extensional viscosity of the micelle solution to the micelle length [64]. By assuming that the micelle length could be related to the FENE-P extensibility parameter, they were able to relate increases in the extensional viscosity to elongation of the micelle lengths, finding significant elongation of the micelles by the flow field.

These solutions are also well-known for displaying a reentrant, or multivalued, flow curve (see Fig. 3.1) whereby the shear stress becomes a multivalued function of shear rate over some typically small range [129, 69, 50]. The presence of a reentrant flow curve is a necessary condition for the development of a vorticity banding instability [50]; this instability is a relatively uncommon phenomenon, but has been observed in charged colloidal suspensions, rodlike colloids, onion surfactants, biphasic polymer blends, and of course dilute WLM solutions [65, 66, 52, 67, 50, 68]. Vorticity banding is related to, but distinct from, the more well-studied shear banding instability where shear rate is a multivalued function of shear stress. Shear banding (also known as gradient banding) occurs at higher concentrations

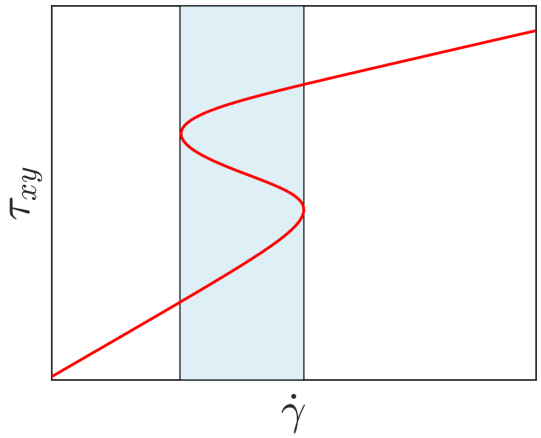


**Figure 3.1:** Example of a reentrant flow curve in which there is a region where the shear stress, $\tau_{xy}$, is a multivalued function of the shear rate, $\dot{\gamma}$. The light blue area shows the reentrant region of the flow curve.

when micelles form entangled networks, and is characterized by the solution separating into a macroscopically "banded" flow along the gradient direction, where separate bands support equal shear stresses but different shear rates [47, 55]. The separation of these two regions is often observable through differences in turbidity and birefringence [130]. There has been extensive theoretical and experimental treatment of this instability (see [47, 57] for comprehensive reviews). In contrast to gradient banding, vorticity banding requires that a single shear rate is able to support multiple shear stresses (i.e., a reentrant flow curve). In circular Couette flow (CCF), this instability manifests as stacked "bands" along the vorticity axis, where adjacent bands support distinct shear stresses but equivalent shear rates. Again, similar to gradient banding, these bands can often be visualized by differences in turbidity and birefringence [47, 50].

The most basic stability analysis that is relevant to these situations is that of Yerushalmi et al. [56]. They studied simple shear flow between parallel plates, with velocity field $v_x = \dot{\gamma} y$, finding that, if $\partial \tau_{xy}/\partial \dot{\gamma} < 0$, the flow is linearly unstable to 1D ($y$-dependent) perturbations. This analysis does not distinguish between nonmonotonic and reentrant flow curves; it depends only on the local slope of the flow curve, not the global behavior. Below, when we describe the "unstable" or "stable" region of the flow curve, it is in the sense of this analysis. The actual nature of flow instabilities of a fluid that can display $\partial \tau_{xy}/\partial \dot{\gamma} < 0$

in simple shear depends on the global nature of both the constitutive behavior and flow geometry. That said, the specific instability predicted by this analysis is 1D, and thus most directly related to gradient banding, in which the shear rate is a multivalued function of shear stress, though it has also been used to understand other instabilities as well [131, 132, 133, 57]. In terms of vorticity banding instabilities, most theoretical research has focused on dense suspensions or through the construction of isotropic-nematic phase diagrams for rigid rods [55, 47]. Olmsted and Lu [134] modified the Doi model for rigid rod suspensions with inhomogeneous terms and found conditions in shear flow that could give rise to phase separation (i.e., banding). Fielding used the diffusive Johnson-Segalman model to show that gradient banded flow can be unstable to vorticity bands [135]. Chacko and coworkers [136] developed a simple continuum model for dense particle suspensions that displayed a constitutive curve with a region where $\partial\tau_{xy}/\partial\dot{\gamma} < 0$; they showed that the flow was linearly unstable to vorticity band formation, as expected, and further found that the vorticity banded flow was unsteady.

In addition to vorticity banding, dilute WLM solutions have demonstrated a group of finger-like instabilities in circular Couette flow that appear as unstructured streaks and branches spanning the flow gap [69, 70]. Using a circular Couette device, Liu and Pine [4] observed these finger-like structures in controlled-shear rate flows of $\sim \mathcal{O}(10^2 - 10^3)$ ppm equilmolar CTAB/NaSal solutions; using small angle light scattering (SALS), they revealed reversible finger-like structures that, upon increasing shear rate, grew outwards from the inner cylinder into the flow gap. The emergence of these structures required a finite induction time, typically on the order of minutes, and resulted in an elevated shear stress corresponding to significant shear-thickening. The authors observed that the fingers repeatedly grew until they reached the outer cylinder before retracting towards the center of the cell and beginning to grow again. Hu and coworkers [71] observed similar structures in a solution of equimolar 7.5 mM TTAA/NaSal that exhibited a reentrant flow curve. Similar to Liu and Pine, the authors observed that increasing either the shear rate or shear stress beyond some critical

value induced shear-thickened structures that originated at the inner cylinder and grew outwards to fill the gap. In stress-controlled experiments, they observed that increasing the applied stress into the multivalued region of the flow curve resulted in a FIS front that steadily grew to some radial position along the gap before stopping and holding at a steady gap location; the point along the gap where the FIS front stopped depended on the applied stress. When increasing the shear stress beyond the multivalued region, the authors observed that the FIS encompassed the entire gap. In shear rate-controlled experiments, the authors observed transient behavior that was similar to the stress-controlled experiments, but found that the steady behavior was different; notably the system was either void of FIS or exhibited FIS that filled the entire gap depending on whether the applied shear rate was below or above the critical value, respectively.

Similar structures have also been observed to develop from interfacial instabilities. Wilson and Khomami have extensively studied interfacial instabilities in polymer melts and found that destabilization of these interfaces is strongly related to a jump in the first normal stress difference across the interface [137, 138, 139]. Pertinent to the current investigation is the structure of the interfacial instability, in which waves were bent and elongated by large shearing stresses, and in the case of compatible polymers 'pools' of material are pulled off the wave to yield thread-like structures; these threads closely resemble the 'fingers' observed in dilute WLM solution instabilities. Further, velocity gradients arising from interface curvature cause the waves to be convected at different rates, resulting in curved or 3D waves. Additionally, Yamani and coworkers [140] observed similar thread-like structures in their investigation of the flow of a planar jet of dilute polymer solution into a water tank. In their study, viscoelastic threads appeared to be sheared off of the main jet column. In the case of dilute wormlike micelle solutions, interface-like regions can manifest between domains of short, isotropically oriented micelles and elongated, highly oriented micelles.

To the best of our knowledge, there have been no computational studies looking at the development of either vorticity bands or finger-like structures in shear flows of dilute

WLM solutions. The main reason for this lack is the limited number of models for studying and predicting the behavior of WLM solutions in complex flows, and in particular models that can predict a reentrant flow curve. One of the first wormlike micelle models is due to Cates and Turner, who proposed a population balance model that accounted for the different stress relaxation mechanisms associated with wormlike micelles, namely micelle scission and rotational diffusion [73, 110]. Though Cates and Turner did not write down an explicit constitutive equation for their model, and moreover the incorporation of a continuous spectrum of micelle lengths is prohibitive for use in computational fluid dynamics (CFD) studies, their formulation has served as a foundation for the development of other widely used WLM models [76, 3]. Bautista and coworkers [113] have developed the BMP model, which couples a fluidity equation for studying thixotropic systems [93] to the Oldroyd-B equation. This model, as well as its many extensions and generalizations [90, 141], has shown good agreement with dilute wormlike micelles in a variety of flows [142], and has recently been used for studying viscoelastoplastic and gradient banding fluids [142]. Tamano and coworkers [99] have taken inspiration from the BMP model and coupled the fluidity equation to both the Giesekus and FENE-P models to form the f-Giesekus and f-FENE-P models, respectively. These models are well-suited for CFD studies because many CFD codes and frameworks have already been developed for the FENE-P and Giesekus models [34, 32], however, these models are unable to predict reentrant flow curves and are therefore unlikely to predict vorticity banding or finger-like instabilities.

In this work, we investigate instability formation in circular Couette flows using the reformulated reactive rod model (RRM-R) [129]. The RRM-R, and its predecessor the RRM [3], model wormlike micelles as reactive Brownian rods undergoing reversible scission and fusion in flow. The model couples evolution equations for the ensemble average orientation of rods and micelle contribution to the solution stress to an evolution equation for the collective length of micelles, where micelle number density and length are constrained by conservation of surfactant molecules. The evolution equation governing micelle length in the RRM-R,

which was inspired by work by Turner and Cates [73], accounts for two forms of micelle fusion: spontaneous and flow-induced, as well as two forms of micelle scission: spontaneous and tension-induced. More details on the modeling framework of the RRM-R are provided in Section 3.2. Using this framework, the RRM-R can capture both shear-thickening and -thinning, flow-induced structure formation, nonzero normal stress differences, and importantly a reentrant flow curve. Moreover, we have shown in our previous work [129] that the RRM-R can be fit to experimental measurements of dilute WLM solution rheology, and can successfully predict the behavior of these solutions in both pure shear and pure extensional flows under both steady and transient conditions. This success in predicting the rheology of WLM solutions, along with the tractability of the RRM-R, makes this model well-suited for studying instability formation in complex flows.

## 3.2 Governing equations

The aim of the present study is to investigate instabilities of dilute wormlike micelle solutions in circular Couette flow. Specifically, we are interested in exploring regimes where the underlying constitutive curve is reentrant as this region of state space is currently poorly understood and can give rise to interesting instabilities. To carry out our analysis we use the RRM-R (reactive rod model - reformulated), which models dilute WLM solutions as suspensions of reactive Brownian rods undergoing reversible scission and growth in flow. The RRM-R has shown qualitative agreement with experimental data of dilute WLM solutions in simple shear and purely extensional flows under both steady state and transient conditions.

The complete derivation of the RRM-R is described in [129] but is summarized below. We note that this modeling framework takes inspiration from theoretical treatments by Cates and Turner [110]. In the RRM-R, dilute wormlike micelle solutions are treated as suspensions of rigid Brownian rods undergoing reversible scission and fusion. Rods can fuse end-to-end (reducing the energetic penalty associated with the micellar end caps), but only when they

are highly aligned – otherwise the energy penalty arising from forming a long but bent micelle is too large for fusion to take place [15, 110]. The application of flow tends to align the rods. This alignment is balanced by rotational diffusivity of the rods acting to return the suspension to isotropy. Consequently, a positive feedback mechanism exists between rod growth and alignment owing to the smaller rotational diffusivity of longer rods. It is assumed that rod growth is countered by hydrodynamic stresses acting along the lengths of the rods, which induce breakage events into shorter rods. Moreover, rods can undergo both spontaneous scission and spontaneous fusion events.

### 3.2.1 Brownian rods

Starting with a suspension of (non-reactive) Brownian rods, consider a uniform collection of rods with length $L_0$, radius $b$, and number density $n_0$ suspended in a Newtonian solvent with viscosity $\eta_s$. The orientation of a single rod is described by the unit director vector $\boldsymbol{u}$. The solution is subjected to an arbitrary flow with local velocity $\boldsymbol{v}$ and transpose velocity gradient $\boldsymbol{K} = \boldsymbol{\nabla v}^\top$. The orientation tensor $\boldsymbol{S}$ describes the average collective orientation of the suspension and is given by the second moment of $\boldsymbol{u}$

$$\boldsymbol{S} = \langle \boldsymbol{uu} \rangle = \int \boldsymbol{uu} \psi \mathrm{d}\boldsymbol{u}, \tag{3.1}$$

where $\psi$ is the probability distribution function of $\boldsymbol{u}$. The time evolution of $\boldsymbol{S}$ in flow is

$$\frac{\mathrm{D}\boldsymbol{S}}{\mathrm{D}t} = -6D_{r,0}\left(\boldsymbol{S} - \frac{1}{3}\boldsymbol{I}\right) + \boldsymbol{K}\cdot\boldsymbol{S}^\top + \boldsymbol{S}\cdot\boldsymbol{K}^\top - 2\boldsymbol{K} : \langle \boldsymbol{uuuu} \rangle, \tag{3.2}$$

where $D_{r,0}$ is the rotational diffusion coefficient of a rod, $\boldsymbol{I}$ is the unit tensor, and the double dot product is defined as $\boldsymbol{A} : \boldsymbol{B} = \mathrm{Tr}(\boldsymbol{A}\cdot\boldsymbol{B}^\top)$ [75].

The total stress of the suspension is given by the sum of the solvent $\boldsymbol{\tau}^N$ and micelle $\boldsymbol{\tau}^m$ contributions

$$\boldsymbol{\tau}^T = \boldsymbol{\tau}^N + \boldsymbol{\tau}^m, \tag{3.3}$$

where

$$\boldsymbol{\tau}^N = 2\eta_s \boldsymbol{D} \tag{3.4}$$

is the Newtonian solvent contribution with rate of deformation tensor $\boldsymbol{D} = \frac{1}{2}(\boldsymbol{K} + \boldsymbol{K}^\top)$ and

$$\boldsymbol{\tau}^m = 3n_0 k_B T \left( \boldsymbol{S} - \frac{1}{3}\boldsymbol{I} \right) + \frac{n_0 k_B T}{2D_{r,0}} \boldsymbol{K} : \langle \boldsymbol{uuuu} \rangle \tag{3.5}$$

is the additional stress due to the presence of rods. Here, $k_B$ is the Boltzmann constant and $T$ is the temperature. Equations (3.2) and (3.5) notably contain the fourth moment $\langle \boldsymbol{uuuu} \rangle$, an evolution equation for which depends on the sixth moment of $\boldsymbol{u}$, which in turn depends on higher moments. To proceed analytically, it is then necessary to supply a closure approximation for the product $\boldsymbol{K} : \langle \boldsymbol{uuuu} \rangle$. While numerous approximations are possible (see, for example: [75, 114, 101]), the RRM-R uses an approximation from Dhont and Briels [103] that interpolates between exact expressions in the limits of isotropy (equilibrium) and complete alignment:

$$\boldsymbol{K} : \langle \boldsymbol{uuuu} \rangle \approx \frac{1}{5}[\boldsymbol{S} \cdot \boldsymbol{D} + \boldsymbol{D} \cdot \boldsymbol{S} - \boldsymbol{S} \cdot \boldsymbol{S} \cdot \boldsymbol{D} - \boldsymbol{D} \cdot \boldsymbol{S} \cdot \boldsymbol{S} + 2\boldsymbol{S} \cdot \boldsymbol{D} \cdot \boldsymbol{S} + 3(\boldsymbol{S} : \boldsymbol{D})\boldsymbol{S}]. \tag{3.6}$$

### 3.2.2 RRM-R

As discussed above, a key feature of the RRM and RRM-R is that they allow micelles, modeled as rigid rods, to undergo reversible scission and growth by allowing the collective length and number density of the suspension to be dynamic properties that evolve with time and flow. This variation is mathematically achieved in the RRM-R by changing the constant rod length $L_0$ to the dynamic length $L$. To make analytical progress and ensure the tractability of the model we assume the system can be characterized by a single, representative length, $L$. Now consider a suspension of rods at equilibrium with number density $n_0$ and equilibrium length $L_0$; the radius $b$ of the rods is taken to be constant. The evolution of length $L$ and

number density $n$ are constrained at all times by the surfactant mass balance

$$nL = n_0 L_0. \tag{3.7}$$

The rotational diffusion constant for a rod of length $L_0$ and radius $b$ is given by [75, 115]

$$D_{r,0} = \frac{3k_B T}{\pi \eta_s L_0^3} \ln\left(\frac{L_0}{2b}\right). \tag{3.8}$$

In the RRM-R, the constant rotational diffusion coefficient of the simple rigid rod model is replaced by the length-dependent coefficient

$$D_r = \frac{D_{r,0}}{L^{*3}} \left(\frac{\ln L^* + m}{m}\right), \tag{3.9}$$

where $L^* = L/L_0$ is the dimensionless micelle length and $m = \ln[L_0/(2b)]$ is a constant related to the initial aspect ratio of the rods. Substituting Eq. (3.9) into Eqs. (3.2) and (3.5), we find

$$\frac{\mathrm{D}\boldsymbol{S}}{\mathrm{D}t} = -6D_r\left(\boldsymbol{S} - \frac{1}{3}\boldsymbol{I}\right) + \boldsymbol{K}\cdot\boldsymbol{S}^\top + \boldsymbol{S}\cdot\boldsymbol{K}^\top - 2\boldsymbol{K} : \langle \boldsymbol{uuuu}\rangle \tag{3.10}$$

and

$$\boldsymbol{\tau}^m = 3nk_BT\left(\boldsymbol{S} - \frac{1}{3}\boldsymbol{I}\right) + \frac{nk_BT}{2D_r}\boldsymbol{K} : \langle \boldsymbol{uuuu}\rangle. \tag{3.11}$$

The orientation of rods in the suspension is tracked by introducing a scalar orientational order parameter

$$\widehat{S} = \sqrt{\frac{3}{2}\widehat{\boldsymbol{S}} : \widehat{\boldsymbol{S}}}, \tag{3.12}$$

where $\widehat{\boldsymbol{S}} = \boldsymbol{S} - \frac{1}{3}\boldsymbol{I}$ is the traceless part of $\boldsymbol{S}$. This order parameter varies between $\widehat{S} = 0$ for isotropic rods and $\widehat{S} = 1$ for perfectly aligned rods. Note that the description and equations above are valid for both the original RRM and the reformulation (RRM-R), the only variation between the two models is in the length evolution equation, discussed below.

To allow for variability of rod length the RRM-R assumes a length evolution equation

that balances growth and breakdown of micelles

$$\frac{\mathrm{D}L}{\mathrm{D}t} = R_g + R_b, \tag{3.13}$$

where $R_g \geq 0$ is the rate of micelle growth and $R_b \leq 0$ is the rate of micelle breakdown. As discussed previously, the RRM-R assumes two forms of growth: spontaneous, $R_{g,s}$ and alignment-induced, $R_{g,a}$ as well as two forms of breakage: spontaneous, $R_{b,s}$, and tension-induced, $R_{b,t}$. Spontaneous growth occurs both in the absence and presence of flow and is assumed to take the form:

$$R_{g,s} = k_{g0} n^2, \tag{3.14}$$

where $k_{g0}$ is a spontaneous growth rate coefficient and the quadratic dependence on number density arises from the bimolecular nature of a collision event. Alignment-induced growth is taken to be the separable product of collision frequency and micelle orientation; the combination of these two terms is crucial to ensure that micelles are only growing when aligned, since the formation of a bent micelle is energetically unfavorable. In our previous work we showed that diffusion-driven collisions dominate convection-driven collisions, except in extremely high shear flows, yielding a growth term of the form:

$$R_{g,a} = k_{ga} n^2 \widehat{S}^2, \tag{3.15}$$

where $k_{ga}$ is the alignment-induced growth coefficient.

Spontaneous breakage, like growth, occurs in both the presence and absence of flow and is assumed to increase with rod length, yielding the form

$$R_{b,s} = -k_{b0} L, \tag{3.16}$$

where $k_{b0}$ is a breakage rate constant. At equilibrium spontaneous growth and breakage

must balance such that

$$0 = n_0^2 k_{g0} - k_{b0} L_0. \tag{3.17}$$

This relation allows $k_{g0}$ to be expressed in terms of $k_{b0}$ and emphasizes the fact that the two constants are not independent parameters. The tension-induced breakage term arises from assuming that as rods become sufficiently long they will be broken down by hydrodynamic stresses oriented along the backbone of the micelles. The tensile force at the midpoint of a rod can be estimated by

$$T \sim \frac{\boldsymbol{S} : \boldsymbol{\tau}_m}{n_0 L_0}. \tag{3.18}$$

Viewing the micelle tension as increasing the likelihood that a micelle will overcome the free energy barrier to scission [15] motivates the use of an Arrhenius-type breakage rate expression:

$$R_{b,t} = -k_{bt} \left[ \exp\left( \frac{a}{L_0} \frac{\boldsymbol{S} : \boldsymbol{\tau}_m}{n_0 k_B T} \right) - 1 \right], \tag{3.19}$$

where $k_{bt}$ is a tension-induced breakage coefficient and $a$ acts as a constant for micelle scission. Note that $Ta$ has units of work, and thus one could view $a$ as the distance the two halves of the micelle need to be pulled apart to break it in half. This term has been structured so that at rest, (i.e. when $\boldsymbol{S} : \boldsymbol{\tau}_m = 0$), the tension-induced breakage rate vanishes entirely.

After a number of simplifications involving the surfactant mass balance Eq. (3.7) and relating spontaneous effects that must balance at equilibrium, we have the overall length evolution equation

$$\frac{\mathrm{D}L}{\mathrm{D}t} = k_{b0} \left( \frac{L_0^3}{L^2} - L \right) + k_{ga} (n_0 L_0)^2 \frac{\widehat{S}^2}{L^2} - k_{bt} \left[ \exp\left( \frac{a}{L_0} \frac{\boldsymbol{S} : \boldsymbol{\tau}^m}{n_0 k_B T} \right) - 1 \right]. \tag{3.20}$$

This equation contains four parameters - $k_{b0}$, $k_{ga}$, $k_{bt}$, and $a$, which are related to the spontaneous breakage, alignment-induced growth, tension-induced breakage, and scission energy of micelles, respectively.

The RRM-R constitutive equations are coupled to conservation of mass and momentum

$$\boldsymbol{\nabla} \cdot \boldsymbol{v} = 0, \tag{3.21}$$

$$\rho \frac{\mathrm{D}\boldsymbol{v}}{\mathrm{D}t} = -\boldsymbol{\nabla} p + \eta_s \nabla^2 \boldsymbol{v} + \boldsymbol{\nabla} \cdot \boldsymbol{\tau}^m, \tag{3.22}$$

where $\boldsymbol{v}$ is the velocity, $p$ is the pressure, $\rho$ is the density of the fluid, $\eta_s$ is the solvent viscosity which is assumed to be Newtonian, and $\boldsymbol{\tau}^m$ is the micelle contribution to the fluid stress.

### 3.2.3 Circular Couette flow

In this work we focus on the behavior of dilute wormlike micelle solutions in circular Couette flow, shown in Fig. 3.2. The inner cylinder has radius $R_I$ and the outer cylinder has radius $R_O$; the gap width $d$ is the difference between the two, $d = R_O = R_I$; in all simulations we fix $d = 1$. The curvature ($\epsilon$) of the system is $\epsilon = d/R_I$. We take the inner cylinder to be stationary and the outer cylinder to rotate with some fixed angular velocity $\Omega_O$, which we can write as the linear azimuthal velocity $U = \Omega_0 R_O$. The height of the cylinder is $h$. In 3D simulations we take all quantities to be periodic in $z$ at the cylinder ends. Using asterisks to denote dimensionless quantities, we render the governing equations dimensionless with the following relations: $\boldsymbol{x} = \boldsymbol{x}^* d$, $\boldsymbol{v} = \boldsymbol{v}^* U$, $t = t^*/\dot{\gamma}$, $p = p^* \eta_s \dot{\gamma}$, $\boldsymbol{\tau}^m = \boldsymbol{\tau}^{m*} G_0$, and $L = L^* L_0$ where $\dot{\gamma} = U/d$ is the characteristic shear rate and $G_0 = n_0 k_B T = 2\eta_m D_{r,0}/15$ is the micelle shear modulus [75]. Substituting these relations into the governing equations and dropping asterisks we are left with the dimensionless equations:

$$\boldsymbol{\nabla} \cdot \boldsymbol{v} = 0, \tag{3.23}$$

$$\mathrm{Re}\frac{\mathrm{D}\boldsymbol{v}}{\mathrm{D}t} = -\boldsymbol{\nabla}p + \nabla^2\boldsymbol{v} + \frac{2}{15}\left(\frac{1-\beta}{\beta}\right)\frac{1}{\mathrm{Pe}}\boldsymbol{\nabla}\cdot\boldsymbol{\tau}^m, \tag{3.24}$$

$$\frac{\mathrm{D}\boldsymbol{S}}{\mathrm{D}t} = -\frac{6}{\mathrm{Pe}L^3}\left(\boldsymbol{S} - \frac{1}{3}\boldsymbol{I}\right)\left(\frac{m+\ln L}{m}\right) + \boldsymbol{K}\cdot\boldsymbol{S}^\top + \boldsymbol{S}\cdot\boldsymbol{K}^\top - 2\boldsymbol{K} : \langle\boldsymbol{uuuu}\rangle\,, \tag{3.25}$$

$$\boldsymbol{\tau}^m = \frac{3}{L}\left(\boldsymbol{S} - \frac{1}{3}\boldsymbol{I}\right) + \frac{\mathrm{Pe}}{2}\left(\frac{mL^2}{m+\ln L}\right)\boldsymbol{K} : \langle\boldsymbol{uuuu}\rangle\,, \tag{3.26}$$

$$\frac{\mathrm{D}L}{\mathrm{D}t} = \frac{1}{\mathrm{Pe}}\left[k_{b0}^*\left(\frac{1}{L^2} - L\right) + k_{ga}^*\frac{\widehat{S}^2}{L^2} - k_{bt}^*\left[\exp\left(a^*\boldsymbol{S} : \boldsymbol{\tau}^m\right) - 1\right]\right]. \tag{3.27}$$

We have introduced several dimensionless quantities. The Reynolds number is the ratio of inertial to viscous forces, defined as $\mathrm{Re} = \rho U d/\eta_s$. The rotational Péclet number is the ratio of the shear rate to the rotational diffusivity of the micelles at equilibrium, defined as $\mathrm{Pe} = \dot{\gamma}/D_{r0}$. In circular Couette flow the shear rate varies with radial position along the gap so that we have an *applied* Péclet number defined with respect to the rotation rate of the outer cylinder, which we write as Pe, and a *local* Péclet number, written as $\mathrm{Pe}_l$, that is computed from the local shear rate in the gap. Finally, $\beta = \eta_s/(\eta_s + \eta_m)$ is the viscosity ratio. We also have four dimensionless groups in the length evolution equation – $k_{b0}^*$, $k_{ga}^*$, $k_{bt}^*$, and $a^*$ – all of which are defined identically to those in the previous work [129]. In order, $k_{b0}^*$ represents the ratio of relaxation due to spontaneous breakage to relaxation due to diffusion (i.e. realignment), $k_{ga}^*$ acts as a measure of the ratio of growth due to alignment to diffusion, $k_{bt}^*$ represents the ratio of relaxation due to tension-induced breakage to relaxation due to diffusion, and $a^*$ functions as a dimensionless length that must be overcome for tension-induced scission to occur. For the rest of this work we will drop the asterisks from these groups.

Equations (3.23) to (3.27) are solved with no-slip boundary conditions at the walls. More details on the boundary conditions for $L$, $\mathbf{S}$, and $p$ are given in Section 3.3. Recently, McCauley and coworkers have shown that wall-slip in concentrated WLM solutions has a profound effect on the shear banding instability, whereby wall-slip acts to decrease the effective shear rate at the walls which then delays the onset of shear-banding [81]. We do

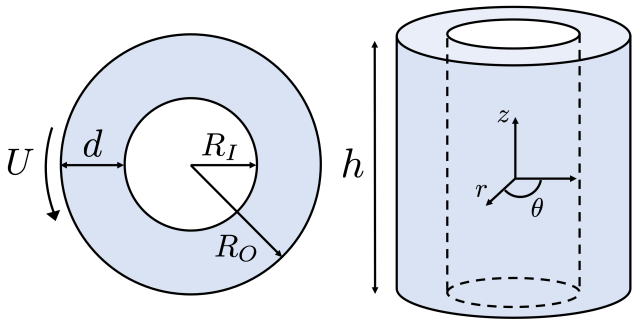


**Figure 3.2:** Schematic of circular Couette geometry. Left: top-down ($r\theta$) view of domain. Right: side view of domain.

not expect wall-slip to occur in the dilute WLM solutions that we are interested in as it typically requires the formation of networks or gel-like phases, such as in concentrated WLM solutions or polymer melts; however, if wall-slip were to occur, we expect similar behavior in that the effective shear rate at the walls will be reduced, thereby delaying the onset of instabilities.

### 3.2.4 Circular Couette flow: steady state

To help analyze the behavior of the RRM-R in circular Couette flow (CCF), we will need to solve for the unidirectional steady state solutions of the system. We assume a purely azimuthal velocity profile that depends only on the radial coordinate, $\boldsymbol{v} = [0, v(r), 0]^\top$. For this velocity profile the only non-zero component of the velocity gradient tensor is the $r\theta$ component, given by

$$\dot{\gamma}_{r\theta} = Dv - \frac{v}{r}, \tag{3.28}$$

where $D = \frac{\partial}{\partial r}$. For a unidirectional steady state velocity profile the equation for the $\theta$-component of the momentum equation Eq. (3.24) is

$$\left(r^2 D^2 + rD - 1\right) v + \frac{2}{15}\frac{1-\beta}{\beta}\frac{1}{\mathrm{Pe}}\left(2r + r^2 D\right)\tau^m_{r\theta} = 0. \tag{3.29}$$

We simplify the constitutive equations by writing the closure equation Eq. (3.6) as

$$\boldsymbol{C} = \boldsymbol{K} : \langle \boldsymbol{uuuu} \rangle. \tag{3.30}$$

We then substitute the velocity profile, which is not yet known, and Eq. (3.28) into Eq. (3.30) to obtain the components of the closure tensor

$$C_{rr} = \frac{1}{5} S_{r\theta} \left(1 - 4S_{rr} - S_{\theta\theta}\right) \dot{\gamma}_{r\theta}, \tag{3.31a}$$

$$C_{r\theta} = -\frac{1}{10} \left(S_{rr}^2 - (2S_{\theta\theta} + 1)S_{rr} - 6S_{r\theta}^2 + S_{\theta\theta}^2 - S_{\theta\theta}\right) \dot{\gamma}_{r\theta}, \tag{3.31b}$$

$$C_{\theta\theta} = -\frac{1}{5} S_{r\theta} \left(-1 + S_{rr} - 4S_{\theta\theta}\right) \dot{\gamma}_{r\theta}, \tag{3.31c}$$

$$C_{zz} = \frac{3}{5} S_{r\theta} S_{zz} \dot{\gamma}_{r\theta}. \tag{3.31d}$$

We can then write the components of the orientation evolution equation

$$\frac{\mathrm{D}S_{rr}}{\mathrm{D}t} = 0 = -\frac{6}{\mathrm{Pe}L^3} \left(\frac{\ln L^* + m}{m}\right) \left(S_{rr} - \frac{1}{3}\right) - 2C_{rr}, \tag{3.32a}$$

$$\frac{\mathrm{D}S_{r\theta}}{\mathrm{D}t} = 0 = -\frac{6}{\mathrm{Pe}L^3} \left(\frac{\ln L^* + m}{m}\right) S_{r\theta} + S_{rr}\dot{\gamma}_{r\theta} - 2C_{r\theta}, \tag{3.32b}$$

$$\frac{\mathrm{D}S_{\theta\theta}}{\mathrm{D}t} = 0 = -\frac{6}{\mathrm{Pe}L^3} \left(\frac{\ln L^* + m}{m}\right) \left(S_{\theta\theta} - \frac{1}{3}\right) + 2S_{r\theta}\dot{\gamma}_{r\theta} - 2C_{\theta\theta}, \tag{3.32c}$$

$$\frac{\mathrm{D}S_{zz}}{\mathrm{D}t} = 0 = -\frac{6}{\mathrm{Pe}L^3} \left(\frac{\ln L^* + m}{m}\right) \left(S_{zz} - \frac{1}{3}\right) - 2C_{zz}. \tag{3.32d}$$

Likewise we have the components of the stress tensor

$$\tau_{rr}^m = \frac{3}{L} \left(S_{rr} - \frac{1}{3}\right) + \frac{m\mathrm{Pe}L^2}{2\left(\ln L + m\right)} C_{rr}, \tag{3.33a}$$

$$\tau_{r\theta}^m = \frac{3}{L} S_{r\theta} + \frac{m\mathrm{Pe}L^2}{2\left(\ln L + m\right)} C_{r\theta}, \tag{3.33b}$$

$$\tau_{\theta\theta}^{m} = \frac{3}{L}\left(S_{\theta\theta} - \frac{1}{3}\right) + \frac{m\mathrm{Pe}L^2}{2\left(\ln L + m\right)}C_{\theta\theta}, \tag{3.33c}$$

$$\tau_{zz}^{m} = \frac{3}{L}\left(S_{zz} - \frac{1}{3}\right) + \frac{m\mathrm{Pe}L^2}{2\left(\ln L + m\right)}C_{zz}, . \tag{3.33d}$$

In this flow the length evolution Eq. (3.27) becomes

$$\frac{\mathrm{D}L}{\mathrm{D}t} = 0 = k_{b0}\left(\frac{1}{L^2} - L\right) + k_{ga}\frac{\widehat{S}^2}{L^2} - k_{bt}\left[\exp\left(a\boldsymbol{S} : \boldsymbol{\tau}^{m}\right) - 1\right], \tag{3.34}$$

with

$$\boldsymbol{S} : \boldsymbol{\tau}^{m} = S_{rr}\tau_{rr}^{m} + S_{\theta\theta}\tau_{\theta\theta}^{m} + S_{zz}\tau_{zz}^{m} + 2S_{r\theta}\tau_{r\theta}^{m}, \tag{3.35}$$

and with scalar orientation parameter

$$\widehat{S} = \left[\frac{3}{2}\left\{\left(S_{rr} - \frac{1}{3}\right)^2 + \left(S_{\theta\theta} - \frac{1}{3}\right)^2 + \left(S_{zz} - \frac{1}{3}\right)^2 + 2S_{r\theta}^2\right\}\right]^{\frac{1}{2}}. \tag{3.36}$$

## 3.3 Computational methods

We solve the governing equations for mass, momentum, micelle orientation, and micelle length using the open-source CFD software OpenFOAM coupled with the viscoelastic solver RheoTool [143, 144, 145]. This framework uses the finite volume method to discretize equations. We have written an additional library for the RRM-R. Details of the numerical implementation of the code as well as validations are given elsewhere [146, 144]. In this study we perform both 2D and 3D numerical simulations of the RRM-R in circular Couette flow. For 3D simulations we take all quantities to be periodic in $z$ at the cylinder ends. In 2D simulations we confine the flow to the $r\theta$-plane and solve only the $rr$, $r\theta$, $\theta\theta$, and $zz$ components of the governing equations. On the cylinder walls we use no-slip and no-penetration boundary conditions for the velocity, zero normal gradient for the pressure, and linear-extrapolation for the micelle length and orientation [144]. The micelle contribution to the stress tensor does not require boundary conditions as it is calculated directly from Eq. (3.26). To ensure

numerical stability of our simulations we use the stress-velocity coupling method provided in RheoTool; since adding stabilization is known to alter transient dynamics, we incorporate a number of inner iterations to the main solver loop (typically 2-5 depending on the degree of stabilization added), which act to decrease the explicitness of the solver [144].

We generate the numerical grid for our problem using the `blockMesh` utility in OpenFOAM. To ensure the resolution of structures in our system and ensure mesh-independency of our solution, we tested four different 2D grid resolutions with densities: M0 = 40,000, M1 = 90,000, M2 = 250,000, and M3 = 640,000. In 3D, we use these same resolutions with 20-80 grid points in $z$. All results presented in this work use the M2 grid, unless otherwise stated. In general, we found that all resolutions showed quantitatively similar dynamics and results. Further, we tested the accuracy of our meshes by comparing time-dependent statistics and dynamics as well as steady state profiles to confirm that our solutions did not depend on the mesh density.

To verify our viscoelastic library for the RRM-R and to look at a variety of both stable and unstable steady state solutions of our system, we also solve Eqs. (3.29) and (3.31) to (3.34) numerically using a Chebyshev pseudospectral method on Gauss-Lobatto nodes. All results presented in this work use $N = 200$ nodes. We solve the discretized system of nonlinear equations using the `fsolve` solver in *MATLAB*. We verified our codes by comparing steady state solutions obtained by the full DNS (OpenFOAM + RheoTool), the pseudospectral method (*MATLAB*) assuming a purely azimuthal flow field, and the numerical solution to our equations in simple shear flow ($\epsilon = 0$). We tested multiple sets of RRM-R parameters at several different Péclet numbers and found agreement in all cases.

## 3.4 Results and Discussion

The organization of this section is as follows: In Section 3.4.1 we compute steady states for a reentrant flow curve and characterize the stability of these states at a variety of different cur-

vatures. We then focus on 2D simulations with $\epsilon = 1$ in Section 3.4.2, and show that unstable regions of the constitutive curve ($\partial\tau_{r\theta}/\partial\dot{\gamma} < 0$) provoke finger-like instabilities. These finger-like structures are characterized by long branches of extended and anisotropically-oriented micelles. In Section 3.4.3 we investigate the appearance of these finger-like structures in 3D and show that the underlying instability is 2D in nature. Finally, in Section 3.4.4, we briefly discuss and analyze the linear stability of vorticity banding in the reentrant system.

### 3.4.1 Steady states in reentrant WLM solutions

The RRM-R length evolution equation, Eq. (3.27), contains four dimensionless parameters that can be tuned to vary the behavior of the desired WLM system. We select values that yield a significantly reentrant constitutive curve so that we can adequately probe and characterize instabilities in this region. The values chosen for the constitutive model are: $m = 3$, $k_{b0} = 10^{-2}$, $k_{ga} = 1500$, $k_{bt} = 10$, and $a = 2.5$, with $\mathrm{Re} = 10^{-1}$ and $\beta = 0.082$. This value of $\beta$ may seem low for modeling dilute viscoelastic solutions, but was chosen to match typical values seen in experiments where the zero-shear viscosity of these solutions is between $4 - 10$ mPa s [4, 5]. We approximate an inertialess flow condition by neglecting the convective terms in the momentum equation and setting $\mathrm{Re} = 0.1$.

In simple shear flow, $\boldsymbol{v} = (\mathrm{Pe}\ y, 0, 0)^T$, these parameters yield the constitutive curves shown in Fig. 3.3. These curves are highly reentrant over almost a decade of Péclet numbers, which will facilitate probing the behavior of this region, specifically sections where $\partial\tau_{xy}/\partial\dot{\gamma} < 0$. The length of micelles for these parameters increases to a maximum of about 11 times the equilibrium length, and the solution shear-thickens by over an order of magnitude. The inset in Fig. 3.3c shows a close-up of the orientation profiles near the turning point into the multivalued region. To clarify the analysis of these flows, we define three distinct solution branches on the shear stress constitutive curve (Fig. 3.3a): the lower, middle, and upper branches with $\tau^T_{xy,low} < \tau^T_{xy,mid} < \tau^T_{xy,up}$. The lower branch extends from $0 < \mathrm{Pe} \lesssim 2.5 \times 10^{-2}$. The middle branch extends from $5 \times 10^{-3} \lesssim \mathrm{Pe} \lesssim 2.5 \times 10^{-2}$, where notably $\partial\tau^m_{xy}/\partial\dot{\gamma} < 0$

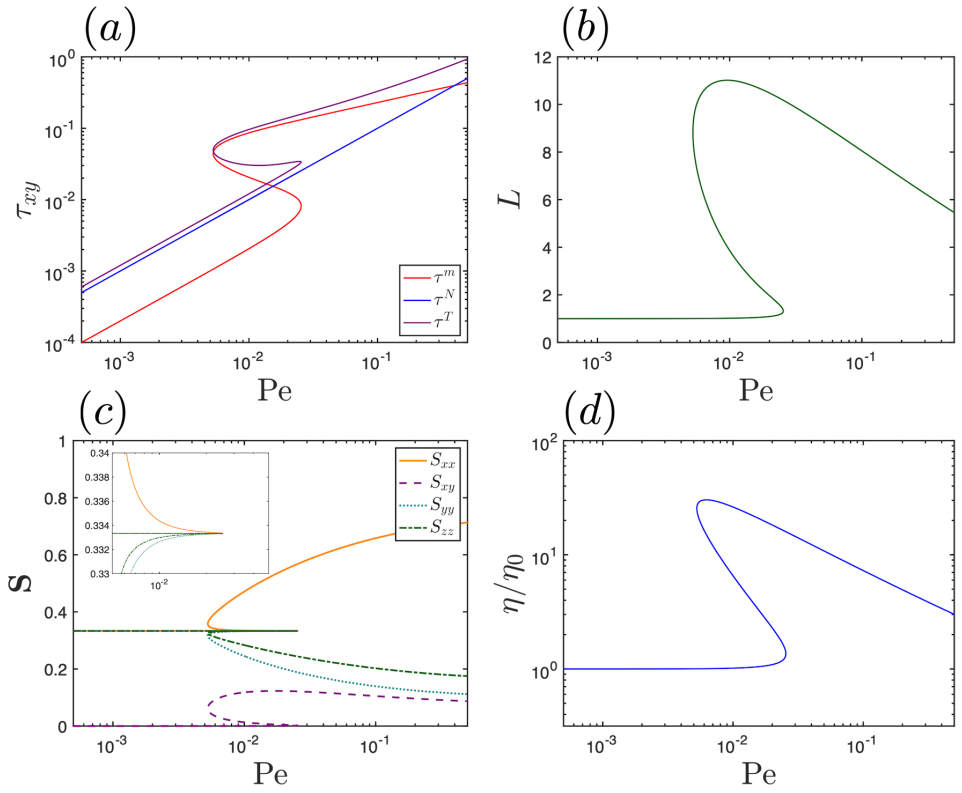


**Figure 3.3:** Constitutive curves for the RRM-R with parameters: $m = 3$, $k_{b0} = 10^{-2}$, $k_{ga} = 1500$, $k_{bt} = 10$, and $a = 2.5$. (a) Micelle (red), Newtonian (blue), and total shear stress (purple), (b) length of micelles, (c) components of the orientation tensor, and (d) normalized viscosity vs. applied Péclet number.

throughout this entire region. Finally, the upper branch extends from $5 \times 10^{-3} \lesssim \mathrm{Pe} < \infty$.

In this work we are primarily interested in circular Couette flow. The notable difference between this flow and simple shear flow is that in CCF all quantities (e.g., stress, length, and orientation) vary across the gap due to the radial dependence of the shear rate. The precise radial dependence of these quantities depends on the underlying curvature of the system. We can understand the role of curvature through the steady state momentum balance, which simplifies to $\tau^T_{r\theta}(r) = \tau^T_{r\theta,I}(R_I/r)^2$, where $\tau^T_{r\theta,I}$ is the total shear stress at the inner cylinder. Rewriting this balance in terms of the curvature and outer cylinder stress ($\tau^T_{r\theta,O}$) we find $\tau^T_{r\theta,O} = \tau^T_{r\theta,I}/(1+\epsilon)^2$. Clearly, as the curvature decreases so does the difference between $\tau^T_{r\theta,O}$ and $\tau^T_{r\theta,I}$, leading to nearly constant properties across the gap. Conversely, as the curvature increases so does the difference between the stresses at the inner and outer cylinders. This radial dependence of the shear rate also complicates the characterization of steady state

solutions for the reentrant flow curve; because the shear stress will vary throughout the gap, certain parts of the domain can lie in unstable regions of the flow curve ($\partial\tau_{r\theta}/\partial\dot{\gamma} < 0$) while the remainder lies in stable regions ($\partial\tau_{r\theta}/\partial\dot{\gamma} > 0$), leading to mixed local stability throughout the gap. Further, because the flow curve is multivalued over a range of Péclet numbers, more than one steady state can exist for a given applied Pe.

To further emphasize the role of curvature and the fact that steady states can encompass both stable and unstable branches, we show the steady state solutions for Pe = 0.01 at several curvatures in Fig. 3.4. All steady states were found using the Chebyshev pseudospectral method described in Section 3.3. The top row shows the (a) local micelle shear stress and (b) local micelle length projected onto the governing constitutive curves where the local Péclet number, $\mathrm{Pe}_l$, is calculated from the velocity profile throughout the gap. The bottom row shows the (c) local micelle shear stress and (d) local micelle length over the gap radius. The line colors show different curvatures where red: $\epsilon = 1.00$, orange: $\epsilon = 0.50$, green: $\epsilon = 0.20$, and blue: $\epsilon = 0.10$. The yellow rectangle indicates the region that is locally unstable ($\partial\tau^m_{r\theta}/\partial\dot{\gamma} < 0$). We only show the micelle stress, and not the total stress, in Fig. 3.4a because the unstable region originates from the micelle contribution to the stress and anywhere where the micelle stress is multivalued so is the total stress. We can see from these plots that at Pe = 0.01 two different steady states exist, one that is on the lower branch and one that is predominantly on the upper branch, but for larger curvatures the upper branch steady state extends into the middle branch. There is of course also a steady state that exists predominantly on the middle branch, however, this steady state is unstable and thus challenging to observe both experimentally and computationally, so for the remainder of this work we will focus solely on the upper and lower branch steady states. For steady states on the lower branch, micelles do not exhibit any pronounced elongation and remain nearly at the equilibrium length. Also on the lower branch, the micelle shear stress at the inner cylinder ($r - R_I = 0$) increases with increasing curvature while at the outer cylinder the micelle shear stress decreases with increasing curvature. This observation will

become important because it shows that the stability region on the lower branch, namely the range of Péclet numbers leading to a stable steady state, decreases with increasing curvature. The micelle shear stresses for all curvatures on this branch are equal around $r - R_I \approx 0.15$ where $\mathrm{Pe}_l \approx 0.01$.

On the upper branch we see that the micelle length varies significantly with curvature. In particular, for $\epsilon = 0.1$ and $\epsilon = 0.2$ the micelle length is nearly constant throughout the gap and micelles are nearly at the maximum degree of elongation prescribed by the constitutive curve. For the larger curvatures the length varies drastically throughout the gap; in the case of the largest curvature, $\epsilon = 1$, the length varies by almost an order of magnitude with maximum elongation occurring close to the inner cylinder. The large range of micelle lengths here results from the sharp change in length that occurs on the middle branch of the constitutive curve (Fig. 3.4b). There is a similar trend in the micelle shear stress on the upper branch as there is on the lower branch, notably the micelle stress at the inner cylinder is largest for the highest curvature. Now, however, we also see that for $\epsilon = 1$ the micelle stress towards the outer cylinder is clearly falling into the unstable middle branch region where $\partial \tau_{r\theta}^m / \partial \dot{\gamma} < 0$, and therefore this steady state solution is unstable to inhomogeneous flow. The instability of this steady state emphasizes the role of curvature in dictating the stability of the system, in particular increasing curvature directly decreases the stability of the solution by increasing the span of shear stresses occupied throughout the gap. Moreover, for systems with low curvature (e.g., $\epsilon = 0.1$) the system can support two steady states that are both stable, which can then allow for the manifestation of vorticity bands. We will elaborate on vorticity banding towards the end of this work. Figure 3.24 in Appendix A shows the same plots as Fig. 3.4 but at $\mathrm{Pe} = 0.0225$.

We summarize the effects of curvature on the stability of steady states in the system with Fig. 3.5. This figure shows the stability of the system for a given curvature and applied Péclet number. The dashed lines show the existence limits for the lower (cyan) and upper (orange) branches (i.e., $\mathrm{Pe}_{max}$ on the lower branch and $\mathrm{Pe}_{min}$ on the upper branch, beyond

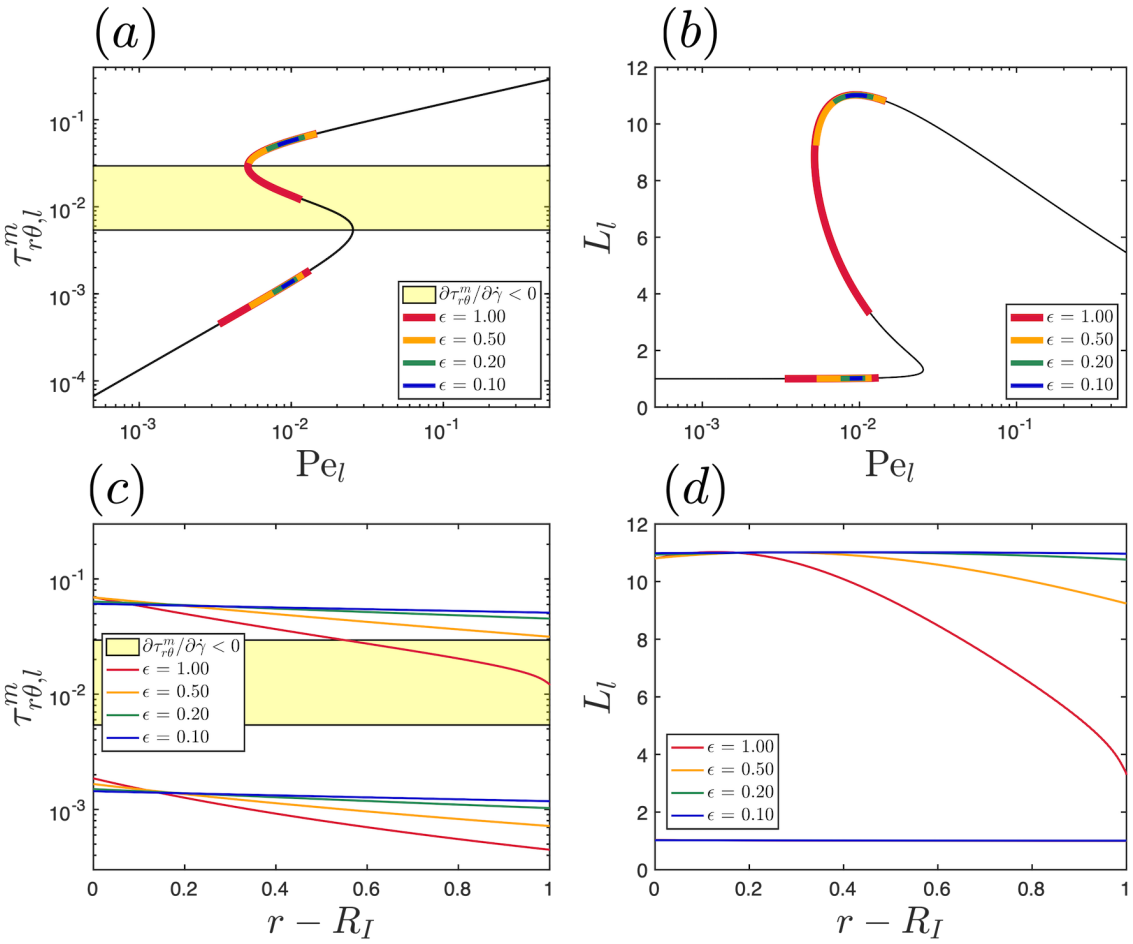


**Figure 3.4:** Upper and lower branch steady states for $\mathrm{Pe} = 0.01$ at varying curvatures. (a) Local micelle shear stress and (b) local micelle length projected onto the governing constitutive curves, where the local Péclet number, $\mathrm{Pe}_l$, is calculated from the velocity profile throughout the gap. (c) Local micelle shear stress and (d) local micelle length over the gap radius. Line colors are red: $\epsilon = 1.00$, orange: $\epsilon = 0.50$, green: $\epsilon = 0.20$, and blue: $\epsilon = 0.10$. The yellow rectangle indicates the unstable region of the flow curve ($\partial\tau^m_{r\theta}/\partial\dot{\gamma} < 0$).

which the branches no longer exist). The cyan markers show the *maximum* Pe value on the *lower* branch that will support a stable steady state for a given curvature; all Pe below this value on the lower branch will be stable, shown by the cyan-shaded region. The orange markers show the *minimum* Pe value on the *upper* branch that will support a stable steady state for a given curvature; all Pe above this value on the upper branch will be stable, shown by the orange-shaded region. The green region shows the range of Pe and $\epsilon$ where both the lower and upper branches exist and are stable. The yellow region shows the range of Pe and $\epsilon$ where both branches are unstable or do not exist. The colored stars show the local micelle shear stress over the gap at the indicated Pe and $\epsilon$. The pink and green stars show locations where only the upper branch exists and is stable for the pink star and unstable for the green. The red star shows an unstable lower branch and a stable upper branch, though it is precariously close to the unstable region. The blue star shows a stable lower branch and unstable upper branch. The yellow star shows a location where only the lower branch exists and it is stable. Finally, the purple star shows a location where both lower and upper branches exist and are stable. We can see from Fig. 3.5 that the range of unstable Pe increases with increasing curvature, though the effects of curvature only start to become evident around $\epsilon \approx 10^{-1}$; for $\epsilon \lesssim 10^{-1}$, the Pe stability range is nearly independent of curvature. For $\epsilon \lesssim 1$, all Pe have some region where they are stable, whether this is on the lower branch or the upper branch.

A full investigation of the effects of the four dimensionless parameters – $k_{b0}$, $k_{ga}$, $k_{bt}$, and $a$ – on the stability diagram shown in Fig. 3.5 is outside the scope of this work. However, it is possible to generally understand the role of each parameter by the effect it has on the degree of reentrant behavior in the flow curve. For example, increasing $k_{ga}$ tends to increase the reentrant region, while increasing $a$ and $k_{bt}$ decreases it. Varying $k_{b0}$ does not play a significant role in altering the size of the reentrant region. Increasing the size of the reentrant region also increases the range of Pe where the flow curve is unstable ($\partial\tau_{r\theta}/\partial\dot{\gamma} < 0$), and thus will tend to destabilize the flow. Further, increasing the size of the reentrant region

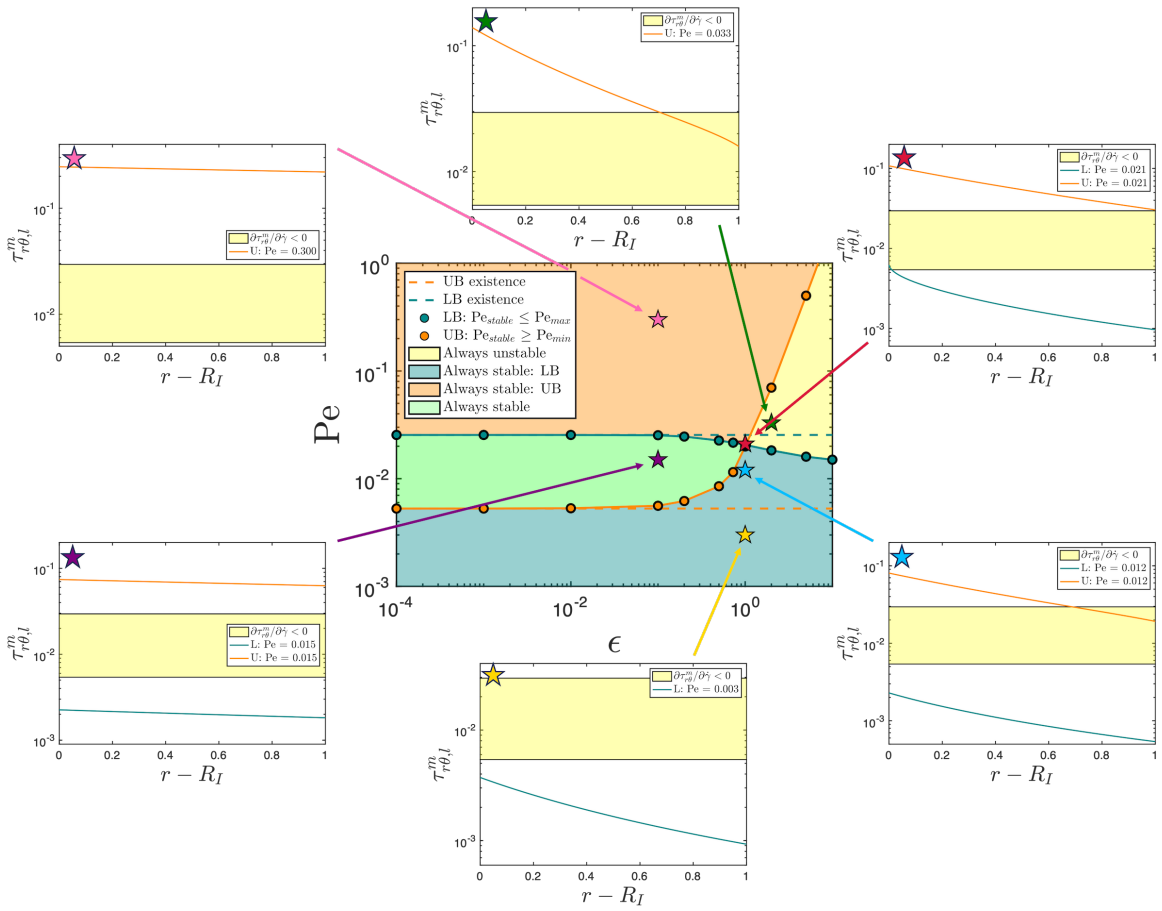


**Figure 3.5:** Shear rate-curvature state-space stability diagram. Dashed lines show the existence limits for the lower (cyan) and upper (orange) branches respectively. The cyan markers are the maximum Pe on the lower branch that will support a steady state; all Pe on the lower branch below this line are stable, shown by the cyan-shaded region. The orange markers are the minimum Pe on the upper branch that will support a steady state; all Pe on the upper branch above this line are stable, shown by the orange-shaded region. In the green-shaded region both the lower and upper branches exist and are stable. In the yellow-shaded region both the lower and upper branches are unstable or do not exist. The stars show the local shear stress profiles across the gap at the indicated Pe and $\epsilon$.

also tends to increase the difference in the viscosity, stress, and micelle length between the upper and lower branches, and will therefore give rise to more extreme gradients for flows that span both branches, which again will destabilize the flow.

Since the majority of this work considers the case of $\epsilon = 1$, it is helpful to further clarify the stability of this system at this curvature. Figure 3.6 shows the steady state local constitutive curve for $\epsilon = 1$. The red markers are the micelle shear stress at the inner cylinder and the blue markers are the micelle shear stress at the outer cylinder. The dashed red and blue lines represent steady states that were not explicitly calculated, but were filled in based on the underlying constitutive curve; all other steady states (shown as markers) were calculated using the Chebyshev pseudospectral code. The purple vertical lines connecting the markers show the local micelle shear stress throughout the gap at that Pe. The yellow rectangle shows the region where, at a given Pe, the flow will fall onto the locally unstable region. This plot completely describes the stability of the system for $\epsilon = 1$ and shows whether the instability will originate at the inner or the outer cylinder. Figure 3.6 emphasizes the features of Fig. 3.5, but importantly it shows specifically where the instability occurs. For example, on the upper branch we find that for Pe $\lesssim 0.022$ the micelle shear stress at the outer cylinder (blue markers) begins to enter the unstable region, indicating that any instability arising in the flow will likely originate close to the outer cylinder.

### 3.4.2 Finger-like instabilities in 2D

As has been discussed extensively, regions of the constitutive curve with a negative shear stress vs. shear rate slope are unstable in nature. Up until now, we have thoroughly investigated the stability of the constitutive curve and how it relates to the geometry curvature, but we have not yet investigated how this instability actually manifests. We now wish to characterize the nature of this instability in dilute WLM solutions using CFD simulations to evolve the governing equations in time. In particular, we wish to force the flow into unstable regions of the constitutive curve to investigate if and how the instability develops, as well as

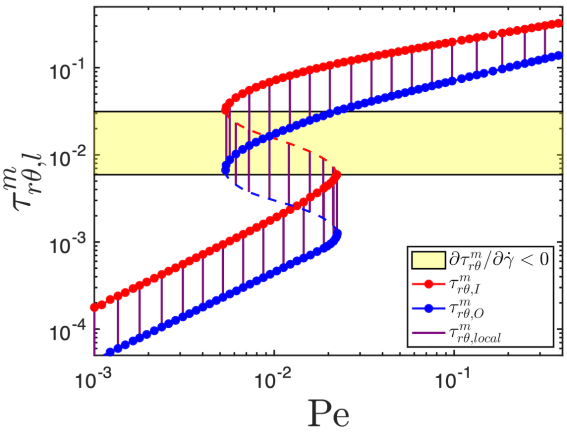


**Figure 3.6:** Steady state local constitutive curve for $\epsilon = 1$. The red markers are the micelle shear stress at the inner cylinder, and the blue markers are the micelle shear stress at the outer cylinder. The dashed red and blue lines represent steady states that were not explicitly calculated. The purple vertical lines connecting the markers show the local micelle shear stress throughout the gap at that Pe. The yellow rectangle shows the region where, at a given Pe, the flow will fall into the locally unstable region.

how the instability evolves. The full details of the simulations are described in Section 4.3.

### Instabilities for increasing shear rates

We begin this investigation by taking a solution at rest and slowly increasing the shear rate to Pe = 0.0225 to force the stress near the inner cylinder into the locally unstable region. The steady states for Pe = 0.0225 are shown in Fig. 3.7, where the upper branch steady state is shown in orange and the lower branch is shown in cyan. We see from (a) and (c) that there is a small region at the inner cylinder where the micelle shear stress of the lower branch steady state begins to enter into the unstable region. The upper branch steady state, however, exists entirely on the stable upper branch; we therefore might expect that any instability will grow initially at the inner cylinder and force the flow to jump from the unstable lower branch to the stable upper branch.

Figure 3.8 shows several snapshots in time of the micelle length, micelle orientation, and radial velocity in this start-up flow with an applied shear rate of Pe = 0.0225. The solution is initially at rest with isotropic micelles at their equilibrium length. Upon flow inception, we see that the growth and alignment of micelles first occurs closest to the inner

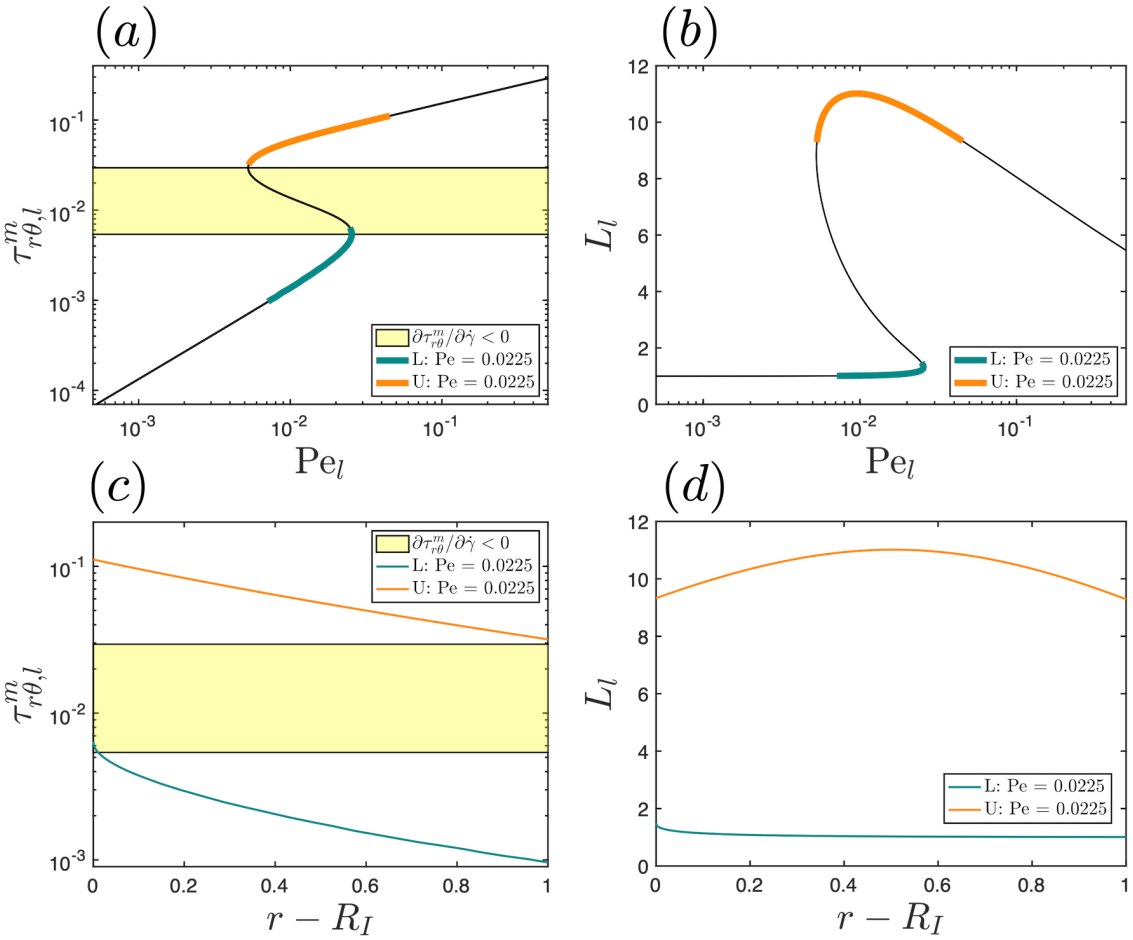


**Figure 3.7:** Upper and lower branch steady states for Pe = 0.0225 at $\epsilon = 1$. (a) Local micelle shear stress and (b) local micelle length projected onto the governing constitutive curves, where the local Péclet number, $\mathrm{Pe}_l$, is calculated from the velocity profile throughout the gap. (c) Local micelle shear stress and (d) local micelle length over the gap radius. The orange line corresponds to the upper branch and the cyan line corresponds to the lower branch. The yellow rectangle indicates the unstable region where $\partial\tau^m_{r\theta}/\partial\dot{\gamma} < 0$.

cylinder, where the shear stress is greatest, and then proceeds outwards through the gap. Note that at all times the surfactant mass balance $n_0 L_0 = nL$ is enforced, so an increase in micelle length is balanced by a decrease in rod number density. This elongation and anisotropy of micelles is associated with a radial inflow localized at the inner cylinder. At $t = 75$ we can see branches of elongated micelles growing outwards throughout the gap that are simultaneously sheared by the flow, resulting in a spiral-like pattern. The branching structures continue to grow outwards until they reach the outer cylinder ($t = 100$), at which point individual branches begin to merge into a crescent-shaped region of lower branch-micelles that rotates continuously at the outer cylinder ($t \geq 200$). In all snapshots it is clear that the elongation and anisotropy of micelles are closely intertwined. At later times we see that the sharp 'interface' separating short and elongated micelles is associated with strong radial flows, which arise through the large jump in the first normal stress difference across the 'interface.' We refer to this separation region as an 'interface' because, although the system consists of only a single phase, the difference between regions of highly elongated and anisotropically-oriented micelles from the nearly equilibrium-length and isotropic micelles is significant enough to give the appearance of phase separation. Notably, the 'interface' and resulting instability we observe closely resembles the work of Wilson and Khomami looking at interfacial instabilities between compatible polymers [139]. In particular, we observe similar wave- and hook-like structures, which in their study arose from shearing stresses close to the interface pulling material across the boundary into the adjacent layer. The present instability displays similar behavior, whereby elongated micelles are sheared into the region of shorter micelles.

At early times there is clearly symmetry in the flow structure that manifests as eight equally-spaced branches in $L$ and $\hat{S}$, as well as eight regions of coupled inflows and outflows. To help understand this symmetry, we consider some small perturbation to the flow of the form $\boldsymbol{B}(\boldsymbol{r}) = \boldsymbol{B}_{ss}(\boldsymbol{r}) + \widehat{\boldsymbol{B}}(\boldsymbol{r}) \exp(im\theta + \sigma t)$, where $\boldsymbol{B}$ is an arbitrary flow variable (e.g., $\boldsymbol{S}$ or $L$), $\boldsymbol{B}_{ss}$ is the steady state value of $\boldsymbol{B}$, $\widehat{\boldsymbol{B}}$ is the perturbation of $\boldsymbol{B}$, $m$ is the azimuthal

wavenumber that determines the azimuthal symmetry of the instability, and $\sigma$ is a complex eigenvalue that determines the stability and growth rate of the instability. We can clearly see from Fig. 3.8 that at $t = 40$ an unstable $m = 8$ mode appears. This mode grows radially outwards until it reaches the outer cylinder, at which point other modes set in, breaking the symmetry of the flow and leading to chaotic fluctuations. We confirmed the appearance of this $m = 8$ mode in the M1, M2, and M3 meshes; Fig. 3.25 in Appendix A shows the comparison at $r = R_I + 0.1d$ and $t = 40$ for the M2 (orange) and M3 (cyan) meshes, which show excellent agreement. We can therefore conclude that the appearance of this mode is not an artifact of the mesh resolution, and that the $m = 8$ is the most unstable mode as it pertains to this flow instability. In many interfacial instability phenomena, the most unstable wavelength is proportional to layer thickness; this is indeed the case in the Wilson and Khomami work mentioned above [139]. We suspect that the same observation holds here: the region of fluid that is in the unstable region of the flow curve is much thinner than the gap, likely leading to selection of a high azimuthal wavenumber for the instability.

Returning to Fig. 3.8, we see that the flow has still not completely evolved to the upper branch even after 450 time units. In particular, we see a crescent-shaped region of lower branch-micelles that rotates continuously near the outer cylinder. This flow state is interesting because it demonstrates the coexistence of complex and simple states: the complex state being this rotating crescent and the simple state being a flow that has fully evolved away from this unstable state and saturated onto the stable upper branch. It is possible that this flow state will eventually evolve to the stable upper branch if given sufficient time. Consider Fig. 3.5, which shows that the $(\epsilon, \mathrm{Pe}) = (1, 0.0225)$ applied here is extremely close to the boundary of Péclet values that are always unstable, and therefore it is possible that the proximity to this unstable region is impeding the evolution of the flow to the stable upper branch.

Indeed, by increasing to $\mathrm{Pe} = 0.024$, so that the upper branch is further from the unstable region, we observe very different behavior. Figure 3.9 shows several snapshots of the micelle

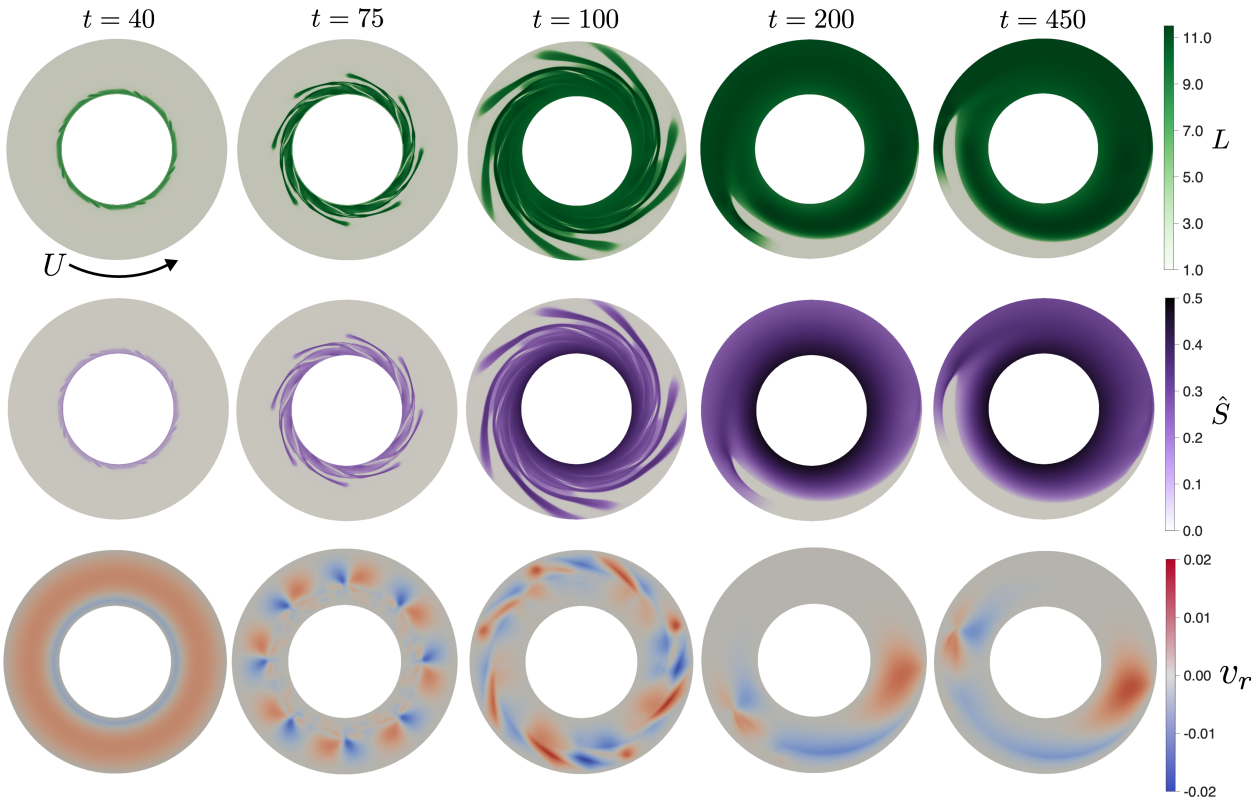


**Figure 3.8:** Snapshots of (top) micelle length, (middle) micelle orientation, and (bottom) radial velocity in start-up of steady shear flow with applied shear rate Pe = 0.0225.

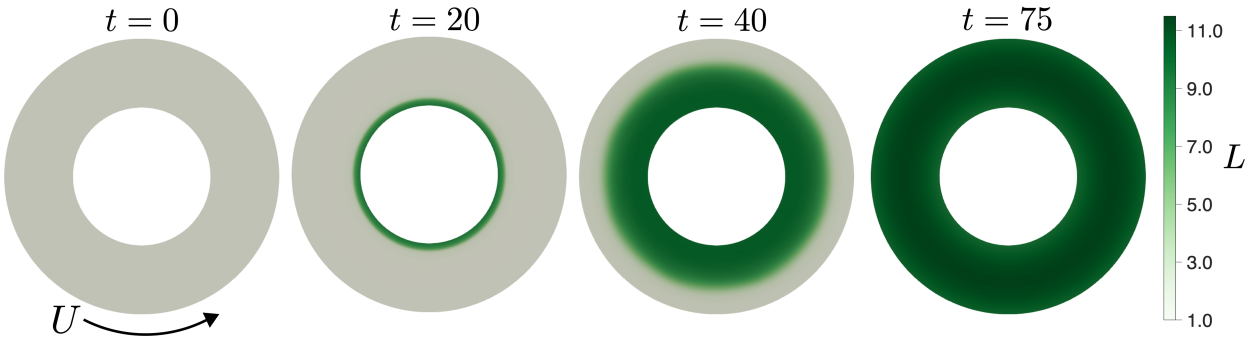


**Figure 3.9:** Snapshots of micelle length in start-up of steady shear flow with applied shear rate $\mathrm{Pe} = 0.024$.

length in this start-up flow. As before, micelle elongation occurs first at the inner cylinder and then extends outwards throughout the gap. At this larger shear rate, however, the branch structures that developed for $\mathrm{Pe} = 0.0225$ are no longer evident as the flow evolves too quickly to the stable upper branch for these branches to materialize. However, we can actually see the faint traces of these structures as well as the $m = 8$ mode in Fig. 3.10. This figure shows a snapshot of micelle length with contours at blue: $L = 8$, yellow: $L = 9$, and red: $L = 10$, all at $t = 45$. The azimuthal contours clearly show the $m = 8$ mode that was previously observed, but now the mode is obscured by the rapid evolution to the upper branch. The outer contour of $L = 10$ is related to the growth of the initial instability and displays the wave-like structure of the $m = 8$ mode, as do the $L = 8$ and $L = 9$ contours; the inner $L = 10$ contour, on the other hand, is due to micelles that have begun saturating on the upper branch, evidenced by the $\theta$-independent profile. By $t = 50$ the flow has fully reached steady state, suggesting that the persistent azimuthally inhomogeneous flow observed for $\mathrm{Pe} = 0.0225$ is indeed related to the proximity to the unstable region.

### Instabilities for decreasing shear rates

Up until now, the investigation has focused on instabilities that arise from increasing Pe so that the stress at the *inner* cylinder enters into the unstable region; we now wish to characterize the instabilities that develop upon decreasing Pe so that the stress at the *outer*

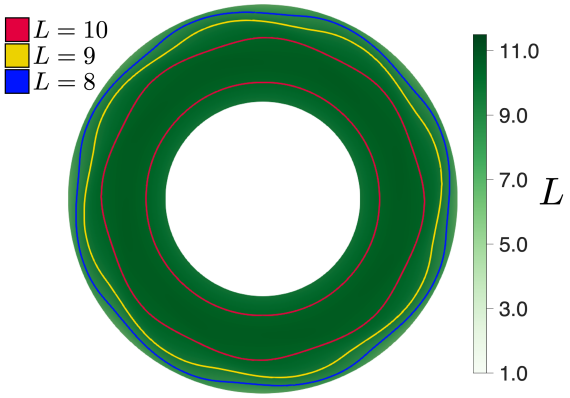


**Figure 3.10:** Snapshot of micelle length with contours at blue: $L = 8$, yellow: $L = 9$, and red: $L = 10$ for start-up of steady shear flow with $\mathrm{Pe} = 0.024$.

cylinder falls into the unstable region. We expect that instabilities will now occur towards the outer cylinder. We begin by taking a steady state at $\mathrm{Pe} = 0.04$, corresponding to flow that is on the stable upper branch, and then dropping the applied Péclet number to $\mathrm{Pe} = 0.015$ so that the stress at the outer cylinder falls into the unstable middle branch region. The steady states for $\mathrm{Pe} = 0.015$ are shown in Fig. 3.11, where the upper branch steady state is shown in orange and the lower branch is shown in cyan. We see from (a) and (c) that for the upper branch steady state there is a small region at the outer cylinder where the micelle shear stress begins to enter into the unstable region. The lower branch steady state, however, is entirely stable.

Figure 3.12 shows several snapshots of the micelle length, micelle orientation, and radial velocity when decreasing from an applied shear rate of $\mathrm{Pe} = 0.04$ to $\mathrm{Pe} = 0.015$. At $t = 0$ we see a nearly homogeneous flow with all micelle lengths above about $L \geq 9$, corresponding to the $\mathrm{Pe} = 0.04$ steady state. This flow slowly gives way over the next $\sim 95$ time units to a profile that exhibits a banded profile along the gradient direction. This banding is very obvious in the length profile but shows up only weakly in the orientation profile; banding at this stage does not appear in the velocity field, indicating that we are not observing traditional gradient banding. At $t = 95$ the micelle length displays an 'interface'-like boundary that splits the flow into two distinct regions. Again, this is not a true interface in the traditional phase separation sense since the flow here is single phase; instead, the

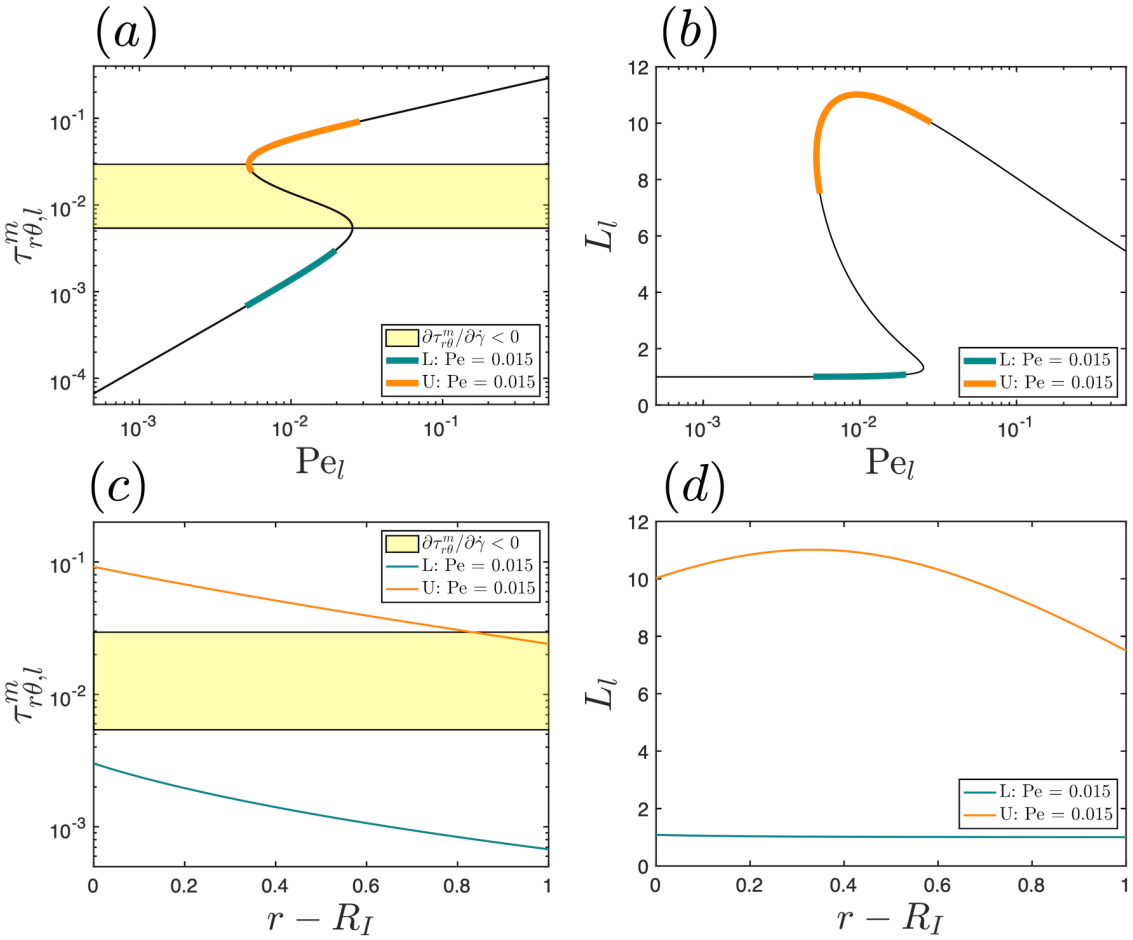


**Figure 3.11:** Upper and lower branch steady states for Pe = 0.015 at $\epsilon = 1$. (a) Local micelle shear stress and (b) local micelle length projected onto the governing constitutive curves, where the local Péclet number, $\mathrm{Pe}_l$, is calculated from the velocity profile throughout the gap. (c) Local micelle shear stress and (d) local micelle length over the gap radius. The orange line corresponds to the upper branch and the cyan line corresponds to the lower branch. The yellow rectangle indicates the unstable region where $\partial\tau^m_{r\theta}/\partial\dot{\gamma} < 0$.

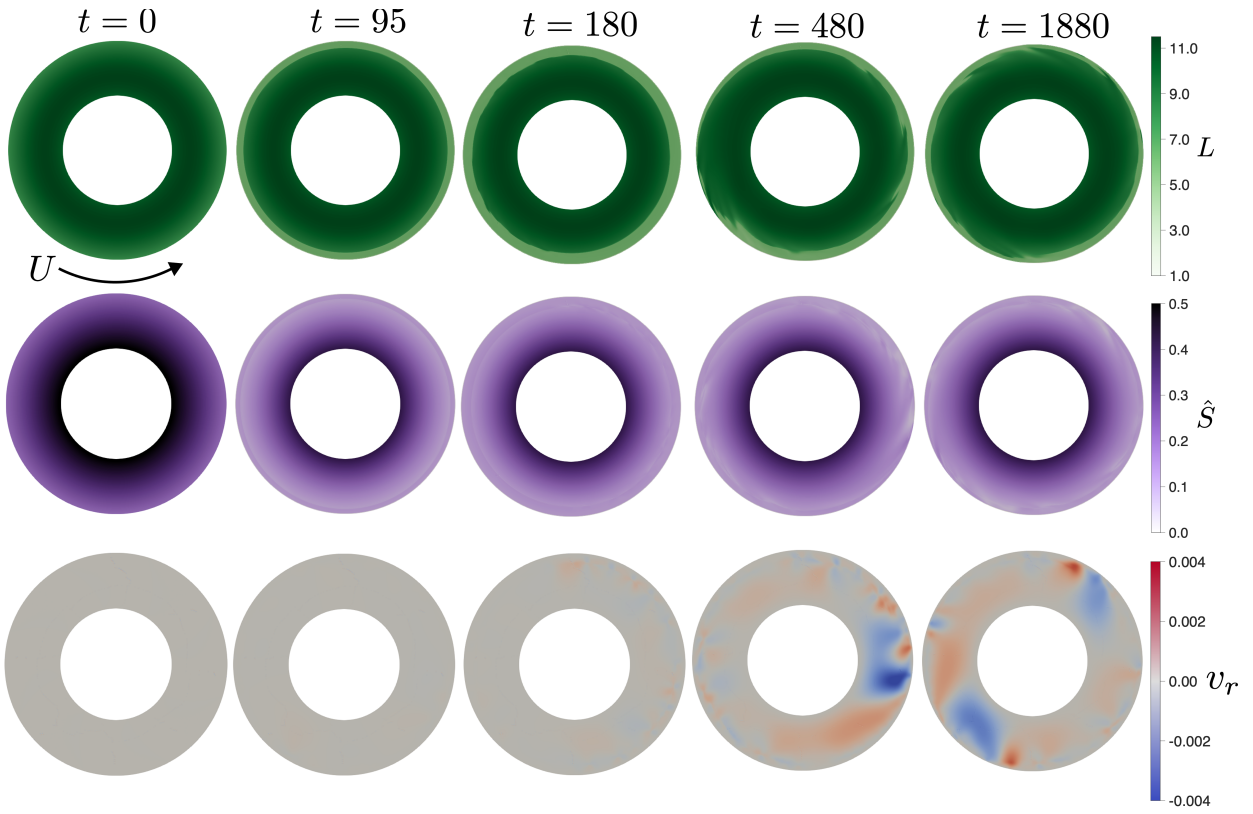


**Figure 3.12:** Snapshots of (top) micelle length, (middle) micelle orientation, and (bottom) radial velocity for decreasing shear flow from an applied shear rate of Pe = 0.04 to Pe = 0.015.

'interface'-like profile we are observing is strictly due to extremely sharp gradients in micelle length. As was discussed above, however, the difference between the two regions is quite significant and gives the appearance of phase separation.

At $t = 180$ we observe that the 'interface'-like profile, which had previously been axisymmetric, has begun to destabilize in the form of non-axisymmetric wisps that rotate with the fluid velocity. These wisps originate in the region of elongated micelles near the inner cylinder and spread outwards throughout the gap. We also begin to see the development of a weak radial flow as the 'interface' destabilizes. This destabilization process continues and grows for several hundred time units until the wispy streaks have fully extended to the outer cylinder ($t = 480$). The resulting chaotic flow state continues to fluctuate with wisps repeatedly growing and retracting, very much resembling the process described by Liu and Pine [4]. At some points ($t = 1880$) the streaks almost fully encompass the gap, but at no

point does the flow ever reach a steady state. The fluctuations of these wisps, and the resulting stress gradients, induce radial flows throughout the domain. Similar to the previous case of Pe = 0.0225, this persistent chaotic flow state demonstrates the coexistence of simple and complex flow states; again, the complex flow state is observed here and the simple state is given by the stable lower branch steady state. Considering Fig. 3.5, Pe = 0.015 is clearly outside the region of Péclet numbers that are always unstable, suggesting that the persistent fluctuations do not result from close proximity to the unstable region. To help us understand why this chaotic flow state does not give way to a steady state we decreased the Péclet number even further, to Pe = 0.01, to see if this lower shear rate would push the flow to the stable lower branch.

Indeed, upon decreasing the applied Péclet number further to Pe = 0.01 we observe that the chaotic flow state subsides and the flow rapidly approaches the stable lower branch. The top row of Fig. 3.13 shows several snapshots of micelle length after decreasing Pe, where we have defined $t = 0$ as the time when the reduced shear rate is implemented. In both $t = 5$ and $t = 10$ we see remnants of the 'interface'-like region amidst the elongated micelle streaks. As time progresses, the 'interface'-like region is no longer apparent and the flow splits into two 'wings' of elongated micelles that gradually thin as they rotate. This decay to the lower branch appears to follow some $m = 2$ dependence that is obscured by other modes present in the chaotic flow state. We expect that this flow will evolve to the lower branch, but the extremely sharp gradients here led to numerical difficulties that prevented us from continuing this simulation. We also investigated dropping a steady state on the upper branch directly to Pe = 0.01, which could potentially avoid any chaotic fluctuations that would obscure specific modes that develop in the decay to the lower branch. The bottom row of Fig. 3.13 shows several snapshots of micelle length for a drop from Pe = 0.025 to Pe = 0.01; we chose Pe = 0.025 as the initial condition rather than Pe = 0.04 so that the reduction in shear rate is less abrupt. In general, we observe very similar behavior to the previous case, but now at $t = 15$ we observe a structure developing that resembles an eight-spoke wheel; this structure

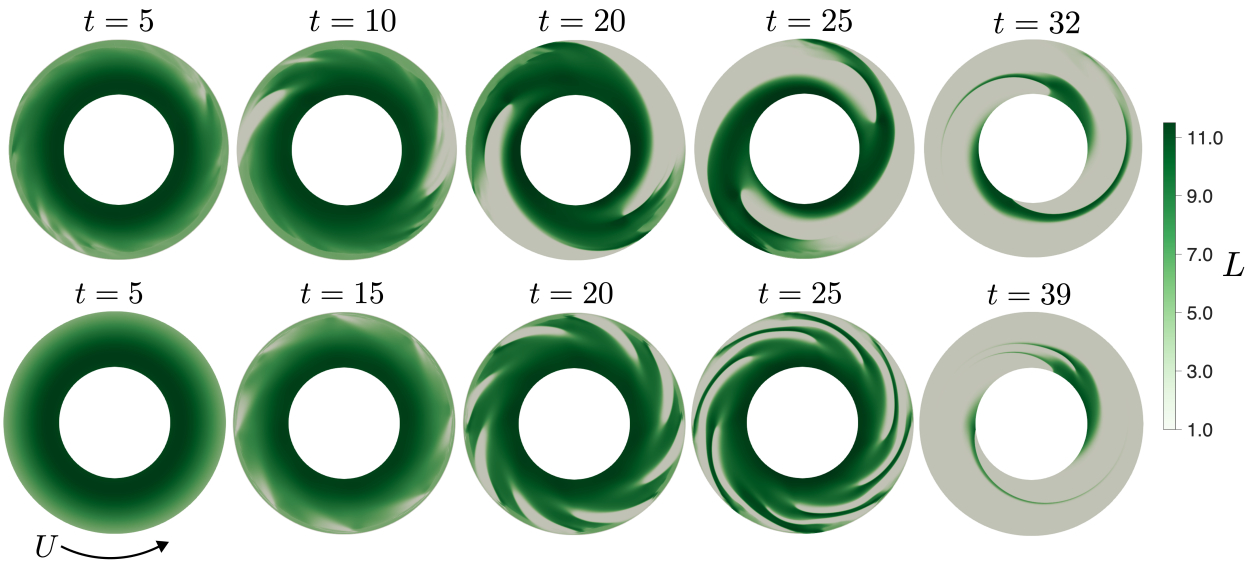


**Figure 3.13:** Top row: Snapshots of micelle length for decreasing shear flow from an applied shear rate of Pe = 0.015 to Pe = 0.01. Bottom row: Snapshots of micelle length for decreasing shear flow from an applied shear rate of Pe = 0.025 to Pe = 0.01.

becomes further resolved at $t = 20$, developing into a spiral-like structure with eight distinct branches. Once again it seems that the $m = 8$ mode is present in the development of this instability. The fact that the drop to Pe = 0.01 caused the flow to settle onto the stable lower branch but the drop to Pe = 0.015 led to chaotic fluctuations suggests that the extent or amount of the flow in the locally unstable region plays a role in the final dynamics of the instability.

### 3.4.3 Finger-like instabilities in 3D

In the final part of this work, we briefly investigate the structure of these finger-like instabilities in 3D. The radial and azimuthal elements of the geometry remain unchanged, but now we simulate a 3D domain with axial height $h = 0.2$ and impose periodic boundary conditions at $z = \pm h/2$. In all 3D simulations we use the M1 mesh for $r\theta$, but now have twenty grid points in $z$ for a total mesh density of $1.8 \times 10^6$ points. This height and number of grid points are admittedly low, but we find that they are suitable for beginning to characterize the structure of these instabilities in 3D. In particular, we will see that the initial 3D structure

that emerges has a wavelength that is much smaller than the height of the cylinder.

**Instabilities for increasing shear rates**

We begin as we did for the 2D scenarios, first by increasing the applied shear rate so that stress at the inner cylinder enters into the unstable middle branch region. Specifically, we take an isotropic solution at rest and apply a constant $\mathrm{Pe} = 0.0225$ that forces the solution into the unstable region. Again, the steady states for $\mathrm{Pe} = 0.0225$ are shown in Fig. 3.7; at steady state there will be no variation along $z$. Figures 3.14 and 3.15 show several $r\theta$ snapshots in time for the micelle length and radial velocity in start-up CCF with an applied shear rate of $\mathrm{Pe} = 0.0225$, where the top row corresponds the center of the cylinder, $z = 0$, and the bottom row corresponds to the top of the cylinder, $z = 0.1$. Figure 3.16 shows the snapshots of micelle length but in the $rz$-plane at $\theta = \pi$, where the inner cylinder is on the left and the outer cylinder is on the right. We can see from these snapshots that up until $t = 40$ the flow is independent of $z$. In fact, at $t = 40$ the flow structure and specifically the $m = 8$ mode that appears is nearly identical to that of the 2D geometry at the same time. A direct comparison of the flow structure at $t = 40$ and $r = R_1 + 0.1d$ for 2D (orange) and 3D (cyan) is shown in Fig. 3.26 in Appendix A; we can see that the micelle length profiles exhibit the same $m = 8$ mode. This once again suggests that the $m = 8$ mode is dominant in driving the flow instability observed here, even considering axial modes, and that at $h = 0.2$ $z$-dependence does not develop until firmly after the 2D instability in the $r\theta$-plane has been established. We can conclude that the flow instability that gives rise the the finger-like structures observed here is 2D in origin, and that 3D effects are secondary to this 2D instability.

At $t = 75$ we see that the slices in Fig. 3.14 now differ and the flow has developed an axial dependence. This $z$-dependence is confirmed by the variation along the vorticity axis in Fig. 3.16. Comparing to $t = 75$ in the 2D simulations (Fig. 3.8), it is clear that the structures in 3D do not retain the same symmetry that they do in 2D. This breaking of the symmetry

results from the presence of axially oriented stresses and flows, whereas in 2D all dynamics are confined to the $r\theta$-plane. The variations in $z$ are much more subtle in the radial velocity snapshots, though they are present; interestingly, at $t = 75$ the 8-mode, manifested as eight coupled inflow/outflow regions, is still quite evident.

Elaborating on the development of 3D structures, Fig. 3.17 shows surfaces of elongated micelles at three different times corresponding to regions of the domain where $L \geq 5$, indicating substantially elongated micelles. The outer surface at each time is bounded by $L = 5$, but even longer micelles are present in the region close to the inner cylinder. We chose these specific times because they show the transition from 2D to 3D structures. At $t = 40$, the structures exist as 2D sheets in $r\theta$ with no variation along $z$. As discussed in Section 3.4.2, these sheets attempt to grow outwards to the outer cylinder but are sheared azimuthally by the flow. At $t = 50$, the first variations along the vorticity axis begin to develop in the form of ripples along the sheet surfaces. These ripples appear to be somewhat sinusoidal in $z$, and although the exact wavelength is unclear, it is close to the thickness of the sheets that emerge from the 2D instability and smaller than the height of the cylinder. Finally, at $t = 60$ the sheets have broken up along $z$ into thread-like, or finger-like, structures, signaling the transition from 2D to 3D.

Altogether these observations emphasize that the flow instability is 2D in origin, and 3D effects arise secondarily to this 2D instability. Returning to Figs. 3.14 and 3.16, at $t = 100$ in we see that the flow has even greater variation along the vorticity axis and the finger-like structures have grown and begun to merge. Notably these finger-like structures closely resemble the finger-like structures observed in experiments. The regions of highly elongated and oriented micelles we observe here would scatter light quite differently than their isotropic and equilibrium-length counterparts, which would give rise to the variations in optics, turbidity, and birefringence observed in experiments.

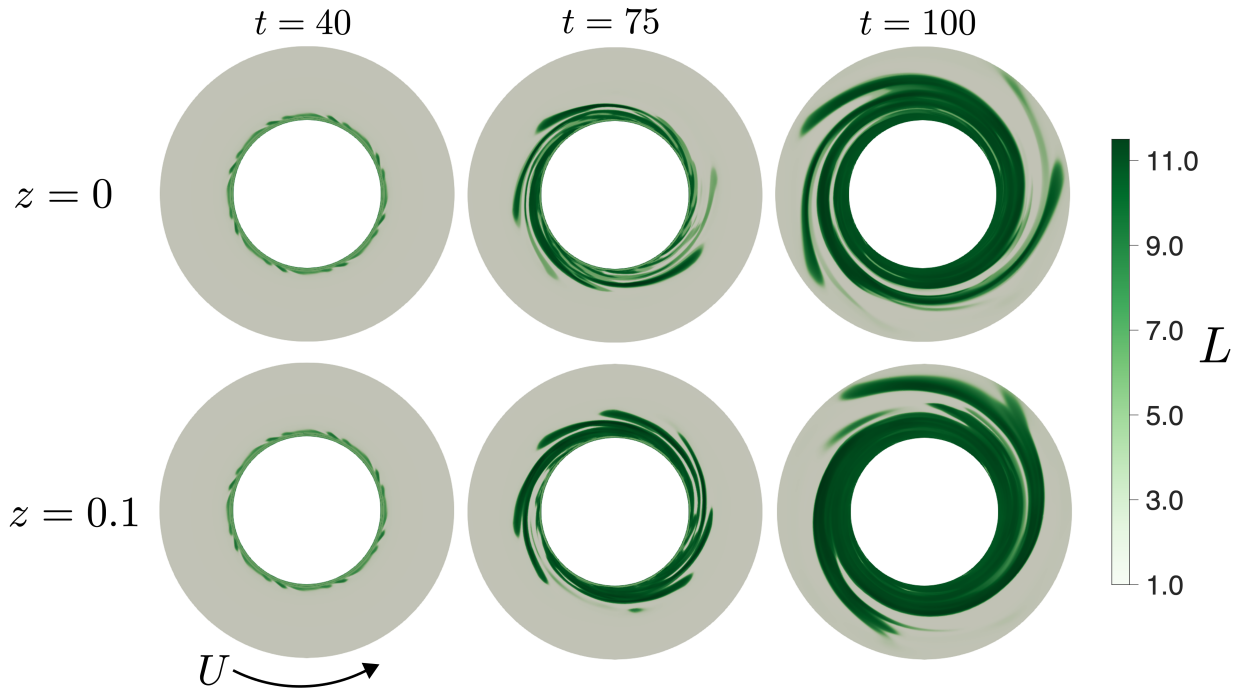


**Figure 3.14:** Snapshots of micelle length for increasing shear flow from rest to an applied shear rate of Pe = 0.0225 in a 3D domain with $R_I = 1$ and $h = 0.2$. Top: $r\theta$-slice at $z = 0$ and bottom: $r\theta$-slice at $z = 0.1$.

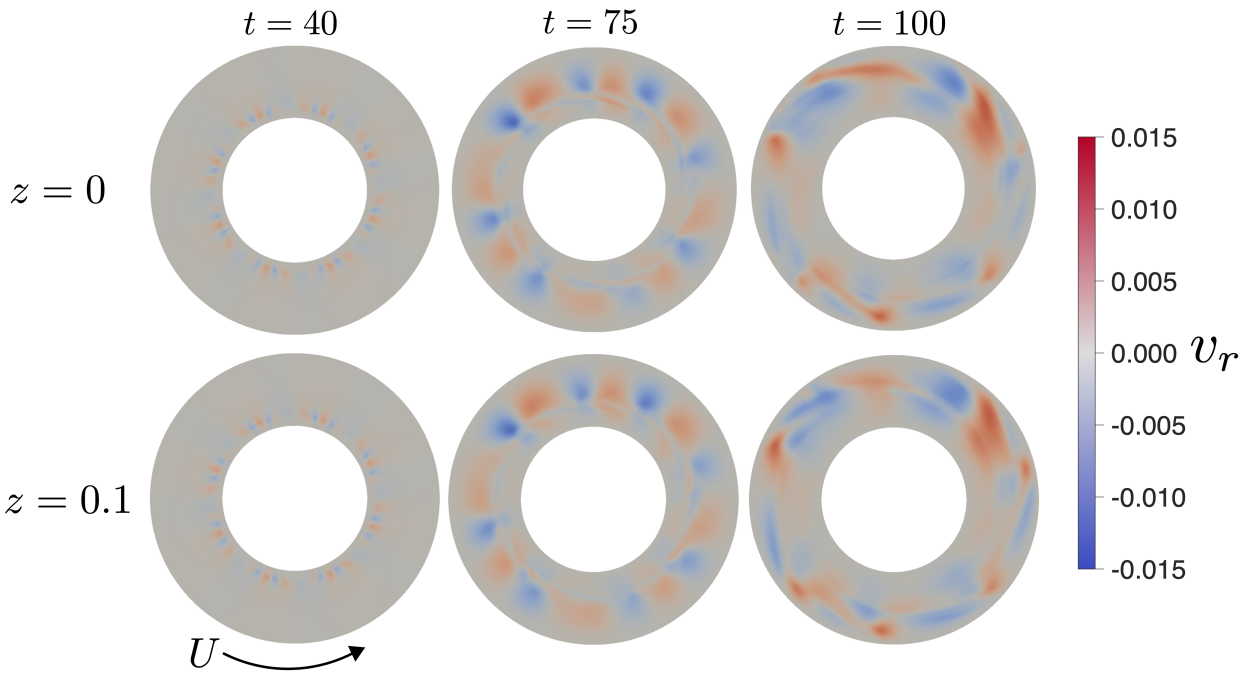


**Figure 3.15:** Snapshots of the radial velocity for increasing shear flow from rest to an applied shear rate of Pe = 0.0225 in a 3D domain with $R_I = 1$ and $h = 0.2$. Top: $r\theta$-slice at $z = 0$ and bottom: $r\theta$-slice at $z = 0.1$.

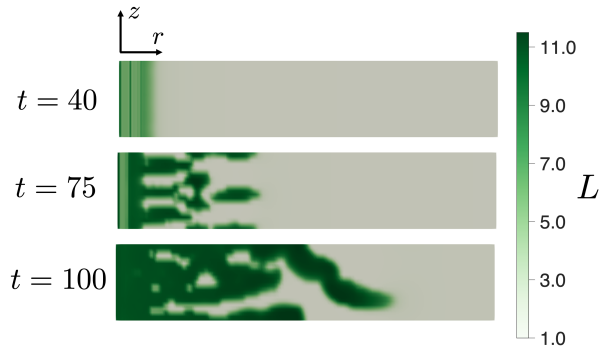


**Figure 3.16:** Snapshots of micelle length in the $rz$-plane at $\theta = \pi$ for increasing shear flow from rest to an applied shear rate of Pe $= 0.0225$ in a 3D domain with $R_I = 1$ and $h = 0.2$. The stationary inner cylinder is on the left and the rotating outer cylinder is on the right.

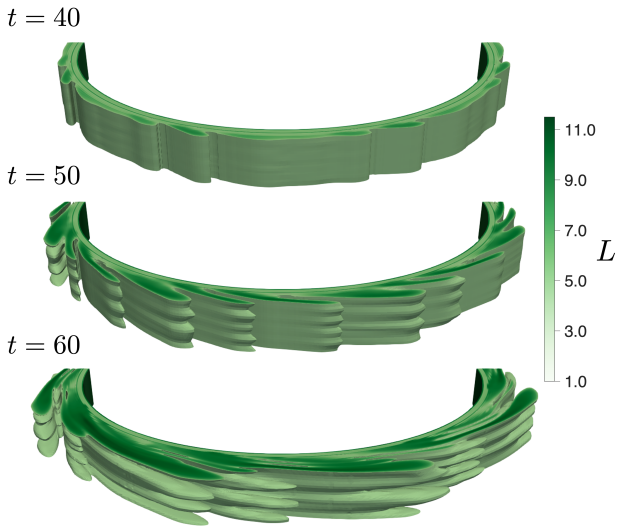


**Figure 3.17:** Structures of micelle length for increasing shear flow from rest to an applied shear rate of Pe $= 0.0225$ in a 3D domain with $R_I = 1$ and $h = 0.2$. Top: $t = 40$, middle: $t = 50$, and bottom: $t = 60$. Structures show regions of $L \geq 5$, indicating substantial micelle elongation.

**Instabilities for decreasing shear rates**

Finally, we again investigate decreasing the applied shear rate on the upper branch so that the stress at the outer cylinder falls into the unstable region, but now in 3D. We once again take a steady state at Pe = 0.04 and decrease to Pe = 0.015. In 2D, we observed that this reduction in shear rate transitioned the flow to a chaotic state characterized by branches of elongated micelles that extended towards the outer cylinder and were simultaneously sheared away by the flow. Figure 3.18 shows several $r\theta$ snapshots in time for the micelle length, where the top row corresponds the center of the cylinder, $z = 0$, and the bottom row corresponds to the top of the cylinder, $z = 0.1$. Figure 3.19 shows these snapshots but in the $rz$-plane at $\theta = \pi$, where the outer cylinder is on the right and the inner cylinder is on the left. The snapshots indicate that the behavior for this particular instability differs significantly between 2D and 3D. Comparing to Fig. 3.12, we see that the branches of elongated micelles are much longer in 3D than 2D; in fact, at $t = 300$ we see that a single branch stretches from nearly $\theta = \pi/2$ to $\theta = 3\pi/2$. Further, there are much fewer branches in 3D than we observed for 2D. A consequence of the fewer branches is that the 'interface'-like region is much more pronounced in 3D than 2D.

We also observe that there is significant variation along the vorticity axis. The $r\theta$ snapshots at both $t = 300$ and $t = 400$ for $z = 0$ show pronounced branching structures, while these same snapshots at $z = 0.1$ show minimal if any branching. The region of elongated micelles also spans further into the gap for $z = 0$. Looking at the $rz$ snapshots, we can see finger-like structures that appear fully grown around $t = 300$ and then proceed to fluctuate in time. We also are likely observing some small grid-scale artifacts in this geometry. However, we have run this exact simulation in a mesh with 50 grid points in $z$ and observed nearly identical structures. We were not able to run this simulation for as long as the 2D case, so we cannot say for certain whether this flow will eventually fall onto the lower branch where a stable steady state exists. However, we have observed that the structures shown at $t = 400$ persist with weak axial and radial fluctuations for nearly two-hundred time units,

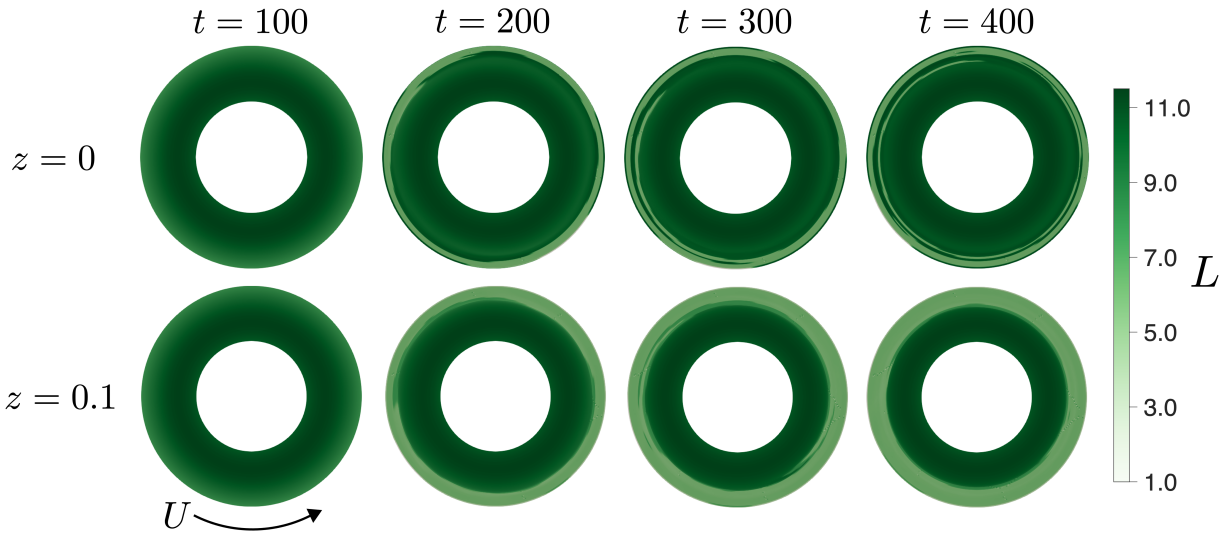


**Figure 3.18:** Snapshots of micelle length when decreasing the shear rate from Pe = 0.04 to Pe = 0.015 in a 3D domain with $R_I = 1$ and $h = 0.2$.

which suggests that like the 2D case the chaotic flow state here will persist indefinitely.

To summarize this section on finger-like instabilities, we found that forcing the stress into the unstable region of the constitutive curve provoked flow structures that very closely resemble observations of finger-like structures in experiments. Notably, the development of these structures requires a finite induction time, as in experiments, and the structures themselves are characterized by regions of elongated and anisotropic micelles that could cause the optical variations measured in experiments; similarly, these structures would produce

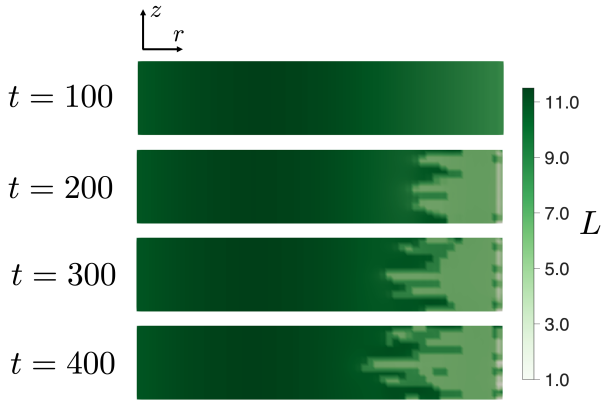


**Figure 3.19:** Snapshots of micelle length in the $rz$-plane at $\theta = \pi$ for decreasing the shear rate from Pe = 0.04 to Pe = 0.015 in a 3D domain with $R_I = 1$ and $h = 0.2$. The stationary inner cylinder is on the left and the rotating outer cylinder is on the right.

different SANS patterns, in agreement with experimental observations. We found that the location of the instability in the gap depends on the region that first enters into the middle branch; if the stress at the inner cylinder enters into the middle branch, the instability will originate at the inner cylinder. In both increasing and decreasing the shear rate into the unstable region, the azimuthal $m = 8$ mode appears; in 3D simulations the azimuthal instability precedes variations along the vorticity axis, indicating that the flow instability is 2D in nature.

### 3.4.4 Vorticity banding

In the final section of this work we briefly discuss vorticity banding in CCF of dilute wormlike micelle solutions. For solutions that display a reentrant constitutive curve, there is a region of shear rates in which two distinct steady state solutions can exist. As we saw for the $\epsilon = 1$ curve, for wide gaps it is likely that only one of the coexisting steady states will be stable because in systems with larger curvatures the range of the shear stress is often broad enough that part of the domain falls into the unstable region of the constitutive curve and is thus susceptible to finger-like instabilities as described above. For systems with lower curvature, however, the range of the local shear stress (and other local quantities) decreases so that the formation of vorticity bands becomes more favorable. Specifically, in Section 3.4.1 we showed that $\tau^T_{r\theta,O} = \tau^T_{r\theta,I}/(1+\epsilon)^2$ and thus as $\epsilon$ increases so does the difference between the stresses at the inner and outer cylinders. Figure 3.20 shows the same stability curve as Fig. 3.6, but now for $\epsilon = 0.1$. Comparing the two, it is clear that the range of applied Péclet numbers that yield two stable steady states is much larger for the lower curvature geometry. For example, consider $\mathrm{Pe} = 10^{-2}$. For $\epsilon = 1$ the lower branch steady state is stable but the upper branch steady state falls into the unstable region; for $\epsilon = 0.1$, however, both lower and upper branch steady states are stable. We can use this increased stability of lower curvature systems to construct a vorticity banded solution.

In experiments, vorticity banding typically arises in controlled-stress devices when the

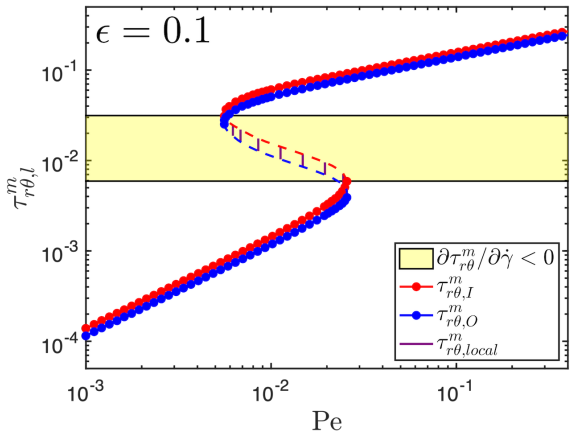


**Figure 3.20:** Steady state local micelle shear stress vs. applied Péclet number for $\epsilon = 0.1$. The red markers are the micelle shear stress at the inner cylinder, and the blue markers are the micelle shear stress at the outer cylinder. The dashed red and blue lines represent steady states that were not explicitly calculated. The purple vertical lines connecting the markers show the local micelle shear stress throughout the gap at that Pe. The yellow rectangle shows the region where, at a given Pe, the flow will fall into the locally unstable region.

applied stress corresponds to the unstable region of the constitutive curve. Applying a controlled-stress boundary condition computationally requires an integral condition that currently cannot be implemented in OpenFOAM; we are therefore limited to controlled-shear rate boundary conditions. It is also possible for vorticity banding to exist for controlled-shear rate conditions, however, an inhomogeneous flow profile will not naturally develop without some inhomogeneous perturbation or initial condition. Thus, although we cannot investigate the development of vorticity banding, we can investigate the dynamics and behavior once it manifests.

To construct a vorticity banded solution, we simply take an initial condition that is vorticity banded. Using the 3D mesh with $h = 1$ and $\epsilon = 0.1$, we construct an initial condition where half of the cylinder is on the upper branch ($z < 0$) and half is on the lower branch ($z > 0$) at an applied shear rate of $\mathrm{Pe} = 0.1$. For brevity we do not show the steady state profiles for each of these solutions, but note that at this Pe both steady states on the upper and lower branches are stable. We ran this vorticity banded state for a significantly long time and found that it is indeed a steady state solution. Figure 3.21 shows snapshots of the final (a) length, (b) $S_{r\theta}$, and (c) the azimuthal velocity where the rotating outer

cylinder is on the right. Figure 3.22 shows plots of these same quantities over the cylinder height at two different radial locations, orange: $r = R_I + 0.1d$ and cyan: $r = R_I + 0.5d$. For $\epsilon = 0.1$, these quantities are nearly independent of radius. We can clearly observe the vorticity banded solution, where the length and orientation are separated along the height of the cylinder into the lower and upper branch solutions.

We have also investigated the linear stability of the vorticity banded system. To accomplish this stability analysis, we applied random perturbations to the length and orientation of the micelles as well as the velocity field. In all cases we applied the perturbation to only one quantity (e.g., only the length and not the velocity or orientation), except for the case of the orientation tensor in which we randomly perturbed all components. We then tracked the perturbations over time to see if they grew, decayed, or stayed constant to determine the stability of the system. Figure 3.23 shows the deviation of these perturbations from steady state for (a) the length and (b) $S_{r\theta}$ over time after some small random perturbation to the vorticity banded steady state. We see that the perturbations die off very quickly and demonstrate exponential decay, indicating that vorticity banding is linear stable. The length exhibits an exponential decay with a slope of $k = -0.60$ at intermediate times. $S_{r\theta}$ shows a constant exponential decay with a slope of $k = -1.00$ for almost all times. For brevity we do not show the decay of the other orientation components or the velocity, but their decay also suggests linear stability. In future work we plan to perform rigorous linear stability analysis on this system to better characterize its stability.

It is important to note that the RRM-R does not include any translational diffusion and therefore the width of the bands as well as the location of the separation 'interface' does not change with time. Again, this is a single phase system so this is not a true interface. The inclusion of translational diffusivity would likely cause the width of these bands to vary with time; however, estimating the translational diffusivity of micelles using $D_{\|} = \frac{k_B T \ln(L/b)}{2\pi\eta_s L}$ [75], and assuming a micelle length of $L \sim \mathcal{O}(10\text{nm})$ and radius of $b \sim \mathcal{O}(1\text{nm})$ at room temperature, we obtain $D_{\|} \sim \mathcal{O}(10^{-11}\text{m}^2\text{s}^{-1})$, which is small enough that the timescale of

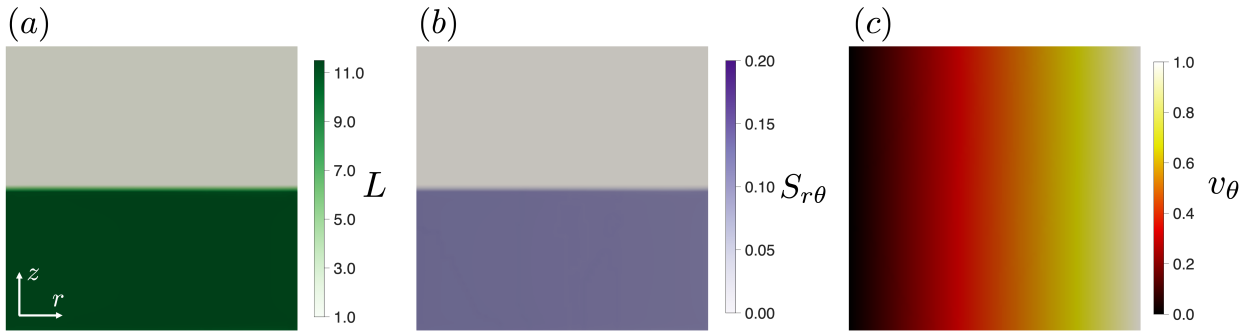


**Figure 3.21:** Snapshots of the final (a) length, (b) $S_{r\theta}$, and (c) azimuthal velocity for a vorticity banded initial condition. The curvature is $\epsilon = 0.1$, the height is $h = 1$, and the applied shear rate is $\mathrm{Pe} = 0.01$. The rotating outer cylinder is on the right.

any band variation would be extraordinary long relative to other timescales in this system. Indeed, we have added diffusive terms to the micelle length and orientation and found that the evolution of the width of the bands requires an unphysically large diffusion constant. Notably, though, for stress-controlled boundary conditions the inclusion of a diffusion term may be important for fully determining the solution state [147, 57]. In future work we plan to investigate the role of diffusivity and stress-controlled boundary conditions on vorticity banded systems. Finally, although the development of vorticity bands from a non-banded state is outside the scope of this work, it is worth mentioning that vorticity banding can be induced by applying perturbations to an initial condition that lies precisely on the unstable middle branch. However, because the RRM-R does not include translational diffusion, there is no mechanism for selection of band width [57], so the width of the bands that develop is determined by the details of the initial perturbation.

## 3.5 Conclusions

This study focuses on instability formation in circular Couette flow of dilute wormlike micelle solutions. We have used the reformulated reactive rod model (RRM-R), which models micelles as reactive Brownian rods, to simulate dilute WLM solutions that exhibit reentrant flow curves. We found that a reentrant flow curve, in which there is some range over which

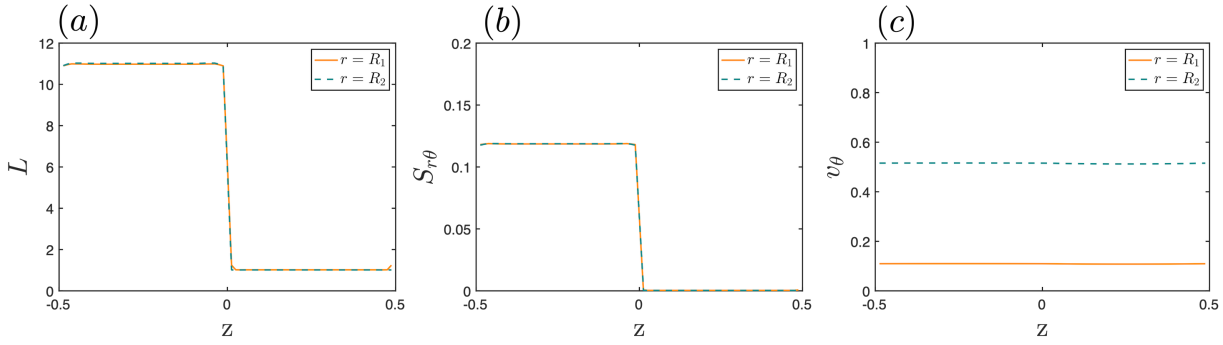


**Figure 3.22:** Plots of final (a) length, (b) $S_{r\theta}$, and (c) azimuthal velocity over the cylinder height at different radial locations for a vorticity banded initial condition. Orange: $r = R_I + 0.1d$ and cyan: $r = R_I + 0.5d$. The curvature is $\epsilon = 0.1$, the height is $h = 1$, and the applied shear rate is $\mathrm{Pe} = 0.01$.

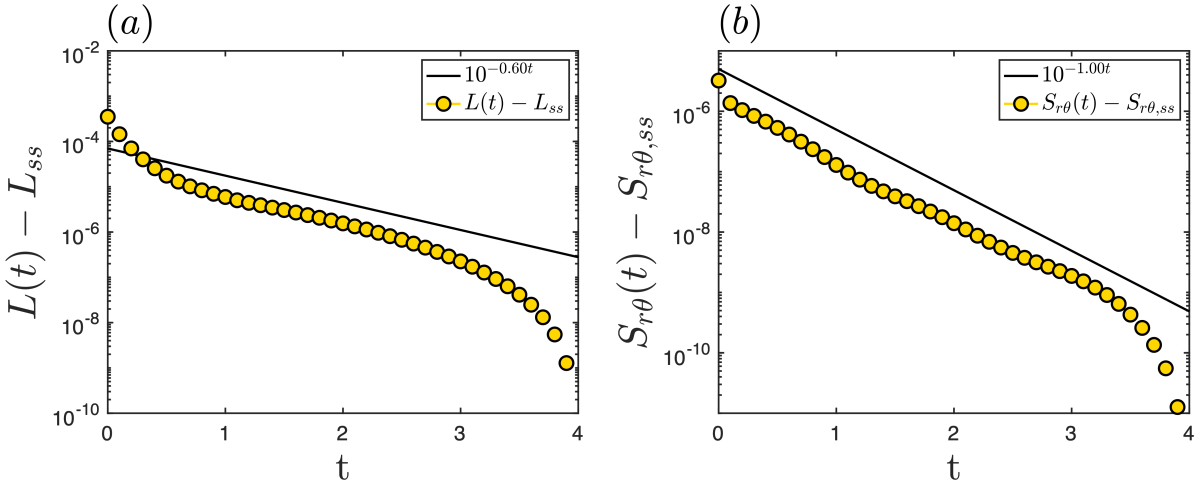


**Figure 3.23:** Plots of deviation from steady state values for (a) length and (b) $S_{r\theta}$ over time after some small random perturbation to a steady vorticity banded state with $\epsilon = 0.1$, $h = 1$, and $\mathrm{Pe} = 0.01$.

the shear stress is a multivalued function of shear rate, can provoke the development of finger-like instabilities. Specifically, we observed that the radial dependence of the shear stress in circular Couette flow allows for solutions where the domain spans both stable, $\partial\tau_{xy}/\partial\dot{\gamma} > 0$, and unstable, $\partial\tau_{xy}/\partial\dot{\gamma} < 0$, regions of the flow curve. We have found that this mixed local stability can lead to complex flow instabilities that originate in the parts of the domain existing in the unstable region of the flow curve, and that these instabilities manifest as finger-like structures comprised of elongated and anisotropically-oriented micelles.

Upon increasing the shear rate so that the shear stress at the inner cylinder entered into this unstable region, we found that 'fingers' or branches form towards the inner cylinder and expand outwards throughout the gap. For all the increasing shear rates tested we observed the presence of an $m = 8$ azimuthal mode in the flow profiles, and this appeared in both 2D and 3D simulations. Moreover, we found that the constitutive instability is 2D in nature and 3D variations are secondary effects. In 3D simulations, this instability manifested as sheet-like structures that were constant along the vorticity axis, and as the instability grew the sheets developed surface ripples that induced breakup into thread-like, or finger-like, structures. We also observed the $m = 8$ mode when decreasing the shear rate so that the stress at the outer cylinder fell into the unstable region. When decreasing the shear rate we found that if the shear rate is reduced to a value such that only a small portion of the local stress falls into the unstable region, the flow will exhibit chaotic fluctuations that persist indefinitely despite a stable steady state existing, indicating the coexistence of simple and complex states. As the shear rate is reduced further, the system rapidly decays to the stable steady state. Finally, we found for decreasing shear rate that the branching structures observed in 3D differ significantly from those in 2D; specifically, the 3D branches are much longer and extend for nearly a radian in the azimuthal direction.

In both cases of either decreasing or increasing the shear rate to force the stress into the unstable region, we found that the branching structures that develop very closely resemble the finger-like structures that have been observed in experiments. Moreover, these branches

grow and retract in a manner that is consistent with experimental observations. These branches consist of highly elongated and oriented micelles that would scatter light differently than isotropic, equilibrium-length rods, giving rise to the various optical differences observed in experiments that show these finger-like structures. To the best of our knowledge, this study is the first computational observation of these finger-like instabilities.

We have also found that the RRM-R can capture vorticity banding, and this banding is only observed in regions where two stable steady states coexist at the same applied Péclet number. A consequence of this fact is that vorticity banding is more readily formed in geometries with lower curvatures since there is a broader range of applied shear rates that can give rise to two coexisting stable steady states. As the curvature of the geometry increases the multivalued stability range decreases. We have also investigated the linear stability of the vorticity banded state through the application of small, random perturbations; in all cases we found that the perturbations die off relatively quickly with some exponential decay, indicating that the vorticity banded state is linearly stable.

## 3.6 Appendix A: Additional figures for CCF

Figure 3.24 shows the same plots as Fig. 3.4 but now for Pe = 0.0225. The inset in (d) shows a close-up of the micelle length. The observations for this Pe are very similar to the previous case of Pe = 0.01. In (d) we see that for all curvatures on the upper branch micelles are nearly at the maximum degree of elongation throughout the entire gap. On the lower branch micelles are nearly completely at the equilibrium length, however, we see from the inset of (d) that for $\epsilon = 1$ the micelles grow very rapidly close to the inner cylinder where the flow is just beginning to enter the middle branch region. In (c) we see that the micelle shear stress at the inner cylinder increases with increasing curvature and this actually causes the micelle stress for $\epsilon = 1$ on the lower branch to enter into the middle region. Specifically, the transition from the lower branch into the unstable middle region occurs at the inner

cylinder, whereas for Pe = 0.01 it occurred at the outer cylinder. We then expect, and we actually see in this work, the instability at this Pe to originate close to the inner cylinder.

Figure 3.25 shows a comparison of the micelle length over $\theta$ at $t = 40$ and $r = R_I + 0.1d$ for the M2 and M3 meshes in start-up of steady shear flow with an applied shear rate of Pe = 0.0225 in a 2D geometry. The orange line corresponds to the M2 mesh and the cyan to the M3 mesh. The similarity of the profiles indicates that the $m = 8$ mode we observe does not depend on mesh resolution.

Figure 3.26 shows a similar profile to Fig. 3.25 but is now comparing the instability in 2D and 3D. Specifically this figures shows the micelle length over $\theta$ at $t = 40$ and $r = R_I + 0.1d$ for start-up of steady shear flow with an applied shear rate of Pe = 0.0225 in 2D (orange) and 3D (cyan). The 3D slice is taken at $z = 0$, but the flow here shows no $z$-dependence. We can clearly see that the initial instability is 2D in nature and that the azimuthal instability dominates any axial instabilities.

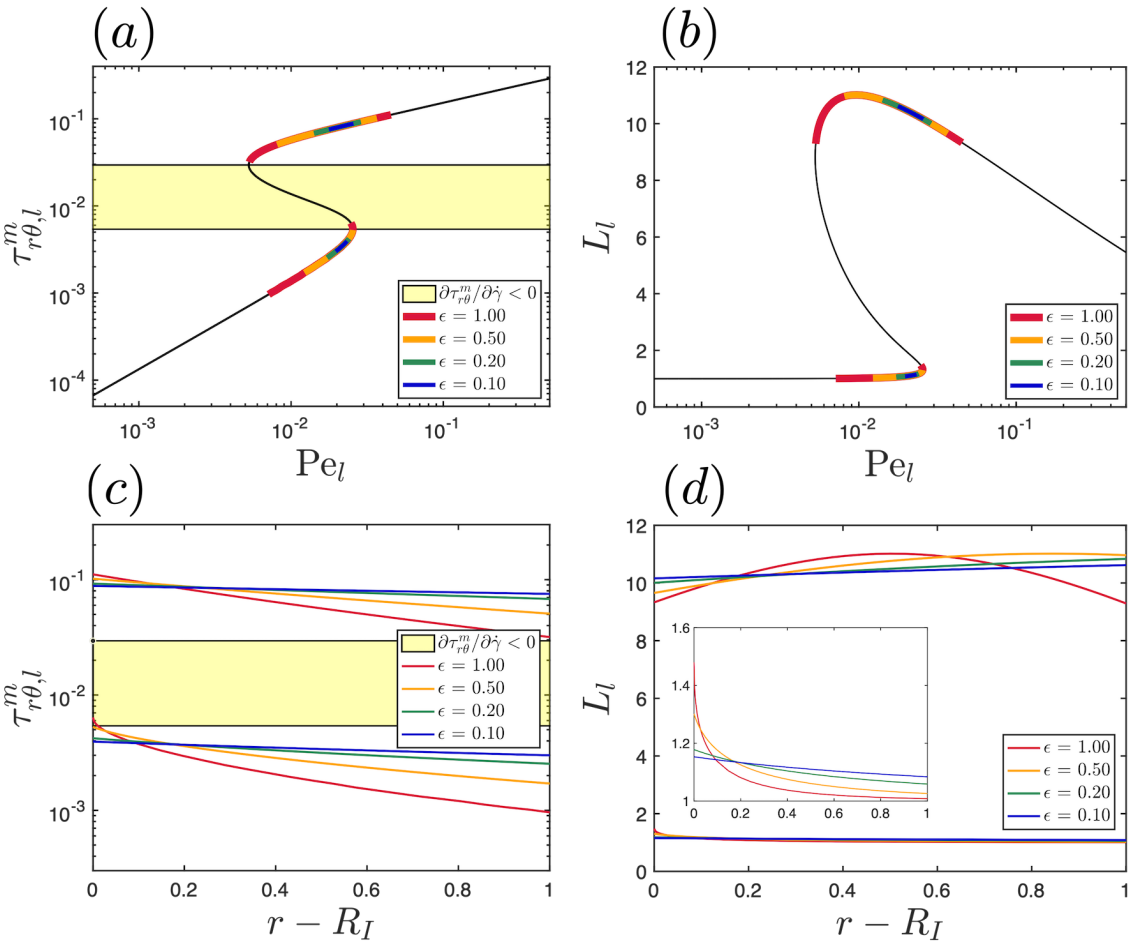


**Figure 3.24:** Upper and lower branch steady states for Pe = 0.0225 at varying curvatures. (a) Local micelle shear stress and (b) local micelle length projected onto the governing constitutive curves, where the local Péclet number, $\mathrm{Pe}_l$, is calculated from the velocity profile throughout the gap. (c) Local micelle shear stress and (d) local micelle length over the gap radius. Line colors are red: $\epsilon = 1.00$, orange: $\epsilon = 0.50$, green: $\epsilon = 0.20$, and blue: $\epsilon = 0.10$. The yellow rectangle indicates the unstable region of the flow curve ($\partial\tau^m_{r\theta}/\partial\dot{\gamma} < 0$).

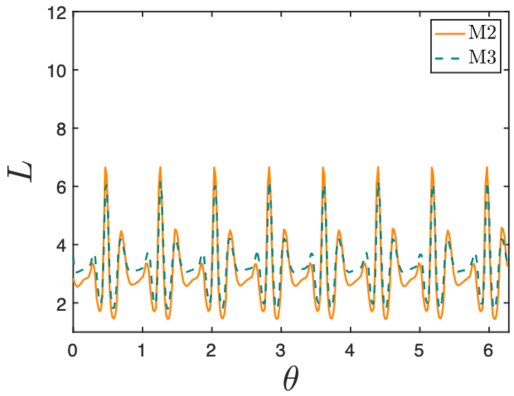


**Figure 3.25:** Plot of micelle length over $\theta$ at $t = 40$ and $r = R_I + 0.1d$ for start-up of steady shear flow with an applied shear rate of Pe = 0.0225. The orange line corresponds to the M2 mesh and the cyan to the M3 mesh.

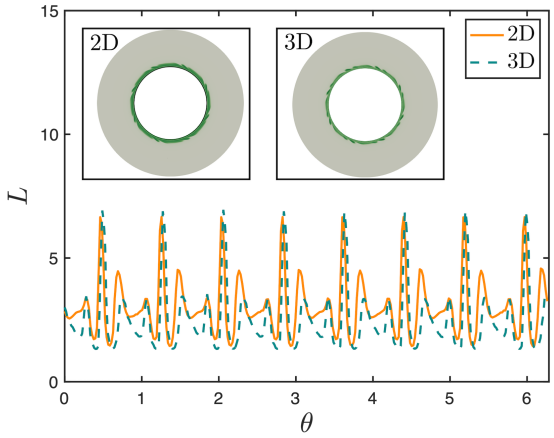


**Figure 3.26:** Micelle length over $\theta$ at $t = 40$ and $r = R_I + 0.1d$ for start-up of steady shear flow with an applied shear rate of $\mathrm{Pe} = 0.0225$ in 2D (orange) and 3D (cyan). The 3D slice is taken at $z = 0$, but the flow here shows no $z$-dependence.

# 4

# Interfacial instabilities in plane Poiseuille flow

In this work, we use computational fluid dynamics simulations to investigate flow instabilities in plane Poiseuille flow of dilute wormlike micelle solutions. Using the reformulated reactive rod model (RRM-R) (Hommel and Graham, 2021), which treats micelles as rigid Brownian rods undergoing reversible scission and fusion in flow, we study the development and behavior of interfacial flow instabilities. In particular, we focus on solutions that exhibit a reentrant constitutive curve, in which there exists some region where the shear stress is a multivalued function of shear rate, and show that the spatial-dependence of the shear stress in plane Poiseuille flow allows for solutions that can 'jump' between stable branches of the constitutive curve. This jumping leads to the development of 'interfaces' separating regions of highly elongated, anisotropically-oriented micelles and regions of near-equilibrium length, isotropic micelles. This separation exhibits strong resemblance to three-layer viscosity-stratified flows, as does the resulting interfacial instability. We find that these interfaces are destabilized by viscosity mismatch and a jump in normal stresses across the interfaces, giving rise to structures that resemble 'fingers' of elongated micelles. We find that the instability structures show both short- and longwave forms, where the longwave forms give rise to mushroom patterns resembling those seen in core-annular channel flow of Newtonian fluids. Finally,

we find that the initial instability is 2D in nature and that 3D variations arise as secondary effects.

## 4.1 Introduction

Surfactants are amphiphilic molecules consisting of hydrophilic head groups bonded to long hydrophobic tails; when dissolved in water at some concentration above the critical micelle concentration (CMC), surfactants self-assemble into larger aggregate structures. The geometry of these structures depends on the size, shape, and chemistry of the surfactant molecules as well as the temperature and salinity of the solution [40, 106, 45, 54]. These aggregate structures can take the form of spherical or rodlike micelles, as well as bilayers. In this work we are interested in wormlike (or rodlike) micelles, which can display a large range of varied structure and behavior depending on the concentration regime. In the dilute regime, wormlike micelles (WLMs) exist as nearly rigid rods with persistence lengths in the range of $\sim \mathcal{O}(10 - 100\text{nm})$ and contour lengths on a similar scale [61, 125, 59, 60, 5]. In the concentrated regime, WLMs can grow far beyond their persistence lengths to form entangled networks and branched structures, transitioning the solution into a highly viscoelastic gel-like phase [126]. In intermediate semi-dilute regimes, the behavior of WLMs can mimic that of either dilute or concentrated systems depending on the applied flow or forcing.

Wormlike micelles are found in a wide variety of commercial and industrial settings. In commercial products micelles are commonly used in detergents, coatings, and emulsifiers, and in industrial processes they have been used as environmentally friendly carrier fluids for oil recovery operations [14] and as drag-reducing agents in closed-loop heating and cooling systems [17, 18]. The drag-reducing capabilities of WLM solutions make them of great practical interest and importance. In fact, WLM solutions have been shown to provide up to an 80% reduction in turbulent drag, which is comparable to the drag-reducing capabilities of widely used polymer solutions [109, 1, 2]. Additionally, WLMs are self-assembling and

thus can overcome the mechanical degradation that plagues polymer solutions. Despite these benefits, the adoption of WLMs as drag-reducing agents has been limited, remaining mostly confined to areas of Japan [17, 18]. This limitation partially stems from chemical considerations regarding the amphiphilic nature of surfactants, specifically that changing the solvent can affect the aggregation and structuring of these molecules [127, 128]; another part of this limitation stems from the fact that the behavior and dynamics of these fluids in complex flows, and specifically the development of instabilities in these flows, is not well understood. In this work, we aim to expand understanding of flow instabilities in dilute WLM solutions and elucidate the mechanisms underlying these instabilities.

Throughout this work we will focus exclusively on wormlike micelles in the dilute to semi-dilute regime. Wormlike micelle solutions in this regime are known to undergo both shear-thickening and shear-thinning, where thickening occurs at moderate shear rates followed by thinning at higher shear rates [9, 10, 11, 12, 13, 62, 61]. This thickening and thinning behavior is related to the formation and subsequent breakdown of flow-induced structure (FIS) that takes the form of elongated and aligned micelles. Specifically, at moderate shear rates WLMs have been observed to align with the flow and undergo significant elongation, whereby the average length of micelles in solution can increase to several times the equilibrium length. This elongation has been observed experimentally by Keller and coworkers using free-fracture electron microscopy [46]. Moreover, while a direct measurement of micelle length in flow is challenging, some researchers have made estimates of the micelle length by analyzing the effect of flow on the solution viscosity. Prud'homme and Warr related the critical strain rate, the strain at which the extensional viscosity is maximized, in an opposed jet device to the length of micelles by assuming that the micelle relaxation time was solely due to scission kinetics [63]. By approximating the tension along the micelle body and assuming an upper bound on the micelle scission energy, they directly related the critical strain rate to the micelle length. Through this analysis and by comparing to the mean micelle length at zero shear rate, the authors determined that micelles were significantly elongated by the

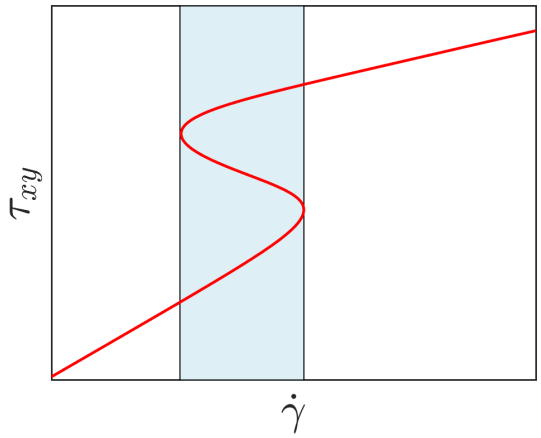


**Figure 4.1:** (Reproduced from Section 3.1) Example of a reentrant flow curve in which there is a region where the shear stress, $\tau_{xy}$, is a multivalued function of the shear rate, $\dot{\gamma}$. The light blue area shows the reentrant region of the flow curve.

extensional flow field. Similarly, Omidvar and coworkers used an asymptotic analysis of the FENE-P model to relate the extensional viscosity of the micelle solution to the micelle length [64]. By assuming that the micelle length could be related to the FENE-P extensibility parameter, they were able to relate increases in the extensional viscosity to elongation of the micelle lengths, finding significant elongation of the micelles by the flow field.

These solutions are also well-known for displaying a reentrant, or multivalued, flow curve (see Fig. 4.1) whereby the shear stress becomes a multivalued function of shear rate over some typically small range [129, 69, 50]. The presence of a reentrant flow curve is a necessary condition for the development of a vorticity banding instability [50]; this instability is a relatively uncommon phenomenon, but has been observed in charged colloidal suspensions, rodlike colloids, onion surfactants, biphasic polymer blends, and of course dilute WLM solutions [65, 66, 52, 67, 50, 68]. In circular Couette flow (CCF), this instability manifests as stacked "bands" along the vorticity axis, where adjacent bands support distinct shear stresses but equivalent shear rates; these bands can often be visualized by differences in turbidity and birefringence [47, 50]. In our previous work we showed that in narrow-gap circular Couette flow a reentrant flow curve can support two coexisting stable steady states, one on each stable branch of the multivalued flow curve, which can give rise to vorticity banding [148]. The curvature of the circular Couette domain must remain small so that the stress variation

within each steady state is minimized, thus preventing the local stress profiles from entering the unstable regions of the flow curve. Vorticity banding is related to, but distinct from, the more well-studied shear banding instability where shear rate is a multivalued function of shear stress. There has been extensive theoretical and experimental treatment of this instability (see [47, 57] for comprehensive reviews).

In addition to vorticity banding, dilute WLM solutions have demonstrated a group of finger-like instabilities in circular Couette flow that appear as unstructured streaks and branches spanning the flow gap [69, 70]. Using a circular Couette device, Liu and Pine [4] observed these finger-like structures in controlled-shear rate flows of $\sim \mathcal{O}(10^2 - 10^3)$ ppm equilmolar CTAB/NaSal solutions; using small angle light scattering (SALS), they revealed reversible finger-like structures that, upon increasing shear rate, grew outwards from the inner cylinder into the flow gap. The authors observed that 'fingers' repeatedly grew until they reached the outer cylinder before retracting towards the center of the cell and beginning to grow again. Hu and coworkers [71] observed similar structures in a solution of equimolar 7.5 mM TTAA/NaSal that exhibited a reentrant flow curve. Similar to Liu and Pine, the authors observed that increasing either the shear rate or shear stress beyond some critical value induced shear-thickened structures that originated at the inner cylinder and grew outwards to fill the gap. The behavior of these structures was also found to differ between stress-controlled and shear-rate controlled experiments.

In our previous work [148], we used the reformulated reactive rod model (RRM-R) to investigate these finger-like instabilities from a computational perspective. The RRM-R, which treats dilute wormlike micelle solutions as suspensions of reactive Brownian rods, is both tractable and able to predict a reentrant flow curve, making it well-suited for implementation in computational fluid dynamics (CFD) simulations. By combining simulations of the RRM-R with theoretical analysis by Yerushalmi and coworkers [56], it was shown that finger-like instabilities can develop when the micelle stress is pushed into the unstable region of the flow curve. The work by Yerushalmi et al. looked at simple shear flow between

parallel plates, with velocity field $v_x = \dot{\gamma} y$, and found that the flow is linearly unstable to 1D ($y$-dependent) perturbations if $\partial \tau_{xy} / \partial \dot{\gamma} < 0$. Their analysis did not distinguish between nonmonotonic and reentrant flow curves; it depends only on the local slope of the flow curve, not the global behavior. In this and the previous work, “unstable" and “stable" regions of the flow curve are defined in the sense of this analysis. The actual nature of flow instabilities of a fluid that can display $\partial \tau_{xy} / \partial \dot{\gamma} < 0$ in simple shear depends on the global nature of both the constitutive behavior and flow geometry. Applying this analysis to the reentrant flow curves observed in dilute wormlike micelle solutions, Fig. 4.1, we see that the stable upper and lower branches of the curve are separated by an unstable middle branch.

Our previous work focused on investigating instabilities of dilute wormlike micelle solutions in circular Couette flow using CFD simulations of the RRM-R combined with the stability analysis by Yerushalmi and coworkers [56]. The simulations were performed by first developing a library for the RRM-R in the open-source software OpenFOAM coupled with the viscoelastic solver RheoTool developed by Pimenta and Alves [143, 144, 145]. Using these simulations, in addition to stability analysis of the steady states, we showed the RRM-R was able to capture finger-like instabilities in CCF. Notably it was found that a reentrant flow curve, and specifically a region where $\partial \tau_{xy} / \partial \dot{\gamma} < 0$, is a necessary condition for the development of finger-like instabilities. In CCF, the shear stress exhibits a radial dependence which can give rise to solutions where the domain spans both stable, $\partial \tau_{xy} / \partial \dot{\gamma} > 0$, and unstable, $\partial \tau_{xy} / \partial \dot{\gamma} < 0$, regions of the flow curve. This mixed local stability can lead to complex flow instabilities that originate in the parts of the domain existing in the unstable region of the flow curve, and that these instabilities manifest as finger-like structures comprised of elongated and anisotropically-oriented micelles. Additionally it was found that these ‘fingers’ grow and retract in a manner that is consistent with experimental observations; moreover, the high elongation and anisotropy of micelles in branches would scatter light differently than isotropic, equilibrium-length rods, giving rise to the various optical differences observed in experiments that show these finger-like structures. It was also observed that the initial

instability in CCF was 2D ($r\theta$) in nature, and that 3D variations arose as secondary effects.

To the best of our knowledge that have been no experimental or computational observations of finger-like structures in pressure-driven channel or pipe flows of dilute wormlike micelle solutions. There has, however, been work studying instabilities in concentrated WLM solutions in pressure-driven flows. These works tend to look at the development and stability of shear banding WLM solutions, particularly the stability of the interface separating high and low shear rate bands. Nghe and coworkers [149] investigated shear banding WLM solutions in planar channel flow and found an interfacial instability associated with velocity modulations along the vorticity axis. They also performed linear stability analysis of the diffusive Johnson-Segalman model and found unstable modes in the vorticity direction, which agreed with the experimental observations; they also found that the instability was driven by a normal stress jump across the interface. Similarly, Yamamoto and coworkers [150] investigated pipe flow of a shear banding WLM solution and observed an unstable transition at high flow rates in which the plug-like velocity profile began to exhibit turbidity in the near-wall high shear rate regions. The authors also coupled experiments to numerical simulations of the modified Bautista-Manero model [98]; although numerical simulations showed reasonable agreement with steady state predictions, the model was unable to predict unstable behavior.

Cromer and coworkers [151] have also investigated pressure-driven channel flows of concentrated WLM solutions that show shear banding using the VCM model. The authors observed the formation of a slip layer at the walls that depends linearly on the driving pressure force. They also found that above a critical pressure drop the flow exhibits an inhomogeneous, shear banding profile. This inhomogeneous flow is characterized by a flat, plug-like region at the channel center connected to high shear rate bands towards either wall, where the bands are connected by a small interfacial region whose width scales as the square of the micelle diffusivity. After the onset of shear banding, increasing the pressure further causes the velocity to decrease and become significantly more flattened. In a follow-up work

these authors performed linear stability analysis on the VCM equations and found an interfacial instability in the streamwise direction that could be suppressed by sufficiently large diffusivities [152].

As for dilute WLM solutions, although there has not been much work looking at pressure-driven channel or pipe flows, there has been work studying these solutions in cross-slot flows. Dubash and coworkers [72] investigated different concentrations of CTAB/NaSal solutions that spanned the dilute (shear-thickening and -thinning) to concentrated (purely shear-thinning) regimes in a microfluidic cross-slot device. The WLM solutions they investigated did not display reentrant flow curves and they did not observe any finger-like instabilities, however, they did observe the development of unsteady flow and a faint birefringent band along the outflow channels. In concentrated solutions the symmetric flow first transitioned to a steady asymmetric flow pattern with lip vortices along the walls of the inlet channel as the flow rate (e.g., extension rate) was increased. As the flow rate was increased further, the flow showed slight 'pulsing' unsteadiness which then became fully unsteady upon increasing the flow rate further. In dilute solutions, the asymmetric instability was bypassed and the flow immediately transitioned from steady to unsteady upon increasing the flow rate. The extension rates where the flow became unsteady corresponded to regions of the flow curve that showed shear-thickening and -thinning. The authors concluded that this instability is elastically driven because it developed at Reynolds numbers below the critical value for instabilities in Newtonian fluids. Cross-slot flows differ from channel flows in that they are extension-dominated rather than shear-dominated, and thus the instabilities that develop in each are likely different. However, understanding cross-slot flows is still useful for studying channel flows because of flow behavior that develops along the inlet and outlet regions as these are shear-dominated.

Returning to finger-like instabilities, similar structures have been observed to develop from interfacial instabilities in polymer solutions. Wilson and Khomami found that the destabilization of interfaces in polymer melts is strongly related to a jump in the first normal

stress difference across the interface [137, 138, 139]. Moreover, as these interfacial instabilities develop they appear as waves that are bent and elongated by large shearing stresses; in the case of compatible polymers threads (also called 'pools') of material are actually pulled off the wave to yield finger-like structures that closely resemble the 'fingers' observed in dilute WLM solution instabilities. Yamani and coworkers [140] have observed similar thread-like structures in their investigation of the flow of a planar jet of dilute polymer solution into a water tank. In their study, viscoelastic threads appeared to be sheared off of the main jet column.

In the case of dilute wormlike micelle solutions, interface-like regions can manifest between domains of short, isotropically oriented micelles and elongated, highly oriented micelles. This interface-like region arises due to the large jump in stress, length, and viscosity around the bend of a reentrant flow curve. In fact, increasing the the shear rate only slightly can cause these properties to increase by over an order of magnitude [42], which in channel flow can begin to resemble viscosity-stratified flows [153]. Flows with viscosity stratification in channel flow typically consist of two or more layers of miscible fluids with different viscosities (e.g, silicone-water); core-annular channel flow refers to geometries where three layers are arranged such that fluid A is close to either wall and fluid B is along the center. Depending on the differences in viscosity, the resulting velocity profiles can show quite dramatic deviations from the parabolic profile observed in pressure-driven flow of Newtonian fluids [154].

There has been extensive research into the stability of stratified flows [154, 153, 155, 156, 157]. Interfacial instabilities in stratified flows are often driven by gradients in viscosity perturbations along the wall-normal direction [155]; viscosity mismatch leads to perturbation vorticity mismatch at the interface that has a destabilizing effect by amplifying the crests and valleys of the interface [154, 158, 156]. Both diffusive and inertial forces also drive destabilization [154], and purely elastic interfacial instabilities are driven by a coupling between the perturbation velocity and a jump in normal stresses across the interface [156]. The structure of interfacial instabilities in stratified flows can vary, but typically takes on an undulating

wave-like appearance where wave crests are dulled or sharpened based on the fluid viscosities [153]. There has also been observations by d'Olce and coworkers [159, 157] showing the formation of 'pearl' and 'mushroom' instability patterns arising from interfacial instabilities of miscible viscosity-stratified fluids. Pearls have a beads-on-string appearance, characterized by long threads with intermittent ellipsoidal or spherical drops spaced at irregular intervals; mushrooms occur as the pearls begin to intersect one another and are characterized by a wide 'mushroom cap' pointed along the streamwise direction that is sheared backward towards a thinner 'mushroom stem.'

In this work, we investigate instability formation in plane Poiseuille flow (PPF) using the reformulated reactive rod model (RRM-R) [129]. The RRM-R, and its predecessor the RRM [3], model wormlike micelles as reactive Brownian rods undergoing reversible scission and fusion in flow. The model couples evolution equations for the ensemble average orientation of rods and micelle contribution to the solution stress to an evolution equation for the collective length of micelles, where micelle number density and length are constrained by conservation of surfactant molecules. The evolution equation governing micelle length in the RRM-R, which was inspired by work by Turner and Cates [73], accounts for two forms of micelle fusion: spontaneous and flow-induced, as well as two forms of micelle scission: spontaneous and tension-induced. More details on the modeling framework of the RRM-R are provided in Section 4.2. Using this framework, the RRM-R can capture both shear-thickening and -thinning, flow-induced structure formation, nonzero normal stress differences, and importantly a reentrant flow curve. We have shown in previous work that the RRM-R can be suitably fit to experimental measurements of dilute WLM solution rheology and can be used to study instabilities that arise due to a reentrant flow curve in CFD simulations [129, 148].

## 4.2 Governing equations

The aim of the present study is to investigate instabilities of dilute wormlike micelle solutions in plane Poiseuille flow. Specifically, we are interested in exploring regimes where the underlying constitutive curve is reentrant as this region of state space is currently poorly understood and can give rise to interesting instabilities. In our previous work [148], we showed that a reentrant flow curve can give rise to finger-like instabilities in circular Couette flow due to the spatial variation of the shear stress and shear rate throughout the flow gap. In the present work, we wish to expand these results to PPF, which also has a shear stress and shear rate that vary spatially along the wall-normal direction. To carry out our analysis we use the RRM-R (reactive rod model - reformulated), which models dilute WLM solutions as suspensions of reactive Brownian rods undergoing reversible scission and growth in flow. The RRM-R has shown qualitative agreement with experimental data of dilute WLM solutions in simple shear and purely extensional flows under both steady state and transient conditions.

The complete derivation of the RRM-R is described in [129] but is summarized below. We note that this modeling framework takes inspiration from theoretical treatments by Cates and Turner [110]. In the RRM-R, dilute wormlike micelle solutions are treated as suspensions of rigid Brownian rods undergoing reversible scission and fusion. Rods can fuse end-to-end (reducing the energetic penalty associated with the micellar end caps), but only when they are highly aligned – otherwise the energy penalty arising from forming a long but bent micelle is too large for fusion to take place [15, 110]. The application of flow tends to align the rods. This alignment is balanced by rotational diffusivity of the rods acting to return the suspension to isotropy. Consequently, a positive feedback mechanism exists between rod growth and alignment owing to the smaller rotational diffusivity of longer rods. It is assumed that rod growth is countered by hydrodynamic stresses acting along the lengths of the rods, which induce breakage events into shorter rods. Moreover, rods can undergo both spontaneous scission and spontaneous fusion events.

### 4.2.1 Brownian rods

Starting with a suspension of (non-reactive) Brownian rods, consider a uniform collection of rods with length $L_0$, radius $b$, and number density $n_0$ suspended in a Newtonian solvent with viscosity $\eta_s$. The orientation of a single rod is described by the unit director vector $\boldsymbol{u}$. The solution is subjected to an arbitrary flow with local velocity $\boldsymbol{v}$ and transpose velocity gradient $\boldsymbol{K} = \boldsymbol{\nabla v}^\top$. The orientation tensor $\boldsymbol{S}$ describes the average collective orientation of the suspension and is given by the second moment of $\boldsymbol{u}$

$$\boldsymbol{S} = \langle \boldsymbol{uu} \rangle = \int \boldsymbol{uu} \psi \mathrm{d}\boldsymbol{u}, \tag{4.1}$$

where $\psi$ is the probability distribution function of $\boldsymbol{u}$. The time evolution of $\boldsymbol{S}$ in flow is

$$\frac{\mathrm{D}\boldsymbol{S}}{\mathrm{D}t} = -6D_{r,0}\left(\boldsymbol{S} - \frac{1}{3}\boldsymbol{I}\right) + \boldsymbol{K}\cdot\boldsymbol{S}^\top + \boldsymbol{S}\cdot\boldsymbol{K}^\top - 2\boldsymbol{K} : \langle \boldsymbol{uuuu} \rangle, \tag{4.2}$$

where $D_{r,0}$ is the rotational diffusion coefficient of a rod, $\boldsymbol{I}$ is the unit tensor, and the double dot product is defined as $\boldsymbol{A} : \boldsymbol{B} = \mathrm{Tr}(\boldsymbol{A}\cdot\boldsymbol{B}^\top)$ [75].

The total stress of the suspension is given by the sum of the solvent $\boldsymbol{\tau}^N$ and micelle $\boldsymbol{\tau}^m$ contributions

$$\boldsymbol{\tau}^T = \boldsymbol{\tau}^N + \boldsymbol{\tau}^m, \tag{4.3}$$

where

$$\boldsymbol{\tau}^N = 2\eta_s \boldsymbol{D} \tag{4.4}$$

is the Newtonian solvent contribution with rate of deformation tensor $\boldsymbol{D} = \frac{1}{2}(\boldsymbol{K} + \boldsymbol{K}^\top)$ and

$$\boldsymbol{\tau}^m = 3n_0 k_B T\left(\boldsymbol{S} - \frac{1}{3}\boldsymbol{I}\right) + \frac{n_0 k_B T}{2D_{r,0}}\boldsymbol{K} : \langle \boldsymbol{uuuu} \rangle \tag{4.5}$$

is the additional stress due to the presence of rods. Here, $k_B$ is the Boltzmann constant and $T$ is the temperature. Equations (4.2) and (4.5) notably contain the fourth moment

$\langle \boldsymbol{uuuu} \rangle$, an evolution equation for which depends on the sixth moment of $\boldsymbol{u}$, which in turn depends on higher moments. To proceed analytically, it is then necessary to supply a closure approximation for the product $\boldsymbol{K} : \langle \boldsymbol{uuuu} \rangle$. While numerous approximations are possible (see, for example: [75, 114, 101]), the RRM-R uses an approximation from Dhont and Briels [103] that interpolates between exact expressions in the limits of isotropy (equilibrium) and complete alignment:

$$\boldsymbol{K} : \langle \boldsymbol{uuuu} \rangle \approx \frac{1}{5}[\boldsymbol{S} \cdot \boldsymbol{D} + \boldsymbol{D} \cdot \boldsymbol{S} - \boldsymbol{S} \cdot \boldsymbol{S} \cdot \boldsymbol{D} - \boldsymbol{D} \cdot \boldsymbol{S} \cdot \boldsymbol{S} + 2\boldsymbol{S} \cdot \boldsymbol{D} \cdot \boldsymbol{S} + 3(\boldsymbol{S} : \boldsymbol{D})\boldsymbol{S}]. \quad (4.6)$$

### 4.2.2 RRM-R

As discussed above, a key feature of the RRM and RRM-R is that they allow micelles, modeled as rigid rods, to undergo reversible scission and growth by allowing the collective length and number density of the suspension to be dynamic properties that evolve with time and flow. This variation is mathematically achieved in the RRM-R by changing the constant rod length $L_0$ to the dynamic length $L$. To make analytical progress and ensure the tractability of the model we assume the system can be characterized by a single, representative length, $L$. Now consider a suspension of rods at equilibrium with number density $n_0$ and equilibrium length $L_0$; the radius $b$ of the rods is taken to be constant. The evolution of length $L$ and number density $n$ are constrained at all times by the surfactant mass balance

$$nL = n_0 L_0. \quad (4.7)$$

The rotational diffusion constant for a rod of length $L_0$ and radius $b$ is given by [75, 115]

$$D_{r,0} = \frac{3k_B T}{\pi \eta_s L_0^3} \ln\left(\frac{L_0}{2b}\right). \quad (4.8)$$

In the RRM-R, the constant rotational diffusion coefficient of the simple rigid rod model is

replaced by the length-dependent coefficient

$$D_r = \frac{D_{r,0}}{L^{*3}} \left( \frac{\ln L^* + m}{m} \right), \tag{4.9}$$

where $L^* = L/L_0$ is the dimensionless micelle length and $m = \ln[L_0/(2b)]$ is a constant related to the initial aspect ratio of the rods. Substituting Eq. (4.9) into Eqs. (4.2) and (4.5), we find

$$\frac{\mathrm{D}\boldsymbol{S}}{\mathrm{D}t} = -6D_r \left( \boldsymbol{S} - \frac{1}{3}\boldsymbol{I} \right) + \boldsymbol{K} \cdot \boldsymbol{S}^\top + \boldsymbol{S} \cdot \boldsymbol{K}^\top - 2\boldsymbol{K} : \langle \boldsymbol{uuuu} \rangle \tag{4.10}$$

and

$$\boldsymbol{\tau}^m = 3nk_BT \left( \boldsymbol{S} - \frac{1}{3}\boldsymbol{I} \right) + \frac{nk_BT}{2D_r} \boldsymbol{K} : \langle \boldsymbol{uuuu} \rangle . \tag{4.11}$$

The orientation of rods in the suspension is tracked by introducing a scalar orientational order parameter

$$\widehat{S} = \sqrt{\frac{3}{2}\widehat{\boldsymbol{S}} : \widehat{\boldsymbol{S}}}, \tag{4.12}$$

where $\widehat{\boldsymbol{S}} = \boldsymbol{S} - \frac{1}{3}\boldsymbol{I}$ is the traceless part of $\boldsymbol{S}$. This order parameter varies between $\widehat{S} = 0$ for isotropic rods and $\widehat{S} = 1$ for perfectly aligned rods. Note that the description and equations above are valid for both the original RRM and the reformulation (RRM-R), the only variation between the two models is in the length evolution equation, discussed below.

To allow for variability of rod length the RRM-R assumes a length evolution equation that balances growth and breakdown of micelles

$$\frac{\mathrm{D}L}{\mathrm{D}t} = R_g + R_b, \tag{4.13}$$

where $R_g \geq 0$ is the rate of micelle growth and $R_b \leq 0$ is the rate of micelle breakdown. As discussed previously, the RRM-R assumes two forms of growth: spontaneous and alignment-induced, and two forms of breakage: spontaneous and tension-induced. Again, the complete derivation can be found in [129]. After a number of simplifications involving the surfactant

mass balance Eq. (4.7), relating spontaneous effects that must balance at equilibrium, we have the overall length evolution equation

$$\frac{\mathrm{D}L}{\mathrm{D}t} = k_{b0}\left(\frac{L_0^3}{L^2} - L\right) + k_{ga}(n_0 L_0)^2 \frac{\widehat{S}^2}{L^2} - k_{bt}\left[\exp\left(\frac{a}{L_0}\frac{\boldsymbol{S}:\boldsymbol{\tau}^m}{n_0 k_B T}\right) - 1\right]. \tag{4.14}$$

This equation contains four parameters - $k_{b0}$, $k_{ga}$, $k_{bt}$, and $a$, which are related to the spontaneous breakage, alignment-induced growth, tension-induced breakage, and scission energy of micelles, respectively.

The RRM-R constitutive equations are coupled to conservation of mass and momentum

$$\boldsymbol{\nabla}\cdot\boldsymbol{v} = 0, \tag{4.15}$$

$$\rho\frac{\mathrm{D}\boldsymbol{v}}{\mathrm{D}t} = -\boldsymbol{\nabla}p + \eta_s\nabla^2\boldsymbol{v} + \boldsymbol{\nabla}\cdot\boldsymbol{\tau}^m, \tag{4.16}$$

where $\boldsymbol{v}$ is the velocity, $p$ is the pressure, $\rho$ is the density of the fluid, $\eta_s$ is the solvent viscosity which is assumed to be Newtonian, and $\boldsymbol{\tau}^m$ is the micelle contribution to the fluid stress.

### 4.2.3 Plane Poiseuille flow

In this work we focus on the behavior of dilute wormlike micelle solutions in plane Poiseuille flow (PPF), shown in Fig. 4.2. We consider a straight channel of length $l$ and height $2d$. The half-channel width is $d$, which in all simulations is fixed at $d = 1$. The bulk of the simulations in this work are 2D, but in 3D simulations the domain also has width $w$ along $z$. The forcing is a constant pressure gradient in the $x$-direction, $\Delta p = p_l - p_0 = 2\eta_s\dot{\gamma}$, which is defined so that the dimensionless Newtonian centerline velocity one. The flow is bounded in $y$ by two stationary walls at $y = \pm d$ and is periodic in $x$ in 2D and $x$ and $z$ in 3D. Using asterisks to denote dimensionless quantities, we render the governing equations dimensionless with the

following relations: $\boldsymbol{x} = \boldsymbol{x}^* d$, $\boldsymbol{v} = \boldsymbol{v}^* U$, $t = t^*/\dot{\gamma}$, $p = p^* \eta_s \dot{\gamma}$, $\boldsymbol{\tau}^m = \boldsymbol{\tau}^{m*} G_0$, and $L = L^* L_0$ where $\dot{\gamma} = U/d$ is the characteristic shear rate and $G_0 = n_0 k_B T = 2\eta_m D_{r,0}/15$ is the micelle shear modulus [75]. Substituting these relations into the governing equations and dropping asterisks we are left with the dimensionless equations:

$$\boldsymbol{\nabla} \cdot \boldsymbol{v} = 0, \tag{4.17}$$

$$\mathrm{Re}\frac{\mathrm{D}\boldsymbol{v}}{\mathrm{D}t} = -\boldsymbol{\nabla} p + \nabla^2 \boldsymbol{v} + \frac{2}{15}\left(\frac{1-\beta}{\beta}\right)\frac{1}{\mathrm{Pe}}\boldsymbol{\nabla} \cdot \boldsymbol{\tau}^m, \tag{4.18}$$

$$\frac{\mathrm{D}\boldsymbol{S}}{\mathrm{D}t} = -\frac{6}{\mathrm{Pe}L^3}\left(\boldsymbol{S} - \frac{1}{3}\boldsymbol{I}\right)\left(\frac{m + \ln L}{m}\right) + \boldsymbol{K} \cdot \boldsymbol{S}^\top + \boldsymbol{S} \cdot \boldsymbol{K}^\top - 2\boldsymbol{K} : \langle \boldsymbol{uuuu} \rangle, \tag{4.19}$$

$$\boldsymbol{\tau}^m = \frac{3}{L}\left(\boldsymbol{S} - \frac{1}{3}\boldsymbol{I}\right) + \frac{\mathrm{Pe}}{2}\left(\frac{mL^2}{m + \ln L}\right)\boldsymbol{K} : \langle \boldsymbol{uuuu} \rangle, \tag{4.20}$$

$$\frac{\mathrm{D}L}{\mathrm{D}t} = \frac{1}{\mathrm{Pe}}\left[k_{b0}^*\left(\frac{1}{L^2} - L\right) + k_{ga}^*\frac{\widehat{S}^2}{L^2} - k_{bt}^*\left[\exp\left(a^* \boldsymbol{S} : \boldsymbol{\tau}^m\right) - 1\right]\right]. \tag{4.21}$$

We have introduced several dimensionless quantities. The Reynolds number is the ratio of inertial to viscous forces, defined as $\mathrm{Re} = \rho U d/\eta_s$. The rotational Péclet number is the ratio of the shear rate to the rotational diffusivity of the micelles at equilibrium, defined as $\mathrm{Pe} = \dot{\gamma}/D_{r,0}$. The dimensionless pressure gradient is $\Delta p^* = 2$ such that the dimensionless Newtonian velocity is given by $v_N^*(y^*) = 1 - y^{*2}$ with shear rate $|\partial v_N^*(y^*)/\partial y^*| = 2y^*$. Since the shear rate in PPF varies with wall-normal position we must define multiple Péclet numbers. In this work the standard Péclet number is defined as $\mathrm{Pe} = \dot{\gamma}(y^* = 0.5)/D_{r,0}$; this is chosen since the Newtonian shear rate is one at $y^* = 0.5$. We can also define a *wall* Péclet number, $\mathrm{Pe}_w = \dot{\gamma}(y^* = 1)/D_{r,0}$, which is the Péclet number experienced at the wall. For a Newtonian flow with velocity $v_N^*(y^*) = 1 - y^{*2}$, $\mathrm{Pe}_w = 2\mathrm{Pe}$, though this relation will vary as the velocity profile changes. Finally, the *local* Péclet number, written as $\mathrm{Pe}_l$, is computed from the local shear rate throughout the channel.

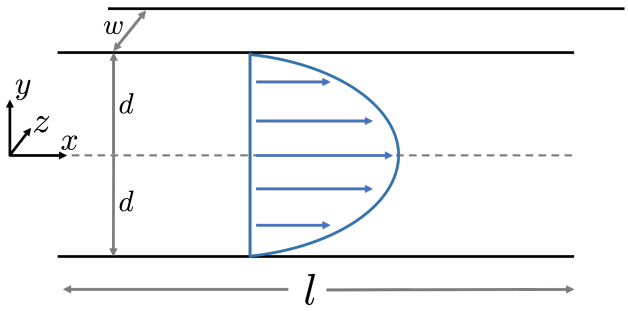


**Figure 4.2:** Schematic of plane Poiseuille geometry.

The parameter, $\beta = \eta_s/(\eta_s + \eta_m)$, is the viscosity ratio. There are four dimensionless groups in the length evolution equation – $k^*_{b0}$, $k^*_{ga}$, $k^*_{bt}$, and $a^*$ – all of which are defined identically to those in the previous work [129]. In order, $k^*_{b0}$ represents the ratio of relaxation due to spontaneous breakage to relaxation due to diffusion (i.e. realignment), $k^*_{ga}$ acts as a measure of the ratio of growth due to alignment to diffusion, $k^*_{bt}$ represents the ratio of relaxation due to tension-induced breakage to relaxation due to diffusion, and $a^*$ functions as a dimensionless length that must be overcome for tension-induced scission to occur. For the rest of this work we will drop the asterisks from these groups. Equations (4.17) to (4.21) are solved with no-slip boundary conditions at the walls. More details on the boundary conditions for $L$, $\mathbf{S}$, and $p$ are given in Section 4.3.

## 4.3 Computational methods

We solve the governing equations for mass, momentum, micelle orientation, and micelle length using the open-source CFD software OpenFOAM coupled with the viscoelastic solver RheoTool [143, 144, 145]. This framework uses the finite volume method to discretize equations. We have written an additional library for the RRM-R. Details of the numerical implementation of the code as well as validations are given elsewhere [146, 144]. In this study we perform both 2D and 3D numerical simulations of the RRM-R in periodic plane Poiseuille flow. For 3D simulations we take all quantities to be periodic in $z$. In 2D simulations we confine the flow to the $xy$-plane and solve only the $xx$, $xy$, $yy$, and $zz$ components of

the governing equations. On the channel walls we use no-slip and no-penetration boundary conditions for the velocity, zero normal gradient for the pressure, and linear-extrapolation for the micelle length and orientation [144]. The micelle contribution to the stress tensor does not require boundary conditions as it is calculated directly from Eq. (4.20). To ensure numerical stability of our simulations we use the stress-velocity coupling method provided in RheoTool; since adding stabilization is known to alter transient dynamics, we incorporate a number of inner iterations to the main solver loop (typically 2-5 depending on the degree of stabilization added), which act to decrease the explicitness of the solver [144]. We have previously verified the accuracy of the viscoelastic library for the RRM-R in [148].

We generate the numerical grid for our problem using the `blockMesh` utility in OpenFOAM. Although we will vary the length of the channel throughout this work to test the wavelength of emergent structures, the majority of the results are in the $l = 3$ domain. Using $l = 3$, we tested the resolution of structures in the system and ensured mesh-independency by testing four different 2D grid resolutions with densities: M0 = 40,000, M1 = 108,000, M2 = 198,000 and M3 = 240,000. In 3D, we use these same resolutions with 20-80 grid points in $z$. All results presented in this work use the M1 grid, unless otherwise stated. In general, we found that all resolutions showed quantitatively similar dynamics and results. Further, we tested the accuracy of our meshes by comparing time-dependent statistics and dynamics as well as steady state profiles to confirm that our solutions did not depend on the mesh density. In domains with length $l \neq 3$ the mesh is altered to maintain the same resolution as the M1 mesh.

## 4.4 Results and Discussion

The organization of this section is as follows: In Section 4.4.1 we show the governing constitutive curves for the RRM-R and discuss the effects of a spatially-dependent stress and how this can promote instabilities for reentrant flows. In Section 4.4.2 we focus on 2D simulations

of the RRM-R in plane Poiseuille flow with a convection-free velocity; we show that at large enough Péclet numbers the flow can jump between the stable lower and upper branches, giving rise to a viscosity-stratified flow with 'interfaces' separating near-wall and central regions of the domain. These interfaces are unstable, leading to fluctuating structures consisting of short wave, long wave, and mixed patterns. In Section 4.4.3 we then investigate the effects of velocity convection and varying Reynolds number, finding that increasing Re tends to delay the formation of interfaces and instabilities. Finally, in Section 4.4.4 we investigate instabilities in 3D domains and find that the initial instability is 2D in nature, and that the structures in 3D differ largely from those observed in 2D.

### 4.4.1 Reentrant plane Poiseuille flow

The RRM-R length evolution equation, Eq. (4.21), contains four dimensionless parameters that can be tuned to vary the behavior of the desired WLM system. We select values that yield a significantly reentrant constitutive curve to adequately probe and characterize instabilities in this region. The values chosen for the constitutive model are: $m = 3$, $k_{b0} = 10^{-2}$, $k_{ga} = 1500$, $k_{bt} = 10$, and $a = 2.5$, with $\mathrm{Re} = 10^{-1}$ and $\beta = 0.082$. This value of $\beta$ may seem low for modeling dilute viscoelastic solutions, but was chosen to match typical values seen in experiments where the zero-shear viscosity of these solutions is between $4-10$ mPa s [4, 5]. We initially approximate an inertialess flow condition by neglecting the convective terms in the momentum equation and setting $\mathrm{Re} = 0.1$. Later in this work we will investigate the effects of inertia and Re.

In simple shear flow, $\boldsymbol{v} = (\mathrm{Pe}\ y, 0, 0)^T$, these parameters yield the constitutive curves shown in Fig. 4.3. These curves are highly reentrant over almost a decade of Péclet numbers, which will facilitate probing the behavior of this region, specifically sections where $\partial\tau_{xy}/\partial\dot{\gamma} < 0$. The length of micelles for these parameters increases to a maximum of about 11 times the equilibrium length, and the solution shear-thickens by over an order of magnitude. The inset in Fig. 4.3c shows a close-up of the orientation profiles near the turning point into the

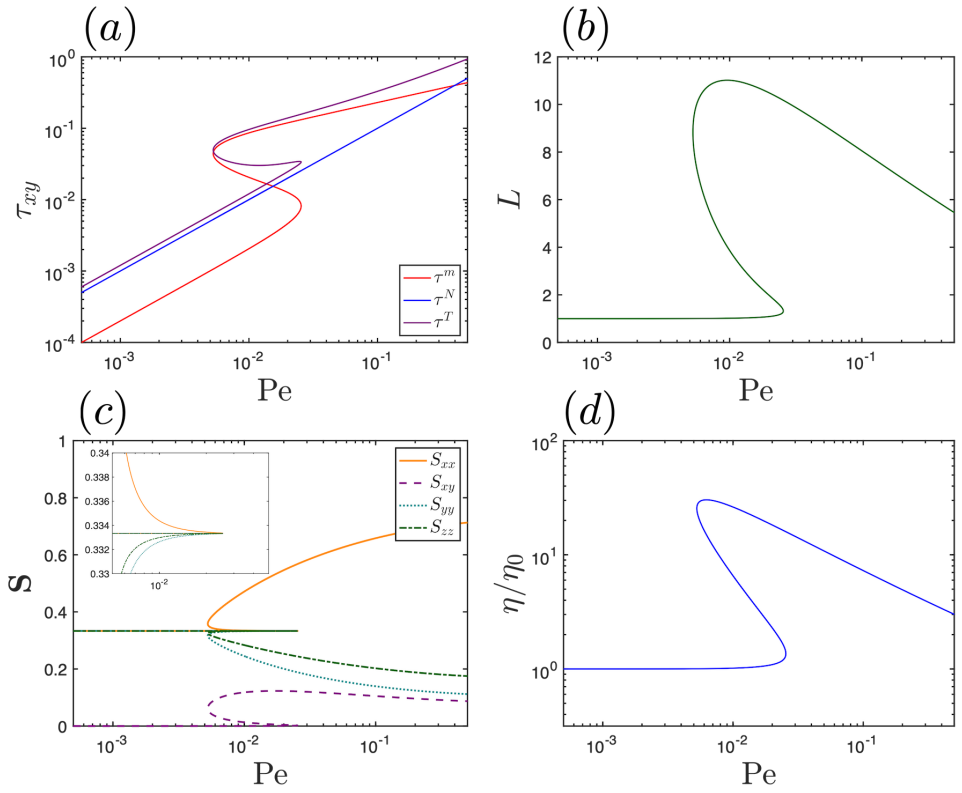


**Figure 4.3:** (Reproduced from Section 3.4.1) Constitutive curves for the RRM-R with parameters: $m = 3$, $k_{b0} = 10^{-2}$, $k_{ga} = 1500$, $k_{bt} = 10$, and $a = 2.5$. (a) Micelle (red), Newtonian (blue), and total shear stress (purple), (b) length of micelles, (c) components of the orientation tensor, and (d) normalized viscosity vs. applied Péclet number.

multivalued region. To clarify the analysis of these flows, we define three distinct solution branches on the shear stress constitutive curve (Fig. 4.3a): the lower, middle, and upper branches with $\tau^T_{xy,low} < \tau^T_{xy,mid} < \tau^T_{xy,up}$. The lower branch extends from $0 < \mathrm{Pe} \lesssim 2.5 \times 10^{-2}$. The middle branch extends from $5 \times 10^{-3} \lesssim \mathrm{Pe} \lesssim 2.5 \times 10^{-2}$, where notably $\partial \tau^m_{xy}/\partial \dot{\gamma} < 0$ throughout this entire region. Finally, the upper branch extends from $5 \times 10^{-3} \lesssim \mathrm{Pe} < \infty$.

In this work we are primarily interested in plane Poiseuille flow. The notable difference between PPF and simple shear flow is that in PPF all quantities (e.g., stress, length, and orientation) vary across the channel due to the dependence of the shear rate on wall-normal position ($y$). For example, in a Newtonian flow the shear stress and shear rate will vary linearly with wall normal position; in the current geometry and non-dimensionalization a Newtonian fluid will show $\dot{\gamma} = 2y$ so that along center of the channel the shear rate actually goes to zero, which can have drastic consequences for a fluid with a reentrant flow curve.

To understand this, consider a case where the Péclet number is set so that at the walls, where the shear rate is largest, the flow exists on the upper branch of the constitutive curve (e.g., Pe = 0.04 for the constitutive curves shown in Fig. 4.3); while the fluid close to the walls will exist on the upper branch, because the shear rate goes to zero the fluid *must* exist on the lower branch at the channel center. Further, because regions of the flow curve where $\partial\tau_{xy}/\partial\dot{\gamma} < 0$ are unstable, the fluid can not smoothly transition between branches and must therefore 'jump' between branches. This 'jump' will result in an interface-like region between fluid on either branch, generating a flow that is highly reminiscent of viscosity-stratified flows, specifically core-annular channel flow since PPF is inherently symmetric [153]. Literature on stratified flows has resoundingly demonstrated that these flows are unstable, in the viscoelastic case this is due to both viscosity mismatch and normal stress jumps, so we expect similar instabilities will arise for dilute WLM solutions that exhibit jumps due to reentrant flow curves. The flow profile in PPF will differ from the CCF profile investigated in our previous work because in CCF the shear stress must vary as $\tau_{r\theta} \sim r^{-2}$, whereas in PPF there are no restrictions. Thus, while in CCF the flow could be forced into unstable regions of the flow curve because of the requirements of the radial dependence, in PPF the flow can jump between branches and avoid the unstable region. This means that while instabilities observed in CCF were reentrant in nature, those in PPF are interfacial in nature.

### 4.4.2 Convection-free interfacial instabilities in 2D

We begin this investigation by considering 2D PPF with a low enough Péclet number such that the flow exists entire on the lower branch of the constitutive curve; at this low Pe there are no reentrant instabilities that can develop. Simulations are performed by taking an a fluid at equilibrium ($L = 1$ and $\mathbf{S} = \boldsymbol{\delta}/3$) and increasing to the set Pe from rest. As a reminder, since the shear rate varies throughout the channel the wall Péclet number ($\mathrm{Pe}_w$) is larger than the applied Péclet number (Pe); for a Newtonian velocity profile $v_N(y) = 1 - y^2$,

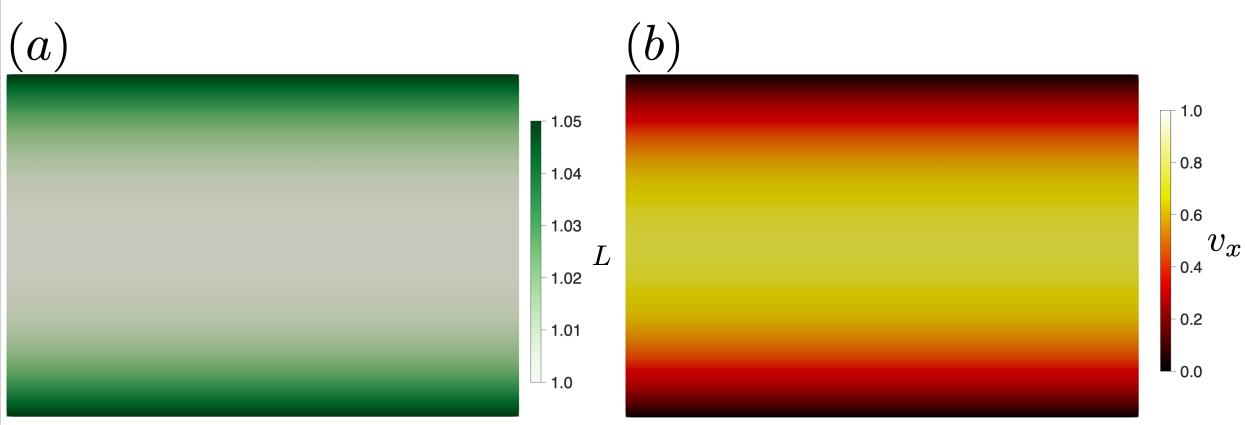


**Figure 4.4:** Steady state (a) micelle length and (b) streamwise velocity for PPF at Pe = 0.01.

such that $\mathrm{Pe}_w = 2\mathrm{Pe}$. The presence of micelles modifies this velocity profile and, as we will see, decreases the shear rate at the walls so that in general $\mathrm{Pe}_w < 2\mathrm{Pe}$. Figure 4.4 shows the steady state (a) micelle length and (b) streamwise velocity profiles for PPF with Pe = 0.01; notice the scale of (a), which shows that micelles are nearly at their equilibrium length with only minor elongation towards the channel walls where the shear rate is largest. The velocity profile is parabolic with a maximum of about $v_x(y = 0) = 0.83$; the reduction in the maximum velocity from the Newtonian case of $v_{x,N}(y = 0) = 1$ arises due to the increased viscosity from the presence of the micelles. No interface is observed at this Pe because there is no jump between branches. The existence entirely on the lower branch is clear in Fig. 4.5, which shows the steady state (a) local micelle length and (b) local micelle shear stress profiles vs. local Péclet number ($\mathrm{Pe}_l$) projected onto the governing constitutive curves for (cyan) Pe = 0.01 and (orange) Pe = 0.015. The plots show that at these low Pe the flow exists entirely on the lower branch and that $\mathrm{Pe}_w$ is indeed less than twice Pe, which arises from a reduction in the streamwise velocity and therefore a reduction in the wall shear rate. It is also apparent that Pe = 0.015 is close to the maximum Pe possible without forcing the flow to jump to the upper branch.

Upon increasing the shear rate further drastically different behavior is observed; at these large Pe values the flow is no longer able to exist entirely on the lower branch. Figure 4.6 shows snapshots in time of the micelle length in start-up PPF with an applied shear rate of

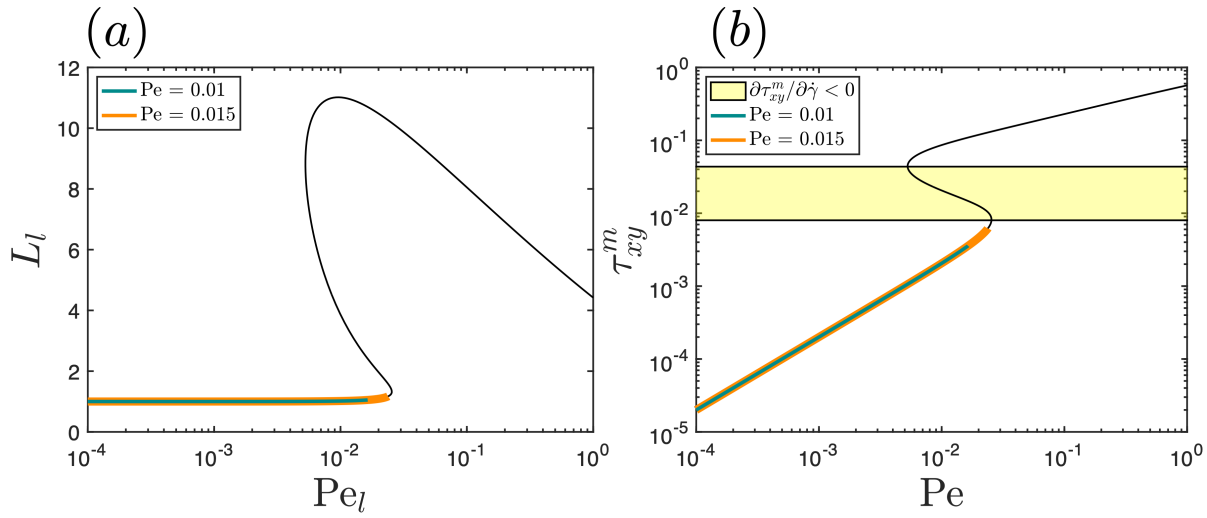


**Figure 4.5:** Steady state (a) local micelle length and (b) local micelle shear profiles vs. local Pe superimposed onto the governing constitutive curves for (cyan) Pe = 0.01 and (orange) Pe = 0.015.

Pe = 0.04. We do not show the micelle orientation parameter ($\widehat{S}$) because in our previous work [148] we found that regions of high-alignment are identical to those that show high-elongation. At early times ($t = 2$ and $t = 5$) micelles begin to elongate near the channel walls where the shear rate is largest. At these times the micelles have already grown far longer than what was observed in the Pe = 0.01 case. At $t = 30$ a very sharp interface-like region has formed; as a note, although this is not a true interface in the sense of separating distinct phases or materials, we will refer to this as an interface because the difference between regions of highly elongated and anisotropically-oriented micelles from the nearly equilibrium-length and isotropic micelles is significant enough to give the appearance of phase separation. Indeed, the interface at $t = 30$ is identical to the interfaces observed in core-annular channel flow of viscosity-stratified miscible fluids. The comparison is even stronger than mere appearance since the flow here consists of a miscible fluid (in the sense that the regions are self-miscible) and is viscosity-stratified. Referencing Fig. 4.3, the region of highly elongated micelles close to the walls is significantly more viscous than that of the near-equilibrium rods at along the channel center.

The flow maintains these sharp interfaces until about $t = 60$, at which time both interfaces begin to destabilize; this destabilization is not surprising since it is well-known that

instabilities in stratified flows are driven by viscosity mismatch and normal stress jumps across the interface, both of which are substantial here. The destabilization process proceeds as wisps of elongated micelles in the slow-moving near-wall region are sheared off by the fast-moving center region. Figure 4.7 shows the corresponding snapshots of the streamwise velocity profiles to Fig. 4.6. The color bar does not capture the velocities at $t = 2$, which has a parabolic profile with a maximum velocity of about $v_x \approx 0.8$, and $t = 5$, which has a parabolic profile with a maximum velocity of about $v_x \approx 0.4$. At $t = 30$ and $t = 60$ the velocity consists of two regions of slow moving fluid close to either wall and a region of much faster moving fluid in the channel center.

Figure 4.8 shows the local streamwise velocity and local shear rate across the channel at several time points and sampled at $x = 1.5$. The velocity dramatically decreases until $t = 30$, at which point the interfaces between branches have fully developed. At this and later times the velocity exhibits a reverse plug-like profile in which the channel center shows a parabolic profile whereas the near-wall regions show almost linear profiles. These profiles are remarkably similar to core-annular channel flow in which the center fluid is less viscous relative to the outer fluid [154]. In fact, this type of core-annular channel flow is exactly mimicked at $t = 30$, but in this case it develops naturally rather than the typical artificially generated core-annular channel flows. This velocity profile gives rise to a shear rate profile in which the magnitude of shear rate increases linearly outwards from the channel center up to the interfaces, at which point the shear rate becomes almost constant. It is also interesting that although the length exhibits dramatic fluctuations, the streamwise velocity exhibits only weak fluctuations.

Returning to Fig. 4.6, the instability has fully disrupted the interface by $t = 200$ and the flow displays an arrowhead-like structure pointing in the streamwise direction. Although this structure may resemble the mushroom patterns observed in core-annular flow of water-natrosol mixtures [159], we refrain from calling these structures mushroom-like since we will see more established mushrooms later in this work. At this time $v_x$ also begins to exhibit an

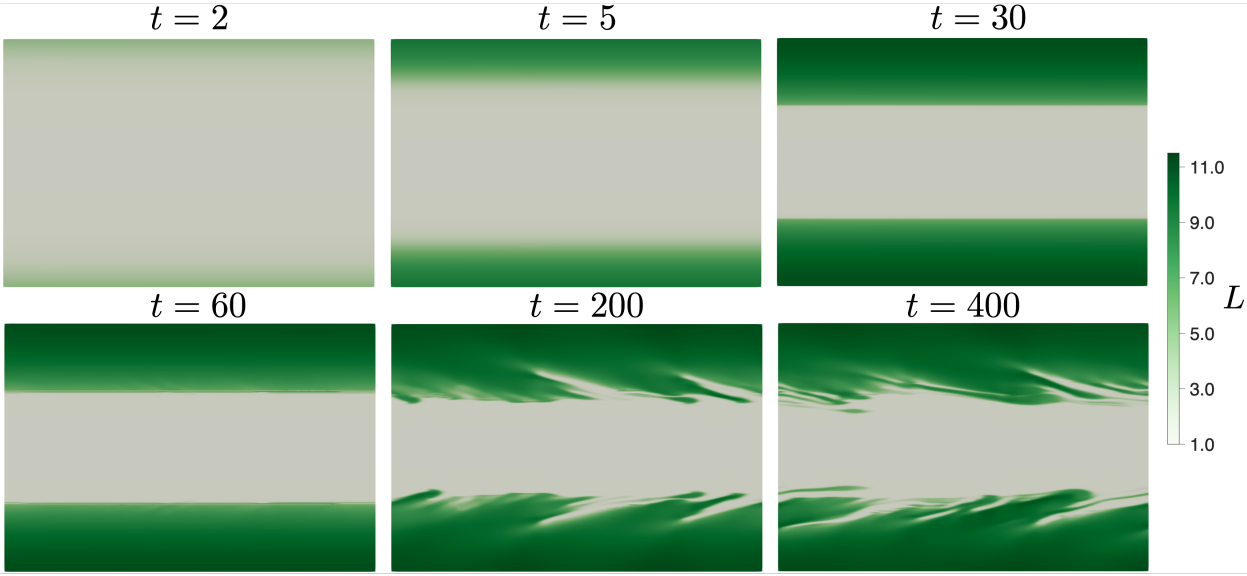


**Figure 4.6:** Snapshots of micelle length for start-up PPF with an applied shear rate of Pe = 0.04.

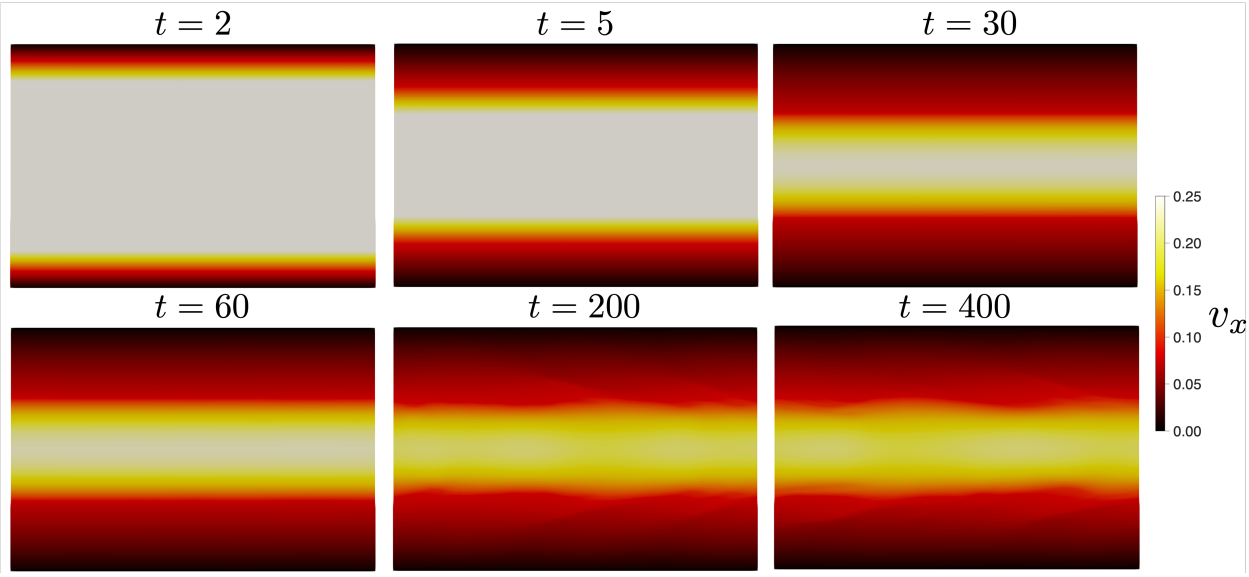


**Figure 4.7:** Snapshots of streamwise velocity for start-up PPF with an applied shear rate of Pe = 0.04.

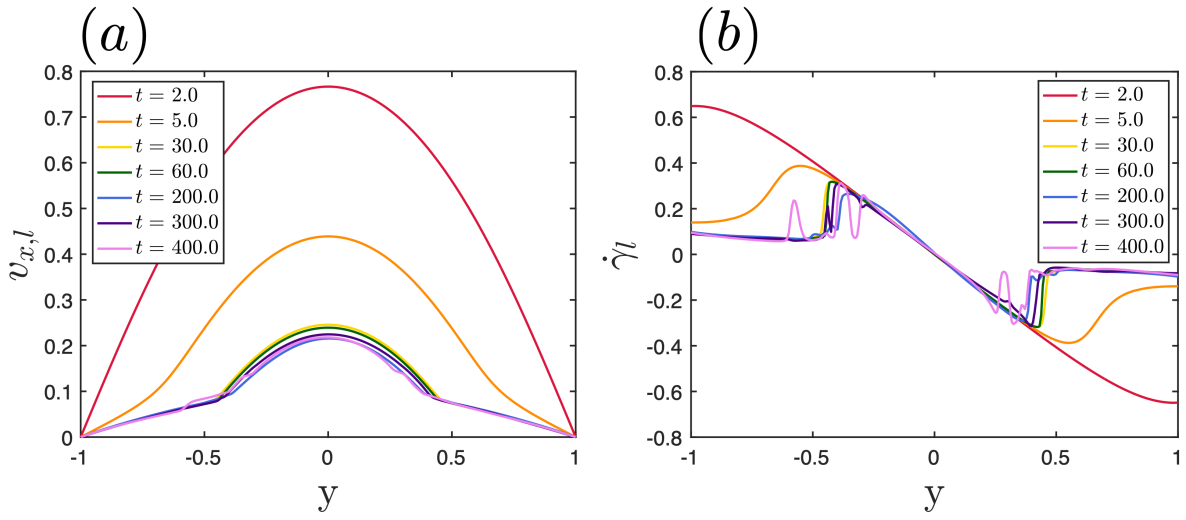


**Figure 4.8:** (a) Local streamwise velocity and (b) local shear rate profiles across the channel over several time points and at $x = 1.5$ for start-up PPF with an applied shear rate of Pe = 0.04.

arrowhead-like structure, albeit a much weaker one, with high-velocity streaks branching out towards the walls from the channel center. These narrow high-velocity streaks correspond to regions of the flow consisting primarily of near-equilibrium micelles; regions of shorter micelles have a significantly lower viscosity which allows fluid to travel faster. Interestingly, at $t = 200$ the micelle length profile is nearly symmetric across the centerline, while at $t = 400$ the symmetry has been reduced. We can understand the existence of symmetry and its disappearance by considering that the flow field at early times should be symmetric over the centerline, which is indeed what we see up until $t = 60$ when both interfaces begin to destabilize in an identical manner. As the destabilization process proceeds, however, it is likely that the instability on either interface grows at different rates, possibly driven by numerical error or possibly driven by the chaotic nature of the instability, thus leading to asymmetric structures. Interestingly, an identical case of start-up PPF with Pe = 0.04 in the M3 mesh actually exhibited asymmetry that developed earlier, which suggests that the difference in the instability growth rates may be more random (i.e., chaotic) and less dependent on numerics. Figure 4.23 in Section 4.6 shows a mesh comparison for start-up PPF with Pe = 0.04.

The onset and sustenance of this instability also provokes wall-normal velocity fluctua-

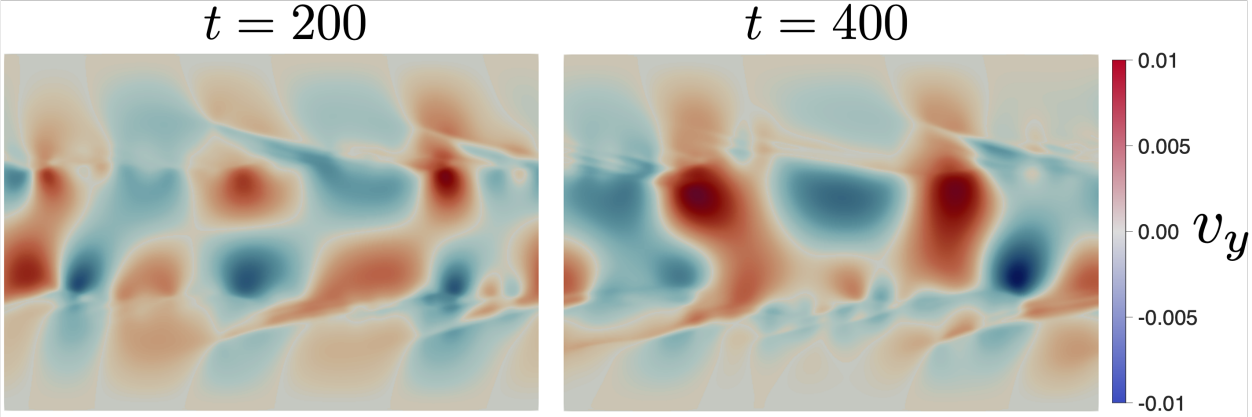


**Figure 4.9:** Snapshots of wall-normal velocity for start-up PPF with an applied shear rate of $\mathrm{Pe} = 0.04$.

tions. Figure 4.9 shows the wall-normal velocity at $t = 200$ and $t = 400$ after the instability has fully developed; prior to the destabilization no wall-normal velocity is observed. These profiles both exhibit alternating regions of positive and negative wall-normal velocity along the streamwise direction, however, it appears as though the wavelength of structures is smaller at $t = 200$ than $t = 400$. Additionally, regions of positive and negative $v_y$ are smaller and flip sign over the centerline at $t = 200$, whereas at $t = 400$ these regions are larger and constant across the centerline.

In our previous work on circular Couette flow, we observed that the onset and early behavior of the finger-like instabilities were both constant in the sense that the structures always exhibited eight branches that grew outwards from the inner cylinder (implicating the $m = 8$ azimuthal wavenumber). In these PPF simulations, however, we have found that the onset and early behavior of the instability can differ between simulations. For example, Fig. 4.10 shows several snapshots of micelle length for start-up PPF with an applied shear rate of $\mathrm{Pe} = 0.04$ and identical initial conditions to those shown in Fig. 4.6. Simply comparing snapshots at $t = 60$ it is clear that the instability develops differently between the two simulations. Again, it is not clear what causes these differences since even identical simulations in the M3 mesh tend to show variations. It is possible that this instability is strongly chaotic and so even very small numerical errors are drastically amplified. It is also

possible that there are two or more dominant modes with similar growth rates driving the observed instability; comparing the two simulations, it appears that if there are two dominant modes driving the instability, one is in-phase and promotes a snake-like pattern and another is out-of-phase, or at least shifted, and promotes the mushroom pattern. Multiple unstable modes have been found in three-layer stratified fluids; for Newtonian fluids two instability modes have been found: a sinuous mode, where the disturbances on the interfaces are in phase (antisymmetric), and a varicose mode, where the disturbances are 180° out of phase (symmetric) [160, 161, 156]. In viscoelastic fluids it has been found that increasing the width of the more elastic component can stabilize longwave varicose modes [162], though the varicose mode may not be the most unstable. Therefore it is reasonable that differences in flow structure are caused by competing symmetric/antisymmetric unstable modes.

Figure 4.10 also differs from the previous simulation in that the flow appears to retain some degree of symmetry for much longer. At $t = 210$ and $t = 407$ the structures exhibit the mushroom-like patterns that have been observed in core-annular channel flow [159]. Indeed we see a 'mushroom cap' structure that is sheared backwards over the 'mushroom stem.' This mushroom pattern exists until about $t = 600$, at which point chaotic fluctuations cause the upper and lower near-wall regions to differ from one another and strong asymmetry sets in (evidenced at $t = 900$). Again, this observation of the mushroom pattern emphasizes the similarity between this flow and core-annular channel flow. Fluid in the near-wall, high shear region exists on the highly viscous upper branch while fluid in the central, low shear region exists on the weakly viscous lower branch, giving the appearance and behavior of a viscosity stratified flow. We also find that the 'mushroom stem' regions, in which the center region of near-equilibrium micelles is squeezed, results in bursts of high velocity fluid. This is clear in Fig. 4.11, which again shows the snapshots of micelle length but now with overlays of streamwise velocity contours. It is clear from $t = 210$ and $t = 407$ that the squeezed regions (corresponding the 'mushroom stem') cause bursts of high velocity fluid. In $t = 900$, when the mushroom has vanished and the center region of near-equilibrium micelles has nearly

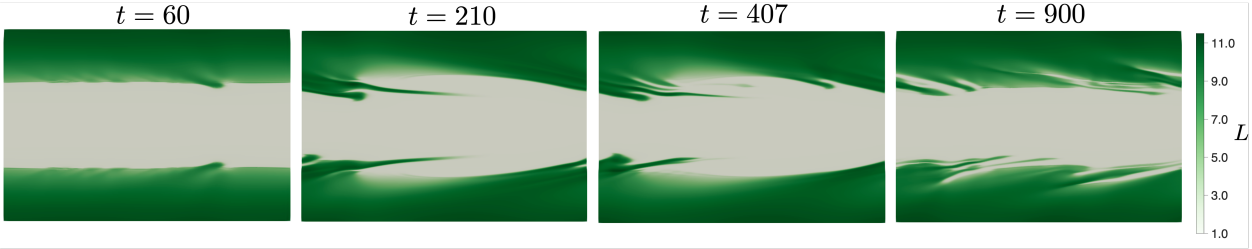


**Figure 4.10:** Snapshots of micelle length for start-up PPF with an applied shear rate of Pe = 0.04.

constant width throughout the entire channel, the velocity shows no bursts and is nearly independent of $x$.

We now want to investigate the development and driving mechanisms of this instability. As discussed previously, interfacial instabilities in the purely elastic case tend to be driven by a jump in normal stresses across the interface. In purely viscous scenarios, viscosity mismatch between layers leads to a vorticity mismatch at the interface that has a destabilizing effect by amplifying the crests and valleys of the interface. Figure 4.12 shows snapshots in time of the micelle shear stress, micelle length, first normal stress difference ($N_1 = \tau_{xx} - \tau_{yy}$), and vorticity ($\omega_z$). We observe that there is both a vorticity mismatch and a normal stress jump across the interfaces in this flow, driven by the differences in micelle length and orientation. Figure 4.24 in Section 4.6 shows snapshots of intermediate times as the instability develops.

Ganpule and Khomami [156] showed that in purely viscous (i.e., Newtonian) core-annular channel flow, when the middle layer is less viscous, as it is here, viscosity mismatch has a destabilizing effect for both sinuous and varicose longwave modes; moreover, they found that the instability did not arise in either the shortwave or longwave limit and that either sinuous or varicose modes could be dominant. These findings are consistent with our own in that there are both shortwave and longwave structures that can be either in-phase or out-of-phase. In the purely elastic case, when the middle layer is less elastic, as it is here, Ganpule and Khomami found that the sinuous mode is the more unstable mode at all wavelengths. Finally, in the viscoelastic case they found that, when the middle layer is less viscous and less elastic, the instability can not be deduced from either the purely viscous or purely elastic cases; in

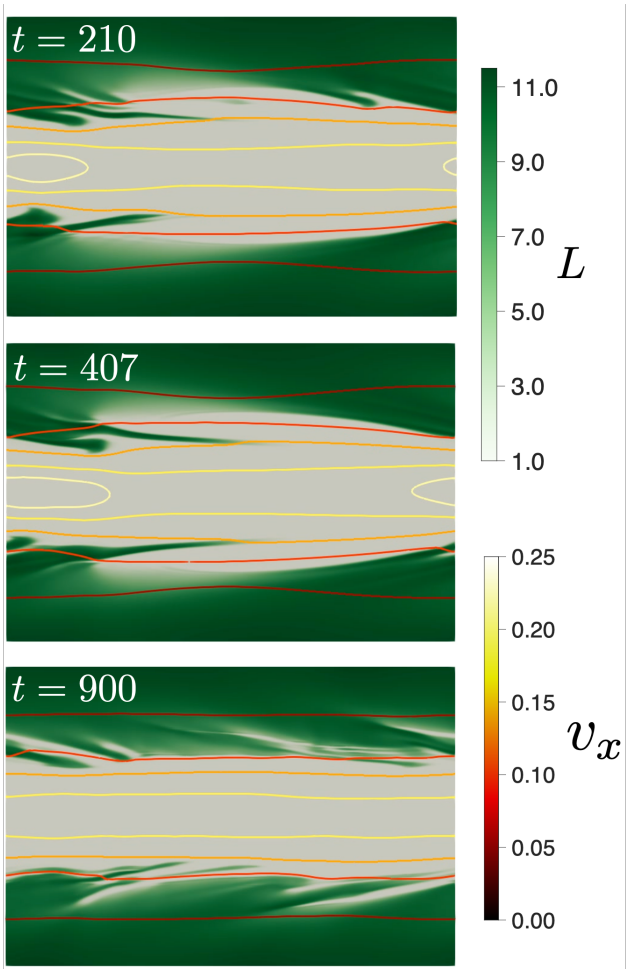


**Figure 4.11:** Snapshots of micelle length with overlays of streamwise velocity contours for start-up PPF with an applied shear rate of Pe = 0.04.

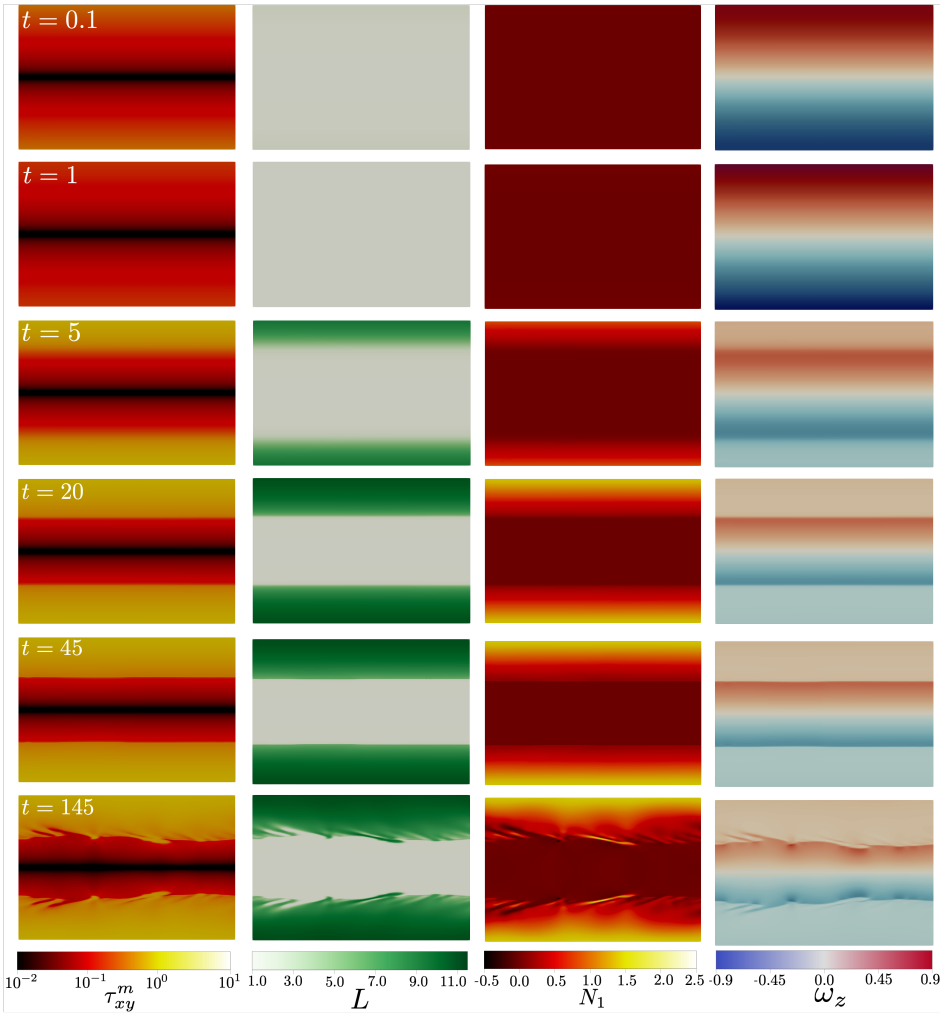


**Figure 4.12:** Snapshots of first column: micelle shear stress, second column: micelle length, third column: first normal stress difference, and fourth column: vorticity for start-up PPF with an applied shear rate of Pe = 0.04.

fact, the sinuous mode was found the always be unstable, regardless of layer width, while the varicose mode was only unstable for wider middle layers and with longer wavelengths. These findings again agree with our own in that there are multiple modes present and the varicose mode, which supports mushroom patterns, occurs at longer wavelengths.

It also must be noted that the reentrant flow curve, and specifically the unstable region where $\partial\tau_{xy}/\partial\dot{\gamma} < 0$, could be driving the observed instability. Consider Fig. 4.13, which shows the (a) local micelle length and (b) local micelle shear vs. local Pe profiles projected onto the governing constitutive curves at times corresponding to the snapshots in Fig. 4.12, where the data is sampled at $x = 1.5$. At early times ($t = 0.1$ and $t = 1$) the flow exists primarily on the

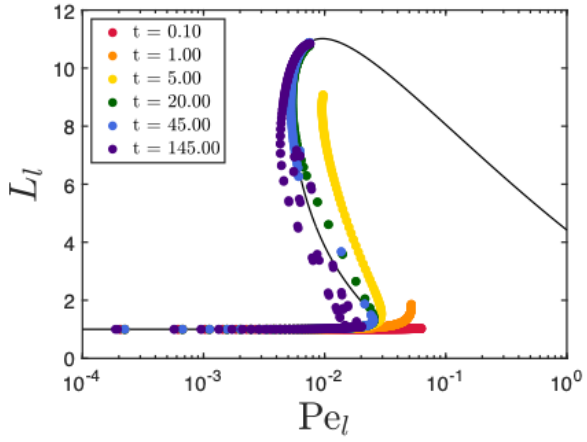


**Figure 4.13:** Several time points of (a) local micelle length and (b) local micelle shear vs. local Pe profiles projected onto the governing constitutive curves for $\mathrm{Pe} = 0.04$.

lower branch but also extends significantly off of the governing constitutive curves at higher Pe. This deviation arises from the velocity field and shear rate reducing rapidly at early times to reach a quasi-steady state prior to the onset of the instability. At $t = 20$ and $t = 45$ the flow begins to reach and settle onto the upper branch of the curves. At $t = 45$ the local profiles show a dramatic split between branches as the flow is unable to settle onto the unstable middle branch; only two points exist close to the middle branch at this time, corresponding to locations directly on the interface. Finally, as the instability grows we see that at $t = 145$ the fluid is bound to the skeleton on the constitutive curve, particularly the stable lower and upper branches, but fluctuates chaotically around the unstable middle branch as fluid 'jumps' between stable branches. This behavior, specifically the destabilization occurring around the unstable regions of the flow curve, makes it challenging to delineate between an instability driven by normal stress and vorticity jumps and one driven by the unstable reentrant flow curve. It is also possible that the multiple mechanisms are working in tandem, in that normal stresses and viscosity mismatch initiate the instability, but the dynamics of the fluctuating flow are driven by the unstable flow curve; it is likely that linear stability analysis could add clarity to this distinction but that is outside the scope of the current work.

Increasing Pe further has the effect of increasing the width of the elongated near-wall

regions and decreasing the width of the near-equilibrium central region. Figure 4.14 shows snapshots of the micelle length at several time instances for Pe = 0.06. The primary interfacial instability observed at Pe = 0.04 is not changed, it is merely pushed closer to the center of the channel. Even the time scale for growth of the instability is largely unchanged with increasing Pe, shown by the slight destabilization occurring at $t = 60$. At $t = 610$ it is apparent that there is both longwave structuring, in the form of the two arrowhead-like structures, as well as shortwave structuring, in the form of the many threads that blur the arrowheads. The coexistence of both long- and shortwaves again suggests competition between multiple unstable modes. At $t = 1500$ it seems that the shortwave structures have been consumed by the longwave mushroom structure, which suggests that the longwave varicose mode is dominant. This mushroom pattern continues to persist for over 1750 time units with no indication of stopping. Figure 4.15 shows streamwise velocity snapshots comparing a time ($t = 610$) that exhibit both short- and longwaves and a time ($t = 1500$) that only exhibits longwave structures. The short- and longwave profile consists of a high speed steak at the center of the channel where the fluid is much less viscous with faint streaks of high speed fluid that extend backwards. The longwave-dominated profile shows a bulbous region of high speed fluid at the channel center that is bounded by the elongated, more viscous region close to the walls.

The similarity at larger Pe is interesting because, as previously mentioned, it has been shown for stratified flows that the width of bands can effect the flow stability, in some cases having a stabilizing effect while in others a destabilizing effect [160]. In particular, for viscoelastic fluids it has been shown that if the velocity profile is convex (meaning a positive jump in shear rate across the interface), the flow can be stabilized when the more elastic component occupies the majority of the channel; by increasing Pe the width of the more elastic bands are in fact increased, which could lead to flow stabilization. However, it has also been shown that if the outer layers are more viscous and more elastic the flow is always unstable to the sinuous mode [162]. Clearly there are complex dynamics underlying the flow

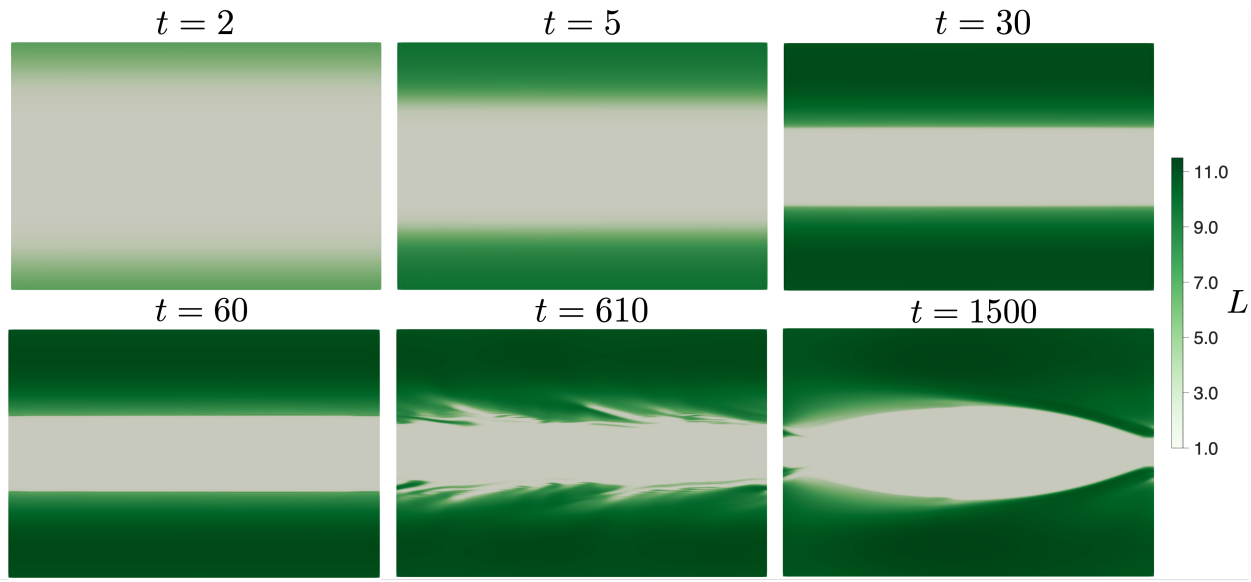


**Figure 4.14:** Snapshots of micelle length for start-up PPF with an applied shear rate of Pe = 0.06.

stability.

### Effects of box length

Before concluding our study on convection-free instabilities in 2D, it is reasonable to question the effects of the box length ($l$) on the structure of the instability. Varying $l$ has the effect of altering the periodicity and wavelength of structures that can exist; decreasing the box length can act to extinguish the appearance of large scale structures. In turbulence it has been shown that small enough box lengths can even suppress turbulent structures [163]. The longest scale structures observed in the present work are the mushroom patterns that appear to be the manifestation of an unstable longwave, even mode.

Figure 4.16 shows snapshots of micelle length for various box lengths in start-up PPF with Pe = 0.04. In order of left-to-right and top-to-bottom the lengths are: $l = 1$, $l = 2$, $l = 4$, $l = 5$, $l = 6$ and $l = 10$. Note that the snapshots shown are selectively chosen to show mushroom patterns if they arise, as these are the longest wavelength structures observed, otherwise they are taken to show the characteristic pattern that persists for the greatest time length. For $l = 1$ and $l = 2$ the flow is dominated by shortwave structures and we do not

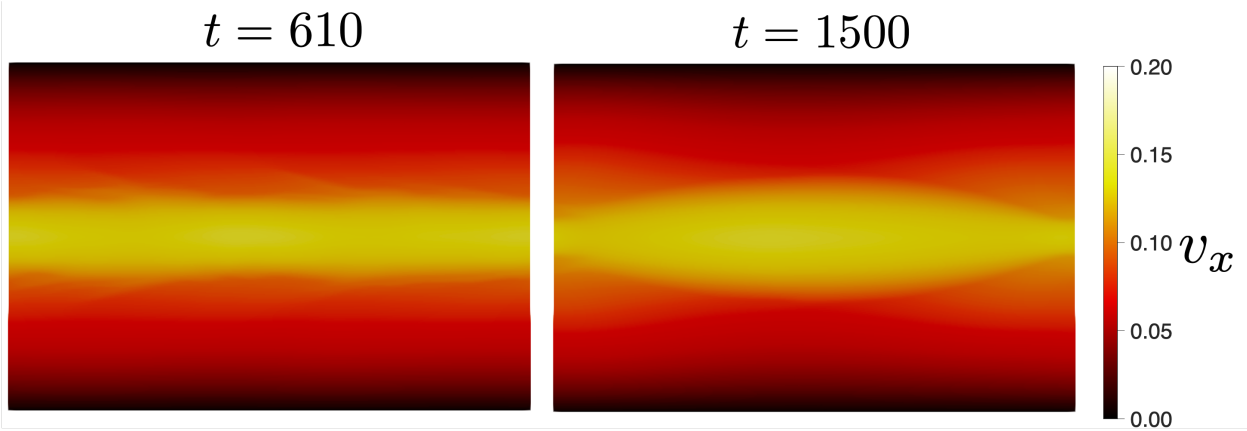


**Figure 4.15:** Snapshots of streamwise velocity at later times for start-up PPF with an applied shear rate of Pe = 0.06.

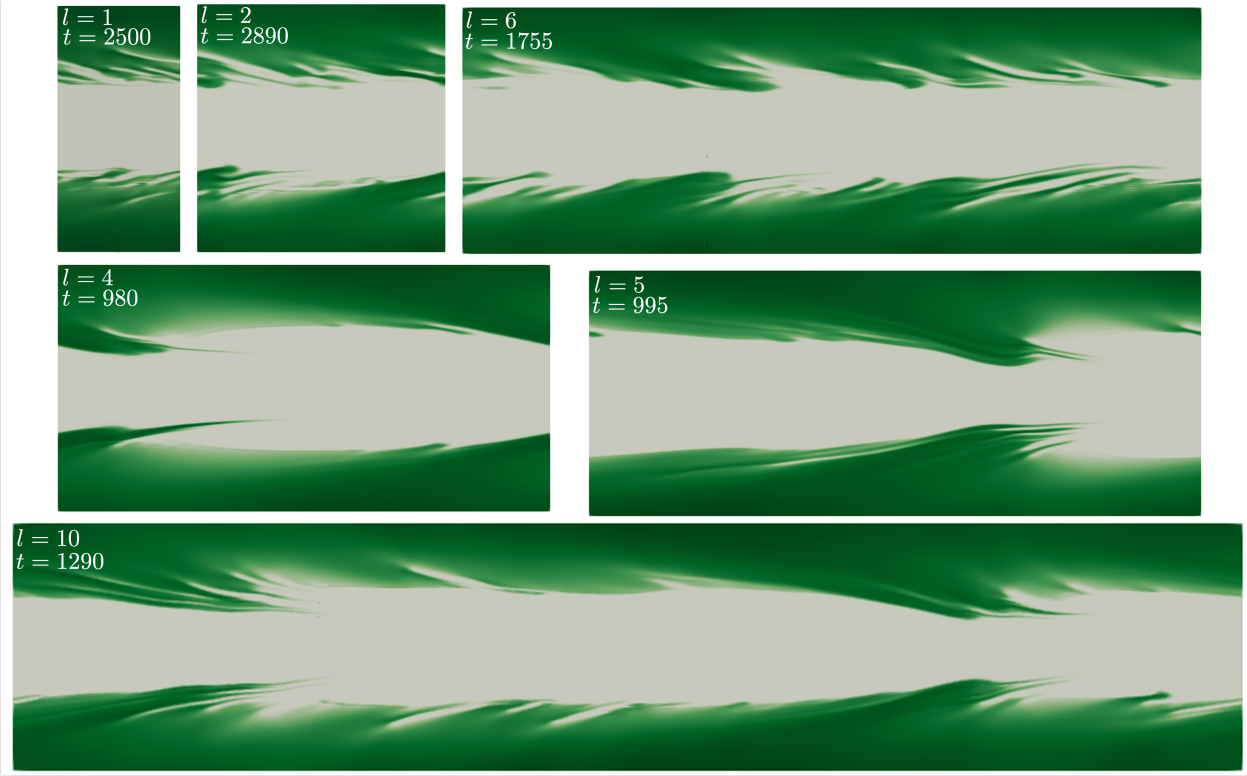


**Figure 4.16:** Snapshots of micelle length in different box lengths, $l$, for start-up PPF with an applied shear rate of Pe = 0.04.

ever observe mushroom patterns. For $l = 2$ there is a trace of an arrowhead that appears, but even after 5000 time units this does not evolve to a more coherent longwave structure. It is likely that at these small box lengths the longwave modes do not to exist. As we saw in Fig. 4.11, the mushroom pattern first appears in box with $l = 3$.

In larger box sizes, $l = 4$ and $l = 5$, the longwave mushroom patterns appear and have approximately the same width in the wall-normal direction but are significantly stretched along the streamwise direction compared to $l = 3$. Despite this stretching it is clear that the base structure is still equivalent to that observed in the $l = 3$ domain. For box sizes with $l = 6$ we do not observe any longwave mushroom patterns even after 5000 time units, rather the flow is dominated by shortwave structures. There are faint traces of multiple arrowhead-like structures that are somewhat blurred by the shortwave structures; these arrowheads may eventually give way to mushroom-like structures but that was not observed in these simulations. For the largest box size of $l = 10$, we actually observe two mushroom patterns, though neither of them are as smooth as the pattern seen in $l = 4$; rather, these mushrooms are highly stretched in the streamwise direction and their boundaries are interspersed with shortwave structures that disrupt the smoothness. This double mushroom structure suggests that the wavelength of these patterns may be around between $l = 3$ and $l = 5$; the boxes smaller than $l = 3$ clearly cannot support the longwave structures, while the $l = 6$ box may be at an intermediate size that is too long to support one mushroom and too short to support two.

### 4.4.3 Interfacial instabilities with convection in 2D

We now wish to investigate the effects of convection on the reentrant instability. To do this we will no longer approximate an inertialess flow condition by neglecting convective terms in the momentum equation, rather we will solve the full momentum equation with convection and vary the Reynolds number (Re). In Newtonian viscosity-stratified flows increasing Re tends to destabilize the flow [156], however, linear stability analysis of viscosity-stratified

Oldroyd-B fluids has shown that if the velocity profile is convex and elastic stratification alone is not enough to preserve stability (the more elastic fluid must be in the larger layer), then increasing the Reynolds number can actually stabilize the flow [162].

In this investigation into the effects of convection we will limit ourselves to Pe = 0.04. Figure 4.17 shows the streamwise-averaged (a) micelle length and (b) micelle shear stress sampled at $y = 0.5$ for varying Re ranging from Re = 0.01 to Re = 100. This location was chosen for sampling because it is where the majority of the fluctuations between lower and upper branches occur. It is clear that increasing Re induces an overshoot in both the micelle length and stress. For Re = 100 the overshoot is quite dramatic and actually leads to a brief oscillation about the steady state. For the lower Re = 0.1 an overshoot is present but it is much weaker than that of the larger values. We can understand this overshoot by considering the fact that increasing Re acts to slow the transfer of momentum, which manifests as an increased duration for the velocity to reach a steady state. Figure 4.18 shows the (a) local streamwise velocity and (b) local shear rate profiles across the channel over several time points and at $x = 1.5$ for the extreme case of Re = 100. This is compared to the convection-free case shown in Fig. 4.8 (note that colors do not correspond to equivalent times). In the convection-free case the velocity reaches a maximum of about $v_x \approx 0.8$ within two time units, whereas for Re = 100 it takes until about $t \approx 30$ to reach a maximum and in this case it is smaller at about $v_x \approx 0.5$. By $t = 30$ the convection-free velocity has already settled onto a steady state of sorts, characterized by the parabolic central region surrounded by the almost linear near-wall regions. The longer duration spent with an increased velocity in the Re = 100 case results in a prolonged increase in the local shear rate, which is the origin of the dramatic overshoot in the micelle length (and therefore also the stress since elongated micelles increase the stress). The large shear rates rapidly orient micelles leading to rapid elongation. However, this prolonged increase in the shear rate is also what causes the dramatic undershoot that follows as the highly elongated micelles are then broken up by the shearing.

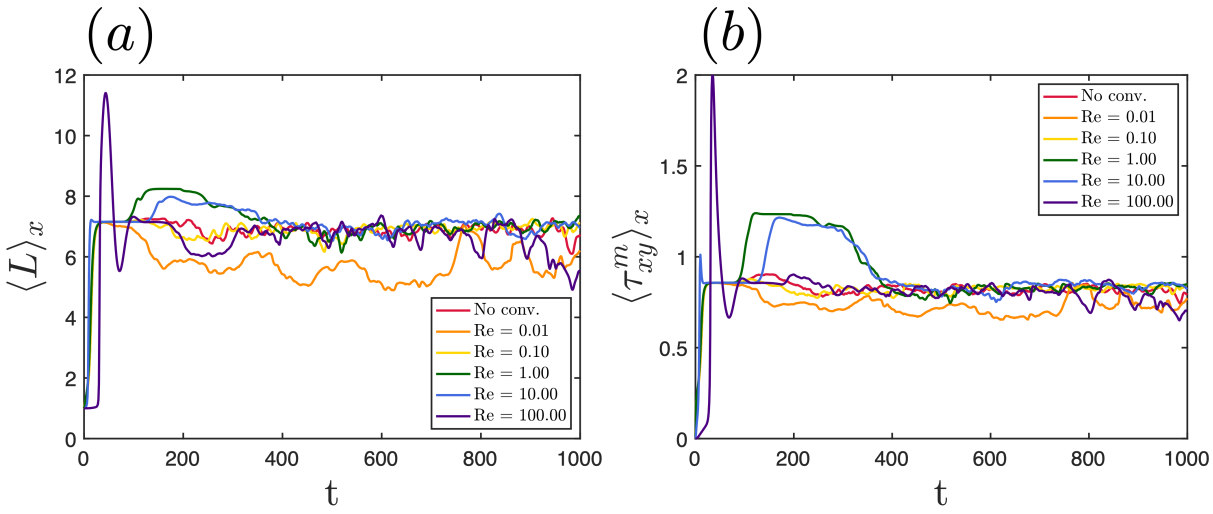


**Figure 4.17:** Streamwise-averaged (a) micelle length and (b) micelle shear stress sampled at $y = 0.5$ for varying Re with Pe $= 0.04$.

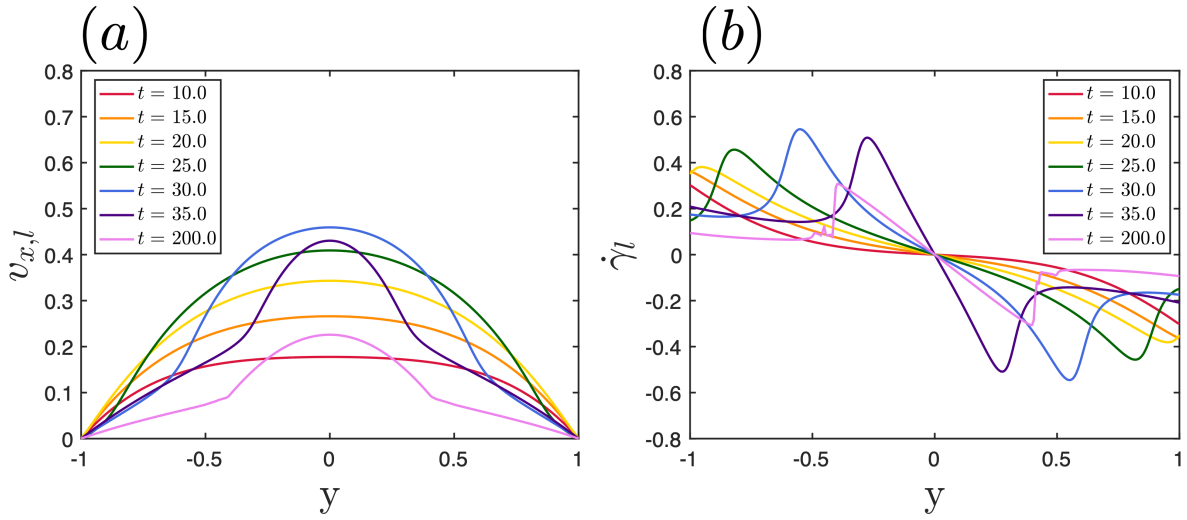


**Figure 4.18:** (a) Local streamwise velocity and (b) local shear rate profiles across the channel over several time points and at $x = 1.5$ for start-up PPF with an applied shear rate of Pe $= 0.04$ and Re $= 100$.

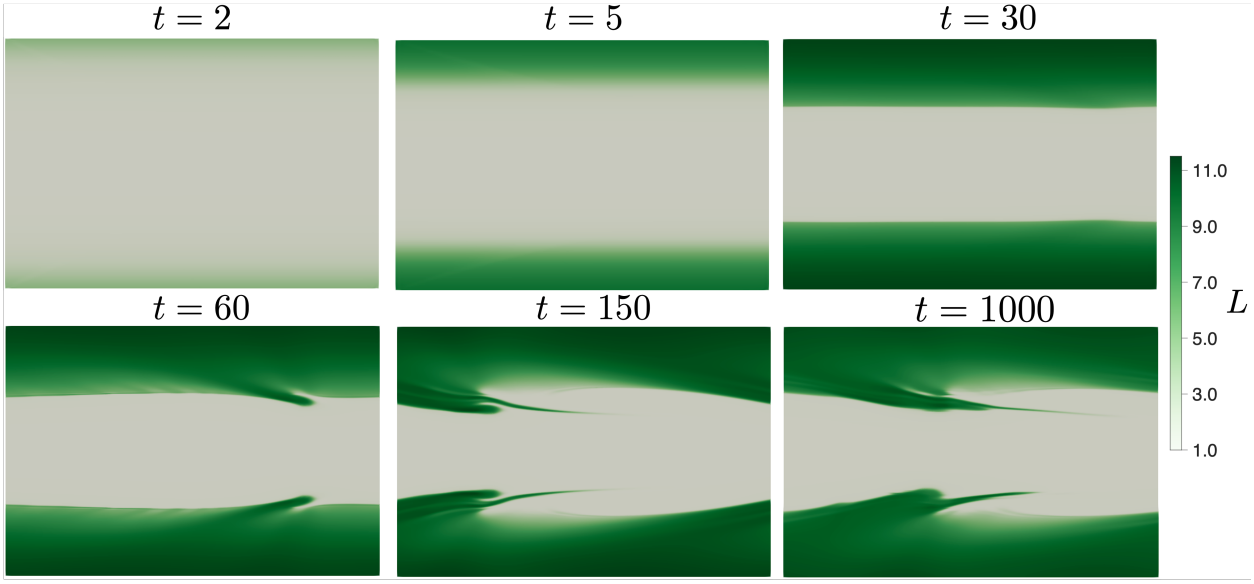


**Figure 4.19:** Snapshots of micelle length for start-up PPF with an applied shear rate of Pe = 0.04 and Re = 0.01.

It is also interesting that for Re = 0.01 the long time fluctuating behavior of both the length and stress seem to be noticeably smaller than the convection-free and other Re cases. It is not immediately obvious what leads to the decreased streamwise average, however, if we turn to Fig. 4.19, which shows snapshots of the micelle length for Re = 0.01, we see that this flow immediately evolves to a mushroom pattern. In fact, this flow shows little if any shortwave structures for its duration; this lack of shortwave structures, which if present would lead to a greater number of fluctuations around the sampling location of $y = 0.5$, is what causes the decreased streamwise averages of length and stress. The mushroom pattern has a width of about 1 centered around the centerline, meaning that $y = 0.5$ is exposed to extended spans of of low stress fluid with equilibrium-length micelles and thus has a lower average stress and length.

Focusing in on the flow with Re = 100, we see a new pattern emerge. Figure 4.20 shows several snapshots of micelle length for Re = 100. At this Re the flow takes much longer to destabilize, first showing signs of an instability around $t = 150$ compared to the $t = 60$ seen in the low Re and convection-free flows. Again, this can be attributed to the reduced transfer of momentum and the over- and undershoots that occur before the flow can fully develop sharp

interfaces. The fact that this flow takes longer to show an instability because of the delay in developing an interface suggests that the instability is driven by the interfacial mechanisms (i.e., viscosity mismatch and normal stress jumps) rather than the unstable region of the flow curve; however, the dynamics and fluctuations following the destabilization of the instability are driven by the reentrant flow curve.

By $t = 350$ the flow has destabilized and shows a mix of short- and longwave structures. At $t = 500$ the shortwave structures have begun to merge and we can see the faint development of more longwave structuring which, by $t = 1015$, has almost evolved into the mushroom patterning. By $t = 1300$ (not shown) the flow exhibits a clean mushroom pattern that persists for several hundred time units. Around 2250 the symmetric structures that make up either side of the mushroom pattern begin to deviate in their phases. This out-of-phase behavior strengthens and persists, and by $t = 3000$ we see an almost sinuous pattern as the structures on either side are almost perfectly out-of-phase. This is interesting because in addition to the varicose mode observed in the mushroom patterns, we now seem to be observing a sinuous mode. Both of these modes have been reported in viscosity-stratified flows [161], which again emphasizes the connections between the reentrant instability observed here for dilute WLM solutions and the interfacial instabilities observed in viscosity-stratified flows.

We can now summarize the effects of convection on the reentrant, or interfacial, instability observed in PPF. In general it was found that convection, specifically at higher Re, tends to delay the instability. This delay was found to occur because of slower momentum transfer and increased time for the flow to develop sharp interfaces. Since it is the sharp interfaces, and specifically the viscosity mismatch and normal stress jump across them, that drive the instability, any delay in interface formation will then delay the instability. At higher Re ($\mathrm{Re} \gtrsim 1$) the flow exhibits a stress overshoot, and for $\mathrm{Re} = 100$ the overshoot is followed by a subsequent oscillation about the steady state. Overshoots and undershoots are observed in many start-up flow of viscoelastic fluids, and are known to occur in the RRM-R in start-up of

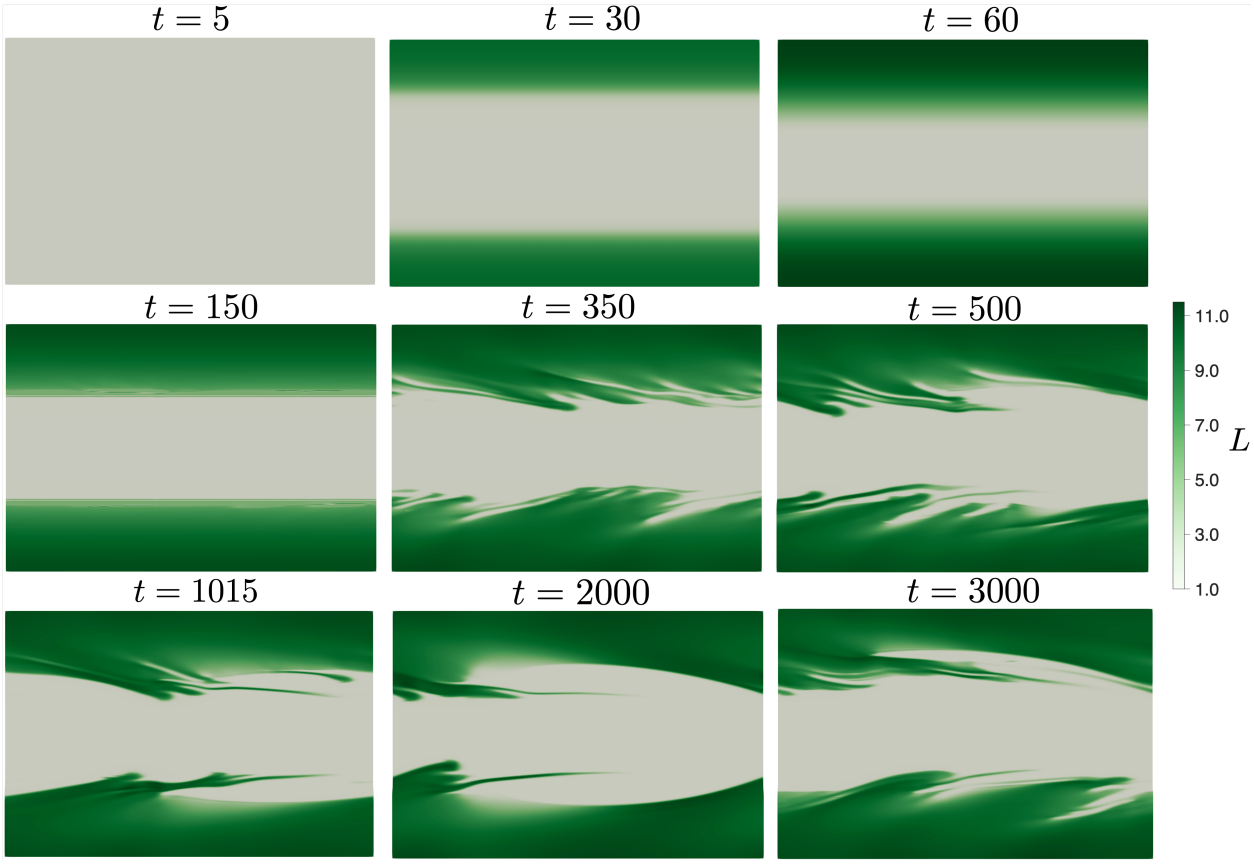


**Figure 4.20:** Snapshots of micelle length for start-up PPF with an applied shear rate of Pe = 0.04 and Re = 100.

steady shear flow [129]. The overshoot is caused by a prolonged time spent with an increased shear rate, which occurs due to the increased time required for the velocity to reduce to its steady state at larger Re; this increased shear rate drives alignment and growth of micelles. For Re = 100, the increased shear rate occurs for long enough that it eventually increases micelles to their maximum length and then begins to break them down as the micelles can not support the increased stress, leading to an undershoot. Finally, at long enough times we observed that the mushroom structures, which suggest the presence of in-phase varicose mode, eventually gave way to a curved, bend-like structure that suggests the presence of an out-of-phase sinuous mode.

### 4.4.4 Convection-free interfacial instabilities in 3D

In the final section of this work we study the consequences of shifting from a 2D to 3D domain on the interfacial instability. The results presented for the 3D domains will focus exclusively on simulations without convection and use the M1 mesh with 20 grid points in $z$ and have a periodic width of $w = 0.1$. This resolution is admittedly low, but was chosen to balance the computational cost of these simulations with the desire to obtain a certain time duration. Before proceeding, we note that our previous work on reentrant instabilities in circular Couette flow showed that the initial instability is 2D in nature ($r\theta$) and that 3D variations along the vorticity axis ($z$) are secondary effects. Moreover, while the development and early behavior of the instability was identical in both 2D and 3D simulations, the long time dynamics differed in that fluctuations in $r\theta$ were weakened and less frequent as the flow was then able to resolve stress along $z$ rather than being confined to 2D. We now wish to investigate the effects of moving from 2D to 3D in plane Poiseuille flow.

Figure 4.21 shows several snapshots of micelle length for 3D simulation with no convection for Pe = 0.04 and $w = 0.1$. The larger snapshots on the left of each time show the $xy$-plane, sampled at $z = 0.05$, while the smaller snapshots on the right show the $yz$-plane, sampled at $x = 0$, and look along the positive streamwise direction. We can see that up until about

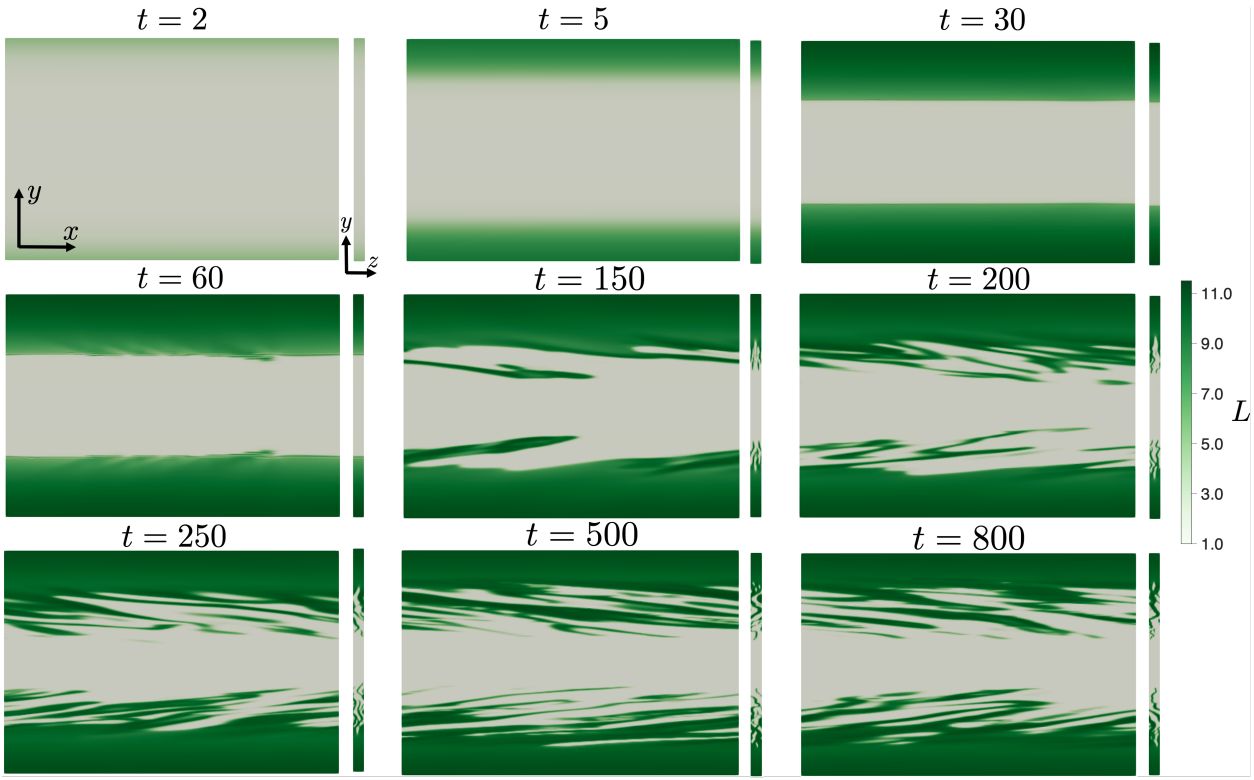


**Figure 4.21:** Snapshots of micelle length in 3D for start-up PPF with an applied shear rate of Pe = 0.04. Time points are indicated above each snapshot; each snapshot shows the a slice in the $xy$-plane on the left, taken at $z = 0.05$, and a slice in the $yz$-plane on the right, taken at $x = 0$. The length is $l = 3$ with width $w = 0.1$.

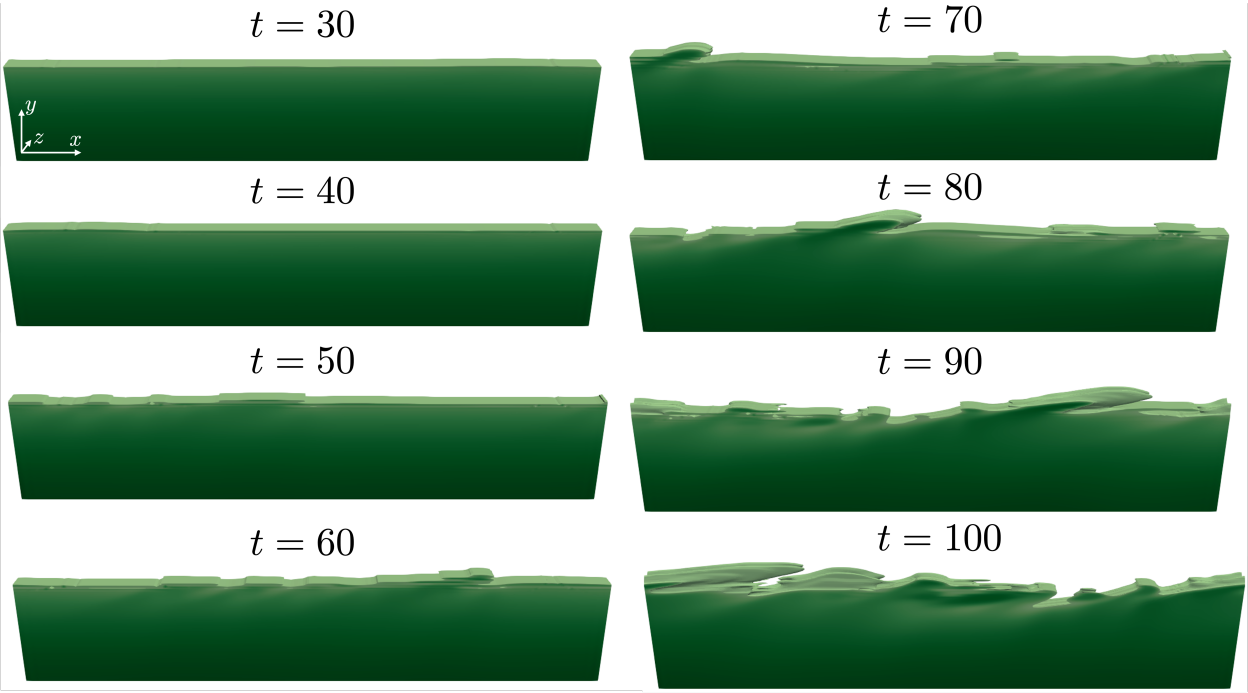


**Figure 4.22:** Structures of micelle length in 3D for start-up PPF with an applied shear rate of $\mathrm{Pe} = 0.04$. Time points are indicated above each snapshot. The length is $l = 3$ with width $w = 0.1$. Only the lower half of the domain ($y \leq 0$) is shown for clarity. Structures show regions of $L \geq 5$, indicating substantial micelle elongation.

$t = 60$ the flow is nearly identical to the 2D scenario shown in Fig. 4.6 and there is no variation along the vorticity axis. This result agrees with the findings in CCF that showed the initial reentrant instability is 2D in nature [148]. At $t = 150$ the flow in the $xy$-plane strongly deviates from the 2D behavior and there are clear variations along $z$. Compared to the 2D scenario, the regions of elongated micelles that fluctuate towards the center of the channel are much thinner and longer; this observation agrees with the results found in CCF, which showed long branches that stretched along $\theta$. It is also clear that at $t = 150$ the flow is already asymmetric. This early asymmetry arises because the flow can relieve stress through the vorticity axis rather than being confined to the $xy$-plane.

At $t = 200$ the flow again deviates strongly from the structures observed in 2D geometries; the fluctuations along $z$ have strengthened and manifest as long 'fingers' that stretch from the walls to the center of the channel. These 'fingers' consist of elongated, anisotropically-oriented micelles that are identical to those observed in CCF. At this time there is a weak

flow in both the wall-normal and vorticity directions. Interestingly, the behavior in $xy$ seem to be a mix of short- and longwave structures in $xy$ but also show no mushroom or sinuous patterns; rather, the structures exist as very long, but broken, threads in $xy$ that are thin in $z$. It is clearly that the choppiness of the threads in $xy$ is due to the wave-like behavior of the 'fingers' in $z$. These threads continue to elongate and breakup, shown in $t = 250$. This behavior then continues through $t = 500$ and $t = 800$ with continual stretching and breaking of the threads as fluctuations continue along $z$. Looking specifically at the $yz$ snapshots, it appears that on average two main fingers can exist on either side of the channel, though there are smaller secondary fingers present. It is likely that by increasing the width of the channel more fingers will develop and persist.

To investigate the development of the instability in 3D, Fig. 4.22 shows snapshots of surfaces of micelle length for this flow. Only the lower half of the domain is shown for clarity. Structures show regions of $L \geq 5$, indicating substantial micelle elongation. From $t = 30$ to $t = 60$ we can see the development of a 2D sheet of elongated micelles that is sheared off from the interface. Up until $t = 60$ there are no variations along $z$, which is consistent with the observations for instabilities in 3D. At $t = 70$, the sheet continues to be sheared off towards the center of the channel by the high velocity in the central region; as this shearing takes place the previously 2D sheet begins to develop ripples along the surface, giving rise to 3D variations. The ripples start to form two dominant 'fingers', the wavelength of which is likely dictated by the width of the channel. At $t = 80$ and $t = 90$ these ripples continue to grow and disrupt the sheet and by $t = 100$ the flow is highly three-dimensional. Again, this process of the flow developing a 2D sheet that develops surfaces ripples that eventually induce 3D fluctuations is identical to the instability process observed in circular Couette flow. We can safely conclude that the instability in PPF is also 2D ($xy$) and that 3D variations arise as secondary effects.

## 4.5 Conclusions

This study focuses on the formation of interfacial instabilities in plane Poiseuille flow of dilute wormlike micelle solutions. We have used the reformulated reactive rod model (RRM-R), which models micelles as reactive Brownian rods, to simulate dilute WLM solutions that exhibit reentrant flow curves. We found that a reentrant flow curve, in which there there exists a region of the flow curve where the shear stress is a multivalued function of shear rate, can provoke the development of interfacial instabilities. In particular, the wall-normal dependence of the shear stress in PPF allows for solutions where the domain can jump between upper and lower branches of the flow curve, resulting in an 'interface' between regions of elongated, anisotropically-oriented micelles and near-equilibrium length, isotropic micelles. This interface straddles the unstable region of the flow curve, $\partial\tau_{xy}/\partial\dot{\gamma} < 0$, such that any perturbations to the interface lead to instability development. Notably, the interface is destabilized both by viscosity mismatch, which leads to a vorticity mismatch across the interface, as well as a normal stress jump between regions. Further, our findings suggest that the initial destabilization is driven by interfacial mechanisms, while the long-time fluctuating behavior is driven by the unstable nature of the flow curve.

At low enough Péclet numbers such that the flows exists entirely on the stable lower branch, no instability was observed. In the convection-free case, as Pe was increased to push the flow onto the upper branch, two interfaces developed separating the central region, consisting of near-equilibrium length micelles, from the near-wall regions, consisting of highly elongated micelles. The fluid containing the shorter micelles is much less viscous than the fluid containing the elongated micelle, leading to the appearance of a viscosity-stratified flow. Before destabilization, this viscosity-stratified flow consisted of a parabolic velocity along the centerline connected to linear velocity profiles close to the walls. The interfaces quickly destabilized, leading to fluctuating structures consisting of 'fingers' or branches of elongated micelles originating in the near-wall regions. In some instances the instability was found to be dominated by shortwave structures comprising short fingers that stretch towards

the centerline but are sheared along the streamwise direction; in other instances the flow was dominated by longwave structures comprising a mushroom pattern that has previously been observed in core-annular channel flow of viscosity-stratified Newtonian fluids [159]. It was found that the flow can alternate between durations where either short- or longwaves dominate, as well as durations where both structures are present.

Increasing the Pe even further (e.g., Pe = 0.06) decreased the width of the central region but did not affect the structures. We also investigated the effects of changing the box length ($l$), which effectively changes the wavelength of structures that can exist in the flow. Decreasing the box length to $l \leq 2$ was found to prevent the formation of long wave structures (e.g., mushroom patterns). At increased box lengths, $l \geq 4$, we observed that the long wave mushroom patterns were still present but now stretched along the streamwise direction. At the largest box length, $l = 10$, two mushrooms were found to coexist along the streamwise direction.

We also investigated the effects of introducing velocity convection and varying the Reynolds number. We found that scenarios with convection were characterized by a delayed formation, and consequently destabilization, of the interfaces, which was attributed to slowed momentum transfer. At larger Reynolds numbers, Re $\gtrsim$ 1, an overshoot was observed in the micelle stress, driven by an overshoot in the micelle length. Similar overshoots have been observed in the start-up of steady shear flow using the RRM-R [129]. The overshoot is attributed to the fact that at larger Re, the velocity and shear rate take longer to reduce to the steady state profile observed when the interfaces form. The longer duration of increased shear is able to align and elongate micelles more than what is seen at lower Re. In the case of Re = 100 an undershoot is observed following the overshoot; at this Re the increased shear occurred for long enough that micelles elongate to their maximum lengths and then are actually broken down by the flow as the stresses become too great. At Re = 100, we observed that the flow transitioned from short- and longwave structures, to an out-of-phase longwave structure (called the mushroom pattern), to in-phase longwave structures (seen as

a sinuous pattern). Both out-of-phase (varicose) and in-phase (sinuous) modes are known to exist in core-annular channel flow [161].

In 3D simulations we found that, just as was found for circular Couette flow [148], the initial instability is 2D in nature and 3D effects arise secondarily. In fact, the early time behavior, including the development and destabilization of the interfaces, is identical in 2D and 3D; however, as the interfaces destabilize in 3D the structures are able to stretch into the vorticity direction, which drastically changes the long time dynamics of the flow. In particular, the 3D simulations show 'fingers' of elongated micelles that undulate in $z$, giving rise to a mix of short- and longwave structures in $xy$. These structures appear choppy in the $xy$ plane as the fluctuations in $z$ cause the 'fingers' to rapidly enter and exit the 2D plane.

This work on plane Poiseuille flow, combined with the previous work on circular Couette flow, shows that reentrant flow curves are abound with interesting and poorly understood instabilities. The mixed stability of reentrant constitutive curves can be exploited by flows with spatially-dependent stress profiles, leading to rich and unexplored dynamics. Future work will look at the behavior of reentrant WLM solutions in cross-slot, porous, and jetting flows to see how reentrant instabilities manifest in these scenarios. Additionally, we plan to perform rigorous linear stability analysis of the RRM-R to determine the exact mechanisms and modes of destabilization.

## 4.6 Appendix A: Additional figures for PPF

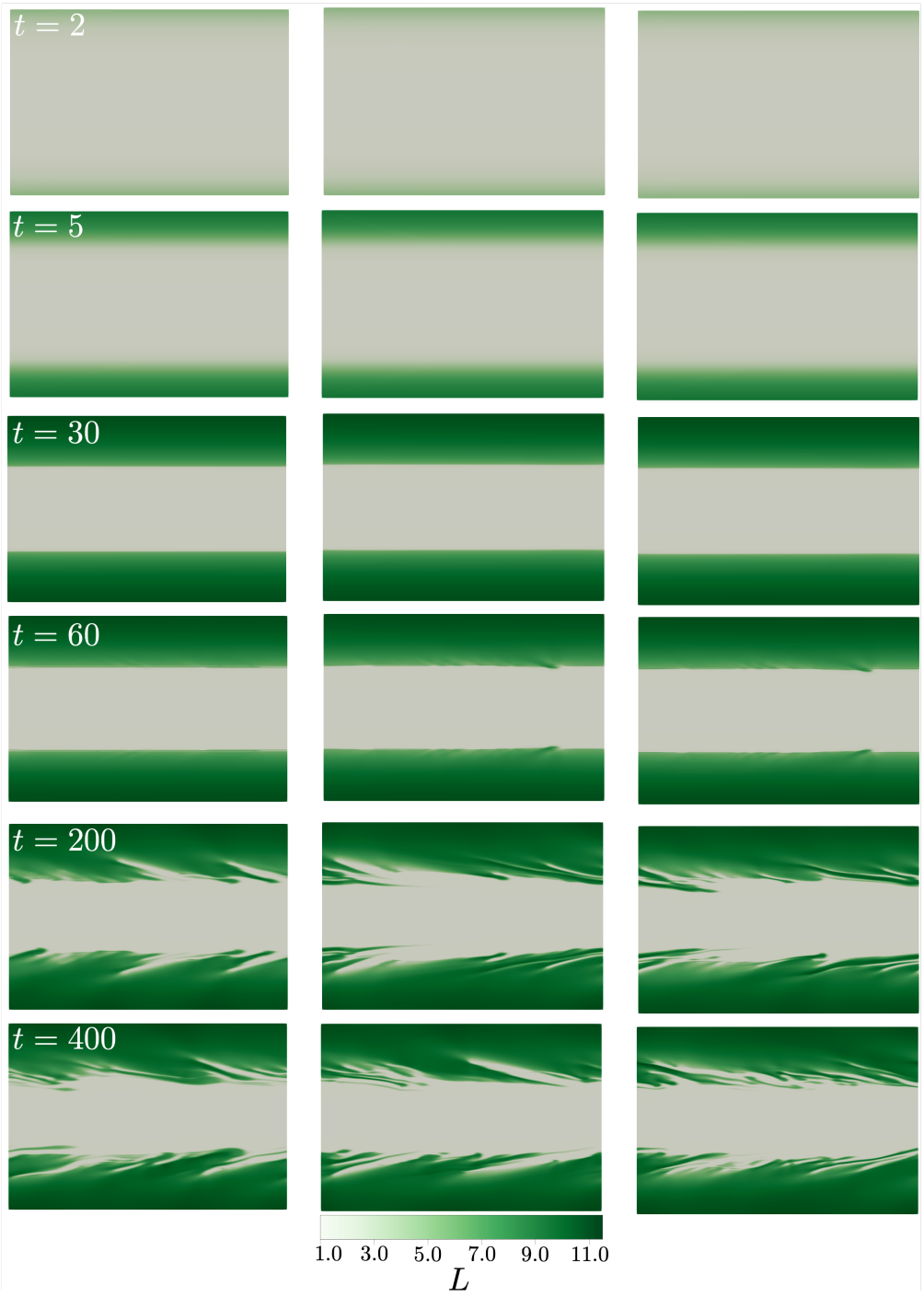


**Figure 4.23:** Snapshots of micelle length for start-up PPF with an applied shear rate of Pe = 0.04. The first column shows simulations run with the M1 mesh, the second column the M2 mesh, and the third column shows simulations run with the M3 mesh.

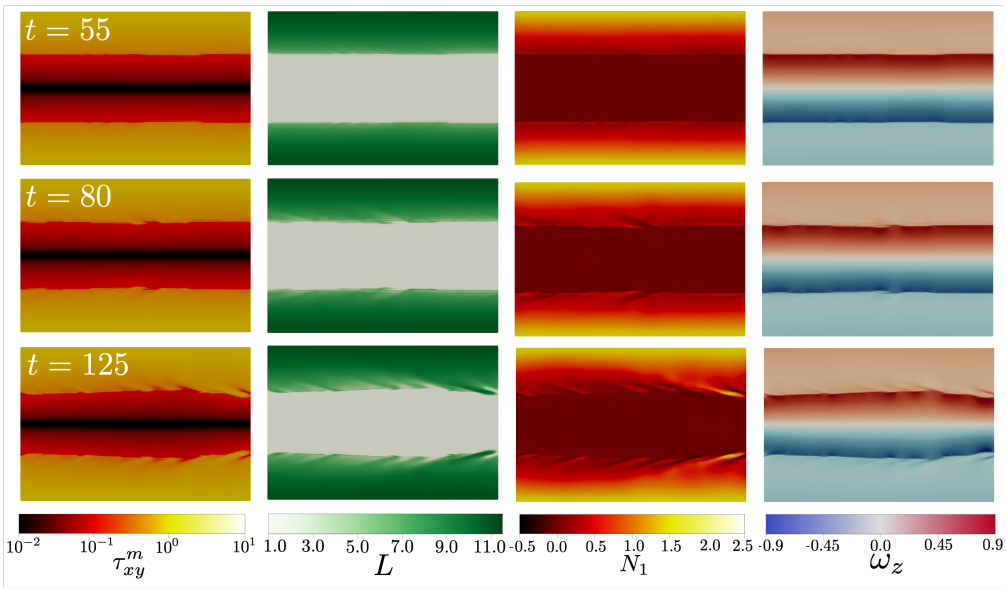


**Figure 4.24:** Intermediate time snapshots of first column: micelle shear stress, second column: micelle length, third column: first normal stress difference, and fourth column: vorticity for start-up PPF with an applied shear rate of Pe = 0.04.

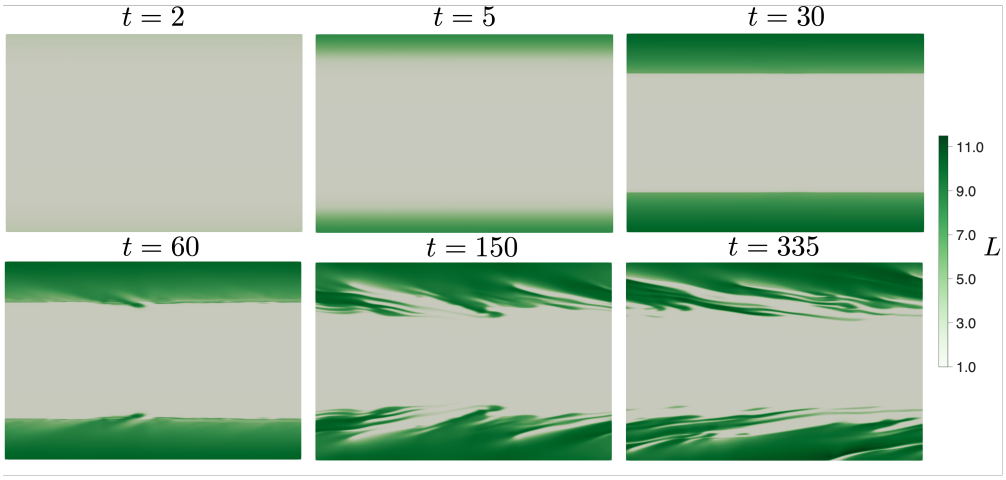


**Figure 4.25:** Snapshots of micelle length for start-up PPF with an applied shear rate of Pe = 0.03.

# 5

# Modeling using non-equilibrium thermodynamics

In this section, we aim to derive thermodynamically consistent models for dilute wormlike micelle solutions using the single generator bracket framework (SGBF) of non-equilibrium thermodynamics (NET). We derive three models, the SM-A, SM-B, and SM-C, by considering a wormlike micelle solution that is fully defined by the state variables: momentum density, orientation density, and a structural variable to track micelle length. These state variables fully define the system Hamiltonian, and are employed in a Poisson bracket framework that has been modified to account for dissipative phenomena in flowing systems [164]. The SM-A and SM-B assume general dissipative dynamics of the micelle length, while the SM-C considers the reaction kinetics and energetics associated with reversible scission and fusion. We show that these models are all thermodynamically admissible. The models derived in this section, particularly the SM-C, are not meant to serve as finalized models, but rather act as proof-of-concepts that models for dilute wormlike micelle solutions can be derived using the SGBF-NET formalism. Since many readers will likely be unfamiliar with non-equilibrium thermodynamics, we also follow [164] to provide an overview and examples on the application of SGBF to develop models for viscoelastic fluids.

The objective of this section is to derive a thermodynamically consistent model that phys-

ically represents dilute wormlike micelle solutions and is able to capture the quintessential rheological features associated with these solutions, namely: shear-thickening and -thinning, flow-induced structure formation, and a reentrant flow curve. Before proceeding, it is important to understand what is meant by the expression 'thermodynamically consistent,' or equivalently a model can be 'thermodynamically admissible.' In this work, and generally in the engineering community, it comprises two main properties: (1) conservation of energy and (2) non-negative entropy generation. It is important to note that the first statement does not imply that the total energy of a system is constant; in many applications, such as in the modeling of many complex fluids, heat effects are considered unimportant so that as mechanical energy is degraded to heat by dissipative forces this energy is essentially lost, at least from the perspective of the system [164]. Importantly, these two properties combine to ensure that a model does not violate the second law of thermodynamics.

We will formalize both of these properties into equations, but first we must consider why we desire a thermodynamically admissible model. As we will see, the derivation of a thermodynamically consistent model is a rigorous exercise and moreover the framework used to derive such a model does not guarantee that a model is thermodynamically consistent, rather it provides the necessary tools and formulation for checking whether or not a model is consistent. Why, then, should we perform the herculean task of deriving such a model when there are plenty of presumably thermodynamically inconsistent models that are perfectly well-suited for describing many fluid systems? There is no simple answer to this question, but we must acknowledge two points. The first is that these other models are not 'perfectly well-suited' because if they do violate the second law of thermodynamics then heat can spontaneously flow from a cold region to a hot one, and that is undoubtedly unphysical. The second point is that to those unfamiliar with non-equilibrium thermodynamics, and specifically working within bracket formalisms, the task of deriving an admissible model may seem extraordinary; however, most of the work needed to derive a model is explained and laid out quite well by a number of previous researchers, and thus deriving new thermodynamically

consistent models does not require reinventing the wheel but rather moulding the existing framework to match current needs.

## 5.1 Introduction

Wormlike micelles are self-assembled structures comprised of amphiphilic surfactant molecules. In the dilute regime, wormlike micelles exist as nearly rigid rods with comparable persistence and contour lengths on the order of $\sim \mathcal{O}(10 - 100\text{nm})$ [61, 125, 59, 60, 5]. In flow, wormlike (or rodlike) micelles in this concentration range are known to exhibit both shear-thickening and shear-thinning [9, 10, 11, 12, 13, 62, 61], reentrant flow curves (e.g., a multivalued shear stress vs. shear rate curve) [50], and the formation of flow-induced structure. Shear-thickening and -thinning behavior is related to the formation and subsequent breakdown of flow-induced structure (FIS), which takes the form of highly elongated and aligned micelles. Specifically, at moderate shear rates WLMs have been observed to align with the flow and undergo significant elongation, whereby the average length of micelles in solution can increase to several times the equilibrium length. This elongation has been observed experimentally by Keller and coworkers using free-fracture electron microscopy [46]. Additionally, due to challenges with making a direct measurement of micelle length, some researchers have made estimates of the micelle length by analyzing the effect of flow on the solution viscosity [63, 64].

Dilute wormlike micelle (WLM) solutions are also known to exhibit a number of unique and complex instabilities. Solutions that demonstrate a reentrant flow curve, in which a single shear rate is able to support multiple stable shear stresses, can support a vorticity banding instability [50]; in vorticity banding, the solutions separates into macroscopically 'banded' flow along the vorticity direction, where separate bands support equivalent shear rates but distinct shear stresses. The separation of these two regions is often observable through differences in turbidity and birefringence [47, 52]. In addition to vorticity banding,

dilute WLM solutions have demonstrated a group of finger-like instabilities in circular Couette flow that appear as unstructured streaks and branches spanning the flow gap [69, 70]. Using a circular Couette device, Liu and Pine [4] observed these finger-like structures in controlled-shear rate flows of $\sim \mathcal{O}(10^2 - 10^3)$ ppm equilmolar CTAB/NaSal solutions; using small angle light scattering (SALS), they revealed reversible finger-like structures that, upon increasing shear rate, grew outwards from the inner cylinder into the flow gap. Hu and coworkers [71] observed similar structures in a solution of equimolar 7.5 mM TTAA/NaSal that exhibited a reentrant flow curve. Similar to Liu and Pine, the authors observed that increasing either the shear rate or shear stress beyond some critical value induced shear-thickened structures that originated at the inner cylinder and grew outwards to fill the gap. These solutions have also been shown to exhibit numerous other instabilities in cross-slot flows [72], extensional flows [10, 13, 30], and shearing flows [11].

There have been numerous models put forth for understanding the rheological behavior and dynamics of dilute wormlike micelle solutions. One of the first attempts to develop a wormlike micelle model was by Cates and Turner, who proposed a population balance model accounting for the different stress relaxation mechanisms associated with wormlike micelles, namely micelle scission and rotational diffusion [73, 110]. Though Cates and Turner did not write down an explicit constitutive equation for their model, and moreover the incorporation of a continuous spectrum of micelle lengths is prohibitive for use in computational fluid dynamics (CFD) studies, their formulation has served as a foundation for the development of other widely used WLM models [76, 3]. Bautista and coworkers [113] have developed the BMP model, which couples a fluidity equation for studying thixotropic systems [93] to the Oldroyd-B equation. This model, as well as its many extensions and generalizations [90, 141], has shown good agreement with dilute wormlike micelles in a variety of flows [142], and has recently been used for studying viscoelastoplastic and gradient banding fluids [142]. Tamano and coworkers [99] have taken inspiration from the BMP model and coupled the fluidity equation to both the Giesekus and FENE-P models to form the f-Giesekus and f-

FENE-P models, respectively. These models are well-suited for CFD studies, however, they are unable to predict reentrant flow curves and are therefore unlikely to predict vorticity banding or finger-like instabilities. Dutta and Graham have developed the the reactive rod model (RRM), which models WLMs as reactive Brownian rods undergoing reversible scission and fusion in flow [3]; this was extended and improved into the reformulated reactive rod model (RRM-R) by Hommel and Graham, who then used it in CFD simulations to study finger-like instabilities and vorticity banding [129, 148].

There has been push over the last several decades in the rheological community to re-visit many models for viscoelastic fluids from a non-equilibrium thermodynamics (NET) perspective, and this push has also extended to deriving new rheological models using NET frameworks. The aim of this push is to ensure the thermodynamic consistency and validity of rheological models, specifically by enforcing conservation of energy and adherence to the second law of thermodynamics [164]. This effort has been largely made possible and lead by pioneering work by Grmela, Morrison, Kaufman, Beris, Edwards, Öttinger, and others [165, 166, 167, 168, 164, 169, 170, 118, 171, 172, 173] aimed at extending the Poisson bracket formalism to dissipative systems, which allows it to be used for developing models for complex fluids. There are currently two primary NET description for describing dissipative systems: the single generator bracket formalism (SGBF), which relies on the Hamiltonian, and the GENERIC formalism (also called double generator bracket formalism), which relies on the entropy functional in addition to the Hamiltonian [174]. In this work we will exclusively employ SGBF, though we note that at the macroscopic scale the two are actually equivalent. Understanding and pursuing the SGBF-NET formalism for deriving models requires a great deal of background, which we will do our best to condense and summarize in the following section to allow for a proper understanding of this work. Additionally, since non-equilibrium thermodynamics is not readily taught in most engineering disciplines, we will also provide suitable examples when possible.

Before proceeding, it is important to mention recent work that has successfully employed

NET for deriving or re-deriving models for viscoelastic fluids. Manero and coworkers [90] have derived the generalized BMP model using an extended irreversible thermodynamics (EIT) formalism. EIT assumes that in addition to the typical conserved hydrodynamic densities (e.g., momentum) there exists a generalized entropy that depends on non-conserved variables in a system; in this way, the state variables describing the systems become a conserved concentration and non-conserved variables representing fluid structure, mass flux, and stress. The generalized BMP model, which is meant to describe semi-dilute solutions, amounts to an Oldroyd-B constitutive equation coupled with an kinetic evolution equation for the fluidity of the system and shown success in predicting shear-thickening and -thinning as well as a non-monotonic (e.g., shear banding) flow curve [7].

Germann and coworkers [88] have used the SGBF to re-derive a thermodynamically consistent version of the VCM model (culminating in the GCB model). These authors successfully incorporated a reversible reaction scheme $A \leftrightarrow 2B$, meant to model the reversible reaction from long to short micelles, providing a clear example of how reactions can be included in viscoelastic models using NET. These authors consider a system described by the total momentum density, total velocity field, and conformation densities for each of the micelle lengths. They employed a standard Hamiltonian for systems described by conformation densities, along with a Flory-Huggins mixing term to account for the entropy of mixing between components. They also modified the chemical potential to form a generalized chemical potential that accounts for Galilean invariance. Using this framework, Germann and coworkers successfully derived the thermodynamically consistent GCB model, which can capture all the features associated with the original VCM model (notable shearbanding through a non-monotonic curve).

In terms of new models, Stephanou and coworkers have used the single-generator bracket formalism (SGBF) of NET to derive thermodynamically consistent models for: thixotropic elasto-viscoplastic materials [175], aggregating blood [104, 176], and cement pastes [177]. Notably, these authors have also employed the reaction dissipation brackets of Germann and

coworkers to account for reacting systems when modeling cement pastes. In their work on modeling red blood cell deformability in Ringer solutions, Stephanou and coworkers have enforced conservation of volume constraints in their system [105].

## 5.2 SGBF-NET Formalism

In this section we provide an overview of the SGBF-NET framework and its application to complex fluids modeling. This section draws heavily from the textbook by Beris and Edwards [164], who have condensed the SGBF-NET framework into an approachable form and provided numerous examples on its applications to modeling. The SGBF-NET formalism is a generalization of the Poisson bracket description, which is the most general description of Newtonian mechanics, that extends the Poisson framework from conservative systems to dissipative systems. The extension to dissipative systems is of course crucially important for studying non-ideal fluid systems due to the presence of viscosity. To derive a set of evolution equations within SGBF-NET, we must follow six steps (each of which will be elaborated on below):

1. Identify a set of suitable state variables, $\mathbf{x} = \{x_1, x_2, ..., x_N\}$, that fully describe the system. For viscoelastic fluids these will typically include a momentum density and a conformation or orientation tensor density, but may also include moments of a distribution if a population balance is present or a structural variable to account for reactions.

2. Define the extended free energy of the system, the Hamiltonian, $H$, as a functional involving the system state variables. In this context, a functional is an integral over the system volume so the Hamiltonian is

$$H(\mathbf{x}) = \int_{\Omega} h(x_1, x_2, ..., x_N; \nabla x_i; \nabla^2 x_i; ...)\mathrm{d}V. \tag{5.1}$$

The Hamiltonian can depend on successive gradients of the state variables.

3. Formulate the Poisson bracket, $\{F, G\}$, which specifies the reversible components of the system dynamics. The Poisson bracket is an antisymmetric, bilinear functional of the Volterra derivatives for any pair of arbitrary functionals $F$ and $G$. As a note, functionals are functions that act on functions. The Poisson bracket also satisfies the Jacobi identity:

$$\{F, \{G, H\}\} + \{G, \{H, F\}\} + \{H, \{F, G\}\} = 0. \tag{5.2}$$

The antisymmetry of the the Poisson bracket ensures that the total energy of the system is conserved, $\{H, H\} = 0$.

4. Formulate the dissipation bracket, $[F, G]$, which specifies the irreversible components of the system dynamics. The dissipation bracket may include viscous dissipation, relaxation phenomena, and reaction kinetics [164, 88, 171].

5. Derive the governing equations from the governing dynamical equation:

$$\frac{\mathrm{d}F}{\mathrm{d}t} = \{F, H\} + [F, H] = \int_\Omega \frac{\delta F}{\delta \mathbf{x}} \cdot \frac{\partial \mathbf{x}}{\partial t} \mathrm{d}V, \tag{5.3}$$

where $\delta F/\delta \mathbf{x}$ are the Volterra derivatives of the functional $F$ with respect to the state variables. This step is similar to the derivation of equations of state from fundamental relations in equilibrium thermodynamics.

6. Verify thermodynamically admissibility by computing $[H, H] \leq 0$. This step typically involves identifying conditions on parameters that appear in the dissipation bracket to ensure $[H, H] \leq 0$.

When the SGBF-NET steps are laid out as they are above, it becomes clear that the process of deriving a thermodynamically admissible model is not out of reach; in fact, the most

challenging part of pursuing and employing the SGBF-NET framework is understanding the background and origins of the bracket formalism and calculus underlying the framework. Although this work will not extensively cover everything about non-equilibrium thermodynamics, we will explain the necessary components to the best of our ability. In what follows, we will go into more detail about each of the six steps and illustrate the use of the SGBF-NET formalism for deriving a thermodynamically consistent Oldroyd-B model.

### 5.2.1 Identification of state variables

The first step in using the SGBF-NET framework for deriving a thermodynamically consistent model is the identification of state variables that properly represent the system. In practice, this should be the fewest number of variables possible such that the Hamiltonian, the total energy of the system, can be fully described. For a Newtonian fluid the momentum density, $m_\alpha$, can be used to fully describe the system. The momentum density is related to the density, $\rho$, and velocity, $v_\alpha$, by $m_\alpha = \rho v_\alpha$. In the non-equilibrium thermodynamics community it is standard to use the Greek alphabet for representing vector and tensor dimensions; in a Cartesian coordinate system $m_\alpha = [m_x, m_y, m_z]^T$. For an Oldroyd-B fluid, which is used to model dilute polymer solutions by treating the polymers as bead-spring dumbbells with a Hookean force law, an additional conformation tensor density, $C_{\alpha\beta}$, is needed to describe the stretching and orientation of the dumbbells [164]. In summary, a Newtonian fluid is represented by the state variable $\mathbf{x} = \{m_\alpha\}$ and an Oldroyd-B fluid is represented by the state variables $\mathbf{x} = \{m_\alpha, C_{\alpha\beta}\}$.

### 5.2.2 Defining the Hamiltonian

After identifying the appropriate state variables, the next task is to define the Hamiltonian, which captures the total extended energy of the system. The Hamiltonian typically involves

a kinetic energy contribution, $K(\mathbf{x})$, and a Helmholtz free energy contribution, $A(\mathbf{x})$,

$$H(\mathbf{x}) = K(\mathbf{x}) + A(\mathbf{x}). \tag{5.4}$$

The Helmholtz free energy is employed, rather than the Gibbs, since incompressible fluid dynamics typically takes place at constant volume. The Helmholtz free energy includes entropic terms and elastic energy terms, as well as terms related to reactions and material structure. For a Newtonian fluid the only contribution to the Hamiltonian comes from the kinetic energy

$$H(\mathbf{x}) = K(\mathbf{x}) = \int_\Omega \frac{m_\alpha m_\alpha}{2\rho} \mathrm{d}V. \tag{5.5}$$

For an Oldroyd-B fluid, the kinetic energy remains unchanged but there is an additional contribution to the Hamiltonian from the Helmholtz free energy

$$H(\mathbf{x}) = K(\mathbf{x}) + A(\mathbf{x}) = \int_\Omega \frac{m_\alpha m_\alpha}{2\rho} + \int_\Omega \frac{1}{2} n K C_{\alpha\alpha} \mathrm{d}V - \int_\Omega \frac{1}{2} n k_B T \ln \det \left( \frac{K}{k_B T} C_{\alpha\beta} \right) \mathrm{d}V, \tag{5.6}$$

where $n$ is the number density of polymers, $K$ is the Hookean spring constant, $k_B$ is the Boltzmann constant, and $T$ is temperature. The first integral represents the elastic potential energy of the dumbbells while the second integral represents interchain entropy.

### 5.2.3 Formulation of the Poisson bracket

Now that the Hamiltonian is defined, the next step is to formulate the appropriate Poisson bracket. The Poisson bracket must accurately capture the reversible dynamics of the system (e.g., convection), be antisymmetric, and satisfy the Jacobi identity. For a Newtonian fluid the Poisson bracket is relatively simple as it only includes the transfer of momentum throughout the fluid:

$$\{F, G\} = -\int_\Omega \left[ \frac{\delta F}{\delta m_\gamma} \nabla_\beta \left( m_\gamma \frac{\delta G}{m_\beta} \right) - \frac{\delta G}{\delta m_\gamma} \nabla_\beta \left( m_\gamma \frac{\delta F}{\delta m_\beta} \right) \right] \mathrm{d}V. \tag{5.7}$$

For an Oldroyd-B fluid, the reversible dynamics include the momentum transfer shown above and additionally include the motion and stretching of dumbbells. It is often helpful to break the Poisson bracket into contributions for each state variable

$$\{F, G\} = \{F, G\}_m + \{F, G\}_C, \tag{5.8}$$

where $\{F, G\}_m$ accounts for momentum density transport, given by Eq. (5.7), and $\{F, G\}_C$ accounts for the transport of the conformation tensor density. While the exact form of $\{F, G\}_C$ can vary depending on the type of time derivative required (e.g., upper convected vs. lower convected), the general form that is often used is [164]:

$$\begin{aligned}\{F, G\}_C = &- \int_\Omega \left[ \frac{\delta F}{\delta C_{\alpha\beta}} \nabla_\gamma \left( \frac{\delta G}{\delta m_\gamma} C_{\alpha\beta} \right) - \frac{\delta G_\gamma}{\delta C_{\alpha\beta}} \nabla_\gamma \left( \frac{\delta F}{\delta m_\gamma} C_{\alpha\beta} \right) \right] \mathrm{d}V \\ &- \int_\Omega C_{\gamma\alpha} \left[ \nabla_\gamma \left( \frac{\delta F}{\delta m_\beta} \right) \frac{\delta G}{\delta C_{\alpha\beta}} - \nabla_\gamma \left( \frac{\delta G}{\delta m_\beta} \right) \frac{\delta F}{\delta C_{\alpha\beta}} \right] \mathrm{d}V \\ &- \int_\Omega C_{\gamma\beta} \left[ \nabla_\gamma \left( \frac{\delta F}{\delta m_\alpha} \right) \frac{\delta G}{\delta C_{\alpha\beta}} - \nabla_\gamma \left( \frac{\delta G}{\delta m_\alpha} \right) \frac{\delta F}{\delta C_{\alpha\beta}} \right] \mathrm{d}V.\end{aligned} \tag{5.9}$$

This form of the Poisson bracket corresponds to an upper convected derivative of the conformation tensor.

### 5.2.4 Formulation of the dissipation bracket

Formulation of the dissipation bracket is very similar to that of the Poisson bracket; the dissipation bracket accounts for the irreversible dynamics of the system, such as viscous dissipation, diffusion, relaxation mechanisms, and reactions, and there is actually a great deal of freedom when it comes to choosing which dissipative processes are present in this bracket [164, 171]. Although this freedom is useful for constructing models that describe a vast array of phenomena, it does require significant attention to ensure that the appropriate physics that best represent a system are captured.

For a Newtonian fluid the only dissipative phenomenon present is viscosity, which is

represented through the dissipative bracket:

$$[F,G] = -\int_\Omega \nabla_\alpha \frac{\delta F}{\delta m_\beta} Q_{\alpha\beta\gamma\epsilon} \nabla_\gamma \frac{\delta G}{\delta m_\epsilon} \mathrm{d}V. \tag{5.10}$$

The $\mathbf{Q}$ matrix is completely general and can represent both anisotropic and isotropic viscous dissipation, but in this work we will restrict ourselves to isotropic dissipation (e.g., $\mathbf{Q} \propto \boldsymbol{\delta\delta}$). Viscoelastic fluids often contain much more intricate dissipative phenomena so it is useful to define a general form for the dissipation bracket [164]:

$$\begin{aligned}
[F,G] = &-\int_\Omega \nabla_\alpha \frac{\delta F}{\delta m_\beta} Q_{\alpha\beta\gamma\epsilon} \nabla_\gamma \frac{\delta G}{\delta m_\epsilon} \mathrm{d}V \\
&-\int_\Omega \frac{\delta F}{\delta C_{\alpha\beta}} \Lambda_{\alpha\beta\gamma\epsilon} \frac{\delta G}{\delta C_{\gamma\epsilon}} \mathrm{d}V \\
&-\int_\Omega \nabla_\gamma \frac{\delta F}{\delta C_{\alpha\beta}} B_{\alpha\beta\gamma\epsilon\eta\nu} \nabla_\nu \frac{\delta G}{\delta C_{\epsilon\eta}} \mathrm{d}V \\
&-\int_\Omega L_{\alpha\beta\gamma\epsilon} \left[ \nabla_\alpha \left( \frac{\delta F}{\delta m_\beta} \right) \frac{\delta G}{\delta C_{\gamma\epsilon}} - \nabla_\alpha \left( \frac{\delta G}{\delta m_\beta} \right) \frac{\delta F}{\delta C_{\gamma\epsilon}} \right] \mathrm{d}V.
\end{aligned} \tag{5.11}$$

$\mathbf{Q}$ is defined the same as above, $\mathbf{\Lambda}$ represents an inverse relaxation time (essentially a rotational diffusivity) that is intrinsic to a material, $\mathbf{B}$ accounts for anisotropic translational diffusivity, and $\mathbf{L}$ accounts for non-affine motion by coupling the velocity gradient and conformation tensor. For a Newtonian fluid, the only transport coefficient retained is

$$Q_{\alpha\beta\gamma\epsilon} = \eta \left( \delta_{\alpha\gamma}\delta_{\beta\epsilon} + \delta_{\alpha\epsilon}\delta_{\beta\gamma} \right), \tag{5.12}$$

where $\eta$ is the fluid viscosity. For an Oldroyd-B fluid, $\mathbf{Q}$ is defined exactly as above, $\mathbf{B} = \mathbf{L} = 0$ since there is no anisotropic translational diffusivity and no non-affine motion, and the relaxation matrix $\mathbf{\Lambda}$ is given as

$$\Lambda_{\alpha\beta\gamma\epsilon} = \frac{1}{2\lambda n K} \left( C_{\alpha\gamma}\delta_{\beta\epsilon} + C_{\alpha\epsilon}\delta_{\beta\gamma} + C_{\beta\gamma}\delta_{\alpha\epsilon} + C_{\beta\epsilon}\delta_{\alpha\gamma} \right), \tag{5.13}$$

where $\lambda$ is the polymer relaxation time [164].

### 5.2.5 Derivation of the governing equations

The derivation of the governing equations tends to be the most tedious technical component of deriving a model using the SGBF-NET framework since it requires a great deal of multivariate calculus and index tracking; however, as long as we pay careful attention, it is not exceptionally challenging. This step involves equating the two equivalent forms of the governing dynamical equation, shown in Eq. (5.3). It is typically easiest to simplify each individual bracket first and then combine the brackets to obtain the governing equations. Starting with Eq. (5.7), we can first write this expression in terms of the Hamiltonian:

$$\{F, H\}_m = -\int_\Omega \left[\frac{\delta F}{\delta m_\gamma}\nabla_\beta\left(m_\gamma\frac{\delta H}{m_\beta}\right) - \frac{\delta H}{\delta m_\gamma}\nabla_\beta\left(m_\gamma\frac{\delta F}{\delta m_\beta}\right)\right] dV. \tag{5.14}$$

To simplify this expression we first note that $\delta H/\delta m_\alpha \equiv m_\alpha/\rho \equiv v_\alpha$ where $v_\alpha$ is the fluid velocity. Substituting this expression into Eq. (5.14) we obtain

$$\{F, H\}_m = -\int_\Omega \left[\frac{\delta F}{\delta m_\gamma}\nabla_\beta\left(\rho v_\beta v_\gamma\right) - v_\gamma\nabla_\beta\left(\rho v_\gamma\frac{\delta F}{\delta m_\beta}\right)\right] dV. \tag{5.15}$$

We can then integrate this expression by parts and make use of the vector identity

$$\boldsymbol{\nabla}\mathbf{v}\cdot\mathbf{v} = \frac{1}{2}\boldsymbol{\nabla}\left(\mathbf{v}\cdot\mathbf{v}\right), \tag{5.16}$$

to obtain

$$\{F, H\}_m = -\int_\Omega \left[\frac{\delta F}{\delta m_\gamma}\nabla_\beta\left(\rho v_\beta v_\gamma\right) - \frac{1}{2}v_\gamma v_\gamma\left(\nabla_\beta\frac{\delta F}{\delta m_\beta}\right)\right] dV. \tag{5.17}$$

Finally, we use the fact that $\delta F/\delta m_\alpha$ is divergence-free to obtain the simplified form of the Poisson bracket for a Newtonian fluid:

$$\{F, H\}_m = -\int_\Omega \left[\frac{\delta F}{\delta m_\gamma}\nabla_\beta\left(\rho v_\beta v_\gamma\right)\right] dV. \tag{5.18}$$

Now turning to the Newtonian dissipation bracket, Eq. (5.10), with $\mathbf{Q}$ given by Eq. (5.12), this bracket immediately simplifies to

$$[F, H] = -\int_\Omega \frac{\delta F}{\delta m_\alpha} \eta \nabla_\beta \nabla_\beta v_\alpha \mathrm{d}V. \tag{5.19}$$

Combining the Poisson and dissipation brackets and substituting these expressions into the governing dynamical equation gives

$$\frac{\mathrm{d}F}{\mathrm{d}t} = \int_\Omega \frac{\delta F}{\delta m_\alpha} \frac{\partial m_\alpha}{\partial t} \mathrm{d}V = -\int_\Omega \left[ \frac{\delta F}{\delta m_\alpha} \nabla_\beta \left( \rho v_\beta v_\alpha \right) \right] dV - \int_\Omega \frac{\delta F}{\delta m_\alpha} \eta \nabla_\beta \nabla_\beta v_\alpha \mathrm{d}V. \tag{5.20}$$

By equating terms multiplied by $\delta F / \delta m_\alpha$ we obtain

$$\frac{\partial m_\alpha}{\partial t} = -\nabla_\beta \left( \rho v_\beta v_\alpha \right) - \eta \nabla_\beta \nabla_\beta v_\alpha - \nabla_\alpha p, \tag{5.21}$$

which can be further simplified to the familiar form of the Navier-Stokes equations for an incompressible Newtonian fluid:

$$\rho \left[ \frac{\partial v_\alpha}{\partial t} + \nabla_\beta \left( v_\beta v_\alpha \right) \right] = -\eta \nabla_\beta \nabla_\beta v_\alpha - \nabla_\alpha p. \tag{5.22}$$

The astute reader will notice the appearance of the pressure seemingly out of nowhere. We have intentionally glossed over the pressure because it arises through properties of operating spaces and functional derivatives that would require significant background to explain; in essence, the pressure arises as a Lagrange multiplier to enforce the incompressibility constraint, but a full explanation is given in Chapter 5.4 of [164]. An identical procedure can be performed on the Poisson and brackets for the Oldroyd-B fluid to obtain the governing equations.

### 5.2.6 Verification of thermodynamic admissibility

Veryifying the thermodynamic admissibility of a given model derived from the SGBF-NET framework can be done before or after the derivation of the governing equations since it only requires a full description of the dissipation bracket and the Hamiltonian. In this step we must compute and enforce $\mathrm{d}H/\mathrm{dt} = [H, H] \leq 0$, which does not require knowledge of the Poisson bracket since $\{H, H\} = 0$ by construction. For the Newtonian fluid we have

$$\begin{aligned}
[H, H] &= -\int_\Omega \nabla_\alpha \frac{\delta H}{\delta m_\beta} Q_{\alpha\beta\gamma\epsilon} \nabla_\gamma \frac{\delta H}{\delta m_\epsilon} \mathrm{d}V \\
&= -\eta \int_\Omega \nabla_\alpha v_\beta \left(\delta_{\alpha\gamma}\delta_{\beta\epsilon} + \delta_{\alpha\epsilon}\delta_{\beta\gamma}\right) \nabla_\gamma v_\epsilon \mathrm{d}V \\
&= -\eta \int_\Omega \left(\nabla_\alpha v_\beta \nabla_\alpha v_\beta + \nabla_\beta v_\alpha \nabla_\beta v_\alpha\right) \mathrm{d}V \\
&= -\eta \int_\Omega \left(K_{\alpha\beta} K_{\alpha\beta}\right)^2 \mathrm{d}V,
\end{aligned} \tag{5.23}$$

where $K_{\alpha\beta} = \nabla_\alpha v_\beta$. Clearly $[H, H] \leq 0$ provided $\eta \geq 0$. Thus we have shown that the general governing equations for an incompressible Newtonian fluid can be derived from the SGBF-NET framework and are indeed thermodynamically admissible. For an Oldroyd-B fluid we must additionally check the dissipation bracket for the relaxation variable, which requires evaluation of the Volterra derivative of the Hamiltonian with respect to the conformation tensor:

$$\frac{\delta H}{\delta C_{\alpha\beta}} = \frac{1}{2} n K \delta_{\alpha\beta} - \frac{1}{2} n k_B T C^{-1}_{\alpha\beta}. \tag{5.24}$$

Continuing the evaluation:

$$\begin{aligned}
[H, H]_\Lambda &= -\int_\Omega \frac{\delta H}{\delta C_{\alpha\beta}} \Lambda_{\alpha\beta\gamma\epsilon} \frac{\delta H}{\delta C_{\gamma\epsilon}} \mathrm{d}V \leq 0 \\
&= -\frac{1}{2\lambda n K} \int_\Omega \frac{\delta H}{\delta C_{\alpha\beta}} \left(C_{\alpha\gamma}\delta_{\beta\epsilon} + C_{\alpha\epsilon}\delta_{\beta\gamma} + C_{\beta\gamma}\delta_{\alpha\epsilon} + C_{\beta\epsilon}\delta_{\alpha\gamma}\right) \frac{\delta H}{\delta C_{\gamma\epsilon}} \mathrm{d}V.
\end{aligned} \tag{5.25}$$

At the moment, we will skip the full simplification of this expression since a similar form will appear later in this work as we derive a model for dilute wormlike micelle solutions using

the SGBF formalism; however, we note that simplification yields a similar constraint as the Newtonian case, specifically that $[H, H]_\Lambda \leq 0$ provided $\lambda \geq 0$.

This concludes the overview of the SGBF-NET formalism and how it can be used to derive and test a thermodynamically admissible model for fluids. In the following sections, we will use the framework we have established to derive a thermodynamically consistent model for dilute wormlike micelle solutions.

## 5.3 Reformulated reactive rod model (RRM-R)

The aim of the present study is to re-derive the reformulated reactive rod model (RRM-R), which models micelles as reactive Brownian rods, using SGBF-NET to ascertain and enforce its thermodynamic admissibility. To begin this, we first provide a summary of the RRM-R and its derivation, though a complete derivation is left to [129]. We note that this modeling framework takes inspiration from theoretical treatments by Cates and Turner [110]. In the RRM-R, dilute wormlike micelle solutions are treated as suspensions of rigid Brownian rods undergoing reversible scission and fusion. Rods can fuse end-to-end (reducing the energetic penalty associated with the micellar end caps), but only when they are highly aligned – otherwise the energy penalty arising from forming a long but bent micelle is too large for fusion to take place [15, 110]. The application of flow tends to align the rods. This alignment is balanced by rotational diffusivity of the rods acting to return the suspension to isotropy. It is assumed that rod growth is countered by hydrodynamic stresses acting along the lengths of the rods, which induce breakage events into shorter rods. Moreover, rods can undergo both spontaneous scission and spontaneous fusion events.

### 5.3.1 Brownian rods

Starting with a suspension of (non-reactive) Brownian rods, consider a uniform collection of rods with length $L_0$, radius $b$, and number density $n_0$ suspended in a Newtonian solvent

with viscosity $\eta_s$. The orientation of a single rod is described by the unit director vector $\boldsymbol{u}$. The solution is subjected to an arbitrary flow with local velocity $\boldsymbol{v}$ and transpose velocity gradient $\boldsymbol{K} = \boldsymbol{\nabla v}^\top$. The orientation tensor $\boldsymbol{Q}$ describes the average collective orientation of the suspension and is given by the second moment of $\boldsymbol{u}$

$$\boldsymbol{Q} = \langle \boldsymbol{uu} \rangle = \int \boldsymbol{uu} \psi \mathrm{d}\boldsymbol{u}, \tag{5.26}$$

where $\psi$ is the probability distribution function of $\boldsymbol{u}$. Note that in the work by Doi and Edward [75] and in the original derivations of the RRM and RRM-R, the orientation tensor was defined as $\boldsymbol{S}$. However, in NET literature the orientation tensor is typically defined as $\boldsymbol{Q}$, where $\boldsymbol{S}$ is reserved for the traceless orientation tensor $\boldsymbol{S} = \boldsymbol{Q} - \boldsymbol{\delta}/3$. In order to remain consistent we will with the non-equilibrium thermodynamics literature, we will adopt the NET notation for the RRM-R; thus the orientation tensor with unit trace is $Q_{\alpha\beta}$ and the traceless orientation tensor is $S_{\alpha\beta} = Q_{\alpha\beta} - \frac{1}{3}\delta_{\alpha\beta}$.

The time evolution of $\boldsymbol{Q}$ in flow is

$$\frac{\mathrm{D}\boldsymbol{Q}}{\mathrm{D}t} = -6D_{r,0}\left(\boldsymbol{Q} - \frac{1}{3}\boldsymbol{I}\right) + \boldsymbol{K}\cdot\boldsymbol{Q}^\top + \boldsymbol{Q}\cdot\boldsymbol{K}^\top - 2\boldsymbol{K} : \langle \boldsymbol{uuuu} \rangle, \tag{5.27}$$

where $D_{r,0}$ is the rotational diffusion coefficient of a rod, $\boldsymbol{I}$ is the unit tensor, and the double dot product is defined as $\boldsymbol{A} : \boldsymbol{B} = \mathrm{Tr}(\boldsymbol{A}\cdot\boldsymbol{B}^\top)$ [75].

The total stress of the suspension is given by the sum of the solvent $\boldsymbol{\tau}^N$ and micelle $\boldsymbol{\tau}^m$ contributions

$$\boldsymbol{\tau}^T = \boldsymbol{\tau}^N + \boldsymbol{\tau}^m, \tag{5.28}$$

where

$$\boldsymbol{\tau}^N = 2\eta_s \boldsymbol{D} \tag{5.29}$$

is the Newtonian solvent contribution with rate of deformation tensor $\boldsymbol{D} = \frac{1}{2}(\boldsymbol{K} + \boldsymbol{K}^\top)$ and

$$\boldsymbol{\tau}^m = 3n_0 k_B T \left( \boldsymbol{Q} - \frac{1}{3}\boldsymbol{I} \right) + \frac{n_0 k_B T}{2D_{r,0}} \boldsymbol{K} : \langle \boldsymbol{uuuu} \rangle \tag{5.30}$$

is the additional stress due to the presence of rods. Here, $k_B$ is the Boltzmann constant and $T$ is the temperature. Equations (5.27) and (5.30) notably contain the fourth moment $\langle \boldsymbol{uuuu} \rangle$, an evolution equation for which depends on the sixth moment of $\boldsymbol{u}$, which in turn depends on higher moments. To proceed analytically, it is then necessary to supply a closure approximation for the product $\boldsymbol{K} : \langle \boldsymbol{uuuu} \rangle$. While numerous approximations are possible (see, for example: [75, 114, 101]), the RRM-R uses an approximation from Dhont and Briels [103] that interpolates between exact expressions in the limits of isotropy (equilibrium) and complete alignment:

$$\boldsymbol{K} : \langle \boldsymbol{uuuu} \rangle \approx \frac{1}{5}[\boldsymbol{Q} \cdot \boldsymbol{D} + \boldsymbol{D} \cdot \boldsymbol{Q} - \boldsymbol{Q} \cdot \boldsymbol{Q} \cdot \boldsymbol{D} - \boldsymbol{D} \cdot \boldsymbol{Q} \cdot \boldsymbol{Q} + 2\boldsymbol{Q} \cdot \boldsymbol{D} \cdot \boldsymbol{Q} + 3(\boldsymbol{Q} : \boldsymbol{D})\boldsymbol{Q}]. \tag{5.31}$$

### 5.3.2 RRM-R

As discussed above, a key feature of the RRM and RRM-R is that they allow micelles, modeled as rigid rods, to undergo reversible scission and growth by allowing the collective length and number density of the suspension to be dynamic properties that evolve with time and flow. This variation is mathematically achieved in the RRM-R by changing the constant rod length $L_0$ to the dynamic length $L$. To make analytical progress and ensure the tractability of the model we assume the system can be characterized by a single, representative length, $L$. Now consider a suspension of rods at equilibrium with number density $n_0$ and equilibrium length $L_0$; the radius $b$ of the rods is taken to be constant. The evolution of length $L$ and number density $n$ are constrained at all times by the surfactant mass balance

$$nL = n_0 L_0. \tag{5.32}$$

The rotational diffusion constant for a rod of length $L_0$ and radius $b$ is given by [75, 115]

$$D_{r,0} = \frac{3k_BT}{\pi\eta_s L_0^3} \ln\left(\frac{L_0}{2b}\right). \tag{5.33}$$

In the RRM-R, the constant rotational diffusion coefficient of the simple rigid rod model is replaced by the length-dependent coefficient

$$D_r = \frac{D_{r,0}}{L^{*3}} \left(\frac{\ln L^* + m}{m}\right), \tag{5.34}$$

where $L^* = L/L_0$ is the dimensionless micelle length and $m = \ln[L_0/(2b)]$ is a constant related to the initial aspect ratio of the rods. Substituting Eq. (5.34) into Eqs. (5.27) and (5.30), we find

$$\frac{\mathrm{D}\boldsymbol{Q}}{\mathrm{D}t} = -6D_r\left(\boldsymbol{Q} - \frac{1}{3}\boldsymbol{I}\right) + \boldsymbol{K}\cdot\boldsymbol{Q}^\top + \boldsymbol{S}\cdot\boldsymbol{K}^\top - 2\boldsymbol{K} : \langle \boldsymbol{uuuu}\rangle \tag{5.35}$$

and

$$\boldsymbol{\tau}^m = 3nk_BT\left(\boldsymbol{Q} - \frac{1}{3}\boldsymbol{I}\right) + \frac{nk_BT}{2D_r}\boldsymbol{K} : \langle \boldsymbol{uuuu}\rangle. \tag{5.36}$$

The orientation of rods in the suspension is tracked by introducing a scalar orientational order parameter

$$\widehat{Q} = \sqrt{\frac{3}{2}\widehat{\boldsymbol{Q}} : \widehat{\boldsymbol{Q}}}, \tag{5.37}$$

where $\widehat{\boldsymbol{Q}} = \boldsymbol{Q} - \frac{1}{3}\boldsymbol{I}$ is the traceless part of $\boldsymbol{Q}$. This order parameter varies between $\widehat{Q} = 0$ for isotropic rods and $\widehat{Q} = 1$ for perfectly aligned rods. Note that the description and equations above are valid for both the original RRM and the reformulation (RRM-R), the only variation between the two models is in the length evolution equation, discussed below.

To allow for variability of rod length the RRM-R assumes a length evolution equation that balances growth and breakdown of micelles

$$\frac{\mathrm{D}L}{\mathrm{D}t} = R_g + R_b, \tag{5.38}$$

where $R_g \geq 0$ is the rate of micelle growth and $R_b \leq 0$ is the rate of micelle breakdown. As discussed previously, the RRM-R assumes two forms of growth: spontaneous and alignment-induced, and two forms of breakage: spontaneous and tension-induced. Again, the complete derivation can be found in [129]. After a number of simplifications involving the surfactant mass balance Eq. (5.32), relating spontaneous effects that must balance at equilibrium, we have the overall length evolution equation

$$\frac{\mathrm{D}L}{\mathrm{D}t} = k_{b0}\left(\frac{L_0^3}{L^2} - L\right) + k_{ga}(n_0 L_0)^2 \frac{\widehat{Q}^2}{L^2} - k_{bt}\left[\exp\left(\frac{a}{L_0}\frac{\boldsymbol{Q} : \boldsymbol{\tau}^m}{n_0 k_B T}\right) - 1\right]. \tag{5.39}$$

This equation contains four parameters - $k_{b0}$, $k_{ga}$, $k_{bt}$, and $a$, which are related to the spontaneous breakage, alignment-induced growth, tension-induced breakage, and scission energy of micelles, respectively.

The RRM-R constitutive equations are coupled to conservation of mass and momentum

$$\boldsymbol{\nabla} \cdot \boldsymbol{v} = 0, \tag{5.40}$$

$$\rho \frac{\mathrm{D}\boldsymbol{v}}{\mathrm{D}t} = -\boldsymbol{\nabla} p + \eta_s \nabla^2 \boldsymbol{v} + \boldsymbol{\nabla} \cdot \boldsymbol{\tau}^m, \tag{5.41}$$

where $\boldsymbol{v}$ is the velocity, $p$ is the pressure, $\rho$ is the density of the fluid, $\eta_s$ is the solvent viscosity which is assumed to be Newtonian, and $\boldsymbol{\tau}^m$ is the micelle contribution to the fluid stress.

## 5.4 Structural model - A (SM-A)

To derive a thermodynamically consistent model for dilute wormlike micelle solutions we will follow the steps outlined in Section 5.2. We also want to express that any model derived should, ideally, bear some resemblance to the RRM-R and reflect the underlying physics of

a dilute wormlike micelle system. Further, similar to the RRM-R, an appropriate model must capture the key rheological features of a dilute wormlike micelle solutions, namely: shear-thickening and -thinning, flow-induced structure formation, and ideally a multivalued flow curve. The ability to predict a multivalued flow curve is not essential since there is still significant value in obtaining a purely shear-thickening/shear-thinning model for WLM solutions that is thermodynamically consistent, however, such a model that is additionally able to capture reentrant behavior would be a significant achievement and extremely valuable. The model in this section is referred to as Structural Model - A (SM-A).

**Identification of state variables**

We begin the derivation by identifying the appropriate state variables to capture the physics in the WLM system. As is always the case, we must consider the momentum density, $m_\alpha = \rho v_\alpha$. We also must consider some tensor field that captures the orientation of micelles; in the RRM-R this is achieved through the orientation tensor $\mathbf{Q}$. The orientation tensor differs from the unconstrained conformation tensor, $\mathbf{C}$, in that $\mathbf{Q}$ obeys the key constraint of unit trace ($\mathrm{tr}(\mathbf{Q}) = 1$). This difference necessitates alterations to the Poisson and dissipation brackets that we will be addressed later. Finally, the RRM-R includes the length variable, $L$, to account for the growth and breakdown of micelle length. In this model, we will introduce the structural variable $\lambda$ that is meant to represent the same growth and breakdown. Again, $\lambda$ is used rather than $L$ to maintain consistency with the NET literature. Thus, the state variables for this model are:

$$\mathbf{x} = \{m_\alpha, Q_{\alpha\beta}, \lambda\}. \tag{5.42}$$

**Defining the Hamiltonian**

The Hamiltonian can be broken up into the kinetic energy, given by Eq. (5.5), and the Helmholtz free energy, $A(\mathbf{x})$, which incudes both elastic and entropic contributions. The

elastic contribution is

$$A_{el}(\mathbf{x}) = \int_{\Omega} \frac{9}{4} n k_B T S_{\alpha\beta} S_{\beta\alpha} \mathrm{d}V, \tag{5.43}$$

where $n$ is the micelle number density [170]. As in the RRM-R, conservation of surfactants (and therefore mass) is enforced by the constraint $n\lambda = n_0\lambda_0$, where $n_0$ and $\lambda_0$ are the micelle number density and length at equilibrium, respectively. This quantity arises to match the governing equations of Doi's original model for liquid crystalline systems [164, 170, 75]. The entropic term is

$$A_{en}(\mathbf{x}) = \int_{\Omega} \frac{n k_B T}{2\lambda_0} \left(\lambda \ln(\lambda/\lambda_0) - \lambda + \lambda_0\right) \mathrm{d}V, \tag{5.44}$$

which accounts for the ideal entropy of mixing for micelles and is constructed to maximize at equilibrium ($\lambda = \lambda_0$) [175, 178, 177].

Since they will be needed in future calculations, it is now useful to calculate the Volterra derivatives of the Hamiltonian with respect to the state variables. Volterra derivatives, also called functional derivatives, arise in the calculus of variations and relate a functional to a change in the function on which the functional depends [179]. As a reminder, functionals are functions that act on functions. As far as we are concerned, Volterra derivatives behave as the standard calculus derivative. The Volterra derivatives of the Hamiltonian are:

$$\frac{\delta H}{\delta m_\alpha} \equiv v_\alpha = \frac{m_\alpha}{\rho}, \tag{5.45}$$

$$\frac{\delta H}{\delta Q_{\alpha\beta}} = \frac{\delta H}{\delta S_{\alpha\beta}} = \frac{9 n_0 k_B T}{2} \frac{\lambda_0}{\lambda} S_{\alpha\beta}, \tag{5.46}$$

$$\frac{\delta H}{\delta \lambda} = n_0 k_B T \frac{\lambda_0}{2} \left[\frac{1}{\lambda\lambda_0} - \frac{1}{\lambda^2} - \frac{9}{2} \frac{S_{\alpha\beta} S_{\beta\alpha}}{\lambda^2}\right]. \tag{5.47}$$

Note that in Eq. (5.47) we have enforced the conservation of surfactants constraint, $n\lambda = n_0\lambda_0$, which indicates that $n$ and $\lambda$ are not independent of one another.

**Formulation of the Poisson bracket**

Now we must formulate the Poisson bracket to describe the reversible dynamics in the micelle system. The Poisson bracket can be broken into three components, one for each state variable:

$$\{F, H\} = \{F, H\}_m + \{F, H\}_Q + \{F, H\}_\lambda, \tag{5.48}$$

where $\{F, H\}_m$ is given by Eq. (5.14). The Poisson bracket for the orientation tensor can be formulated from the corresponding bracket for the conformation tensor Eq. (5.9). We must modify this expression to account for the fact that while the conformation tensor $C_{\alpha\beta}$ is unconstrained, the orientation tensor $Q_{\alpha\beta}$ must satisfy the constraint $Q_{\alpha\alpha} = 1$. To perform this modification we must make used of the mapping

$$\frac{C_{\alpha\beta}}{C_{\alpha\alpha}} \equiv Q_{\alpha\beta}, \tag{5.49}$$

which maps an arbitrary tensor to a tensor with unit trace [164]. The Volterra derivatives are likewise modified

$$\frac{\delta F}{\delta C_{\alpha\alpha}} = \frac{\delta F}{\delta Q_{\gamma\epsilon}} \frac{1}{C_{\eta\eta}} \left[\delta_{\alpha\gamma}\delta_{\beta\epsilon} - Q_{\gamma\epsilon}\delta_{\alpha\beta}\right]. \tag{5.50}$$

Applying these transformations to Eq. (5.9) gives the Poisson bracket for the orientation tensor

$$\begin{aligned}
\{F, H\}_Q = &- \int_\Omega Q_{\alpha\beta} \left[ \frac{\delta F}{\delta m_\gamma} \nabla_\gamma \frac{\delta H}{\delta Q_{\alpha\beta}} - \frac{\delta H_\gamma}{\delta m_\gamma} \nabla_\gamma \frac{\delta F}{\delta Q_{\alpha\beta}} \right] dV \\
&- \int_\Omega Q_{\alpha\gamma} \left[ \nabla_\gamma \left( \frac{\delta F}{\delta m_\beta} \right) \frac{\delta H}{\delta Q_{\alpha\beta}} - \nabla_\gamma \left( \frac{\delta H}{\delta m_\beta} \right) \frac{\delta F}{\delta Q_{\alpha\beta}} \right] dV \\
&- \int_\Omega Q_{\beta\gamma} \left[ \nabla_\gamma \left( \frac{\delta F}{\delta m_\alpha} \right) \frac{\delta H}{\delta Q_{\alpha\beta}} - \nabla_\gamma \left( \frac{\delta H}{\delta m_\alpha} \right) \frac{\delta F}{\delta Q_{\alpha\beta}} \right] dV \\
&+ 2 \int_\Omega Q_{\gamma\epsilon} Q_{\alpha\beta} \left[ \nabla_\beta \left( \frac{\delta F}{\delta m_\alpha} \right) \frac{\delta H}{\delta Q_{\gamma\epsilon}} - \nabla_\beta \left( \frac{\delta H}{\delta m_\alpha} \right) \frac{\delta F}{\delta Q_{\gamma\epsilon}} \right] dV.
\end{aligned} \tag{5.51}$$

Notice that Eq. (5.51) differs from Eq. (5.9) by an additional integral that depends on the fourth order term $Q_{\gamma\epsilon}Q_{\alpha\beta}$; recall that $Q_{\alpha\beta} = \langle u_\alpha u_\beta \rangle$ so that the fourth order $Q_{\gamma\epsilon}Q_{\alpha\beta} =$

$\langle u_\gamma u_\epsilon u_\alpha u_\beta \rangle$. This term arises in a similar manner to the fourth order term in Eq. (3.2), which was derived from a microstructural framework rather than the thermodynamic framework used here.

The Poisson bracket for the structural variable $\lambda$ must be formulated. In this work, as is often best practice in NET literature, we will start with the most general expression and then simplify it as needed. The typical form of the Poisson bracket for a structural variable is [177, 169, 171]:

$$\begin{aligned}\{F,G\}_\lambda = &-\int_\Omega \left[\frac{\delta F}{\delta \lambda}\nabla_\beta\left(\lambda\frac{\delta G}{\delta m_\beta}\right) - \frac{\delta G}{\delta \lambda}\nabla_\beta\left(\lambda\frac{\delta F}{\delta m_\beta}\right)\right] dV \\ &-\int_\Omega g_{\alpha\beta}\left[\frac{\delta G}{\delta \lambda}\nabla_\beta\left(\lambda\frac{\delta F}{\delta m_\alpha}\right) - \frac{\delta F}{\delta \lambda}\nabla_\beta\left(\lambda\frac{\delta G}{\delta m_\alpha}\right)\right] dV,\end{aligned} \tag{5.52}$$

where $g_{\alpha\beta}$ is an arbitrary function of $\lambda$ and $\mathbf{Q}$ that couples the evolution of the structural variable to the velocity gradient. Comparing to Eq. (5.7), it is clear that the first integral accounts for the time rate of change and convection of $\lambda$ (i.e., this first integral will amount to the material derivative of $\lambda$). The tensor $g_{\alpha\beta}$, although arbitrary in a sense, must actually satisfy the Jacobi identity and can be written in the most general form using the Cayley-Hamilton theorem

$$\mathbf{g} = g_1\mathbf{Q} + g_2\mathbf{I} + g_3\mathbf{Q}^{-1}, \tag{5.53}$$

where the scalar coefficients are functions of $\lambda$ and the invariants of $\mathbf{Q}$, given by Eq. (1.20) [171]. To satisfy the Jacobi identity the scalar coefficients must satisfy the conditions

$$\begin{aligned} g_1\frac{\partial g_2}{\partial \lambda} - g_2\frac{\partial g_1}{\partial \lambda} &= 2\left(\frac{\partial g_1}{\partial I_2} - \frac{\partial g_2}{\partial I_1}\right), \\ g_1\frac{\partial g_3}{\partial \lambda} - g_3\frac{\partial g_1}{\partial \lambda} &= 2\left(\frac{\partial g_1}{\partial I_3} - \frac{\partial g_3}{\partial I_1}\right), \\ g_2\frac{\partial g_3}{\partial \lambda} - g_3\frac{\partial g_2}{\partial \lambda} &= 2\left(\frac{\partial g_2}{\partial I_3} - \frac{\partial g_3}{\partial I_2}\right). \end{aligned} \tag{5.54}$$

These conditions are extremely generally and importantly it is not easy to verify that $g_i$ satisfy them, often necessitating the use of symbolic means [180]. However, the satisfaction

of these conditions can often be simplified by setting one or more of the coefficients to zero [171]. Equations (5.7), (5.48), (5.51) and (5.52) complete the description of the Poisson bracket for this system.

**Formulation of the dissipation bracket**

Formulating the dissipation bracket requires describing all of the irreversible dynamics of the system. Again, it useful to retain the most general expression possible and then simplify and remove terms when deemed appropriate later. Similar to the Poisson bracket, we will break the dissipation bracket into three terms for each of the state variables

$$[F, H] = [F, H]_m + [F, H]_Q + [F, H]_\lambda, \tag{5.55}$$

where $[F, H]_m$ is obtained by writing Eq. (5.10) in terms of the Hamiltonian; we also now include an additional term $R_{\alpha\beta\gamma\epsilon}$ that couples the non-Newtonian stress to the velocity field:

$$\begin{aligned}[F, G]_m = &- \int_\Omega \nabla_\alpha \frac{\delta F}{\delta m_\beta} Q_{\alpha\beta\gamma\epsilon} \nabla_\gamma \frac{\delta G}{\delta m_\epsilon} \mathrm{d}V \\ &- \int_\Omega \nabla_\alpha \frac{\delta F}{\delta m_\beta} R_{\alpha\beta\gamma\epsilon} \nabla_\gamma \frac{\delta G}{\delta m_\epsilon} \mathrm{d}V,\end{aligned} \tag{5.56}$$

with $Q_{\alpha\beta\gamma\epsilon}$ corresponding to isotropic viscous dissipation and defined by Eq. (5.12).

The dissipation bracket for the orientation tensor is quite similar to Eq. (5.11):

$$\begin{aligned}[F, H]_Q = &- \int_\Omega \frac{\delta F}{\delta Q_{\alpha\beta}} P_{\alpha\beta\gamma\epsilon} \frac{\delta H}{\delta Q_{\gamma\epsilon}} \mathrm{d}V \\ &- \int_\Omega \nabla_\gamma \frac{\delta F}{\delta Q_{\alpha\beta}} B_{\alpha\beta\gamma\epsilon\eta\nu} \nabla_\nu \frac{\delta H}{\delta Q_{\epsilon\eta}} \mathrm{d}V \\ &- \int_\Omega L_{\alpha\beta\gamma\epsilon} \left[ \nabla_\alpha \left( \frac{\delta F}{\delta m_\beta} \right) \frac{\delta H}{\delta Q_{\gamma\epsilon}} - \nabla_\alpha \left( \frac{\delta H}{\delta m_\beta} \right) \frac{\delta F}{\delta Q_{\gamma\epsilon}} \right] \mathrm{d}V \\ &- \int_\Omega L_{\eta\zeta\gamma\gamma} Q_{\alpha\beta} \left[ \nabla_\eta \left( \frac{\delta F}{\delta m_\zeta} \right) \frac{\delta H}{\delta Q_{\alpha\beta}} - \nabla_\eta \left( \frac{\delta H}{\delta m_\zeta} \right) \frac{\delta F}{\delta Q_{\alpha\beta}} \right] \mathrm{d}V,\end{aligned} \tag{5.57}$$

where $P_{\alpha\beta\gamma\epsilon}$ accounts for rotational diffusion, $B_{\alpha\beta\gamma\epsilon\eta\nu}$ accounts for translational diffusion,

$L_{\alpha\beta\gamma\epsilon}$ accounts for non-affine motion, and the fourth integral arises from the mapping from the unconstrained to the constrained tensor. Even though we wish to remain general, we will immediately set $\mathbf{B} = 0$ since at this time we do not wish to include translational diffusion.

Finally, the dissipation bracket for the structural variable is

$$[F, H]_\lambda = -\int_\Omega \frac{\delta F}{\delta \lambda} \Lambda \frac{\delta H}{\delta \lambda}, \tag{5.58}$$

where $\Lambda$ is inversely proportional to a relaxation time associated with the structure [175]. Equations (5.55) to (5.58) fully describe the dissipation bracket for this system. Since the goal of this work is to derive a thermodynamically consistent version of the RRM-R, we will not yet define each of the transport coefficients; rather we will derive the governing equations with the arbitrary coefficients and compare these to the RRM-R to determine what the coefficients need to be.

**Derivation of the governing equations**

Having defined the Hamiltonian and both the Poisson and dissipation brackets we are now at the stage of deriving the governing equations for this system. As discussed in Section 5.2.5, this step mostly involves employing integration-by-parts and vector calculus identities to rewrite the brackets in a desirable form. After a not insignificant amount of math and index tracking, the governing equations are:

$$\rho \left( \frac{\partial v_\alpha}{\partial t} + v_\beta \nabla_\beta v_\alpha \right) = -\nabla_\alpha P + Q_{\alpha\beta\gamma\epsilon} \nabla_\beta \nabla_\gamma v_\epsilon + \nabla_\beta T_{\alpha\beta}, \tag{5.59}$$

$$\begin{aligned} T_{\alpha\beta} = 2 \left( S_{\gamma\beta} + \frac{1}{3}\delta_{\gamma\beta} \right) \frac{\delta H}{\delta Q_{\alpha\gamma}} - 2 \left( S_{\alpha\beta} + \frac{1}{3}\delta_{\alpha\beta} \right) S_{\gamma\epsilon} \frac{\delta H}{\delta Q_{\gamma\epsilon}} \\ - g_{\alpha\beta} \frac{\delta H}{\delta \lambda} + L_{\alpha\beta\gamma\epsilon} \frac{\delta H}{\delta Q_{\gamma\epsilon}} + R_{\alpha\beta\gamma\epsilon} \nabla_\gamma v_\epsilon, \end{aligned} \tag{5.60}$$

$$\frac{\partial Q}{\partial t} + v_\gamma \nabla_\gamma Q_{\alpha\beta} = Q_{\alpha\gamma}\nabla_\gamma v_\beta + Q_{\beta\gamma}\nabla_\gamma v_\alpha - 2Q_{\alpha\beta}Q_{\gamma\epsilon}\nabla_\gamma v_\epsilon - P_{\alpha\beta\gamma\epsilon}\frac{\delta H}{\delta Q_{\gamma\epsilon}} + L_{\gamma\epsilon\alpha\beta}\nabla_\gamma v_\epsilon \tag{5.61}$$

$$\frac{\partial \lambda}{\partial t} + v_\gamma \nabla_\gamma \lambda = g_{\alpha\beta}\nabla_\beta v_\alpha - \Lambda \frac{\partial H}{\partial \lambda}. \tag{5.62}$$

The stress is written as $T_{\alpha\beta}$ to remain consistent with NET literature. In order these equations describe the momentum, stress, orientation, and structure evolution. Even without substituting the Volterra derivatives or defining the transport coefficients, these equations bear strong resemblance to the RRM-R governing equations.

We can now substitute the Volterra derivatives, Eqs. (5.45) to (5.47), into the governing equations as well as define and substitute in the transport coefficients. As noted, $Q_{\alpha\beta\gamma\epsilon}$ is given by Eq. (5.12). The matrix $P_{\alpha\beta\gamma\epsilon}$ that describes rotational diffusion is defined by

$$P_{\alpha\beta\gamma\epsilon} = \frac{3D_r}{4nk_BT}\left(\delta_{\alpha\gamma}\delta_{\beta\epsilon} + \delta_{\alpha\epsilon}\delta_{\beta\gamma}\right), \tag{5.63}$$

where the coefficient is designed to match units and the form of the equations in the RRM-R [170]. The RRM-R does not include non-affine motion, thus $\mathbf{L} = 0$. Finally, we set

$$R_{\alpha\beta\gamma\epsilon} = \frac{nk_BT}{2D_r}Q_{\alpha\beta}Q_{\gamma\epsilon}. \tag{5.64}$$

This form is chosen so that the evolution equations for the stress and orientation include the same dependence on the fourth order tensor $Q_{\alpha\beta}Q_{\gamma\epsilon} = \langle u_\alpha u_\beta u_\gamma u_\epsilon \rangle$. At the moment $\mathbf{g}$ and $\Lambda$ are left arbitrary until the final forms of the equations are known. The governing equations become

$$\rho\left(\frac{\partial v_\alpha}{\partial t} + v_\beta \nabla_\beta v_\alpha\right) = -\nabla_\alpha P + \eta_s \nabla_\beta \nabla_\beta v_\alpha + \nabla_\beta T_{\alpha\beta}, \tag{5.65}$$

$$\frac{T_{\alpha\beta}}{n_0 k_B T} = \frac{3\lambda_0}{\lambda}\left(Q_{\alpha\beta} - \frac{1}{3}\delta_{\alpha\beta}\right) + \frac{\lambda_0}{2\lambda D_r}Q_{\alpha\beta}Q_{\gamma\epsilon}\nabla_\gamma v_\epsilon + \frac{9\lambda_0}{\lambda}\left(S_{\gamma\beta}S_{\alpha\gamma} - Q_{\alpha\beta}S_{\gamma\epsilon}S_{\gamma\epsilon}\right) - \frac{1}{2}g_{\alpha\beta}\left[\frac{1}{\lambda} - \frac{\lambda_0}{\lambda^2} - \frac{9\lambda_0}{2}\frac{S_{\alpha\beta}S_{\alpha\beta}}{\lambda^2}\right], \tag{5.66}$$

$$\begin{aligned}\frac{\partial Q}{\partial t} + v_\gamma \nabla_\gamma Q_{\alpha\beta} &= -6D_r \left( Q_{\alpha\beta} - \frac{1}{3}\delta_{\alpha\beta} \right) \\ &+ Q_{\alpha\gamma}\nabla_\gamma v_\beta + Q_{\beta\gamma}\nabla_\gamma v_\alpha - 2Q_{\alpha\beta}Q_{\gamma\epsilon}\nabla_\gamma v_\epsilon\end{aligned} \tag{5.67}$$

$$\frac{\partial \lambda}{\partial t} + v_\gamma \nabla_\gamma \lambda = g_{\alpha\beta}\nabla_\beta v_\alpha - \Lambda \frac{n_0 k_B T}{2} \left[ \frac{1}{\lambda} - \frac{\lambda_0}{\lambda^2} - \frac{9\lambda_0}{2} \frac{S_{\alpha\beta}S_{\alpha\beta}}{\lambda^2} \right]. \tag{5.68}$$

Before defining $\mathbf{g}$ and $\Lambda$ it is first instructive to compare the above equations to the RRM-R. First, consider the evolution equation for the orientation tensor above, Eq. (5.67), and in the RRM-R, Eq. (5.35). Notice that these two expressions are identical except for the coupling to the velocity gradient. This difference can be remedied by changing the supplied closure approximation in the RRM-R; currently, the RRM-R relies on the Dhont and Briels closure approximation, Eq. (5.31), but other closure approximations exist. In fact, one of the simplest closure approximations is the quadratic closure by Doi [80], who approximated

$$\langle u_\alpha u_\beta u_\gamma u_\epsilon \rangle \nabla_\gamma v_\epsilon \approx Q_{\alpha\beta}Q_{\gamma\epsilon}\nabla_\gamma v_\epsilon. \tag{5.69}$$

Substituting this expression into Eq. (5.35) rather than the Dhont and Briels closure yields an identical expression to the one derived from the SGBF. Thus, using NET we can derive similar, and potentially equivalent, expressions to the RRM-R.

It should be noted that in Eq. (5.61), prior to disregarding the non-affine motion by setting $\mathbf{L} = 0$, we can see that $\mathbf{L}$ also couples to the velocity gradient; it may be possible to identify a form of $\mathbf{L}$ that would match the closure approximation by Dhont and Briels so that the NET evolution equation matches that of the RRM-R. In this case, the interpretation of $\mathbf{L}$ as non-affine motion would be lost. Moreover, the non-affine matrix $\mathbf{L}$ also appears in the stress equation, Eq. (5.60), and is coupled to the Volterra derivative of the Hamiltonian with respect to $\mathbf{Q}$ (which is proportional to $\mathbf{S}$). Consequently, even if the NET orientation equation matched the RRM-R orientation equation with the Dhont and Briels closure, the disagreement would then be transferred to the stress equations.

Now comparing Eq. (5.66) and Eq. (5.36), we see that just like the orientation equations

there is a mismatch in the coupling to the velocity gradient, but, also just like the orientation equations, this is resolved by using the quadratic closure in the RRM-R rather than the Dhont and Briels closure. There are two additional problems, however, the first being the stress arising from the coupling of the structural variable to the velocity gradient through $g_{\alpha\beta}$. This coupling leads to an additional stress proportional to $\delta H/\delta\lambda$ (the last term in Eq. (5.66)) that is not present in the RRM-R; consequently, if we want to match the RRM-R governing equations as closely as possible we must set $g_{\alpha\beta} = 0$. The second problem with the stress equation is that it matches the RRM-R stress only up to linear terms in $S_{\alpha\beta}$; this problem is not easily remedied as it arises through the nature of the derivations (the interested reader can turn to [170] or chapter 11.6 of [164] for further discussion). We can not simply disregard the higher-order terms, so for the moment we will accept that the NET equations and RRM-R equations will only match up to linear terms.

Finally, we must address the evolution equations for the micelle length, $L$, denoted as the structural variable, $\lambda$, in the SGBF derivation. Immediately it is clear that the RRM-R and SM-A length evolution equations differ significantly, most notably in that the SM-A does not show the exponential breakage term present in the RRM-R. The SM-A does show the alignment induced growth term proportional to $\sim Q^2/L^2$, and also shows spontaneous growth ($\sim 1/\lambda$) and breakage ($\sim 1/\lambda^2$), though the signs are flipped compared to the RRM-R (i.e., growth corresponds to breakage terms and vice versa). In addition to the stress equations, the length evolution equations also suggest that $g_{\alpha\beta} = 0$ to match the RRM-R since no direct dependence on the velocity gradient appears in the RRM-R length equation. The form of Eq. (5.68) does present a potential problem in that the only breakage term is proportional to $\sim 1/\lambda$ and may not be strong enough to balance growth terms; to address this challenge, we must be careful in choosing the form of $\Lambda$.

Before ascertaining the thermodynamic admissibility of the SM-A, we first wish to non-dimensionalize the governing equations. Using asterisks to denote dimensionless quantities, we render the governing equations dimensionless with the following relations: $\boldsymbol{x} = \boldsymbol{x}^* d$,

$\boldsymbol{v} = \boldsymbol{v}^* U$, $t = t^*/\dot{\gamma}$, $p = p^* \eta_s \dot{\gamma}$, $\boldsymbol{\tau}^m = \boldsymbol{\tau}^{m*} G_0$, and $\lambda = \lambda^* \lambda_0$ where $\dot{\gamma} = U/d$ is the characteristic shear rate and $G_0 = n_0 k_B T = 2\eta_m D_{r,0}/15$ is the micelle shear modulus. Substituting these relations into the governing equations and dropping asterisks we are left with the dimensionless equations:

$$\nabla_\alpha v_\alpha = 0, \tag{5.70}$$

$$\mathrm{Re}\left(\frac{\partial v_\alpha}{\partial t} + v_\beta \nabla_\beta v_\alpha\right) = -\nabla_\alpha P + \nabla_\beta \nabla_\beta v_\alpha + \frac{2}{15}\left(\frac{1-\beta}{\beta}\right)\frac{1}{\mathrm{Pe}} \nabla_\beta T_{\alpha\beta}, \tag{5.71}$$

$$T_{\alpha\beta} = \frac{3}{\lambda}\left(Q_{\alpha\beta} - \frac{1}{3}\delta_{\alpha\beta}\right) + \frac{1}{2\lambda D_r} Q_{\alpha\beta} Q_{\gamma\epsilon} \nabla_\gamma v_\epsilon + \frac{9}{\lambda}\left(S_{\gamma\beta} S_{\alpha\gamma} - Q_{\alpha\beta} S_{\gamma\epsilon} S_{\gamma\epsilon}\right), \tag{5.72}$$

$$\frac{\mathrm{D}Q}{\mathrm{D}t} = -\frac{6}{\mathrm{Pe}\lambda^3}\left(Q_{\alpha\beta} - \frac{1}{3}\delta_{\alpha\beta}\right) + Q_{\alpha\gamma}\nabla_\gamma v_\beta + Q_{\beta\gamma}\nabla_\gamma v_\alpha - 2Q_{\alpha\beta}Q_{\gamma\epsilon}\nabla_\gamma v_\epsilon \tag{5.73}$$

$$\frac{\mathrm{D}\lambda}{\mathrm{D}t} = \frac{\Lambda}{2}\left[\frac{1}{\lambda^2} + \frac{9}{2}\frac{S_{\alpha\beta}S_{\alpha\beta}}{\lambda^2} - \frac{1}{\lambda}\right], \tag{5.74}$$

where we have applied Eq. (3.9) for the diffusion constant and included conservation of mass. We have also applied non-dimensionalization to the transport coefficient for structure relaxation

$$\Lambda = \frac{\Lambda^*}{n_0 k_B T}. \tag{5.75}$$

We have introduced several dimensionless quantities. The Reynolds number is the ratio of inertial and viscous forces, defined as $\mathrm{Re} = \rho U d/\eta_s$. The rotational Péclet number is the ratio of the shear rate to the rotational diffusivity of the micelles at equilibrium, defined as $\mathrm{Pe} = \dot{\gamma}/D_{r0}$. Finally, $\beta = \eta_s/(\eta_s + \eta_m)$ is the viscosity ratio.

**Verification of thermodynamic admissibility**

The final step of developing the SM-A is to verify its thermodynamic admissibility, which requires a description of the dissipation bracket and the Hamiltonian. In this step we must compute and enforce the constraint $\mathrm{d}H/\mathrm{dt} = [H, H] \leq 0$, which does not require knowledge of the Poisson bracket since $\{H, H\} = 0$ by construction. It is helpful to perform this analysis for each contribution to the dissipation bracket individually if possible. We have

already shown that the Newtonian viscous contribution, proportional to $Q_{\alpha\beta\gamma\epsilon}$, satisfies this constraint. The second term in the momentum dissipation bracket, proportional to $R_{\alpha\beta\gamma\epsilon}$, is

$$\begin{aligned}
[H,H]_R &= -\int_\Omega \nabla_\alpha \frac{\delta H}{\delta m_\beta} R_{\alpha\beta\gamma\epsilon} \nabla_\gamma \frac{\delta H}{\delta m_\epsilon} \mathrm{d}V \\
&= -\int_\Omega \nabla_\alpha v_\beta \left( \frac{nk_BT}{2D_r} Q_{\alpha\beta} Q_{\gamma\epsilon} \right) \nabla_\gamma v_\epsilon \mathrm{d}V \\
&= -\frac{nk_BT}{2D_r} \int_\Omega K_{\alpha\beta} Q_{\alpha\beta} Q_{\gamma\epsilon} K_{\gamma\epsilon} \mathrm{d}V, \\
&= -\frac{nk_BT}{2D_r} \int_\Omega \left( K_{\alpha\beta} Q_{\alpha\beta} \right)^2 \mathrm{d}V,
\end{aligned} \tag{5.76}$$

where $K_{\alpha\beta} = \nabla_\alpha v_\beta$; thus $[H,H]_R \leq 0$ provided $nk_BT/D_r \geq 0$, which is always true. Next we turn our attention to the dissipation bracket for the orientation tensor, which depends on $P_{\alpha\beta\gamma\epsilon}$:

$$\begin{aligned}
[H,H]_Q &= -\int_\Omega \frac{\delta H}{\delta Q_{\alpha\beta}} P_{\alpha\beta\gamma\epsilon} \frac{\delta H}{\delta Q_{\gamma\epsilon}} \mathrm{d}V \\
&= -\int_\Omega \left( \frac{9n_0k_BT}{2} \frac{\lambda_0}{\lambda} S_{\alpha\beta} \right) \left( \frac{3D_r}{4nk_BT} \left( \delta_{\alpha\gamma}\delta_{\beta\epsilon} + \delta_{\alpha\epsilon}\delta_{\beta\gamma} \right) \right) \left( \frac{9n_0k_BT}{2} \frac{\lambda_0}{\lambda} S_{\gamma\epsilon} \right) \mathrm{d}V \\
&= -\frac{243}{8} nk_BTD_r \int_\Omega S_{\alpha\beta} S_{\beta\alpha} \mathrm{d}V.
\end{aligned} \tag{5.77}$$

Through the same constraint as above we have $[H,H]_Q \leq 0$. Finally, we must consider the dissipation bracket for the relaxation of the structural variable:

$$\begin{aligned}
[H,H]_\lambda &= -\int_\Omega \frac{\delta H}{\delta \lambda} \Lambda \frac{\delta H}{\delta \lambda} \mathrm{d}V \\
&= -\int_\Omega \Lambda \left( \frac{\delta H}{\delta \lambda} \right)^2,
\end{aligned} \tag{5.78}$$

which clearly satisfies $[H,H] \leq 0$ provided $\Lambda \geq 0$. Thus we have shown that the governing equations for the SM-A model are indeed thermodynamically admissible provided a few physical constraints are enforced.

## 5.5 Structural model - B (SM-B)

The derivation of the second structural micelle model (SM-B) follows exactly the same derivation as that of SM-A, shown above in Section 5.4, but we now assume a constant elastic modulus $G_0 = nk_BT$. This is equivalent to relaxing the conservation of surfactants constraint by assuming $n = n_0$; consequently the relation $n\lambda = n_0\lambda_0$ is no longer enforced such that $n$ and $\lambda$ are now independent of one another. According to the picture presented in the RRM-R, there should never be a constant modulus because in order for micelles to grow the number density of rods must change. However, we can justify a constant number density by assuming that there are a number of free spherical micelles in the bulk which can change shape and exchange surfactants with the rodlike micelles to maintain a constant number density of rods. There is experimental evidence to support the coexistence of rodlike and spherical micelles in solution, so this assumption is not baseless [181]. Moreover, the presence of a dilute concentration of spherical micelles would have minimal, if any, effect on the solution viscosity or viscoelasticity [15]. This change should not necessarily lead to violations of conservation of mass, however it does weaken the connection to the physical picture of dilute wormlike micelle solutions. By not enforcing conservation of surfactants we are losing the idea that micelles are self-assembled structures that are in balance with their surfactant constituents. As we will see, although we are losing some of the physical meaning, we are gaining a simpler mathematical structure.

The only difference between SM-A and SM-B is a change in the Volterra derivative of the Hamiltonian with respect to the structural variable. This change arises due to the fact that $n$ and $\lambda$ are now treated as independent. Rewriting the Hamiltonian with $G_0 = nk_BT$ we have:

$$H(\mathbf{x}) = \int_\Omega \frac{G_0}{2\lambda_0}\left(\lambda \ln(\lambda/\lambda_0) - \lambda + \lambda_0\right) \mathrm{d}V + \int_\Omega \frac{9}{4} G_0 S_{\alpha\beta} S_{\beta\alpha} \mathrm{d}V. \tag{5.79}$$

The Volterra derivatives are:

$$\frac{\delta H}{\delta m_\alpha} \equiv v_\alpha = \frac{m_\alpha}{\rho}, \tag{5.80}$$

$$\frac{\delta H}{\delta Q_{\alpha\beta}} = \frac{\delta H}{\delta S_{\alpha\beta}} = \frac{9G_0}{2} S_{\alpha\beta}, \tag{5.81}$$

$$\frac{\delta H}{\delta \lambda} = \frac{G_0}{2} \frac{\ln(\lambda/\lambda_0)}{\lambda_0}. \tag{5.82}$$

Taking the same transport coefficients as they were defined in Section 5.4, the governing equations are:

$$\rho \left( \frac{\partial v_\alpha}{\partial t} + v_\beta \nabla_\beta v_\alpha \right) = -\nabla_\alpha P + \eta_s \nabla_\beta \nabla_\beta v_\alpha + \nabla_\beta T_{\alpha\beta}, \tag{5.83}$$

$$\begin{aligned} \frac{T_{\alpha\beta}}{G_0} = 3 \left( Q_{\alpha\beta} - \frac{1}{3}\delta_{\alpha\beta} \right) + \frac{1}{2D_r} Q_{\alpha\beta} Q_{\gamma\epsilon} \nabla_\gamma v_\epsilon + 9 \left( S_{\gamma\beta} S_{\alpha\gamma} - Q_{\alpha\beta} S_{\gamma\epsilon} S_{\gamma\epsilon} \right) \\ - \frac{1}{2} g_{\alpha\beta} \frac{\ln(\lambda/\lambda_0)}{\lambda_0}, \end{aligned} \tag{5.84}$$

$$\begin{aligned} \frac{\partial Q}{\partial t} + v_\gamma \nabla_\gamma Q_{\alpha\beta} = -6D_r \left( Q_{\alpha\beta} - \frac{1}{3}\delta_{\alpha\beta} \right) \\ + Q_{\alpha\gamma} \nabla_\gamma v_\beta + Q_{\beta\gamma} \nabla_\gamma v_\alpha - 2 Q_{\alpha\beta} Q_{\gamma\epsilon} \nabla_\gamma v_\epsilon \end{aligned} \tag{5.85}$$

$$\frac{\partial \lambda}{\partial t} + v_\gamma \nabla_\gamma \lambda = g_{\alpha\beta} \nabla_\beta v_\alpha - \Lambda \frac{G_0}{2} \frac{\ln(\lambda/\lambda_0)}{\lambda_0}. \tag{5.86}$$

As for the SM-A, we have currently left $\Lambda$ and $g_{\alpha\beta}$ unspecified, though in we expect $g_{\alpha\beta} = 0$. This model has the same structure as the SM-A, but assuming a constant modulus greatly simplifies the Volterra derivative for the structural variable, which consequently simplifies the evolution equation for length. If $g_{\alpha\beta} = 0$, the main difference between this model and the SM-A is in the term for structural relaxation ($\Lambda$). On closer inspection, however, many terms in the micelle stress lose the inverse dependence on length. It is not clear how this change in dependence will manifest, but this change furthers the divide between this model and the RRM-R. We do not expect this model will be suitable for describing dilute WLM solutions, but we have included it to show how small changes to the Hamiltonian can have a strong effect on the resulting governing equations. For completeness, using the similarities between this model and the SM-A it is easy to show that this model is also thermodynamically admissible provided the same constraints are enforced.

## 5.6 Structural model - C (SM-C)

The final model we will discuss is the derivation of the SM-C; this derivation will differ greatly from the derivations of the SM-A and SM-B as it will now directly consider the thermodynamics of a reaction scheme. This section takes inspiration from work by Germann and coworkers who derived a thermodynamically consistent iteration of the VCM model, so-called as the GCB model [88], and draws heavily from ch. 12 of [164]. We want to be clear that this section is meant as a proof-of-concept to show that reaction kinetics introduced through the dissipation bracket can be used for modeling dilute wormlike micelle solutions; the model derived in this section is not finalized, and as we will discuss, requires further analysis and investigation.

In the SM-C model we consider the reversible reaction of a long micelle, $A$, into two shorter micelles, $B$; the shorter micelles, $B$, can fuse to form a longer micelle, $A$. This reaction is described by

$$\mathrm{A} \underset{\mathrm{r}_b}{\overset{\mathrm{r}_f}{\rightleftharpoons}} 2\,\mathrm{B}, \tag{5.87}$$

where $r_f$ and $r_b$ are the rates of the forward and reverse reactions, respectively. In order to retain similarity with the RRM-R, which does not incorporate a population balance but rather assumes monodispersity of micelles, let us also enforce a monodispersity constraint here such that mass is always uniformly distributed throughout the micelles [182]. Consider a system of $n$ micelles each with length $A$; if a single one of these micelles breaks into two shorter micelles of length $B$, then the system consists of $n+1$ micelles, where $n-1$ of these have length $A$ and two of these have length $B$; if we enforce monodispersity, each of these micelles must instantaneously redistribute mass such that the system consists of $n+1$ micelles each with length $C = \frac{n-1}{n}A$. If we now take the limit of large $n$, which is the case even for dilute wormlike micelle solutions, we find $C \approx A$. An identical argument holds for fusion reactions. Therefore, if we consider the reaction scheme as consisting of a series of individual reactions where in between each successive reaction mass is redistributed to

maintain monodispersity, we can approximate:

$$\mathrm{A} \underset{\mathrm{r}_b}{\overset{\mathrm{r}_f}{\rightleftharpoons}} 2\,\mathrm{A}. \tag{5.88}$$

This expression may seem dubious since it could easily lead to violation of mass conservation; we can attempt to justify this, however, by again assuming that there are a number of free spherical micelles in the bulk that can change shape and exchange surfactants with the rodlike micelles to ensure mass conservation. This justification may seem flimsy, but it does allow us to proceed in developing the framework for modeling dilute WLM solutions using a NET reaction scheme. In future work we plan to introduce population balance modeling with a moment formulation [183]. The remainder of this section follows the steps outlined above for deriving a model using SGBF.

**Identification of state variables**

We consider a dilute solution of wormlike micelles with rod number density $n$, length $\lambda$, orientation tensor $Q_{\alpha\beta}$, total momentum density $m_\alpha$, total velocity field $v_\alpha$, and total mass density $\rho = \rho_s + \sum_i^\nu \rho_i$ for $\nu$ components participating in the reactions. All components are assumed to move at the same velocity. Typically for systems involving reactions the state variables must account contributions ($i$) from each component:

$$\mathbf{x} = \{m_\alpha, Q^i_{\alpha\beta}, \lambda^i, \rho_i\}, \quad i = 1, .., \nu. \tag{5.89}$$

In the current system we are considering a single reaction component, $A$, and the structural variable and number density (and therefore also the mass density) of $A$ are coupled such that the state variables reduce to:

$$\mathbf{x} = \{m_\alpha, Q^A_{\alpha\beta}, \lambda^A\}. \tag{5.90}$$

For the remainder of this work we will drop the $A$ superscripts as these can only refer to one component.

**Defining the Hamiltonian**

The Hamiltonian can be broken up into the kinetic energy, given by Eq. (5.5), and the Helmholtz free energy, $A(\mathbf{x})$, which incudes both elastic and entropic contributions. The elastic contribution is

$$A_{el}(\mathbf{x}) = \int_{\Omega} \frac{9}{4} n k_B T S_{\alpha\beta} S_{\beta\alpha} \mathrm{d}V, \tag{5.91}$$

As in the RRM-R, conservation of surfactants (and therefore mass) is enforced by the constraint $n\lambda = n_0\lambda_0$, where $n_0$ and $\lambda_0$ are the micelle number density and length at equilibrium, respectively. The entropic term is

$$A_{en}(\mathbf{x}) = n k_B T \ln \phi_A + n_s k_B T \ln \phi_s, \tag{5.92}$$

where $n_s$ is the number density of the solvent, $\phi_A$ is the volume fraction of micelles, and $\phi_s$ is the volume fraction of solvent molecules. Note that $\phi_A = n\lambda\pi b^2 = n_0\lambda_0\pi b^2$ is constant. This entropic contribution is a Flory-Huggins term accounting for the random mixing of micelles with the solvent [88].

The Volterra derivatives of the Hamiltonian are:

$$\frac{\delta H}{\delta m_\alpha} \equiv v_\alpha = \frac{m_\alpha}{\rho}, \tag{5.93}$$

$$\frac{\delta H}{\delta Q_{\alpha\beta}} = \frac{\delta H}{\delta S_{\alpha\beta}} = \frac{9 n k_B T}{2} S_{\alpha\beta}, \tag{5.94}$$

$$\frac{\delta H}{\delta \lambda} = -\frac{n_0 k_B T \lambda_0}{\lambda^2} \left[ \frac{9}{4} S_{\alpha\beta} S_{\beta\alpha} + \ln \phi_A \right]. \tag{5.95}$$

**Formulation of the Poisson bracket**

The Poisson brackets are identical to those used in the SM-A and SM-B, Eqs. (5.7), (5.48), (5.51) and (5.52). Notably, introducing a reaction scheme changes the irreversible dynamics of the system but not the reversible.

**Formulation of the dissipation bracket**

The real difficulty of introducing reaction schemes into the SGBF framework is seen in properly formulating the dissipation bracket. Formulating the dissipation bracket requires describing all of the irreversible dynamics of the system, which in the presence of reactions means considering reaction and fluxes. As was done for the SM-A and SM-B models, we will break the dissipation bracket into three terms for each of the state variables and an additional term for the dissipative forces of the reaction:

$$[F, H] = [F, H]_m + [F, H]_Q + [F, H]_\lambda + [F, H]_{\text{rxn}}, \tag{5.96}$$

where $[F, H]_m$, $[F, H]_Q$, and $[F, H]_\lambda$ are given by Eqs. (5.56) to (5.58), respectively.

To develop the reaction dissipation bracket we first assume that the forward (+) and reverse (−) fluxes, $J^\mp$ of the reaction take the standard Arrhenius dependence on their affinities, $A^\mp$, such that

$$J^\mp = k(p, T) \exp\left(-\frac{A^\mp}{RT}\right), \tag{5.97}$$

where $k(p, T)$ is the net reaction rate and depends on pressure and temperature and $R$ is the ideal gas constant [88, 164]. The affinity accounts for mass density transfer and is given by

$$A^\mp = -\sum_{i=1}^{\nu} \gamma_i^\mp \mu_i, \tag{5.98}$$

where $i$ is the system component, $\nu$ is the number of components, $\gamma_i$ is the stoichiometric coefficient of component $i$ in the reaction, and $\mu_i$ is the molar chemical potential of component

$i$ and given by

$$\mu_i = M_i \frac{\delta H}{\delta \rho_i}. \tag{5.99}$$

Here, $M_i$ and $\rho_i$ are the molecular weight and density of component $i$, respectively. Germann and coworkers [88] modifed the chemical potential to account for other non-equilibrium changes associated with the reaction (e.g., transfer of momentum or orientation density)

$$\mu_i = M_i \left( \frac{\delta H}{\delta \rho_i} + \frac{m_\alpha^i}{\rho_i} \left( \frac{\delta H}{\delta m_\alpha^i} \right)^* + \frac{C_{\alpha\beta}^i}{\rho_i} \frac{\delta H}{\delta C_{\alpha\beta}^i} \right), \tag{5.100}$$

where $\delta \cdot / \delta m_\alpha^i$ must be modified to ensure the extra stress is Galilean invariant

$$\left( \frac{\delta \cdot}{\delta m_\alpha^i} \right)^* = \frac{\delta \cdot}{\delta m_\alpha^i} - \sum_{k=1}^{v} \frac{\rho_k}{\rho} \frac{\delta \cdot}{\delta m_\alpha^k}. \tag{5.101}$$

Following this approach and accounting for the constrained orientation density rather than the unconstrained conformation density we have

$$\mu_i = M_i \left( \frac{\delta H}{\delta \rho_i} + \frac{m_\alpha^i}{\rho_i} \left( \frac{\delta H}{\delta m_\alpha^i} \right)^* + \frac{Q_{\alpha\beta}^i}{\rho_i} \frac{\delta H}{\delta Q_{\alpha\beta}^i} \right). \tag{5.102}$$

As a note, it is unclear in literature whether the denominator of the summation in the Galilean invariant modification should be the total mass density ($\rho$) or should be the total mass density of species that participate in reactions ($\rho_{tot}$) [88, 176]. The distinction here is important for accurately capturing the chemical potential. Moreover, since we are considering a single component reaction, if we opt for the latter interpretation of $\rho_{tot}$ in the denominator, the second term in the modified chemical potential, proportional to the Volterra derivative of the Hamiltonian with respect to the momentum density, will vanish. Likewise the Galilean invariant term in the reaction dissipation bracket will vanish. In literature, this appears to be the common result; Germann and coworkers [88] even express: "As a consequence, the fluxes do not bear a direct dependence on the local mean velocity field." This is the interpretation that we will employ for the rest of this work, with the caveat that

it may need to be reevaluated at a later point.

We can now write the most general description of reaction dissipation bracket [164]:

$$\begin{aligned}
[F,H]_{rxn} = &- \int \sum_{j=1}^{N} J_j^- \sum_{i=1}^{\nu} \gamma_{ji}^- M_i \left\{ \left( \frac{\delta F}{\delta \rho_i} + \frac{m_\alpha^i}{\rho_i} \left( \frac{\delta F}{\delta m_\alpha^i} \right)^* + \frac{Q_{\alpha\beta}^i}{\rho_i} \frac{\delta F}{\delta Q_{\alpha\beta}^i} \right) \right. \\
&\left. + \frac{1}{\sum_{k=1}^{N} \gamma_{jk}^+ M_k} \sum_{p=1}^{N} \gamma_{jp}^+ M_p \left( \frac{\delta F}{\delta \rho_p} + \frac{m_\alpha^i}{\rho_i} \left( \frac{\delta F}{\delta m_\alpha^p} \right)^* + \frac{Q_{\alpha\beta}^i}{\rho_i} \frac{\delta F}{\delta Q_{\alpha\beta}^p} \right) \right\} dV \\
&- \int \sum_{j=1}^{N} J_j^+ \sum_{i=1}^{\nu} \gamma_{ji}^+ M_i \left\{ \left( \frac{\delta F}{\delta \rho_i} + \frac{m_\alpha^i}{\rho_i} \left( \frac{\delta F}{\delta m_\alpha^i} \right)^* + \frac{Q_{\alpha\beta}^i}{\rho_i} \frac{\delta F}{\delta Q_{\alpha\beta}^i} \right) \right. \\
&\left. + \frac{1}{\sum_{k=1}^{N} \gamma_{jk}^- M_k} \sum_{p=1}^{N} \gamma_{jp}^- M_p \left( \frac{\delta F}{\delta \rho_p} + \frac{m_\alpha^i}{\rho_i} \left( \frac{\delta F}{\delta m_\alpha^p} \right)^* + \frac{Q_{\alpha\beta}^i}{\rho_i} \frac{\delta F}{\delta Q_{\alpha\beta}^p} \right) \right\} dV.
\end{aligned} \tag{5.103}$$

This expression accounts for $N$ reactions and $\nu$ components in the system.

The reaction bracket can be simplified by substituting quantities associated with the current reaction scheme, Eq. (5.88): $\gamma^+ = -1$ and $\gamma^- = 2$. Using these stoichiometric coefficients and the fact that we only consider a single reaction the dissipation bracket for the reaction becomes

$$[F,H]_{rxn} = \int_\Omega (J^- - 2J^+) M_A \left( \frac{\delta F}{\delta \rho_A} + \frac{Q_{\alpha\beta}}{\rho_A} \frac{\delta F}{\delta Q_{\alpha\beta}} \right) dV, \tag{5.104}$$

where

$$J^- = k_1 \exp\left( -2 \frac{\mu_A}{RT} \right), \tag{5.105a}$$

$$J^+ = k_1 \exp\left( \frac{\mu_A}{RT} \right). \tag{5.105b}$$

To simplify the general chemical potential it is useful to provide a few change of variables:

$$\frac{\delta H}{\delta \rho_A} = \frac{\delta H}{\delta n_A} \frac{\partial n_A}{\partial \rho_A} = \frac{\delta H}{\delta n_A} \left( \frac{N_{Av}}{M_A} \right), \tag{5.106}$$

$$\frac{\delta H}{\delta n_A} = \frac{\delta H}{\delta \lambda} \frac{\partial \lambda}{\partial n_A} = \frac{\delta H}{\delta \lambda} \left( -\frac{\lambda^2}{n_0 \lambda_0} \right), \tag{5.107}$$

where $n_i = \rho_i N_{Av}/M_A = n_0\lambda_0/\lambda$ and $N_{Av}$ is Avogadro's number. The chemical potential is then given bys

$$\begin{aligned}\mu_A &= -\frac{N_{Av}\lambda^2}{n_0\lambda_0}\frac{\delta H}{\delta\lambda} + M_A\frac{Q_{\alpha\beta}}{\rho_A}\frac{\delta H}{\delta Q_{\alpha\beta}} \\ &= N_{Av}k_BT\left(\frac{9}{2}Q_{\alpha\beta}S_{\alpha\beta} - \frac{9}{4}S_{\alpha\beta}S_{\beta\alpha} + \ln\phi_A\right).\end{aligned} \tag{5.108}$$

Finally, to complete the dissipation bracket we must define the net reaction rate, which is equal to the difference of the forward and reverse rates, $k_1 = r_f n - r_b n^2$. This completes the description of the dissipation bracket. Note that this framework is meant to initially retain generality and then be narrowed down as more information about the dissipative processes, and specifically the reaction scheme, are known.

**Derivation of the governing equations**

We are now at the stage of deriving the governing equations for the SM-C. Following the standard procedure:

$$\nabla_\alpha v_\alpha = 0, \tag{5.109}$$

$$\rho\left(\frac{\partial v_\alpha}{\partial t} + v_\beta\nabla_\beta v_\alpha\right) = -\nabla_\alpha P + Q_{\alpha\beta\gamma\epsilon}\nabla_\beta\nabla_\gamma v_\epsilon + \nabla_\beta T_{\alpha\beta}, \tag{5.110}$$

$$\begin{aligned}T_{\alpha\beta} = 2\left(S_{\gamma\beta} + \frac{1}{3}\delta_{\gamma\beta}\right)\frac{\delta H}{\delta Q_{\alpha\gamma}} - 2\left(S_{\alpha\beta} + \frac{1}{3}\delta_{\alpha\beta}\right)S_{\gamma\epsilon}\frac{\delta H}{\delta Q_{\gamma\epsilon}} \\ -g_{\alpha\beta}\frac{\delta H}{\delta\lambda} + L_{\alpha\beta\gamma\epsilon}\frac{\delta H}{\delta Q_{\gamma\epsilon}} + R_{\alpha\beta\gamma\epsilon}\nabla_\gamma v_\epsilon,\end{aligned} \tag{5.111}$$

$$\begin{aligned}\frac{\partial Q}{\partial t} + v_\gamma\nabla_\gamma Q_{\alpha\beta} = Q_{\alpha\gamma}\nabla_\gamma v_\beta + Q_{\beta\gamma}\nabla_\gamma v_\alpha - 2Q_{\alpha\beta}Q_{\gamma\epsilon}\nabla_\gamma v_\epsilon \\ -P_{\alpha\beta\gamma\epsilon}\frac{\delta H}{\delta Q_{\gamma\epsilon}} + L_{\gamma\epsilon\alpha\beta}\nabla_\gamma v_\epsilon + (J^- - 2J^+)\frac{Q_{\alpha\beta}}{\rho_A},\end{aligned} \tag{5.112}$$

$$\frac{\partial\lambda}{\partial t} + v_\gamma\nabla_\gamma\lambda = g_{\alpha\beta}\nabla_\beta v_\alpha - \Lambda\frac{\partial H}{\partial\lambda} - \frac{N_{Av}\lambda^2}{n_0\lambda_0}(J^- - 2J^+), \tag{5.113}$$

where

$$J^- = \left(r_f n - r_b n^2\right)\exp\left(-2\left[\frac{9}{2}Q_{\alpha\beta}S_{\alpha\beta} - \frac{9}{4}S_{\alpha\beta}S_{\beta\alpha} + \ln\phi_A\right]\right), \tag{5.114a}$$

$$J^+ = \left(r_f n - r_b n^2\right) \exp\left(\frac{9}{2} Q_{\alpha\beta} S_{\alpha\beta} - \frac{9}{4} S_{\alpha\beta} S_{\beta\alpha} + \ln \phi_A\right). \tag{5.114b}$$

We can further simplify these expressions by adopting the definitions used in the SM-A such that $g_{\alpha\beta} = 0$, $\mathbf{L} = 0$, and $R_{\alpha\beta\gamma\epsilon}$ defined in Eq. (5.64), as well as substituting in the Volterra derivatives:

$$\nabla_\alpha v_\alpha = 0, \tag{5.115}$$

$$\rho\left(\frac{\partial v_\alpha}{\partial t} + v_\beta \nabla_\beta v_\alpha\right) = -\nabla_\alpha P + Q_{\alpha\beta\gamma\epsilon} \nabla_\beta \nabla_\gamma v_\epsilon + \nabla_\beta T_{\alpha\beta}, \tag{5.116}$$

$$\frac{T_{\alpha\beta}}{n_0 k_B T} = \frac{3\lambda_0}{\lambda}\left(Q_{\alpha\beta} - \frac{1}{3}\delta_{\alpha\beta}\right) + \frac{\lambda_0}{2\lambda D_r} Q_{\alpha\beta} Q_{\gamma\epsilon} \nabla_\gamma v_\epsilon + \frac{9\lambda_0}{\lambda}\left(S_{\gamma\beta} S_{\alpha\gamma} - Q_{\alpha\beta} S_{\gamma\epsilon} S_{\gamma\epsilon}\right), \tag{5.117}$$

$$\begin{aligned} \frac{\partial Q}{\partial t} + v_\gamma \nabla_\gamma Q_{\alpha\beta} = {} & Q_{\alpha\gamma} \nabla_\gamma v_\beta + Q_{\beta\gamma} \nabla_\gamma v_\alpha - 2 Q_{\alpha\beta} Q_{\gamma\epsilon} \nabla_\gamma v_\epsilon \\ & -6 D_r \left(Q_{\alpha\beta} - \frac{1}{3}\delta_{\alpha\beta}\right) + (J^- - 2J^+) \frac{Q_{\alpha\beta}}{\rho_A}, \end{aligned} \tag{5.118}$$

$$\frac{\partial \lambda}{\partial t} + v_\gamma \nabla_\gamma \lambda = -\Lambda \frac{n_0 k_B T}{2}\left[\frac{1}{\lambda} - \frac{\lambda_0}{\lambda^2} - \frac{9\lambda_0}{2} \frac{S_{\alpha\beta} S_{\alpha\beta}}{\lambda^2}\right] - \frac{N_{Av} \lambda^2}{n_0 \lambda_0}(J^- - 2J^+). \tag{5.119}$$

As we can see, the consequence of including reaction dynamics into the dissipation bracket directly alters the equations for the orientation and length, which will of course indirectly effect the velocity field and stress. There is further freedom in the above governing equations in that we have again not specified the structural relaxation variable and we have not specified the forward and reverse reaction rates. These reaction rates could be taken to be constant for simplicity, or could depend on the state variables. For example, the fusion reaction rate could be assumed to depend on the orientation of micelles while the breakage could depend on micelle length. Finally, by including reaction kinetics through the dissipation bracket we can obtain the exponential term that is present in the original RRM-R. Perhaps by modifying the Hamiltonian slightly, which would effect the chemical potentials, the exponentials here could more strongly resemble the one in the RRM-R.

To conclude this section, we would like to emphasize that the above derivation of the SM-C is not meant to be final. There are a few points that still must be addressed, such as

the mass density in the Galilean invariance modification, before this model can be complete. This section is rather meant to serve as a proof-of-concept to show that reaction kinetics introduced into the SGBF-NET formalism can be used to derive a model for dilute wormlike micelle solutions.

**Verification of thermodynamic admissibility**

Finally, we must verify the thermodynamic consistency of the SM-C. The only term we must address is the dissipation bracket for the reaction kinetics, all other terms are identical to the SM-A and have been shown to be thermodynamically admissible in Section 5.4. For the reaction terms:

$$\begin{aligned}[H,H]_{rxn} &= \int_\Omega (J^- - 2J^+) M_A \left( \frac{\delta H}{\delta \rho_A} + \frac{Q_{\alpha\beta}}{\rho_A} \frac{\delta H}{\delta Q_{\alpha\beta}} \right) dV \\ &= \int_\Omega (J^- - 2J^+) M_A \left( N_{Av} k_B T \left[ \frac{9}{4} S_{\alpha\beta} S_{\beta\alpha} + \ln \phi_A \right] + \frac{9}{2} \frac{n k_B T}{\rho_A} Q_{\alpha\beta} S_{\alpha\beta} \right) dV.\end{aligned} \tag{5.120}$$

Unlike the other dissipation brackets we have analyzed, this one does not simplify to an easily enforceable constraint to maintain thermodynamic admissibility. Rather, we are left with conditions on the forward and reverse fluxes. The exponentials in the fluxes are always positive, but the negative in $J^-$ means that $J^- < J^+$ However, we also must consider the total reaction rate $k_1 = r_f n - r_b n^2$:

$$\begin{aligned}J^- - 2J^+ = (r_b n^2 - r_f n) \Bigg[ &\exp\left( \frac{9}{2} Q_{\alpha\beta} S_{\alpha\beta} - \frac{9}{4} S_{\alpha\beta} S_{\beta\alpha} + \ln \phi_A \right) \\ &- \exp\left( -2 \left[ \frac{9}{2} Q_{\alpha\beta} S_{\alpha\beta} - \frac{9}{4} S_{\alpha\beta} S_{\beta\alpha} + \ln \phi_A \right] \right) \Bigg].\end{aligned} \tag{5.121}$$

In order for $J^- - 2J^+ < 0$ we require $r_b < r_f/n$ or alternatively $r_b < r_f \lambda / n_0 \lambda_0$; this constraint is not particularly challenging to resolve, but it does become more challenging to satisfy as micelles break apart. Thus we have demonstrated that with the imposition of certain constraints the SM-C model is thermodynamically consistent.

## 5.7 Conclusions

In this work we have provided an overview of the single generator bracket formalism of non-equilibrium thermodynamics; using the SGBF, we have derived three separate models that are meant to represent dilute wormlike micelle solutions. These models all consider a system that is fully described by a momentum density, orientation density, and a structural variable representing micelle length. Two of the models, the SM-A and SM-B, consider a scenario where the structural variable is subject to general dissipation dynamics. We have shown that these two models are thermodynamically consistent. We have also derived the SM-C model, which again considers a structural variable but now incorporates a reversible reaction scheme to model micelle scission and fusion. The derivation of SM-C is based on work by Germann and coworkers [88], who use a generalized chemical potential with modifications to account for Galilean invariance. We have expanded on this framework to consider the potential of a system described by a constrained orientation tensor rather than an unconstrained conformation tensor. We have also shown that, under appropriate constrains applied to the forward and reverse reaction rates, the SM-C can also be thermodynamically consistent.

As discussed, the models developed in this work, particularly the SM-C, are not meant to be finalized; rather, much of the work here is meant to serve as proof-of-concept, that the SGBF can be used to derive thermodynamically consistent models for dilute wormlike micelle solutions. Out of the three models derived, the SM-A shows the most potential and completion for studying WLM solutions. In the future, we plan to further the derivation of the SM-C and potentially incorporate a reversible reaction $\mathrm{A} \underset{\mathrm{r}_b}{\overset{\mathrm{r}_f}{\rightleftharpoons}} 2\,\mathrm{B}$, that considers a population of micelle lengths. This framework can also be extended to treat the micelle lengths as some distribution (e.g., exponential [15]), where the moments can be tracked to reconstruct the distribution and account for the effects of micelles on the stress and velocity fields [183].

# 6

# Conclusions and Future Work

## 6.1 General summary

In this thesis, we have developed a model for dilute wormlike micelle solutions and used this model in computational fluid dynamics simulations to understand instabilities in these flows. We have also shown how non-equilibrium thermodynamics can be used for deriving thermodynamically consistent models for viscoelastic fluids, and specifically wormlike micelle solutions. Motivated by the numerous applications and ubiquity of wormlike micelles, we have demonstrated the capabilities of the model we have derived, the reformulated reactive rod model (RRM-R), in accurately predicting experimental observations; moreover, we have shown that the RRM-R is well-suited for understanding finger-like and interfacial instabilities, as well as vorticity banding, in complex flows.

In Chapter 2, we developed a model for dilute wormlike micelle solutions, the reformulated reactive rod model (RRM-R); the RRM-R, which models micelles as reactive Brownian rods undergoing reversible scission and fusion, iterated upon a previous model (the RRM) in order to establish the model on a more physical grounding and improve predictions of experimental results and transient dynamics. We demonstrated that the RRM-R can predict many of the key rheological features of dilute wormlike micelle solutions: shear-thickening and -thinning, non-zero normal stress differences, and a reentrant flow curve. We then showed that the

RRM-R is capable of predicting both steady and transient dynamics, which confirms its potential for studying instability formation, and showed that it can be successfully fit to experimental data. This model takes a large step towards developing simulation tools for understanding complex phenomena in dilute wormlike micelle solutions.

In Chapter 3 we employed the RRM-R in computational fluid dynamics simulations to study the development of instabilities in circular Couette flow, focusing both on 'finger-like' instabilities that have been observed in experiments and poorly-understood vorticity banding. We applied a stability analysis of the steady states and found that the spatial-dependence of the stress supports flow profiles with mixed local stabilities. Combining this analysis with simulations, we discovered that the RRM-R can capture finger-like instabilities that manifest as finger-like structures of highly elongated, anisotropically-oriented micelles. We also determined that the instability is 2D in nature, with 3D variations arising as secondary effects. To the best of our knowledge, this is the first computational study able to uncover finger-like instabilities, and the first to connect the instability to the reentrant nature of the flow curve. In this chapter we also found that the RRM-R can predict and capture linearly stable vorticity banding.

In Chapter 4 we extended the work on circular Couette flow to study instabilities in plane Poiseuille flow of dilute wormlike micelle solutions. Again, we found that the spatial-dependence of the stress is crucial as it forces the flow to 'jump' between upper and lower branches of the constitutive curve; this jumping gives rise to a state that resembles viscosity-stratified flows, and specifically core-annular channel flow. We identified that the 'interface' between regions is unstable, as it is in viscosity-stratified flows, due to viscosity mismatch and a normal stress jump across the interface. The resulting instability resembled the finger-like structures observed in circular Couette flow, but now both longwave and shortwave structures appear; the longwave structures are observed to resemble mushroom patterns seen in core-annular channel flow. We also found that, just as in circular Couette flow, the initial instability was 2D in nature and 3D variations developed secondarily.

Finally, in Chapter 5 we switched focus to develop a thermodynamically consistent version of the RRM-R. We ultimately derived three models which bear some resemblance to the RRM-R, but each contains subtle differences. To develop these models we employed the generalized bracket framework of non-equilibrium thermodynamics, which enabled enforcement of conservation of energy and non-negative entropy generation. Of the three models derived, two were based on the general evolution and relaxation of a structural variable, while the third considered the dynamics of micelles through the lens of a reversible reaction. Using the single generator bracket formalism, we showed the three models were thermodynamically admissible provided they satisfy a few minor constraints.

In the following sections, we provide and emphasize several directions for future research. These future directions are focused on (1) improvements to the RRM-R to account for micelle flexibility and population distributions, (2) investigating the RRM-R in new flow types and domains, and (3) using the RRM-R to study more complex instabilities, turbulence, and drag reduction in dilute wormlike micelle solutions.

## 6.2 Future work

In this section we outline several potential extensions of the work described in this thesis. These ideas and preliminary results are motivated by remaining questions in the field of complex fluids, recent advances and results for dilute wormlike micelle solutions, or are simply interesting in their own right.

### 6.2.1 Effects of the RRM-R flow curve on instabilities

The RRM-R can predict a vast array of rheological behavior by varying the four model parameters, as demonstrated in Figs. 2.1 and 2.2. In this thesis we have exclusively focused on solutions that are both shear-thickening and -thinning and exhibit a reentrant region, however it is likely that parameters that promote other rheological behavior, or even the

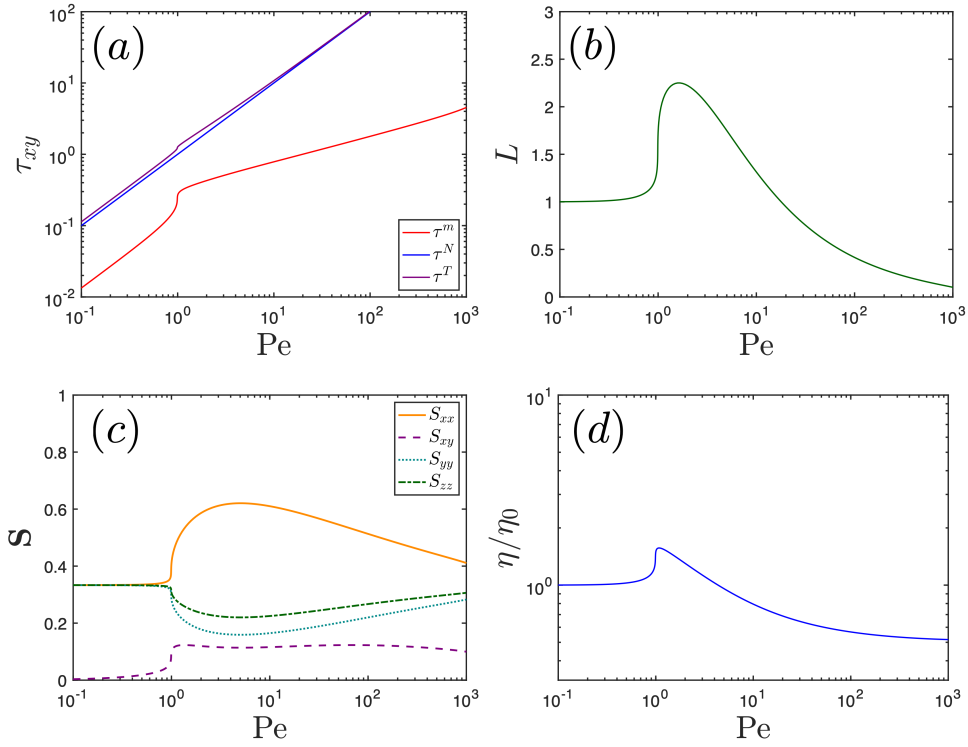


**Figure 6.1:** Constitutive curves for the RRM-R with parameters: $m = 3$, $k_{b0} = 10$, $k_{ga} = 1200$, $k_{bt} = 7$, and $a = 3.5$. (a) Micelle (red), Newtonian (blue), and total shear stress (purple), (b) length of micelles, (c) components of the orientation tensor, and (d) normalized viscosity vs. applied Péclet number.

same rheological behavior just to different extents, are also interesting.

### Non-reentrant flow curves

For example, consider Fig. 6.1, which shows the (a) micelle (red), Newtonian (blue), and total shear stress (purple), (b) length of micelles, (c) components of the orientation tensor, and (d) normalized viscosity vs. applied Péclet number for the RRM-R with $m = 3$, $k_{b0} = 10$, $k_{ga} = 1200$, $k_{bt} = 7$, $a = 3.5$, $\mathrm{Re} = 0.1$, and $\beta = 0.1$. These curves are only weakly shear-thickening and -thinning due to a decreased maximum elongation of micelles compared to the flow curves investigated in Chapter 3; importantly, these curves also do not exhibit any reentrant region, and thus we expect the instabilities arising from the unstable region of the flow curve will be suppressed.

Figure 6.2 shows the steady the steady state (a) total shear stress, (b) micelle length,

(c) $S_{r\theta}$, and (d) $S_{\theta\theta}$ for these non-reentrant parameters in circular Couette flow for varying curvatures at Pe = 2; the black dashed line corresponds to the simple shear values ($\epsilon \to 0$) in which there is no spatial dependence of the rheological quantities. Figure 6.3 shows the corresponding $\theta$-averaged transient profiles of (a) total shear stress, (b) micelle shear stress, (c) $S_{r\theta}$, and (d) micelle length for start-up of steady CCF flow with Pe = 2; the different line styles correspond to sampling at different radial locations, where $R_1$ is close to the inner cylinder, $R_2$ is in the middle of the gap, and $R_3$ is close to the outer cylinder. We can see an overshot in the micelle shear stress caused by over-alignment in the $r\theta$-direction, as seen in [129]. We do not, however, observe the development of any instabilities.

Since the constitutive curve is not multivalued we do not expect reentrant instabilities (e.g., finger-like instabilities) to emerge, however, there are other viscoelastic instabilities in CCF that may appear in certain circumstances, but are not observed here. For example, the viscoelastic Taylor-Couette instability is a well-known and well-studied instability arising in non-inertial CCF of viscoelastic (e.g., Oldroyd-B) fluids [184, 185]. In this instability, the stretching of polymers along curved streamlines creates normal stresses that couple to the perturbation radial flow, which then increases the stretching of polymers and consequently the normal stresses. There has been extensive theoretical research into this instability, particularly using linear stability analysis [186, 187]. Dilute wormlike micelle solutions are much less elastic than polymer solutions since they can not stretch to store elastic energy as polymers can, however, this reduced elasticity does not necessarily preclude the formation of a viscoelastic Taylor-Couette instability. Moreover, there is a simple Newtonian Taylor-Couette instability that could be modified by the presence of dilute WLMs [188]. It would be interesting to use the RRM-R to investigate both the viscoelastic and Newtonian instabilities. It would also be interesting to use RRM-R parameters that have been used to fit true experimental data, as in Fig. 2.4, to see if instabilities arise.

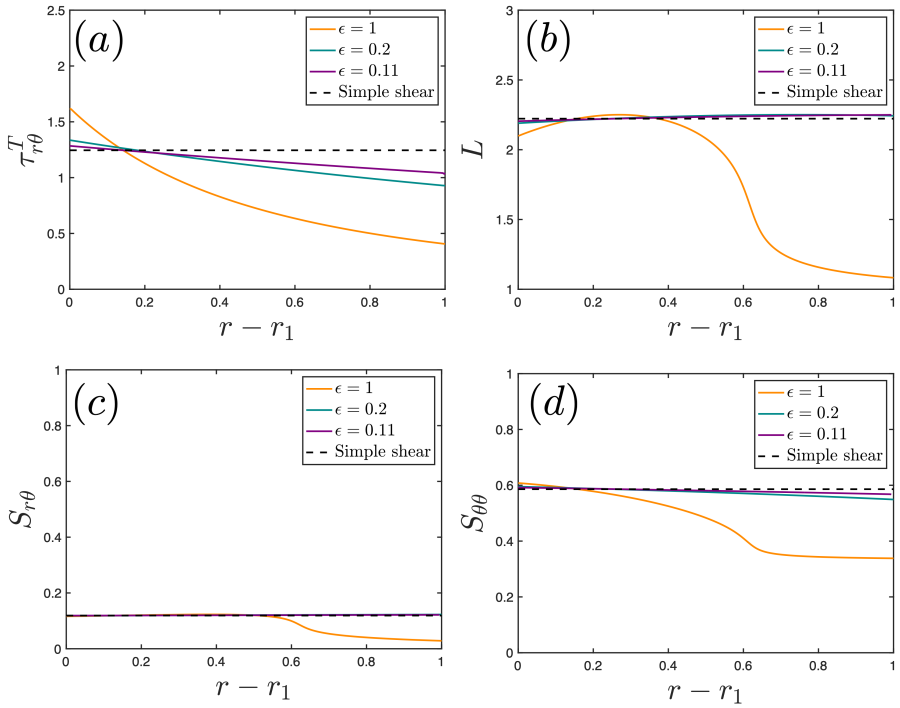


**Figure 6.2:** Steady state (a) total shear stress, (b) micelle length, (c) $S_{r\theta}$, and (d) $S_{\theta\theta}$ in circular Couette flow for varying curvatures (different line styles) at Pe = 2. The dashed black line corresponds to the simple shear (i.e., zero curvature) limit.

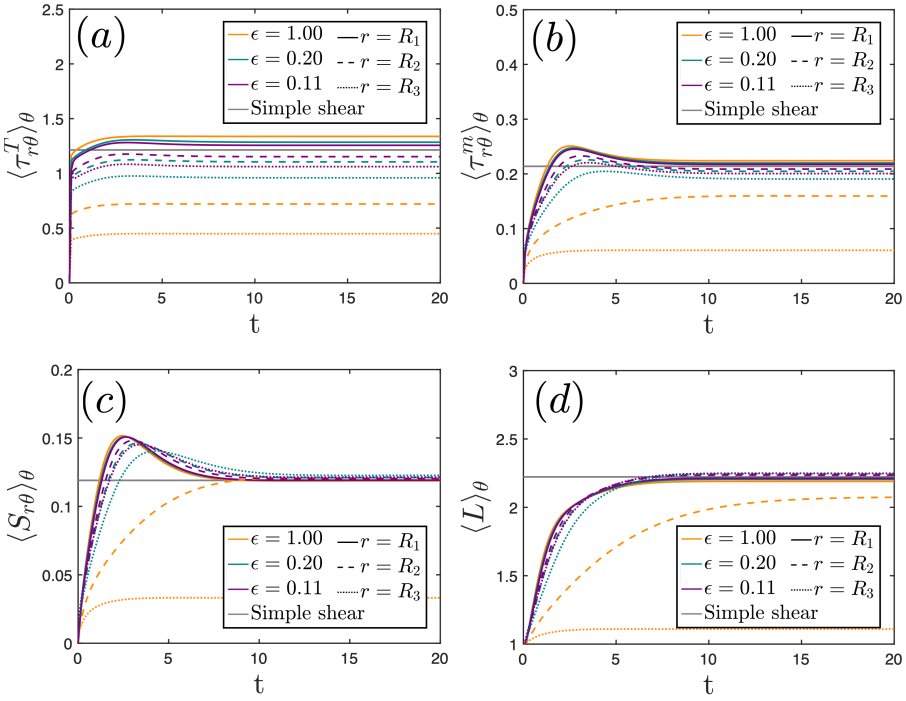


**Figure 6.3:** $\theta$-averaged (a) total shear stress, (b) micelle shear stress, (c) $S_{r\theta}$, and (d) micelle length for start-up of CCF flow with Pe = 2; line styles correspond to sampling at different radial locations: $R_1$ is close to the inner cylinder, $R_2$ is in the middle of the gap, and $R_3$ is close to the outer cylinder.

**Other reentrant flow curves**

One of the key findings of Chapter 3 was the presence of the $m = 8$ mode, where $m$ is the azimuthal wavenumber, in the development of the finger-like instability. This mode was present for both increasing and decreasing into the unstable region of the constitutive curve, and it would be interesting and useful to uncover the origin of this mode and determine if it is present for other RRM-R flow curves. To address the latter question, we have performed simulations with different reentrant flow curves, shown in Fig. 6.4; all parameters are the same as those used in Chapter 3 except for $k_{ga}$ which is now changed to vary the degree of reentrant behavior. Figure 6.5 shows snapshots of the micelle length for the new constitutive curves. We find that in all cases the $m = 8$ mode again appears as the stress is pushed into the unstable region of the flow curves, indicating that this mode, at least in the RRM-R, is driving the formation of finger-like structures. Answering the former question regarding the origin of this mode would require linear stability analysis of the RRM-R governing equations in CCF. We have attempted to perform this analysis, however, the high degree of nonlinearity in the RRM-R poses a large hurdle for these calculations. Linear stability analysis has the potential to answer many questions surrounding instabilities in dilute WLM solutions, including into the development and behavior of vorticity banding; eager readers are encouraged to take this challenge on!

### 6.2.2 Instabilities in other geometries

This thesis has focused on dynamics and instabilities in simple shear, circular Couette, and plane Poiseuille flows, but there are numerous other flow types that are both relevant to practical applications and have the potential to demonstrate unexplored behaviors. In particular, the work in prior sections has focused on shear-dominated flows while leaving extension-dominated flows untouched. Recent work by Dubash and coworkers [72] has shown a transition to unsteady flow in microfluidic cross-slot flow of a dilute wormlike micelle solution. The transition from steady to unsteady flow occurred when increasing the extension

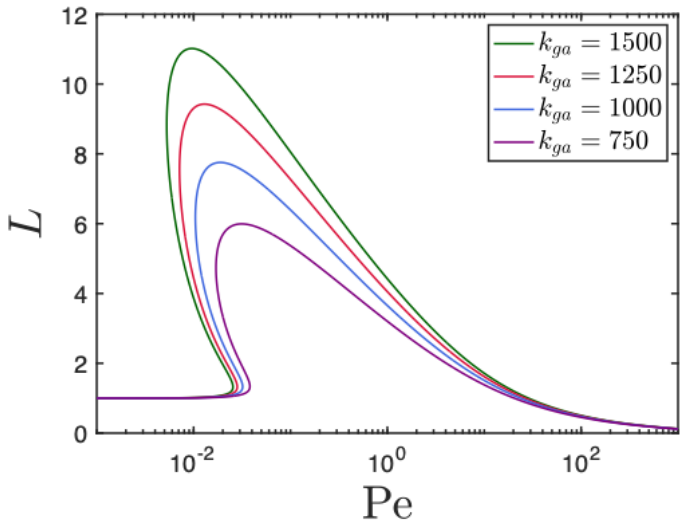


**Figure 6.4:** Micelle length vs. Pe for the RRM-R with parameters: $m = 3$, $k_{b0} = 10^{-2}$, $k_{bt} = 10$, $a = 2.5$, and varying $k_{ga}$.

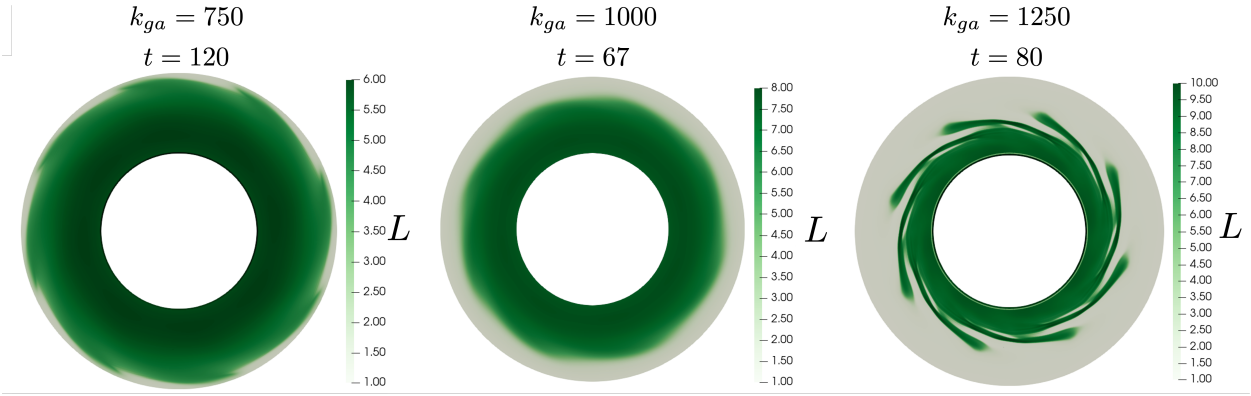


**Figure 6.5:** Snapshots of initial reentrant instability formation for the RRM-R with parameters: $m = 3$, $k_{b0} = 10^{-2}$, $k_{bt} = 10$, $a = 2.5$, and varying $k_{ga}$.

rate to regions of the flow curve that exhibited shear-thickening; notably, the transition to unsteady flow bypassed a transition to steady asymmetric flow that was observed for more concentrated (shear-thinning) WLM solutions.

### Cross-slot flow

We have performed preliminary simulations with the RRM-R in cross-slot flows to investigate the appearance of instabilities in this geometry. Figure 6.6 shows a schematic of the cross-slot flow studied in this work. Flow enters through the horizontal arms with uniform non-dimensional velocity $U = 1$ and isotropic, equilibrium length micelles. Flow exits through the vertical arms with a zero-gradient pressure boundary condition. The half-channel width is $d = 1$. The non-dimensionalization is the same as for PPF. The length of the inlet channels is long enough such that the flow reaches steady state long before reaching the domain center. Since this flow is extension-dominated it is useful to reframe the constitutive curves used for PPF and CCF to account for extensional flow. The values chosen for the RRM-R are the same as those used for PPF and CCF: $m = 3$, $k_{b0} = 10^{-2}$, $k_{ga} = 1500$, $k_{bt} = 10$, and $a = 2.5$, with $\mathrm{Re} = 10^{-1}$ and $\beta = 0.082$. We again approximate an inertialess flow condition by neglecting the convective terms in the momentum equation and setting $\mathrm{Re} = 0.1$. In uniaxial extensional flow, $\boldsymbol{v} = [-\mathrm{Pe}x/2, -\mathrm{Pe}y/2, \mathrm{Pe}z]^\top$, these parameters yield the constitutive curves shown in Fig. 6.7. Note that because of symmetry $S_{xx} = S_{yy}$. These curves are quite similar to the simple shear curves, Fig. 4.3, but now the Pe at which the reentrant begins is decreased; this means that reentrant instabilities are likely to set in at lower Pe than what was observed for shear-dominated flows.

Figure 6.8 shows snapshots of micelle length at $t = 80$ for cross-slot flow with $\mathrm{Pe} = 0.005$. The top figure shows the inlet channels and the bottom figure shows the outlet channels. The first thing to observe is that micelles are extended beyond what is dictated by either of the pure shear or pure extension constitutive curves; this heightened extension may be due to the mixed flow present in the central region. At first glance the flow in the inlet

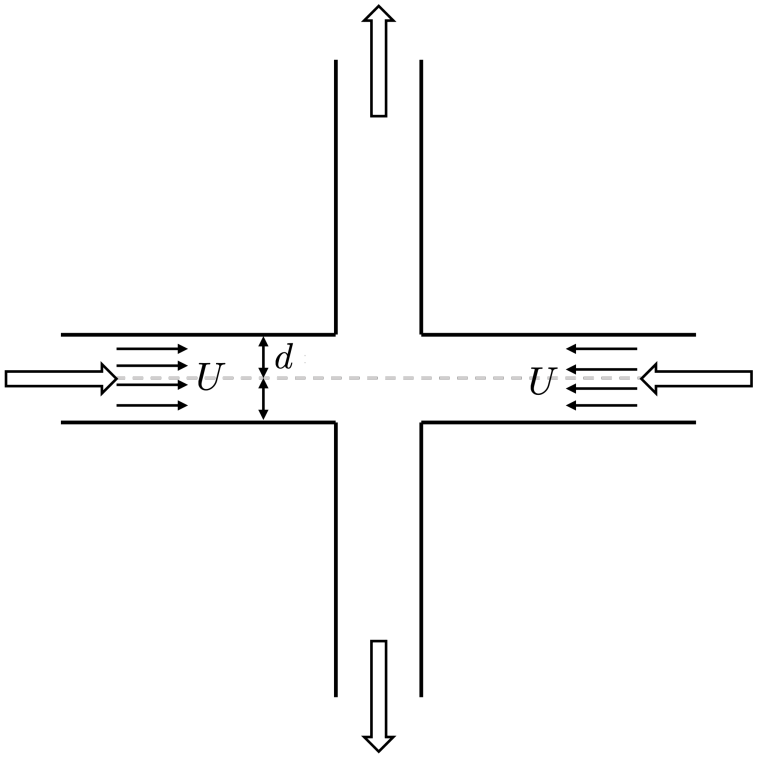


**Figure 6.6:** Schematic of cross-slot flow. Flow enters through the horizontal arms with uniform velocity $U$ and isotropic, equilibrium length micelles. Flow exits through the vertical arms with a zero-gradient pressure boundary condition. The half-channel width is $d = 1$.

channels does not appear interesting; however, upon closer inspection, there are faint streaks of elongated micelles towards the centerline of the inlets that break off from the near-wall regions of elongated micelles. The streaks are also symmetric across the centerline. As these streaks reach the center of the geometry they blend with the near-wall regions. The truly interesting behavior occurs along the outlet channels. There is an extremely thin band of elongated micelles along the centerline of the outlets that fades with distance from the domain center. This thin band consists of highly elongated and anisotropic micelles, and would thus produce a birefringent band; similar birefringent bands have been observed in experiments [72].

Also in the outlets we see that the separation between the near-wall and central regions fluctuates with time; these fluctuations consist of wave-like structures, just as was observed in PPF flow. These structures are much more wave-like compared to the more finger-like structures observed in PPF; it does not seem like the structural differences are due to time (or

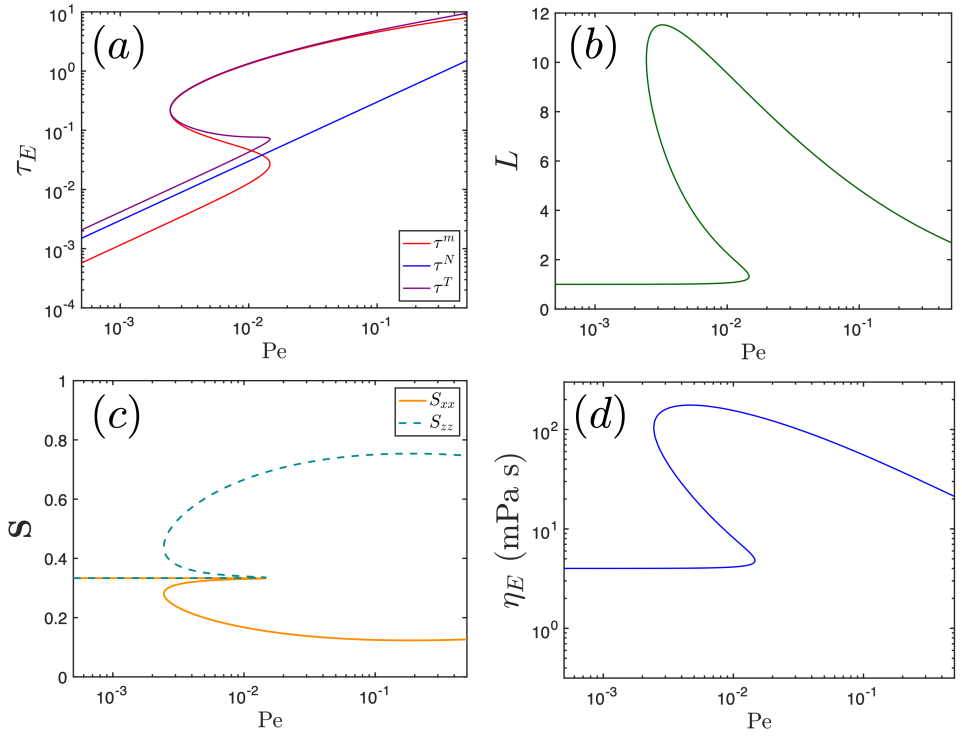


**Figure 6.7:** Constitutive curves for the RRM-R in uniaxial extensional flow with parameters: $m = 3$, $k_{b0} = 10^{-2}$, $k_{ga} = 1500$, $k_{bt} = 10$, and $a = 2.5$. (a) Micelle (red), Newtonian (blue), and total shear stress (purple), (b) length of micelles, (c) components of the orientation tensor, and (d) normalized viscosity vs. applied Péclet number.

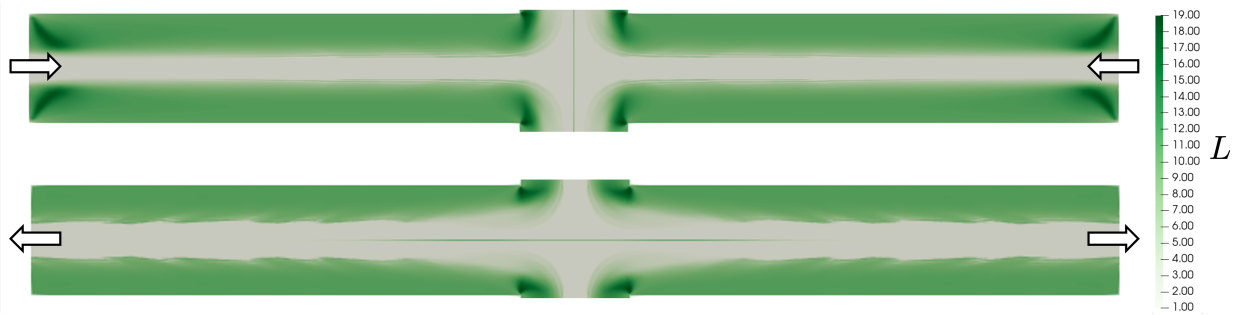


**Figure 6.8:** Snapshots of micelle length at $t = 80$ for cross-slot flow with Pe = 0.005. The top figure shows the inlet channels and the bottom figure shows the outlet channels.

equivalently, channel length) because towards the outlets the structures begin to fade; this fading suggests that the instability may arise due to extensional stretching and subsequent relaxing as the micelles pass through the center of the domain. Future work could identify the origin of this instability by projecting the micelle length and stress onto the governing constitutive curves to see if the flow is entering unstable regions of the flow curves. It would also be helpful to understand the long-time dynamics in the outlets, which could be achieved by increasing the outlet channel lengths. A longer channel would show if the structures truly are fading towards the outlet.

Figure 6.9 shows snapshots of micelle length at $t = 10$ for cross-slot flow with Pe = 0.015. Again we see drastically elongated micelles. At this larger Pe no unsteady or fluctuating structures are observed in either the inlets or outlets; it is surprising to not observe reentrant instabilities in any of the channels since, as discussed for PPF, the shear rate profile forces the flow to jump between stable branches which results in an unstable interface between elongated and equilibrium-length micelles. Based on the time taken for instabilities to develop in PPF, it is possible that the development of an instability in this flow would require a longer channel length (this would give more time for the interface to destabilize). Again there is an extremely strong birefringent band along the outlets that agrees well with experimental observations [72] of dilute WLM solutions in cross-slot flow.

These results show that cross-slot flows of dilute WLM solutions can show a variety of unexplored behaviors. It would be interesting to understand why an instability is not

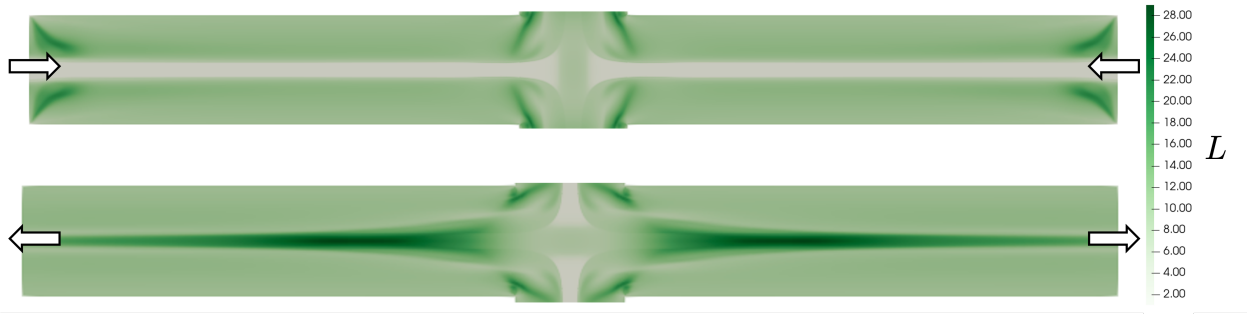


**Figure 6.9:** Snapshots of micelle length at $t = 10$ for cross-slot flow with Pe $= 0.015$. The top figure shows the inlet channels and the bottom figure shows the outlet channels.

seen for higher Pe, and why micelles are elongated far beyond the values prescribed by the governing flow curves. Future work should also look at the effects of inertia; it is known that viscoelastic instabilities often involve interplay between inertial and elastic forces. From a computational perspective, adding inertia and increasing the Reynolds number would also likely stabilize these flows and allow for larger time steps. Currently these cross-slot simulations are numerically unstable, particularly at the inlet where the $U = 1$ velocity profile does not satisfy the boundary conditions and leads to a sharp pressure jump.

### Porous media flow

One of the primary applications of wormlike micelle solutions is in oil-recovery, specifically as fracturing fluids [14]. Oil recovery operations have historically used polymer additive solutions as carrier fluids (CFs) for propping agents (proppants). Proppants (e.g. sand, ceramics) prevent closure of human-made fractures in oil wells, which is essential for maximizing oil recovery and minimizing impacts on local environments [189, 190]. Effective carrier fluids exhibit both high viscosity regimes for transporting suspended proppants and low viscosity regimes for promoting proppant settling and CF removal. Carrier fluids are typically long-chain, crosslinked polysaccharides in brine that form viscoelastic gels; these gels are suitably viscous for proppant transport, but as fractures constrict, water in the gel is squeezed out leaving behind the proppant and a mass of polymer cake. This impermeable cake restricts oil flow, forcing usage of enzymatic or oxidative breakers to degrade the residual

polymer. Unfortunately, enzymatic breakers are nearly inactive at the high temperatures of most non-shallow oil wells, and oxidative breakers can catalyze environmentally hazardous halogenation pathways. This low efficiency and environmental toxicity of polymer-based carrier fluids has led to interest in alternative viscoelastic solutions.

Wormlike micelle solutions present an attractive alternative to traditional carrier fluids due to their tunable viscoelasticity and wide range of chemical compositions, which can be exploited to meet the needs of environmentally sensitive and marine regions. In addition to flow, the viscoelasticity of WLM solutions can be manipulated by surfactant and counterion chemistry, concentration, and temperature. Further, the onset of oil flow through fractures causes a polar to non-polar transition of the WLM solution solvent that disassembles micelles and decreases viscosity. Given the advantages of using WLM solutions as CFs, it is valuable to model and test the behavior of these solutions under fracturing conditions from a perspective that considers the chemical, temperature, and flow effects that make them ideal candidates.

A first step in testing WLM solutions in oil-recovery environments is to simulate the RRM-R in flows that reflect porous environments. Recent work by Kumar and coworkers [191, 192, 193] have looked at flows of dilute polymer solutions modeled as FENE-P fluids in channel flows with confinements. The confinements occur between two cylinders, meant to represent the porous flow that is common in oil-field settings. They found that the formation of instabilities in these confined flow depends on the blockage ratio and spacing of successive confinements. Additionally, they observed complex flow patterns in the form of eddies that arose for closely spaced confinements. These results suggest that simulations of the RRM-R in cylindrically-confined flows, as well as other porous geometries, can be used for studying WLM solutions in oil-field environments.

### CaBER and DoS

The rheological field has recently begun to show increased interest in transient extensional rheology because of the practical important of understanding pinching and droplet dynam-

ics for printing, pharmaceutical, and emulsion applications [194, 195, 196]. The two main experimental techniques for measuring transient extensional rheology are Capillary Breakup Extensional Rheometry (CaBER) and Dripping-onto-Substrate (DOS). Both of these techniques involve creating a thin fluid filament that is allowed to thin with time; the behavior and duration of the thinning process can then be related to relaxation times associated with the fluid. These techniques are especially useful for viscoelastic fluids that can show multiple relaxation times. Anna and McKinley [197] have developed analytical results for extracting relaxation times from CaBER for viscoelastic fluids; their analysis can easily be extended to the RRM-R. Moreover, there is also the potential to use arbitrary Lagrangian-Eulerian techniques for modeling free surface flows in order to simulate filaments and dripping processes [198].

**Plane Couette flow**

Plane Couette flow (PCF) is characterized by a fluid confined by two parallel plates, where the lower plate is stationary and the upper plates translates with constant velocity $V$. This set-up gives rise to a linear velocity profile and a constant shear rate throughout the channel. In 2D, this geometry reduces to simple shear flow, but in 3D fluctuations are possible along the vorticity axis ($z$). A schematic of PCF is shown in Fig. 6.10; the streamwise direction is $x$, the wall-normal or gradient direction is $y$, and the vorticity direction is $z$. Plane Couette flow is a promising domain for studying dilute WLM solutions because of the potential for vorticity banding to arise. Just as in circular Couette flow, vorticity banding can develop at shear rates in which the flow curve is multivalued and a single shear rate can support multiple stable steady stresses. It is likely that vorticity banding is more stable in PCF than CCF because of the spatial dependence of the shear rate in CCF; this spatial dependence, especially for wide-gap flows, can destabilize the flow if the stress variation across the gap is too large (and will thus fall into unstable regions of the flow curve).

As was the case for CCF in Chapter 3, vorticity banding will not naturally arise for shear

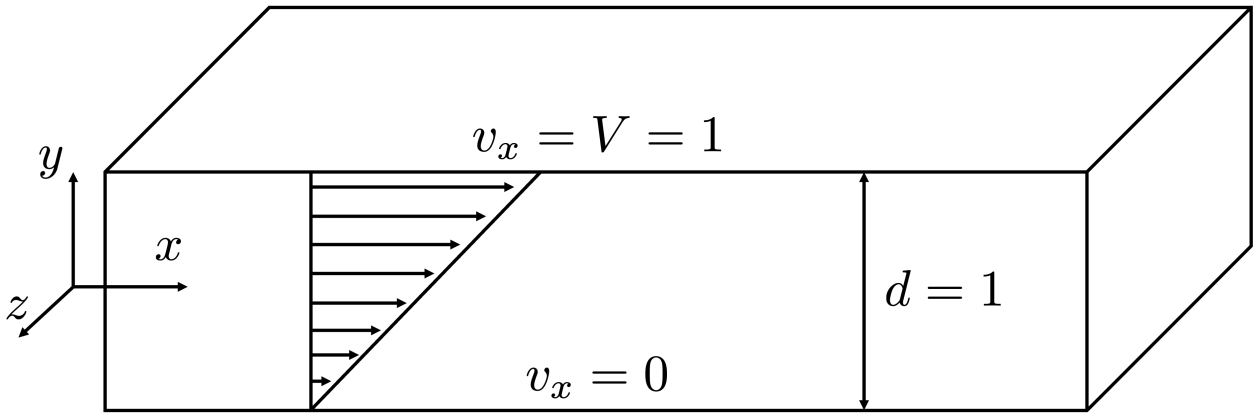


**Figure 6.10:** Schematic of plane Couette flow.

rate-controlled boundary conditions; however, vorticity banding can develop if the initial condition is vorticity banded, or with suitable perturbations applied to the flow. Figure 6.11 shows an example of perturbations that can be applied to the initial condition to induce vorticity banding. The figure shows (a) micelle length and (b) orientation parameter over time and averaged over $xy$ at two different vorticity locations. The flow was seeded with an initial condition directly on the unstable region of the flow curve (i.e., middle branch); at $z = z^+$ the micelle length was perturbed up slightly, and at $z = z^-$ it was perturbed down slightly. The flow evolves to a vorticity banded state, showing that small perturbations can be applied to promote vorticity banding. We have also taken vorticity banded conditions and evolved these with time, shown in Fig. 6.12. We found that the vorticity banded state was a steady state and linearly stable to perturbations.

In future work it would be useful to understand the effect of random perturbations to the initial condition. We have attempted to apply random perturbations, however, since the RRM-R does not include translational diffusion it is impossible for the flow to smooth out the sharp gradients that arise in the wall-normal direction, creating a numerical instability. We have also added translational diffusion to the RRM-R, but we have not yet used this model to look at the effect on the random perturbations. Moreover, the translational diffusion that must be applied in order to see macroscopic effects over reasonable time scales is much larger than the true translational diffusion found in experiments. Future work should look at

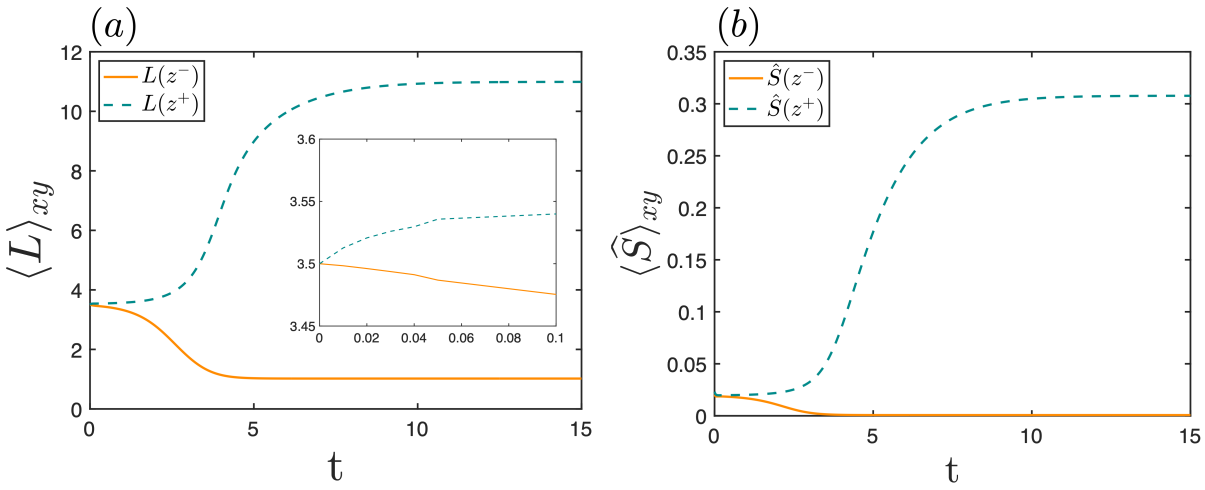


**Figure 6.11:** (a) Micelle length and (b) orientation parameter over time and averaged over $xy$ at two different vorticity locations. The flow was seeded with an initial condition directly on the unstable region of the flow curve (i.e., middle branch); at $z = z^+$ the micelle length was perturbed up slightly, and at $z = z^-$ it was perturbed down slightly.


**Figure 6.12:** Snapshot of micelle length for vorticity banded flow at long times. The initial condition was vorticity banded.

adding experimentally-relevant diffusivities to the RRM-R and test the effects on vorticity banding and other instabilities and behaviors.

### 6.2.3 Linear stability analysis

In addition to numerical simulations, linear stability analysis can be used to analyze the RRM-R in a variety of simple flow types. Linear stability analysis (LSA) has been used for decades in fluid dynamics literature as a way of investigating the stability of flows to small perturbations [188, 199]. LSA has been used successfully for both Newtonian and non-Newtonian fluids [186, 187] and offers the potential to uncover the mechanisms and driving forces behind instabilities observed in the RRM-R. In particular, LSA of the RRM-R in circular Couette flow could identify the origin of the $m = 8$ mode found in the development of finger-like instabilities; additionally, LSA could help to understand the development of the interfacial instabilities observed in plane Poiseuille flow and show whether it is viscosity mismatch, normal stress jumps, or some other mechanism driving the instability. In all the future work suggested here, it is our opinion that linear stability analysis is the most promising and offers the most rewards (in the form of both knowledge and publications)!

We have previously attempted to perform linear stability analysis of the RRM-R in CCF, PCF, and simple shear flows, however, the high degree of nonlinearity in the RRM-R greatly complicates the calculations. In LSA, we consider small perturbations to a steady state; for the RRM-R it is reasonable to look at perturbations to the length, orientation, pressure, and velocity of the steady state; these perturbations are written as

$$\mathbf{B}(\mathbf{x}, t) = \mathbf{B}_{ss}(\mathbf{x}) + \mathbf{B}'(\mathbf{x}, t), \tag{6.1}$$

where $\mathbf{B}(\mathbf{x}, t)$ is an arbitrary state variable (e.g., $L$ or $\mathbf{S}$) that can depend on space and time, $\mathbf{B}_{ss}(\mathbf{x})$ is the steady state value of $\mathbf{B}$, and $\mathbf{B}'(\mathbf{x}, t)$ is a small perturbation to $\mathbf{B}$ that can depend on space and time. This form is substituted into the governing equations of

the RRM-R, coupled with conservation of mass and momentum, and then the equations are linearized; linearization involves ignoring terms that are quadratic in perturbation in order to investigate first order effects. Once the equations are linearized, it is typical to seek normal mode solutions for the perturbed variables of the form:

$$\mathbf{B}'(\mathbf{x},t) = \widehat{\mathbf{B}}(\mathbf{x}) \exp\left(ik_j\mathbf{x} - i\omega t\right), \tag{6.2}$$

where $\widehat{\mathbf{B}}$ is an amplitude, $k_j$ are the spatial wavenumbers, and $\omega$ is the complex growth rate. If there are any modes where the imaginary part of $\omega$, $\omega_I$, is positive than the flow is unstable to linear perturbations. This technique allows for identification of the most unstable modes, which would be extremely useful for understanding reentrant and interfacial instabilities as well as vorticity banding in the RRM-R.

### 6.2.4 Effects of inertia on finger-like instabilities

In Chapter 3 we investigated finger-like instabilities in circular Couette flow; in this work, we approximated an inertialess flow condition by neglecting velocity convection. Since many industrially relevant processes are not inertialess, it would be useful for future work to focus on the effects of inertia on finger-like instabilities. In Chapter 4 we showed that reintroducing velocity convection and increasing the Reynolds number tended to delay the formation of the instability by delaying the time for a sharp interface to form. The finger-like instabilities observed in CCF do not rely on the formation and destabilization of a sharp interface, so it is not clear what the exact effects of inertia will be.

We have preliminarily attempted to answer this question by simulations in CCF with velocity convection. Figure 6.13 shows snapshots of micelle length for CCF with $\mathrm{Pe} = 0.0225$ and velocity convection. The first column contains snapshots at $t = 40$, the second at $t = 65$, and the times of snapshots in the third column are specified on the figure. From top to bottom the rows are: $\mathrm{Re} = 10^{-6}$, $\mathrm{Re} = 10^{-4}$, $\mathrm{Re} = 10^{-2}$, $\mathrm{Re} = 10^{1}$. We can see from $t = 40$

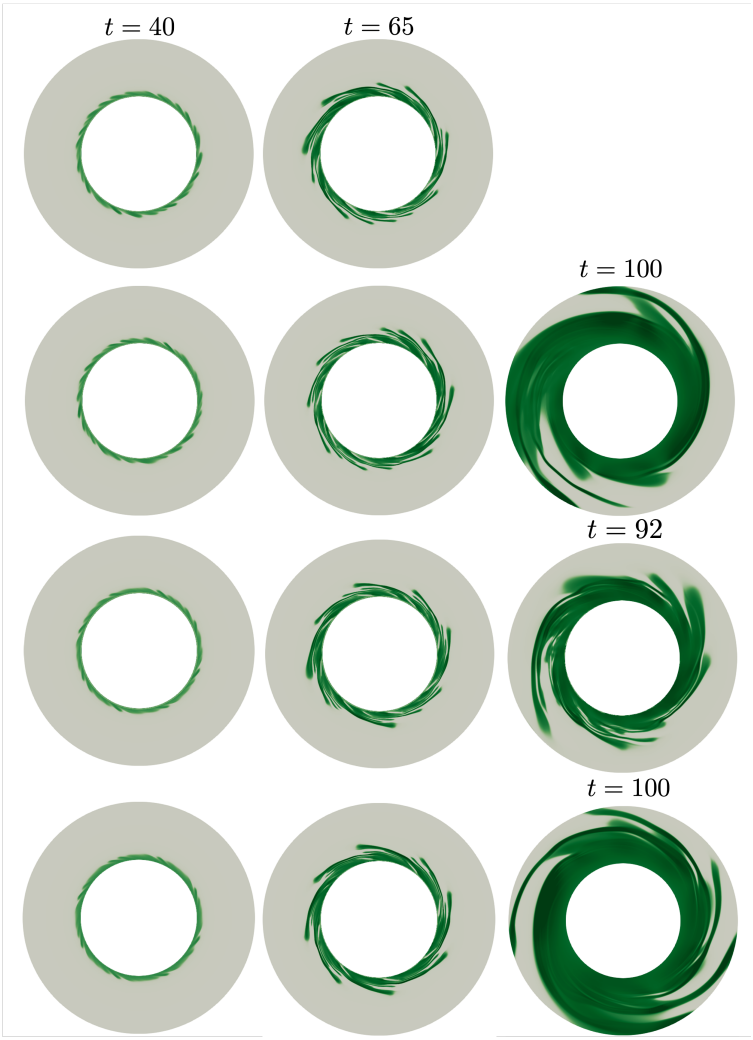


**Figure 6.13:** Snapshots of micelle length for CCF with Pe = 0.0225 and velocity convection. The first column contains snapshots at $t = 40$, the second at $t = 65$, and the times of snapshots in the third column are specified on the figure. From top to bottom the rows are: $\mathrm{Re} = 10^{-6}$, $\mathrm{Re} = 10^{-4}$, $\mathrm{Re} = 10^{-2}$, $\mathrm{Re} = 10^{1}$.

that the initial instability observed in the convection-free simulations is maintained; again the $m = 8$ mode appears to be present. The late time behavior is drastically different than the convection-free case, however; symmetry is seen to break earlier and regions of elongated micelles consist of thinner threads that reach outwards toward the outer wall. Future work should look more rigorously at the role of inertia in the growth of the finger-like instabilities.

### 6.2.5 Improvements to the RRM-R

This thesis has demonstrated that the RRM-R is well-suited for describing an array of rheological features associated with dilute WLM solutions, can be fit to a variety of experimental data, and can be used to understand complex instabilities in these flows. Despite these successes, there are certain improvements that can be made to the RRM-R. One improvement is the transition from treating the system with a single length to instead treating the system as a population of lengths; one direction could follow the approach of the VCM model [76] and introduce a second length. A reaction scheme could then be set up between the short length and long length, where the reaction rate depends on the alignment, length, and stress of the rods. Another approach is to model a distribution of lengths; Larson [15] has shown that the distribution of wormlike micelle lengths is exponential at equilibrium. There has also been recent work modeling distributions with their moments, which could be implemented in the RRM-R to retain tractability [183]. Population balance modeling can even be done in a thermodynamically consistent framework [88].

Additionally, while dilute WLMs are nearly linear and nearly rigid, they do still exhibit some degree of flexibility that can effect their stress and orientation. Introducing bending into the RRM-R could be done as a way of giving micelles an additional relaxation mechanism. Following Doi [75], let $\mathbf{R}(s)$ be a position along the micelle backbone at the contour length $s$. A unit vector tangent to the micelle is given by

$$\mathbf{u}(s) = \frac{\partial \mathbf{R}}{\partial s}. \tag{6.3}$$

For a linear rod $\mathbf{u}(s)$ is a constant. Consequently, $\partial \mathbf{u}/\partial s = 0$ and the bending energy must be a quadratic of $\partial \mathbf{u}/\partial s$. This motivates a form

$$U_{\text{bend}} = \frac{1}{2} E \int_0^L \left( \frac{\partial \mathbf{u}}{\partial s} \right)^2 \mathrm{d}s, \tag{6.4}$$

where $E$ is an energetic constant. Introducing this bending energy into the RRM-R could increase computational cost, but may result in more physical behavior.

### 6.2.6 Drag reduction and elastoinertial turbulence

One of the overarching goals of developing and studying the RRM-R has been to understand drag reduction in surfactant-additive solutions. It has been known for several decades that the addition of a small amount of polymer molecules can significantly reduce turbulent drag by up to 80% [1, 16]. Interestingly, while drag reduction is found to increase with increasing polymer concentration, the drag reduction eventually asymptotes and no further drag reduction is observed for increasing concentration; this maximum extent of drag reduction, called the maximum drag reduction asymptote (MDRA), appears to be independent of polymer chemistry [32]. The drag reducing capabilities of polymer additives have made them essential tools in many applications involving the transport of fluid, from oil pipelines to heating and cooling districts [33]. Unfortunately, polymer additives do suffer from mechanical degradation in regions of high shear or extension, such as those seen in the pumps needed to drive fluid, requiring the need for constant replacement in order to maintain the desired levels of drag reduction.

More recent research has shown that dilute surfactant solutions forming wormlike micelles also provide significant levels of drag reduction, comparable to the levels seen in polymer solutions [2]. As in the polymer case, the extent of drag reduction in surfactant solutions is also seen to asymptote. Figure 6.14 shows a plot of friction factor vs. Reynolds number measured in various experiments of polymer and surfactant solutions. It is desirable to have the lowest friction factor, $f = \Delta p d/\rho L U^2$, possible. The dashed black line shows the friction factor for Newtonian turbulence, which is obviously quite large compared to the other data shown. The solid black line corresponds to laminar flow, which gives the lowest drag possible. The blue markers show experimental data of various surfactant-additive systems, and the other colored markers show the experimental data for various polymer-

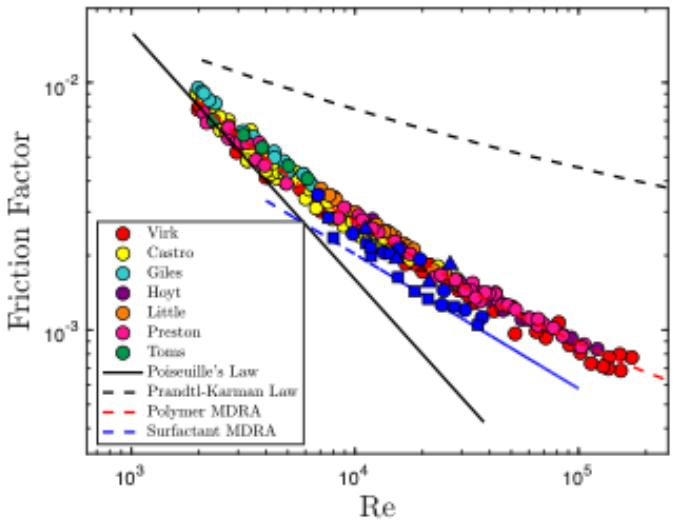


**Figure 6.14:** (Reproduced from Section 1.1.1) Friction factor vs. Reynolds number for a variety of polymer and surfactant systems [1, 2].

additive systems. The red and blue lines are empirical fits for the polymer and surfactant MDRA, respectively. The drag-reducing capabilities of micelle solutions clearly rivals that of polymers; additionally, micelles are self-assembled structures, meaning that they are not susceptible to the mechanical degradation that polymers are. This self-assembly, combined with their incredible drag reduction, makes WLM solutions ideal candidates for reducing drag in the transport of fluids.

There has been a great deal of research into the mechanisms of drag reduction in polymer solutions [34, 32, 33, 35, 36, 37]. Research has demonstrated that polymer solutions show a transition from inertial turbulence, which we will refer to as Newtonian turbulence, to elastoinertial turbulence (EIT). While Newtonian turbulence is dominated by quasi-streamwise vortices, EIT tends to be dominated by spanwise-oriented vortices [36]. There has been little, if any, research into the mechanisms of drag reduction in surfactant-additive solutions, nor has there been research into the structure of turbulence in these solutions. Does turbulence in WLM solutions resemble Newtonian or elastoinertial turbulence, or does it resemble something else entirely? The RRM-R shows great potential in answering this question and other surrounding drag reduction and turbulence in WLM solutions. Future work should focus on implementing the RRM-R in direct numerical simulations of channel flow; while the RRM-R

is already implemented in the open source software OpenFOAM, full analysis of turbulence would benefit from in-house DNS. It may also be worth exploring the Python-based software Dedalus [200], as this has shown success in studying viscoelastic flows and EIT.

# Bibliography


[1] P. S. Virk, Drag reduction fundamentals, AIChE Journal 21 (4) (1975) 625–656.

[2] J. L. Zakin, J. Myska, Z. Chara, New limiting drag reduction and velocity profile asymptotes for nonpolymeric additives systems, AIChE Journal 42 (12) (1996) 3544–3546.

[3] S. Dutta, M. D. Graham, Mechanistic constitutive model for wormlike micelle solutions with flow-induced structure formation, Journal of Non-Newtonian Fluid Mechanics 251 (2018) 97–106. doi:10.1016/j.jnnfm.2017.12.001.

[4] C. heng Liu, D. J. Pine, Shear-induced gelation and fracture in micellar solutions, Physical Review Letters 77 (1996) 2121–2124. doi:10.1103/PhysRevLett.77.2121.

[5] D. Ohlendorf, W. Interthal, H. Hoffmann, Surfactant systems for drag reduction: Physico-chemical properties and rheological behaviour, Rheologica Acta 25 (1986) 468–486, persistence length and thickening. doi:10.1007/BF01774397.

[6] S. Tamano, Y. Ohashi, Y. Morinishi, Dynamics of falling droplet and elongational properties of dilute nonionic surfactant solutions with drag-reducing ability, Physics of Fluids 29 (5) (2017) 053104.

[7] G. Landázuri, E. R. Macías, J. P. García-Sandoval, E. Hernández, O. Manero, J. E. Puig, F. Bautista, On the modelling of the shear thickening behavior in micellar solutions, Rheologica Acta 55 (7) (2016) 547–558.

[8] L. M. Walker, P. Moldenaers, J.-F. Berret, Macroscopic response of wormlike micelles to elongational flow, Langmuir 12 (26) (1996) 6309–6314.

[9] C. Perge, M.-A. Fardin, S. Manneville, Surfactant micelles: Model systems for flow instabilities of complex fluids, The European Physical Journal E 37 (4) (2014) 23.

[10] S. Wu, H. Mohammadigoushki, Sphere sedimentation in wormlike micelles: Effect of micellar relaxation spectrum and gradients in micellar extensions, Journal of Rheology 62 (5) (2018) 1061–1069.

[11] H. Mohammadigoushki, S. J. Muller, Inertio-elastic instability in taylor-couette flow of a model wormlike micellar system, Journal of Rheology 61 (4) (2017) 683–696.

[12] M. A. Fardin, S. Lerouge, Instabilities in wormlike micelle systems, The European Physical Journal E 35 (2012) 91, shear banding. doi:10.1140/epje/i2012-12091-0.

[13] A. Bhardwaj, E. Miller, J. P. Rothstein, Filament stretching and capillary breakup extensional rheometry measurements of viscoelastic wormlike micelle solutions, Journal of Rheology 51 (4) (2007) 693–719.

[14] J. Yang, Viscoelastic wormlike micelles and their applications, Current Opinion in Colloid & Interface Science 7 (2002) 276–281. doi:10.1016/S1359-0294(02)00071-7.

[15] R. G. Larson, The structure and rheology of complex fluids, Oxford University Press, 1999.

[16] T. B. A., Some observations on the flow of linear polymer solutions through straight tubes at large reynolds numbers, Proc. 1st Intl Congr. Rheol. 2 (1949) 135–141.

[17] T. Saeki, Flow properties and heat transfer of drag-reducing surfactant solutions, Developments in Heat Transfer 1 (2011) 8–9.

[18] A. Krope, L. C. Lipus, Drag reducing surfactants for district heating, Applied Thermal Engineering 30 (8-9) (2010) 833–838.

[19] S. Spagnolie, Complex Fluids in Biological Systems, Springer New York, 2015. doi:10.1007/978-1-4939-2065-5.

[20] B. Wei, L. Romero-Zerón, D. Rodrigue, Oil displacement mechanisms of viscoelastic polymers in enhanced oil recovery (eor): a review, Journal of Petroleum Exploration and Production Technology 4 (2014) 113–121. doi:10.1007/s13202-013-0087-5.

[21] A. Sadeghi, L. Beccai, B. Mazzolai, Innovative soft robots based on electro-rheological fluids, IEEE, 2012, pp. 4237–4242. doi:10.1109/IROS.2012.6385846.

[22] I. Brevik, Temperature variation in the dark cosmic fluid in the late universe, Modern Physics Letters A 31 (2016) 1650050. doi:10.1142/S0217732316500504.

[23] P. Partal, J. M. Franco, Non-newtonian fluids, Rheology: encyclopaedia of life support systems (EOLSS), UNESCO. Eolss, Oxford (2010) 96–119.

[24] R. B. Bird, R. C. Armstrong, O. Hassager, Dynamics of polymeric liquids, John Wiley & Sons, 1987.

[25] A. Morozov, S. E. Spagnolie, Introduction to Complex Fluids, 2015, pp. 3–52. doi:10.1007/978-1-4939-2065-5_1.

[26] M. D. Graham, Microhydrodynamics, Brownian Motion, and Complex Fluids, Cambridge University Press, 2018. doi:10.1017/9781139175876.

[27] P. Coussot, Yield stress fluid flows: A review of experimental data, Journal of Non-Newtonian Fluid Mechanics 211 (2014) 31–49. doi:10.1016/j.jnnfm.2014.05.006.

[28] R. I. Tanner, A theory of die-swell, Journal of Polymer Science Part A-2: Polymer Physics 8 (1970) 2067–2078. doi:10.1002/pol.1970.160081203.

[29] S. H. Spiegelberg, G. H. McKinley, Stress relaxation and elastic decohesion of viscoelastic polymer solutions in extensional flow, Journal of Non-Newtonian Fluid Mechanics 67 (1996) 49–76. doi:10.1016/S0377-0257(96)01475-9.

[30] S. M. Recktenwald, S. J. Haward, A. Q. Shen, N. Willenbacher, Heterogeneous flow inside threads of low viscosity fluids leads to anomalous long filament lifetimes, Scientific Reports 9 (2019) 7110. doi:10.1038/s41598-019-43590-z.

[31] R. Lochhead, et al., The use of polymers in cosmetic products, Cosmetic science and technology 13 (2017) 171–221.

[32] Y. Dubief, V. E. Terrapon, B. Hof, Elasto-inertial turbulence, Annual Review of Fluid Mechanics 55 (2023) 675–705. doi:10.1146/annurev-fluid-032822-025933.

[33] C. M. White, M. G. Mungal, Mechanics and prediction of turbulent drag reduction with polymer additives, Annual Review of Fluid Mechanics 40 (2008) 235–256. doi:10.1146/annurev.fluid.40.111406.102156.

[34] A. Shekar, R. M. McMullen, B. J. McKeon, M. D. Graham, Self-sustained elastoinertial tollmien–schlichting waves, Journal of Fluid Mechanics 897 (2020) A3. doi:10.1017/jfm.2020.372.

[35] M. D. Graham, Drag reduction in turbulent flow of polymer solutions, Rheology Reviews (2004) 143–17–.

[36] Y. Dubief, V. E. Terrapon, J. Soria, On the mechanism of elasto-inertial turbulence, Physics of Fluids 25 (11 2013). doi:10.1063/1.4820142.

[37] D. Samanta, Y. Dubief, M. Holzner, C. Schäfer, A. N. Morozov, C. Wagner, B. Hof, Elasto-inertial turbulence, Proceedings of the National Academy of Sciences 110 (2013) 10557–10562. doi:10.1073/pnas.1219666110.

[38] J. D. Peterson, W. Zou, R. G. Larson, M. E. Cates, Wormlike micelles revisited: A comparison of models for linear rheology, Journal of Non-Newtonian Fluid Mechanics 322 (2023) 105149.

[39] Y.-Y. Luk, N. L. Abbott, Applications of functional surfactants, Current opinion in colloid & interface science 7 (5-6) (2002) 267–275.

[40] J. N. Israelachvili, Intermolecular and Surface Forces, Elsevier, 2011. doi:10.1016/C2009-0-21560-1.

[41] C. Barentin, A. J. Liu, Shear thickening in dilute solutions of wormlike micelles, Europhysics Letters (EPL) 55 (2001) 432–438. doi:10.1209/epl/i2001-00432-x.

[42] J. Dehmoune, J.-P. Decruppe, O. Greffier, H. Xu, Rheometric and rheo-optical investigation on the effect of the aliphatic chain length of the surfactant on the shear thickening of dilute worm-like micellar solutions, Rheologica Acta 46 (2007) 1121–1129. doi:10.1007/s00397-007-0206-7.

[43] J. P. Rothstein, Transient extensional rheology of wormlike micelle solutions, Journal of Rheology 47 (2003) 1227–1247, extensional hardening. doi:10.1122/1.1603242.

[44] J.-Y. Lee, J. J. Magda, H. Hu, R. G. Larson, Cone angle effects, radial pressure profile, and second normal stress difference for shear-thickening wormlike micelles, Journal of Rheology 46 (2002) 195–208, normal stress difference. doi:10.1122/1.1428319.

[45] S. Lerouge, J.-F. Berret, Shear-Induced Transitions and Instabilities in Surfactant Wormlike Micelles, 2009, pp. 1–71. doi:10.1007/12_2009_13.

[46] S. L. Keller, P. Boltenhagen, D. J. Pine, J. A. Zasadzinski, Direct observation of shear-induced structures in wormlike micellar solutions by freeze-fracture electron microscopy, Physical Review Letters 80 (1998) 2725–2728, flow induced structure. doi:10.1103/PhysRevLett.80.2725.

[47] J. K. G. Dhont, W. J. Briels, Gradient and vorticity banding, Rheologica Acta 47 (2008) 257–281, shear and vorticity banding. doi:10.1007/s00397-007-0245-0.

[48] J.-B. Salmon, A. Colin, S. Manneville, F. Molino, Velocity profiles in shear-banding wormlike micelles, Physical Review Letters 90 (2003) 228303, shear banding. doi:10.1103/PhysRevLett.90.228303.

[49] L. M. Walker, Rheology and structure of worm-like micelles, Current Opinion in Colloid and Interface Science 6 (2001) 451–456. doi:10.1016/S1359-0294(01)00116-9.

[50] V. Herle, J. Kohlbrecher, B. Pfister, P. Fischer, E. J. Windhab, Alternating vorticity bands in a solution of wormlike micelles, Physical Review Letters 99 (2007) 158302, vorticity banding. doi:10.1103/PhysRevLett.99.158302.

[51] J. Goveas, P. Olmsted, A minimal model for vorticity and gradient banding in complex fluids, The European Physical Journal E 6 (2001) 79–89. doi:10.1007/s101890170030.

[52] G. M. H. Wilkins, P. D. Olmsted, Vorticity banding during the lamellar-to-onion transition in a lyotropic surfactant solution in shear flow, The European Physical Journal E 21 (2006) 133. doi:10.1140/epje/i2006-10053-9.

[53] T. Shikata, H. Hirata, T. Kotaka, Micelle formation of detergent molecules in aqueous media. 2. role of free salicylate ions on viscoelastic properties of aqueous cetyltrimethylammonium bromide-sodium salicylate solutions, Langmuir 4 (1988) 354–359. doi:10.1021/la00080a019.

[54] M. E. Cates, S. M. Fielding, Rheology of giant micelles, Advances in Physics 55 (2006) 799–879. doi:10.1080/00018730601082029.

[55] P. D. Olmsted, Two-state shear diagrams for complex fluids in shear flow, Europhysics Letters (EPL) 48 (1999) 339–345, shear banding. doi:10.1209/epl/i1999-00486-2.

[56] J. Yerushalmi, S. Katz, R. Shinnar, The stability of steady shear flows of some viscoelastic fluids, Chemical Engineering Science 25 (1970) 1891–1902. doi:10.1016/0009-2509(70)87007-5.

[57] P. D. Olmsted, Perspectives on shear banding in complex fluids, Rheologica Acta 47 (2008) 283–300. doi:10.1007/s00397-008-0260-9.

[58] H. von Berlepsch, L. Harnau, P. Reineker, Persistence length of wormlike micelles from dynamic light scattering, The Journal of Physical Chemistry B 102 (1998) 7518–7522, persistence length. doi:10.1021/jp980677x.

[59] W. Zou, R. G. Larson, A mesoscopic simulation method for predicting the rheology of semi-dilute wormlike micellar solutions, Journal of Rheology 58 (2014) 681–721, persistence length. doi:10.1122/1.4868875.

[60] T. Imae, The flexibility of rodlike micelles in aqueous solutions and the crossover concentrations among dilute, semidilute, and concentrated regimes, Colloid and Polymer Science 267 (1989) 707–713, persistence length. doi:10.1007/BF01524373.

[61] J.-F. Berret, R. Gamez-Corrales, J. Oberdisse, L. M. Walker, P. Lindner, Flow-structure relationship of shear-thickening surfactant solutions, Europhysics Letters (EPL) 41 (1998) 677–682, persistence length. doi:10.1209/epl/i1998-00213-1.

[62] M. R. Rojas, A. J. Müller, A. E. Sáez, Shear rheology and porous media flow of wormlike micelle solutions formed by mixtures of surfactants of opposite charge, Journal of Colloid and Interface Science 326 (2008) 221–226, flow induced structure. doi:10.1016/j.jcis.2008.07.022.

[63] R. K. Prud'homme, G. G. Warr, Elongational flow of solutions of rodlike micelles, Langmuir 10 (1994) 3419–3426, elongation of length. doi:10.1021/la00022a010.

[64] R. Omidvar, A. Dalili, A. Mir, H. Mohammadigoushki, Exploring sensitivity of the extensional flow to wormlike micellar structure, Journal of Non-Newtonian Fluid Mechanics 252 (2018) 48–56. doi:10.1016/j.jnnfm.2017.12.002.

[65] L. Chen, C. Zukoski, B. Ackerson, H. Hanley, G. Straty, J. Barker, C. Glinka, Structural changes and orientaional order in a sheared colloidal suspension, Physical Review Letters 69 (4) (1992) 688.

[66] J. K. Dhont, M. P. Lettinga, Z. Dogic, T. A. Lenstra, H. Wang, S. Rathgeber, P. Carletto, L. Willner, H. Frielinghaus, P. Lindner, Shear-banding and microstructure of colloids in shear flow, Faraday discussions 123 (2003) 157–172.

[67] S. Caserta, S. Guido, Vorticity banding in biphasic polymer blends, Langmuir 28 (47) (2012) 16254–16262.

[68] A. Mütze, P. Heunemann, P. Fischer, On the appearance of vorticity and gradient shear bands in wormlike micellar solutions of different cpcl/salt systems, Journal of Rheology 58 (6) (2014) 1647–1672.

[69] P. Boltenhagen, Y. Hu, E. Matthys, D. Pine, Observation of bulk phase separation and coexistence in a sheared micellar solution, Physical review letters 79 (12) (1997) 2359.

[70] P. Boltenhagen, Y. Hu, E. Matthys, D. Pine, Inhomogeneous structure formation and shear-thickening in worm-like micellar solutions, EPL (Europhysics Letters) 38 (5) (1997) 389.

[71] Y. T. Hu, P. Boltenhagen, D. J. Pine, Shear thickening in low-concentration solutions of wormlike micelles. i. direct visualization of transient behavior and phase transitions, Journal of Rheology 42 (1998) 1185–1208, shear thickening and thinning. doi:10.1122/1.550926.

[72] N. Dubash, P. Cheung, A. Q. Shen, Elastic instabilities in a microfluidic cross-slot flow of wormlike micellar solutions, Soft Matter 8 (2012) 5847. doi:10.1039/c2sm25215e.

[73] M. S. Turner, M. E. Cates, Flow-induced phase transitions in rod-like micelles, Journal of Physics: Condensed Matter 4 (1992) 3719–3741. doi:10.1088/0953-8984/4/14/005.

[74] M. E. Cates, M. S. Turner, Flow-induced gelation of rodlike micelles, Europhysics Letters (EPL) 11 (1990) 681–686. doi:10.1209/0295-5075/11/7/017.

[75] M. Doi, S. F. Edwards, The theory of polymer dynamics, Claredon Press, Oxford (1986). doi:10.1016/S1359-0286(96)80106-9.

[76] P. A. Vasquez, G. H. McKinley, L. P. Cook, A network scission model for wormlike micellar solutions, Journal of Non-Newtonian Fluid Mechanics 144 (2007) 122–139. doi:10.1016/j.jnnfm.2007.03.007.

[77] C. J. Pipe, N. J. Kim, P. A. Vasquez, L. P. Cook, G. H. McKinley, Wormlike micellar solutions: Ii. comparison between experimental data and scission model predictions, Journal of Rheology 54 (2010) 881–913. doi:10.1122/1.3439729.

[78] L. Zhou, G. H. McKinley, L. P. Cook, Wormlike micellar solutions: Iii. vcm model predictions in steady and transient shearing flows, Journal of Non-Newtonian Fluid Mechanics 211 (2014) 70–83. doi:10.1016/j.jnnfm.2014.06.003.

[79] M. E. Cates, Flow behaviour of entangled surfactant micelles, Journal of Physics: Condensed Matter 8 (1996) 9167–9176. doi:10.1088/0953-8984/8/47/006.

[80] M. Doi, Molecular dynamics and rheological properties of concentrated solutions of rodlike polymers in isotropic and liquid crystalline phases, Journal of Polymer Science: Polymer Physics Edition 19 (1981) 229–243. doi:10.1002/pol.1981.180190205.

[81] P. J. McCauley, M. A. Calabrese, S. Kumar, Interplay of wall slip and shear banding in wormlike micelle solutions, Journal of Non-Newtonian Fluid Mechanics 321 (2023) 105103. doi:10.1016/j.jnnfm.2023.105103.

[82] S. Varchanis, S. J. Haward, C. C. Hopkins, J. Tsamopoulos, A. Q. Shen, Evaluation of constitutive models for shear-banding wormlike micellar solutions in simple and complex flows, Journal of Non-Newtonian Fluid Mechanics 307 (2022) 104855. doi:10.1016/j.jnnfm.2022.104855.

[83] L. Zhou, L. Cook, G. H. McKinley, Probing shear-banding transitions of the vcm model for entangled wormlike micellar solutions using large amplitude oscillatory shear (laos) deformations, Journal of Non-Newtonian Fluid Mechanics 165 (2010) 1462–1472. doi:10.1016/j.jnnfm.2010.07.009.

[84] H. Mohammadigoushki, A. Dalili, L. Zhou, P. Cook, Transient evolution of flow profiles in a shear banding wormlike micellar solution: experimental results and a comparison with the vcm model, Soft Matter 15 (2019) 5483–5494. doi:10.1039/C9SM00816K.

[85] C. Sasmal, Flow of wormlike micellar solutions through a long micropore with step expansion and contraction, Physics of Fluids 32 (1) (2020).

[86] C. Sasmal, Unsteady motion past a sphere translating steadily in wormlike micellar solutions: A numerical analysis, Journal of Fluid Mechanics 912 (2021) A52.

[87] M. B. Khan, C. Sasmal, Flow dynamics of wormlike micellar solutions through a model porous media, arXiv preprint arXiv:2107.09453 (2021).

[88] N. Germann, L. Cook, A. Beris, Nonequilibrium thermodynamic modeling of the structure and rheology of concentrated wormlike micellar solutions, Journal of Non-Newtonian Fluid Mechanics 196 (2013) 51–57. doi:10.1016/j.jnnfm.2012.12.010.

[89] F. Bautista, J. Soltero, J. Pérez-López, J. Puig, O. Manero, On the shear banding flow of elongated micellar solutions, Journal of Non-Newtonian Fluid Mechanics 94 (2000) 57–66. doi:10.1016/S0377-0257(00)00128-2.

[90] O. Manero, J. Pérez-López, J. Escalante, J. Puig, F. Bautista, A thermodynamic approach to rheology of complex fluids: The generalized bmp model, Journal of Non-Newtonian Fluid Mechanics 146 (2007) 22–29. doi:10.1016/j.jnnfm.2007.02.012.

[91] J. Oldroyd, On the formulation of rheological equations of state, Proceedings of the Royal Society of London. Series A. Mathematical and Physical Sciences 200 (1950) 523–541. doi:10.1098/rspa.1950.0035.

[92] E. S. Shaqfeh, B. Khomami, The oldroyd-b fluid in elastic instabilities, turbulence and particle suspensions, Journal of Non-Newtonian Fluid Mechanics 298 (2021) 104672. doi:10.1016/j.jnnfm.2021.104672.

[93] A. G. Fredrickson, A model for the thixotropy of suspensions, AIChE Journal 16 (1970) 436–441. doi:10.1002/aic.690160321.

[94] H. A. Castillo, H. J. Wilson, Elastic instabilities in pressure-driven channel flow of thixotropic-viscoelasto-plastic fluids, Journal of Non-Newtonian Fluid Mechanics 261 (2018) 10–24. doi:10.1016/j.jnnfm.2018.07.009.

[95] J. E. López-Aguilar, O. Resendiz-Tolentino, H. R. Tamaddon-Jahromi, M. Ellero, O. Manero, Flow past a sphere: Numerical predictions of thixo-viscoelastoplastic wormlike micellar solutions, Journal of Non-Newtonian Fluid Mechanics 309 (2022) 104902. doi:10.1016/j.jnnfm.2022.104902.

[96] H. A. C. Sánchez, J. Bertoco, A. Castelo, M. S. B. de Araújo, Numerical simulation of a thixotropic-viscoelastic model in expansion-contraction geometries, SSRN Electronic Journal (2022). doi:10.2139/ssrn.4048814.

[97] F. Bautista, J. F. A. Soltero, E. R. Macías, J. E. Puig, O. Manero, Irreversible thermodynamics approach and modeling of shear-banding flow of wormlike micelles, The Journal of Physical Chemistry B 106 (2002) 13018–13026. doi:10.1021/jp0206370.

[98] E. Boek, J. Padding, V. Anderson, P. J. Tardy, J. Crawshaw, J. A. Pearson, Constitutive equations for extensional flow of wormlike micelles: stability analysis of the bautista–manero model, Journal of Non-Newtonian Fluid Mechanics 126 (2005) 39–46. doi:10.1016/j.jnnfm.2005.01.001.

[99] S. Tamano, S. Hamanaka, Y. Nakano, Y. Morinishi, T. Yamada, Rheological modeling of both shear-thickening and thinning behaviors through constitutive equations, Journal of Non-Newtonian Fluid Mechanics 283 (2020) 104339. doi:10.1016/j.jnnfm.2020.104339.

[100] J. K. G. Dhont, W. J. Briels, Rod-Like Brownian Particles in Shear Flow: Sections 3.1– 3.9, Wiley-VCH Verlag GmbH & Co. KGaA, 2004, pp. 147–216, closures. doi:10.1002/9783527617067.ch3a.

[101] M. G. Forest, Q. Wang, Monodomain response of finite-aspect-ratio macromolecules in shear and related linear flows, Rheologica Acta 42 (2003) 20–46, closures. doi:10.1007/s00397-002-0252-0.

[102] P. T. Corona, K. Dai, M. E. Helgeson, L. Leal, Testing orientational closure approximations in dilute and non-dilute suspensions with rheo-sans, Journal of Non-Newtonian Fluid Mechanics 315 (2023) 105014, closures. doi:10.1016/j.jnnfm.2023.105014.

[103] J. K. Dhont, W. Briels, Viscoelasticity of suspensions of long, rigid rods, Colloids and Surfaces A: Physicochemical and Engineering Aspects 213 (2003) 131–156. doi:10.1016/S0927-7757(02)00508-3.

[104] P. S. Stephanou, A constitutive hemorheological model addressing both the deformability and aggregation of red blood cells, Physics of Fluids 32 (10 2020). doi:10.1063/5.0022493.

[105] P. S. Stephanou, I. C. Tsimouri, A constitutive hemorheological model addressing the deformability of red blood cells in ringer solutions, Soft Matter 16 (32) (2020) 7585–7597.

[106] C. Oelschlaeger, P. Suwita, N. Willenbacher, Effect of counterion binding efficiency on structure and dynamics of wormlike micelles, Langmuir 26 (10) (2010) 7045–7053.

[107] S. R. Raghavan, E. W. Kaler, Highly viscoelastic wormlike micellar solutions formed by cationic surfactants with long unsaturated tails, Langmuir 17 (2) (2001) 300–306.

[108] I. Wunderlich, H. Hoffmann, H. Rehage, Flow birefringence and rheological measurements on shear induced micellar structures, Rheologica Acta 26 (6) (1987) 532–542.

[109] J. L. Zakin, A. J. Maxson, T. Saeki, P. F. Sullivan, Turbulent Drag-reduction Applications of Surfactant Solutions, in: C. A. Dreiss, Y. Feng (Eds.), Wormlike Micelles: Advances in Systems, Characterization and Applications, Royal Society of Chemistry, 2017, pp. 353–378.

[110] M. Cates, M. Turner, Flow-induced gelation of rodlike micelles, EPL (Europhysics Letters) 11 (7) (1990) 681.

[111] J. D. Peterson, M. Cates, A full-chain tube-based constitutive model for living linear polymers, Journal of Rheology 64 (6) (2020) 1465–1496.

[112] A. A. Adams, M. J. Solomon, R. G. Larson, A nonlinear kinetic-rheology model for reversible scission and deformation of unentangled wormlike micelles, Journal of Rheology 62 (6) (2018) 1419–1427.

[113] F. Bautista, J. De Santos, J. Puig, O. Manero, Understanding thixotropic and antithixotropic behavior of viscoelastic micellar solutions and liquid crystalline dispersions. i. the model, Journal of Non-Newtonian Fluid Mechanics 80 (2-3) (1999) 93–113.

[114] J. K. Dhont, W. J. Briels, Rod-like brownian particles in shear flow, Soft Matter: Complex Colloidal Suspensions, edited by G. Gompper, M. Schick 2 (2006).

[115] M. D. Graham, Microhydrodynamics, Brownian Motion, and Complex Fluids, Cambridge Texts in Applied Mathematics, Cambridge University Press, Cambridge, 2018.

[116] S. Wu, H. Mohammadigoushki, Flow of a model shear-thickening micellar fluid past a falling sphere, Physical Review Fluids 4 (7) (2019) 073303.

[117] E. Hinch, L. Leal, The effect of brownian motion on the rheological properties of a suspension of non-spherical particles, Journal of Fluid Mechanics 52 (4) (1972) 683–712.

[118] H. Öttinger, A note on rigid dumbbell solutions at high shear rates, Journal of Rheology 32 (2) (1988) 135–143.

[119] S. Hofmann, A. Rauscher, H. Hoffmann, Shear induced micellar structures, Berichte der Bunsengesellschaft für physikalische Chemie 95 (2) (1991) 153–164.

[120] R. Oda, V. Weber, P. Lindner, D. Pine, E. Mendes, F. Schosseler, Time-resolved small-angle neutron scattering study of shear-thickening surfactant solutions after the cessation of flow, Langmuir 16 (11) (2000) 4859–4863.

[121] S. Yamamoto, S.-a. Hyodo, Mesoscopic simulation of the crossing dynamics at an entanglement point of surfactant threadlike micelles, The Journal of chemical physics 122 (20) (2005) 204907.

[122] J.-F. Berret, Transient rheology of wormlike micelles, Langmuir 13 (8) (1997) 2227–2234.

[123] M. D. Graham, Drag reduction and the dynamics of turbulence in simple and complex fluids, Physics of Fluids 26 (10) (2014) 625–656.

[124] J. P. Rothstein, Strong flows of viscoelastic wormlike micelle solutions, Rheol. Rev 2008 (2008) 1–46.

[125] H. von Berlepsch, L. Harnau, P. Reineker, Persistence length of wormlike micelles from dynamic light scattering, The Journal of Physical Chemistry B 102 (39) (1998) 7518–7522.

[126] M. E. Helgeson, T. K. Hodgdon, E. W. Kaler, N. J. Wagner, A systematic study of equilibrium structure, thermodynamics, and rheology of aqueous ctab/nano3 wormlike micelles, Journal of Colloid and Interface Science 349 (1) (2010) 1–12.

[127] L. K. Shrestha, M. Yamamoto, S. Arima, K. Aramaki, Charge-free reverse wormlike micelles in nonaqueous media, Langmuir 27 (6) (2011) 2340–2348.

[128] S.-H. Tung, Y.-E. Huang, S. R. Raghavan, Contrasting effects of temperature on the rheology of normal and reverse wormlike micelles, Langmuir 23 (2) (2007) 372–376.

[129] R. J. Hommel, M. D. Graham, Constitutive modeling of dilute wormlike micelle solutions: Shear-induced structure and transient dynamics, Journal of Non-Newtonian Fluid Mechanics 295 (2021) 104606.

[130] J. Decruppe, R. Cressely, R. Makhloufi, E. Cappelaere, Flow birefringence experiments showing a shear-banding structure in a ctab solution, Colloid and Polymer Science 273 (4) (1995) 346–351.

[131] M. Cromer, M. C. Villet, G. H. Fredrickson, L. G. Leal, Shear banding in polymer solutions, Physics of Fluids 25 (5) (2013) 051703.

[132] T. Divoux, M. A. Fardin, S. Manneville, S. Lerouge, Shear banding of complex fluids, Annual Review of Fluid Mechanics 48 (2016) 81–103.

[133] C. J. Petrie, M. M. Denn, Instabilities in polymer processing, AIChE Journal 22 (2) (1976) 209–236.

[134] P. Olmsted, C. David Lu, Phase coexistence of complex fluids in shear flow, Faraday Discussions 112 (1999) 183–194.

[135] S. M. Fielding, Vorticity structuring and velocity rolls triggered by gradient shear bands, Physical Review E 76 (1) (2007) 016311.

[136] R. N. Chacko, R. Mari, M. E. Cates, S. M. Fielding, Dynamic vorticity banding in discontinuously shear thickening suspensions, Physical Review Letters 121 (10) (2018) 108003.

[137] G. M. Wilson, B. Khomami, An experimental investigation of interfacial instabilities in multilayer flow of viscoelastic fluids: Part 1. incompatible polymer systems, Journal of Non-Newtonian Fluid Mechanics 45 (3) (1992) 355–384.

[138] G. M. Wilson, B. Khomami, An experimental investigation of interfacial instabilities in multilayer flow of viscoelastic fluids. part 2. elastic and nonlinear effects in incompatible polymer systems, Journal of Rheology 37 (2) (1993) 315–339.

[139] G. M. Wilson, B. Khomami, An experimental investigation of interfacial instabilities in multilayer flow of viscoelastic fluids. 3. compatible polymer systems, Journal of Rheology 37 (2) (1993) 341–354.

[140] S. Yamani, Y. Raj, T. A. Zaki, G. H. McKinley, I. Bischofberger, Spatiotemporal signatures of elastoinertial turbulence in viscoelastic planar jets, Physical Review Fluids 8 (6) (2023) 064610.

[141] J. López-Aguilar, M. Webster, H. Tamaddon-Jahromi, O. Manero, Predictions for circular contraction-expansion flows with viscoelastoplastic & thixotropic fluids, Journal of Non-Newtonian Fluid Mechanics 261 (2018) 188–210.

[142] J. E. Lopez-Aguilar, O. Resendiz-Tolentino, H. R. Tamaddon-Jahromi, M. Ellero, O. Manero, Flow past a sphere: Numerical predictions of thixo-viscoelastoplastic wormlike micellar solutions, Journal of Non-Newtonian Fluid Mechanics 309 (2022) 104902.

[143] H. Jasak, A. Jemcov, Z. Tukovic, et al., Openfoam: A c++ library for complex physics simulations, in: International workshop on coupled methods in numerical dynamics, Vol. 1000, 2007, pp. 1–20.

[144] F. Pimenta, M. Alves, Stabilization of an open-source finite-volume solver for viscoelastic fluid flows, Journal of Non-Newtonian Fluid Mechanics 239 (2017) 85–104.

[145] F. Pimenta, M. Alves, rheotool, `https://github.com/fppimenta/rheoTool` (2016).

[146] J. Favero, A. Secchi, N. Cardozo, H. Jasak, Viscoelastic flow analysis using the software openfoam and differential constitutive equations, Journal of Non-Newtonian Fluid Mechanics 165 (23-24) (2010) 1625–1636.

[147] C.-Y. D. Lu, P. D. Olmsted, R. Ball, Effects of nonlocal stress on the determination of shear banding flow, Physical Review Letters 84 (4) (2000) 642.

[148] R. J. Hommel, M. D. Graham, Flow instabilities in circular couette flow of wormlike micelle solutions with a reentrant flow curve, Journal of Non-Newtonian Fluid Mechanics 324 (2024) 105183. doi:10.1016/j.jnnfm.2023.105183.

[149] P. Nghe, S. M. Fielding, P. Tabeling, A. Ajdari, Interfacially driven instability in the microchannel flow of a shear-banding fluid, Physical Review Letters 104 (2010) 248303. doi:10.1103/PhysRevLett.104.248303.

[150] T. Yamamoto, T. Hashimoto, A. Yamashita, Flow analysis for wormlike micellar solutions in an axisymmetric capillary channel, Rheologica Acta 47 (2008) 963–974. doi:10.1007/s00397-008-0288-x.

[151] M. Cromer, L. P. Cook, G. H. McKinley, Pressure-driven flow of wormlike micellar solutions in rectilinear microchannels, Journal of Non-Newtonian Fluid Mechanics 166 (2011) 180–193. doi:10.1016/j.jnnfm.2010.11.007.

[152] M. Cromer, L. Cook, G. H. McKinley, Interfacial instability of pressure-driven channel flow for a two-species model of entangled wormlike micellar solutions, Journal of Non-Newtonian Fluid Mechanics 166 (2011) 566–577. doi:10.1016/j.jnnfm.2011.01.005.

[153] R. Govindarajan, K. C. Sahu, Instabilities in viscosity-stratified flow, Annual Review of Fluid Mechanics 46 (2014) 331–353. doi:10.1146/annurev-fluid-010313-141351.

[154] L. Talon, E. Meiburg, Plane poiseuille flow of miscible layers with different viscosities: instabilities in the stokes flow regime, Journal of Fluid Mechanics 686 (2011) 484–506. doi:10.1017/jfm.2011.341.

[155] K. C. Sahu, H. Ding, P. Valluri, O. K. Matar, Linear stability analysis and numerical simulation of miscible two-layer channel flow, Physics of Fluids 21 (4 2009). doi:10.1063/1.3116285.

[156] H. K. Ganpule, B. Khomami, A theoretical investigation of interfacial instabilities in the three layer superposed channel flow of viscoelastic fluids, Journal of Non-Newtonian Fluid Mechanics 79 (1998) 315–360. doi:10.1016/S0377-0257(98)00114-1.

[157] M. d'Olce, J. Martin, N. Rakotomalala, D. Salin, L. Talon, Convective/absolute instability in miscible core-annular flow. part 1: Experiments, Journal of Fluid Mechanics 618 (2009) 305–322. doi:10.1017/S0022112008004230.

[158] E. J. Hinch, A note on the mechanism of the instability at the interface between two shearing fluids, Journal of Fluid Mechanics 144 (1984) 463–465. doi:10.1017/S0022112084001695.

[159] M. d'Olce, J. Martin, N. Rakotomalala, D. Salin, L. Talon, Pearl and mushroom instability patterns in two miscible fluids' core annular flows, Physics of Fluids 20 (2 2008). doi:10.1063/1.2838582.

[160] C.-H. Li, Instability of three-layer viscous stratified flow, The Physics of Fluids 12 (1969) 2473–2481. doi:10.1063/1.1692383.

[161] P. Than, F. Rosso, D. Joseph, Instability of poiseuille flow of two immiscible liquids with different viscosities in a channel, International Journal of Engineering Science 25 (1987) 189–204. doi:10.1016/0020-7225(87)90005-X.

[162] P. Laure, H. L. Meur, Y. Demay, J. Saut, S. Scotto, Linear stability of multilayer plane poiseuille flows of oldroyd b fluids, Journal of Non-Newtonian Fluid Mechanics 71 (1997) 1–23. doi:10.1016/S0377-0257(97)00011-6.

[163] J. Jiménez, P. Moin, The minimal flow unit in near-wall turbulence, Journal of Fluid Mechanics 225 (1991) 213–240. doi:10.1017/S0022112091002033.

[164] A. N. Beris, B. J. Edwards, Thermodynamics of flowing systems: with internal microstructure, no. 36, Oxford University Press, USA, 1994.

[165] M. Grmela, Bracket formulation of dissipative fluid mechanics equations, Physics Letters A 102 (1984) 355–358. doi:10.1016/0375-9601(84)90297-4.

[166] P. J. Morrison, Bracket formulation for irreversible classical fields, Physics Letters A 100 (1984) 423–427. doi:10.1016/0375-9601(84)90635-2.

[167] A. N. Kaufman, Dissipative hamiltonian systems: A unifying principle, Physics Letters A 100 (1984) 419–422. doi:10.1016/0375-9601(84)90634-0.

[168] A. N. Beris, B. J. Edwards, Poisson bracket formulation of viscoelastic flow equations of differential type: A unified approach, Journal of Rheology 34 (1990) 503–538. doi:10.1122/1.550094.

[169] M. Grmela, H. C. Öttinger, Dynamics and thermodynamics of complex fluids. i. development of a general formalism, Physical Review E 56 (6) (1997) 6620.

[170] B. J. Edwards, Evaluation of the thermodynamic consistency of closure approximations in several models proposed for the description of liquid crystalline dynamics, Journal of Non-Equilibrium Thermodynamics 27 (1) (2002) 5–24.

[171] H. C. Öttinger, Beyond Equilibrium Thermodynamics, Wiley, 2005. doi:10.1002/0471727903.

[172] A. N. Beris, B. J. Edwards, Poisson bracket formulation of incompressible flow equations in continuum mechanics, Journal of Rheology 34 (1990) 55–78. doi:10.1122/1.550114.

[173] B. J. Edwards, A. N. Beris, M. Grmela, Generalized constitutive equation for polymeric liquid crystals part 1. model formulation using the hamiltonian (poisson bracket) formulation, Journal of Non-Newtonian Fluid Mechanics 35 (1990) 51–72. doi:10.1016/0377-0257(90)85072-7.

[174] A. N. Beris, B. J. Edwards, Dissipation in nonequilibrium thermodynamics and its connection to the rayleighian functional, Physics of Fluids 36 (1 2024). doi:10.1063/5.0180407.

[175] P. S. Stephanou, G. G. Georgiou, A nonequilibrium thermodynamics perspective of thixotropy, The Journal of Chemical Physics 149 (24) (2018).

[176] I. C. Tsimouri, P. S. Stephanou, V. G. Mavrantzas, A constitutive rheological model for agglomerating blood derived from nonequilibrium thermodynamics, Physics of Fluids 30 (3 2018). doi:10.1063/1.5016913.

[177] A. K. Ioannou, P. S. Stephanou, Nonequilibrium thermodynamics modeling of the rheological response of cement pastes, Journal of Rheology 67 (4) (2023) 849–849.

[178] P. S. Stephanou, On the consistent modeling of shear-thickening polymer solutions, Physics of Fluids 33 (6) (2021).

[179] M. Giaquinta, S. Hildebrandt, Calculus of Variations I, Vol. 310, Springer Berlin Heidelberg, 2004. doi:10.1007/978-3-662-03278-7.

[180] M. Kröger, M. Hütter, H. C. Öttinger, Symbolic test of the jacobi identity for given generalized 'poisson'bracket, Computer physics communications 137 (2) (2001) 325–340.

[181] P. R. Majhi, P. L. Dubin, X. Feng, X. Guo, F. A. M. Leermakers, C. Tribet, Coexistence of spheres and rods in micellar solution of dodecyldimethylamine oxide, The Journal of Physical Chemistry B 108 (2004) 5980–5988. doi:10.1021/jp0374307.

[182] P. M. Mwasame, A. N. Beris, R. B. Diemer, N. J. Wagner, A constitutive equation for thixotropic suspensions with yield stress by coarse-graining a population balance model, AIChE Journal 63 (2017) 517–531. doi:10.1002/aic.15574.

[183] S. Jariwala, R. Song, J. B. Hipp, R. B. Diemer, N. J. Wagner, A. N. Beris, A polydisperse model for thixotropic elasto-viscoplastic suspensions of aggregating particles using population balances, AIChE Journal 69 (10 2023). doi:10.1002/aic.18184.

[184] R. G. Larson, E. S. G. Shaqfeh, S. J. Muller, A purely elastic instability in taylor–couette flow, Journal of Fluid Mechanics 218 573. doi:10.1017/S0022112090001124.

[185] S. Muller, E. Shaqfeh, R. Larson, Experimental studies of the onset of oscillatory instability in viscoelastic taylor-couette flow, Journal of Non-Newtonian Fluid Mechanics 46 (1993) 315–330. doi:10.1016/0377-0257(93)85053-D.

[186] M. Avgousti, A. Beris, Viscoelastic taylor–couette flow: bifurcation analysis in the presence of symmetries, Proceedings of the Royal Society of London. Series A: Mathematical and Physical Sciences 443 (1993) 17–37. doi:10.1098/rspa.1993.0129.

[187] M. Avgousti, A. N. Beris, Non-axisymmetric modes in viscoelastic taylor-couette flow, Journal of Non-Newtonian Fluid Mechanics 50 (1993) 225–251. doi:10.1016/0377-0257(93)80033-8.

[188] D. J. Acheson, Elementary Fluid Dynamics, Vol. 89, Clarendon Press, 1991. doi:10.1121/1.400751.

[189] S. Ezrahi, E. Tuval, A. Aserin, Properties, main applications and perspectives of worm micelles, Advances in Colloid and Interface Science 128-130 (2006) 77–102. doi:10.1016/j.cis.2006.11.017.

[190] A. R. Acharya, Particle transport in viscous and viscoelastic fracturing fluids, SPE Production Engineering 1 (1986) 104–110. doi:10.2118/13179-PA.

[191] M. Kumar, A. M. Ardekani, Elastic instabilities between two cylinders confined in a channel, Physics of Fluids 33 (7 2021). doi:10.1063/5.0057497.

[192] M. Kumar, S. Aramideh, C. A. Browne, S. S. Datta, A. M. Ardekani, Numerical investigation of multistability in the unstable flow of a polymer solution through porous media, Physical Review Fluids 6 (2021) 033304. doi:10.1103/PhysRevFluids.6.033304.

[193] M. Kumar, D. M. Walkama, A. M. Ardekani, J. S. Guasto, Stress and stretching regulate dispersion in viscoelastic porous media flows, Soft Matter 19 (2023) 6761–6770. doi:10.1039/D3SM00224A.

[194] J. Dinic, L. N. Jimenez, V. Sharma, Pinch-off dynamics and dripping-onto-substrate (dos) rheometry of complex fluids, Lab on a Chip 17 (2017) 460–473. doi:10.1039/C6LC01155A.

[195] J. Dinic, V. Sharma, Macromolecular relaxation, strain, and extensibility determine elastocapillary thinning and extensional viscosity of polymer solutions, Proceedings of the National Academy of Sciences 116 (2019) 8766–8774. doi:10.1073/pnas.1820277116.

[196] D. Y. Zhang, M. A. Calabrese, Temperature-controlled dripping-onto-substrate (dos) extensional rheometry of polymer micelle solutions, Soft Matter 18 (2022) 3993–4008. doi:10.1039/D2SM00377E.

[197] S. L. Anna, G. H. McKinley, Elasto-capillary thinning and breakup of model elastic liquids, Journal of Rheology 45 (2001) 115–138. doi:10.1122/1.1332389.

[198] K. Sujatha, H. Matallah, M. Banaai, M. Webster, Computational predictions for viscoelastic filament stretching flows: Ale methods and free-surface techniques (cm and vof), Journal of Non-Newtonian Fluid Mechanics 137 (2006) 81–102. doi:10.1016/j.jnnfm.2006.03.009.

[199] G. I. Taylor, Viii. stability of a viscous liquid contained between two rotating cylinders, Philosophical Transactions of the Royal Society of London. Series A, Containing Papers of a Mathematical or Physical Character 223 (1923) 289–343. doi:10.1098/rsta.1923.0008.

[200] K. J. Burns, G. M. Vasil, J. S. Oishi, D. Lecoanet, B. P. Brown, Dedalus: A flexible framework for numerical simulations with spectral methods, Physical Review Research 2 (2020) 023068. doi:10.1103/PhysRevResearch.2.023068.